Modelling and Simulation of Faceted Boundary Structures and Dynamics in FCC Crystalline Materials

Wu Zhaoxuan

National University of Singapore

Submitted to the NUS Graduate School for Integrative Sciences and Engineering
in partial fulfillment of the requirements for the degree of

Doctor of Philosophy

December 2010

I would like to dedicate this Thesis to my family.

Acknowledgements

This Thesis would not have been possible without the inspiration and encouragement from my supervisors, Professor Zhang Yongwei and Professor David J. Srolovitz. I am fortunate to work with both of them during my four years of graduate study.

I would like to express my sincere gratitude to Professor Zhang for helping me in every aspect of research and life, and for demonstrating his knowledge and creativity in research. Professor Zhang also patiently went through all my writings, including this Thesis.

I am very much indebted to Professor Srolovitz for guiding me throughout the four years and the numerous hours he spent working with me on my papers in a "word by word" fashion. I have all my respect for his patience, knowledge and wisdom.

I would also like to thank Dr. Zeng Kaiyang for serving on my thesis advisory committee and Dr. Jerry Quek, Dr. Mark Jhon for reading my Thesis and providing valuable suggestions for improvement on this Thesis. My thanks also go to all the faculty and technical staffs at the NUS Graduate School for Integrative Sciences and Engineering and the Department of Materials Science and Engineering, where most of my research work were carried out.

I am grateful to Professor Huajian Gao and Professor Peter Gumbsch for inspiring and useful discussions during their visits to the Institute of High Performance Computing (IHPC).

My research has been supported by the Agency for Science, Technology and Research (A*STAR), Singapore. I gratefully acknowledge the financial support and the use of computing resources at the A*STAR Computational Resource Centre, Singapore.

Abstract

Large scale molecular dynamics (MD) simulations are employed to study faceted grain boundaries' defect structures and dynamics in face-centered cubic (FCC) crystalline metals. In particular, two problems: (1) the plastic deformation of nanotwinned FCC metals; (2) the finite length grain boundary faceting are investigated in detail. The plastic deformation of nanotwinned copper is studied through MD simulations employing an embedded-atom method (EAM) potential. Two dislocation-twin interaction mechanisms that explain the observation of both ultrahigh strength and ductility in nanotwinned FCC metals are found. First, the interaction of a 60° dislocation with a twin boundary leads to the formation of a $\{001\}\langle 110\rangle$ Lomer dislocation which, in turn, dissociates into Shockley, stair-rod and Frank partial dislocations. Second, the interaction of a 30° Shockley partial dislocation with a twin boundary generates three new Shockley partials during twin-mediated slip transfer. The generation of a high-density of Shockley partial dislocations on several different slip systems contributes to the observed ultrahigh ductility while the formation of sessile stair-rod and Frank partial dislocations (together with the presence of the twin boundaries themselves) explain observations of ultrahigh strength.

Furthermore, polycrystalline MD simulations show that the plastic deformation of nanotwinned copper is initiated by the nucleations of partial dislocation at grain boundary triple junctions. Both dislocations crossing twin boundaries and dislocation-induced twin migrations are observed in the simulations. For the dislocation crossing mechanism, 60° dislocations frequently cross slip onto $\{001\}$ planes in twin grains and form Lomer dislocations, constituting the dominant crossing mechanism. We further examine the effect of twin spacing on this dominant Lomer dislocation mechanism through a series of specifically-designed nanotwinned copper samples over a wide range of twin spacing. The simulations show

that a transition in the dominant dislocation mechanism occurs at a small critical twin spacing. While at large twin spacing, cross-slip and dissociation of the Lomer dislocations create dislocation locks which restrict and block dislocation motion and thus enhance strength. At twin spacing below the critical size, cross-slip does not occur, steps on the twin boundaries form and deformation is much more planar. These twin steps can migrate and serve as dislocation nucleation sites, thus softening the material. Based on these mechanistic observations, a simple, analytical model for the critical twin spacing is proposed and the predicted critical twin spacing is shown to be in excellent agreement both with respect to the atomistic simulations and experimental observation. This suggests the above dislocation mechanism transition is a source of the observed transition in nanotwinned copper strength.

For the problem of finite length grain boundary faceting, both symmetrical and asymmetrical aluminium grain boundary faceting are studied with MD simulations employing two EAM potentials. Facets formation, coarsening, reversible phase transition of $\Sigma 3\{110\}$ boundary into $\Sigma 3\{112\}$ twin and vice versa are demonstrated in the simulations and the results are are shown to be consistent with earlier experimental study and theoretical model. The $\Sigma 11\{002\}_1/\{667\}_2$ boundary shows faceting into $\{225\}_1/\{441\}_2$ and $\{667\}_1/\{001\}_2$ boundaries and coarsens with a slower rate when compared to $\Sigma 3\{112\}$ facets. However, facets formed by $\{111\}_1/\{112\}_2$ and $\{001\}_1/\{110\}_2$ boundaries from a $\{116\}_1/\{662\}_2$ boundary is stable against finite temperature annealing. In the above faceted boundary, elastic strain energy induced by atomic mismatch across the boundary creates barriers to facet coarsening. Grain boundary tension is too small to stabilize the finite length faceting in both $\Sigma 3\{112\}$ twin and asymmetrical $\{111\}_1/\{112\}_2$ and $\{001\}_1/\{110\}_2$ facets. The observed finite facet sizes are dictated by facet coarsening kinetics which can be strongly retarded by deep local energy minima associated with atomic matching across the boundary.

Contents

List of Figures

List of Tables

Nomenclature

Roman Symbols

n	Coordination Number
$\boldsymbol{a}$	Lattice Vector
a	Cubic Lattice Parameter

Greek Symbols

η_2	Conjugate Twinning Direction
η_1	Twinning Direction
$\boldsymbol{\xi}_n$	Lattice Basis Vector
$\boldsymbol{\gamma}_{ssf}$	Stable Stacking Fault Energy
$\boldsymbol{\gamma}_{usf}$	Unstable Stacking Fault Energy
$\boldsymbol{\gamma}_{utm}$	Unstable Twin Boundary Migration Energy

Superscripts

$\boldsymbol{a}^*$	Reciprocal Lattice Vector
G^{ij}	Reciprocal Metric Tensor
$\boldsymbol{c}^j$	Reciprocal Primitive Vectors

Subscripts

c_p	Central Symmetry Parameter

K_2	Conjugate Twinning Plane
G_{ij}	Metric Tensor
$\boldsymbol{c}_i$	Lattice Primitive Vector
K_1	Twinning Plane
$\boldsymbol{e}_i$	Cartesian Basis Vector

Chapter 1

Introduction

Research in materials science can be broadly classified into two categories: (1) experimental study; (2) theoretical modelling. Apart from the above two conventional approaches, a new method, computational modelling, has emerged together with a half-century relentless advance in integrated circuits technology [3]. Computational methods, varying from the scale-independent finite element analysis to first principle electronic structure calculation, have been developed to study problems across a wide range of spatial and temporal scales in materials science and engineering. Computational simulations, or computational experiments, often have great advantages over conventional methods. They provide precise controls on system variables, easy tests of extreme conditions and in some cases, offer both atomistic spatial and temporal resolutions simultaneously which are usually difficult to access in experiments. Computational methods including continuum modelling and atomistic simulations are becoming an indispensable approach in many fields of materials research. With no exception, we made an extensive use of computer simulations for the study of defects in crystalline materials in this Thesis.

The field of materials research is broad in terms of material type, structure and function. Among those materials used in our daily life, crystalline materials including metals and semiconductors are of exceptional importance. The study of crystalline materials has two parts: (1) perfect crystals; (2) imperfect crystals [4]. The former studies crystals where atoms are sitting on regular repeating sites and all atoms are well coordinated. Various material properties, such as quantum states, lattice structures, elastic properties, etc., can be readily obtained via first principle calculations. The latter, the study of imperfect crystals, is associated with crystalline defects of various dimensions. It is well recognized that crystalline materials' properties are

often strongly influenced by their underlying microstructures, which in turn are characterized by crystalline defects. For example, in semiconducting materials, the dopant concentration governs these materials' conductivity. One-dimensional line defects, or dislocations, play a deterministic role in the plastic deformation of many metals. Higher dimensional defects like interfacial boundaries control materials' microstructure evolution and their subsequent properties. In general, the study of defects becomes more difficult with increasing dimensionality. It becomes more complicated when material properties are determined by the interactions of the various defects of different dimensions. Such examples include interfacial strengthening in alloys and multi-layered composites where interactions between dislocations and interfaces determine the various mechanical properties of these materials.

While crystalline defects have many forms and properties, a generalized study or theory for all of them is difficult. Among the various types of defect, grain boundaries, being 2-dimensional defects, have one of the most complex defect structures. A grain boundary has 5 macroscopic degrees of freedom (3 relating to the orientation of the crystallographic axes of one grain to those of the other and 2 to the inclination of the boundary plane) and 3 microscopic degrees of freedom (corresponding to rigid body translations of one grain relative to the other). The latter are not usually specified since nature is free to choose the translation state that, for example, corresponds to the minimum free energy. These eight parameters are, however, the minimum number of degrees of freedom. There are, of course, many more microscopic degrees of freedom, corresponding to the arrangement of the atoms within the boundary plane. These too may be found by the minimization of the free energy of the system with respect to atomic coordinates (and composition) with the five macroscopic degrees of freedom specified. Given the above large number of degrees of freedom in specifying a grain boundary, it is without doubt that our understanding of grain boundaries and their contribution towards material properties remains incomplete and various important issues concerning grain boundaries remain open.

Although the types of grain boundaries are enormous, there are some grain boundaries which are of special interest. Faceted grain boundaries are such examples due to their frequent occurrence in crystalline materials. The most special type of faceted boundary is the twin boundary. Various types of twin boundaries including deformation twins, transformation twins and growth twins with twin sizes ranging from a few hundred to a few nanometers are observed in metallic systems [5–20]. Most notably, pure polycrystalline Cu with a high density of growth nanotwins exhibits a combination of attractive properties, such as simultaneous ultrahigh strength, ductility, electric conductivity and strain hardening [12, 13]. Currently, there

is a considerable research effort in understanding and designing nanotwinned metals for future engineering applications.

Twins are very special faceted boundaries. Faceted of grain boundaries with more general structures have also been observed experimentally on the micrometer scale in nominally pure Zn [21], Au [22–24], Al [23], Cu [25], Ag [26], and Ni [27], as well as in alloys such as Cu-Bi [28]. Nanometer scale grain boundary facets have been observed in Au [24, 29], Al [30], α-Al_2O_3 [31], $SrTiO_3$ [32], and $BaTiO_3$ [33]. While in many cases, faceting appears to be irregular, there are several observations of nano-faceting (also described as fine hill and valley structures), for which the facet lengths are nearly constant. Such examples include Al [34], Au [29], and α-Al_2O_3 [31].

In this Thesis, we focus on studying faceted grain boundaries in face-centered cubic (FCC) metals. In particular, two problems are examined in detail. The first problem is on the plastic deformation of FCC Cu with coherent growth nanotwins and the second is on the length scales of grain boundary faceting. Metallic systems grown by electro-deposition, such as Pd [35], Cd [35], Ag [36], Au [37], Cu [12], or sputtering, such as Cu [11], Cu/304 stainless steel [38], tend to contain a high density of growth nanotwins. These resulting materials often exhibit unusual, yet attractive properties such as ultrahigh strength, ductility, strain hardening and conductivity. While it is evident that the growth nanotwins have a dominant role in the plastic deformation of these metals, the atomistic mechanisms operating during plastic deformations and hence their actual contributions towards the observed material properties are unclear. For the latter problem concerning more generally faceted boundaries, the factors determining facets length scale are unclear and have attracted many research effort from both experimentalists and theoreticians throughout the last few decades. We select these two problems because of their importance in the current materials research and their shared boundary structure (both are faceted). We employ molecular dynamics (MD) simulations together with continuum elastic theory in this study. While MD simulations provide the necessary spatial and temporal resolution for those defects and their evolution in crystalline materials, continuum theory allows us to extrapolate to more general cases and predict material properties beyond simulation results. In the following, we introduce the two classes of problems together with a brief summary of the main findings of this work.

1.1 Plastic Deformation of Nanotwinned FCC Metals

1.1.1 Problem Statement

Producing materials with optimized properties has been a constant goal of materials research and engineering. For engineering materials such as metals and their alloys, increasing their strength and ductility is a critical concern. For metallic materials, strengthening is usually achieved through microstructure manipulation. Most commonly, the microstructural length scales used to manipulate the mechanical properties of metals are associated with particle (precipitates, second phase particles,...) or interface (grain boundaries, twins,...) separation. Unfortunately, increases in alloy strength through grain refinement at microstructural length scales are usually accompanied by a concomitant decrease in ductility. It is clear that refinement only at microstructural length scales is insufficient to optimize these two competing mechanical properties and this often poses a dilemma to the materials science community in materials design.

Recent advances in growth techniques have made it possible to refine both microstructure length scales and characters, thus offering opportunities for optimizing material properties previously unachievable. One particular example is pure metals with coherent growth nanotwins which are special boundaries with a faceted interface. Twins are especially good for controlling strength because of their extraordinary stability relative to other microstructural features [10]. The small microstructual length scales inherent in nanomaterials open the door to the development of ultra-high-strength metals [10–20]. Interestingly, some nanotwinned metals paradoxically exhibit both high strength and high ductility; e.g., in Cu [11–14] and Co [15]. Most notably, Lu et al. [12] synthesized ultra-fine pure crystalline Cu containing a high density of growth twins via a pulsed electrodeposition technique. The resulting material is unusual in that it simultaneously exhibits high yield strength, high ductility, high strain-rate sensitivity and high electric conductivity [10, 39, 40].

High resolution transmission electron microscopy (TEM) studies of those nanotwinned metal samples revealed dislocation pile-ups at twin boundaries [10], suggesting that the enhanced mechanical strength is associated with the effectiveness of twin boundaries as barriers to dislocation motion. Jin et al. [18, 20] studied the mechanisms of interaction between dislocations and twins in different FCC metals. While they found that these interactions can generate dislocation locks, the detailed interaction mechanisms are both material- and loading

condition-dependent. Zhu et al. [19] showed that twin boundaries are deep traps for screw dislocations and suggested that twin boundary mediated slip transfer is the rate-controlling mechanism for the observed increased strain rate sensitivity with increasing twin density. All of these studies indicate the ultrahigh strength of nanotwinned crystalline metals is related to nanotwin induced interface strengthening. The increase in strength with decreasing grain size/twin spacing is based upon the interfaces serving as barriers to dislocation migration, resulting (in some cases) in dislocation pile-ups at the interfaces; this is the so-called Hall-Petch effect [41, 42] in which the yield stress σ_y scales with the grain/twin size d as $\sigma_y = \sigma_y^0 + A/\sqrt{d}$, where σ_y^0 and A are constants. While it is clear that nanotwins provide strong barriers to dislocation motions and enhance the resulting materials' strength, the origin of the observed ultrahigh ductility and the detailed atomistic mechanisms by which twin boundaries lead to strain hardening are not well understood.

In addition to the ultrahigh strength and ductility, Lu et al. [43] also demonstrated that in pure, nanotwinned Cu, the yield strength exhibits a maximum strength at a small, finite twin spacing. They found that while the strength goes through a maximum at a critical twin spacing λ_c, the strain hardening and ductility increase monotonically with decreasing twin spacing. Earlier simulations [44, 45] were unable to reproduce this transition in strengthening behavior at twin spacings below the experimentally observed critical twin spacing $\lambda_c \sim 15$ nm. The existence of a maximum in the strength, with no minimum in the ductility, suggests the existence of a heretofore unrecognized length scale in the classical strength of metals picture. Understanding on the origin of the above observed ultrahigh ductility and the atomistic mechanisms by which twin boundaries lead to strain hardening and strength transition is essential for better engineering this class of materials. Hence in this work, we employ MD simulations together with continuum elastic theory to examine the following questions related to this unique microstructure:

1. What are the dislocation-twin interaction mechanisms responsible for the experimentally observed simultaneous ultrahigh strength and ductility?

2. What governs the strength transition at the small, critical twin spacing?

1.1.2 Main Findings

Through large scale MD simulations employing an embedded-atom method (EAM) [46] potential, the plastic deformation of nanotwinned Cu are studied in detail. Based upon these

simulations, the sequence of dislocation events associated with the initiation of plastic deformation, dislocation interactions with twin boundaries, dislocation multiplications and deformation debris formations are revealed. Two new dislocation mechanisms that explain the observation of both ultrahigh strength and ductility found in this class of microstructures are discovered. These two mechanisms are: (1) the interaction of a 60° dislocation with a twin boundary that leads to the formation of a $\{001\}\langle 110\rangle$ Lomer dislocation which, in turn, dissociates into Shockley, stair-rod and Frank partial dislocations; (2) the interaction of a 30° Shockley partial dislocation with a twin boundary which generates three new Shockley partials during twin-mediated slip transfer. The generation of a high-density of Shockley partial dislocations on several different slip systems contributes to the observed ultrahigh ductility while the formation of sessile stair-rod and Frank partial dislocations (together with the presence of the twin boundaries themselves) explain observations of ultrahigh strength.

In order to study the strength transition as a function of twin spacings, MD simulations of the plastic deformation of nanotwinned polycrystalline Cu are performed. The simulations show that the materials' plastic deformation is initiated by partial dislocation nucleations at grain boundary triple junctions. Both dislocations crossing twin boundaries and dislocation-induced twin migrations are observed in the simulations. For the dislocation crossing mechanism, 60° dislocations frequently cross slip onto $\{001\}$ planes in twin grains and form Lomer dislocations, constituting the dominant crossing mechanism. We further examine the effect of twin spacing on this dominant Lomer dislocation mechanism through a series of specifically-designed nanotwinned Cu samples over a wide range of twin spacing. A transition in the dominant dislocation mechanism occurring at a small critical twin spacing is found. While at large twin spacing, cross-slip and dissociation of the Lomer dislocations create dislocation locks which restrict and block dislocation motion and thus enhance strength, at twin spacing below the critical size, cross-slip does not occur, steps on the twin boundaries form and deformation is much more planar. These twin steps can migrate and serve as dislocation nucleation sites, thus softening the material. Based on these mechanistic observations, a simple, analytical model for the critical twin spacing based on dislocation line tension is proposed and it is shown that the predicted critical twin spacing is in excellent agreement both with respect to the atomistic simulations and experimental observation. We suggest the above dislocation mechanism transition is a source of the observed transition in nanotwinned Cu strength.

1.2 Grain Boundary Finite Length Faceting

1.2.1 Problem Statement

The coherent growth twin boundaries as discussed in Section. 1.1 are very special types of faceted grain boundary. They exhibit extraordinary stability and thus enhance the materials' properties. There are many other, more general types of faceted grain boundaries that exhibit a diverse range of faceting patterns, regularity and facet lengths. Some of them also undergo phase transitions at different temperatures. One of the central questions concerning the grain boundary finite length faceting is whether facet size and faceting patterns are determined by thermodynamic equilibrium considerations or kinetics [30]. Herring [47] provided the thermodynamic condition for minimizing the grain boundary free energy with respect to boundary inclination but did not predict facet size, since the only contribution to the boundary thermodynamics he considered is the grain boundary energy itself (energy per unit area). Several subsequent analyses suggest that facet length scales are determined thermodynamically by the energy of facet junctions (one-dimensional defects) and the interactions between them. Sutton and Balluffi [48] argued that facet lengths are determined by the competition between the dislocation character of the junctions and the line forces arising from the different interface stress tensors of the two forming facets. Hamilton et al. [49] challenged this assertion (through density functional theory calculations, embedded-atom method simulations and continuum elasticity analyses) by showing that the grain boundary stress is much too small to stabilize the observed finite facet length of $\Sigma 3\{112\}$ type facets in a $\Sigma 3\{110\}$ grain boundary in Al. It is dangerous, however, to draw general conclusions from such a study since it focused only on this special facet. It is also unclear whether such observations can be extrapolated to more general grain boundaries where faceting is observed. Hence in the second part of this work, we address the following central question:

What controls the length scales of these generally faceted grain boundaries?

1.2.2 Main Findings

We perform MD simulations for a set of generally faceted grain boundaries and study their stability, phase transition and length scales. We focus on FCC Al, both because grain boundaries in Al have been widely studied via experiment and simulation and because grain boundary

faceting has been observed in this system. Some earlier results [49] are generalized by employing two different interatomic potentials for Al, simulating very large grain boundaries and considering two asymmetric grain boundaries $\{002\}_1/\{667\}_2$ and $\{116\}_1/\{662\}_2$, in addition to the symmetric $\Sigma3\{110\}$ grain boundary examined by Hamilton et al. [49]. We also cycle the boundaries over a wide range of temperatures in order to allow thermally activated coarsening and, in some cases, to observe the facet-defaceting transition. While the present results confirm the presence of the $\Sigma3\{110\}$ boundary faceting behavior reported earlier [49], we demonstrate that this is a very special case. In the more general case of asymmetric boundaries, facet coarsening either does not occur or is extraordinarily sluggish and the facet length scale is dictated by atomic matching that necessarily introduces extremely large barriers to facet migration - a necessary step in facet coarsening.

1.3 Outline of the Thesis

The Thesis is organized into Chapters by the respective problem investigation. Chapter 2 gives a brief review of basic notations, theory and simulation methods used in this Thesis. We present this immediately following this introduction so that we can standardize notations, naming conventions and basic theories to facilitate the communication with readers of all backgrounds. With that, a review of the earlier works on interfacial strengthening and in particular, Cu with a high density of growth nanotwins is postponed to Chapter 3. Chapter 4 focuses on MD simulations on the plastic deformation of nanotwinned Cu and describes detailed dislocation twin interaction mechanisms. Chapter 5 studies the dislocation mechanism transition as a function of twin spacing where both MD simulations on polycrystalline Cu sample and samples with specifically designed twin spacing are presented. Chapter 6 studies the problem of grain boundaries finite length faceting. This Thesis is concluded in Chapter 7.

Chapter 2

Theory and Simulation Methods

2.1 Mathematical Notations

A standard notation gives much convenience in conveying the underlying theory. We adopt the standard notation of vectors and tensors that is described in this section. In this Thesis, vectors are written in lower case bold fonts, such as

$$\boldsymbol{a},\ \boldsymbol{b},\ \boldsymbol{c},\ \text{etc.} \tag{2.1}$$

and higher order tensors are written in capital case bold fonts, such as

$$\boldsymbol{A},\ \boldsymbol{B},\ \boldsymbol{C},\ \text{etc.} \tag{2.2}$$

The vector dot product, cross product and tensor product are written respectively as:

$$\boldsymbol{a}\cdot\boldsymbol{b},\ \boldsymbol{a}\times\boldsymbol{b},\ \boldsymbol{ab} \tag{2.3}$$

There is an exception to the above convention when we describe the FCC dislocation slip systems using the Thompson's tetrahedron (see Section. 2.2.2.3).

We adopt the summation convention in basis expansions of vectors and tensors, i.e., summation over a repeated index is implied if no exception is given. For example, the vector can be written in basis notation as

$$\boldsymbol{x} = x^i\boldsymbol{e}_i = x^1\boldsymbol{e}_1 + x^2\boldsymbol{e}_2 + x^3\boldsymbol{e}_3 \tag{2.4}$$

and second order tensors are written as

$$\boldsymbol{A} = A^{ij}\boldsymbol{e}_i\boldsymbol{e}_j \tag{2.5}$$

It is usually assumed that the summation indices range from 1 to n, where n is the dimension of the space. Exceptions to the summation rule are made when the indices are enclosed in parentheses, i.e.,

$$a_{(i)}x_{(i)} \tag{2.6}$$

No summation is implied for the above term.

We also use the Kronecker delta tensor and permutation tensor as defined below

$$\delta_{ij} = \delta_i^j = \delta^{ij} = \begin{cases} 1 & \text{if } i = j \\ 0 & \text{if } i \neq j \end{cases} \tag{2.7}$$

$$e_{ijk} = e^{ijk} = \begin{cases} 1 & \text{if } ijk \text{ is an even permutation of 123} \\ -1 & \text{if } ijk \text{ is an odd permutation of 123} \\ 0 & \text{otherwise} \end{cases} \tag{2.8}$$

2.2 Crystallography

2.2.1 Crystal Structures

The structure of a perfect crystal can be described by a combination of lattice and basis, where lattice is an arrangement of mathematical points with a regular periodic pattern in 2 or 3 dimensions, basis is a particle or object at lattice points.

$$Crystal = Lattice + Basis \tag{2.9}$$

Lattices can be categorized according to their symmetry properties. Two lattices are different from each other if they possess different symmetry properties. In 2 and 3 dimensions, there are a total of 5 and 14 different lattices (see Ref. [50–53] for details). These lattices are called Bravais lattices and are named after Auguste Bravais for first proving these exact numbers [53].

A Bravais lattice can be represented by a linear combination of its smallest repeating vectors $\boldsymbol{c}_i$, known as primitive vectors. The position of any lattice point $\boldsymbol{a}$ can be expressed as a

linear combination of $\boldsymbol{c}_i$, i.e.,

$$\boldsymbol{a} = n^i \boldsymbol{c}_i \tag{2.10}$$

These primitive vectors form a parallelepiped known as the primitive cell. The volume of the primitive cell is

$$V_c = \boldsymbol{c}_1 \cdot (\boldsymbol{c}_2 \times \boldsymbol{c}_3) \tag{2.11}$$

Primitive vectors can be expressed in some cartesian coordinates as

$$\boldsymbol{c}_i = A_i^j \boldsymbol{e}_j \tag{2.12}$$

where $\boldsymbol{e}_i \cdot \boldsymbol{e}_i = \delta_{ij}$. Hence the lattice point in Eqn. 2.10 can be written as

$$\boldsymbol{a} = n^i A_i^j \boldsymbol{e}_j \tag{2.13}$$

In Eqn. 2.10, lattice points with two n^i same lie on same lines and those sharing one n^i lie on same planes.

Three additional vectors can be defined by taking the cross product of the primitive vectors $(\boldsymbol{c}_1, \boldsymbol{c}_2, \boldsymbol{c}_3)$ in permutation as

$$\boldsymbol{c}^1 = \frac{\boldsymbol{c}_2 \times \boldsymbol{c}_3}{\boldsymbol{c}_1 \cdot (\boldsymbol{c}_2 \times \boldsymbol{c}_3)} = \frac{\boldsymbol{c}_2 \times \boldsymbol{c}_3}{V_c} \tag{2.14a}$$

$$\boldsymbol{c}^2 = \frac{\boldsymbol{c}_3 \times \boldsymbol{c}_1}{\boldsymbol{c}_2 \cdot (\boldsymbol{c}_3 \times \boldsymbol{c}_1)} = \frac{\boldsymbol{c}_3 \times \boldsymbol{c}_1}{V_c} \tag{2.14b}$$

$$\boldsymbol{c}^3 = \frac{\boldsymbol{c}_1 \times \boldsymbol{c}_2}{\boldsymbol{c}_3 \cdot (\boldsymbol{c}_1 \times \boldsymbol{c}_2)} = \frac{\boldsymbol{c}_1 \times \boldsymbol{c}_2}{V_c} \tag{2.14c}$$

where the scaling factor V_c is chosen so that

$$\boldsymbol{c}_j \cdot \boldsymbol{c}^i = \delta_j^i \tag{2.15}$$

These three vectors form a parallelepiped with volume

$$V^c = \boldsymbol{c}^1 \cdot \left(\boldsymbol{c}^2 \times \boldsymbol{c}^3\right) = \frac{1}{V_c} \tag{2.16}$$

Eqn. 2.14 can also be written as

$$\boldsymbol{c}_1 = \frac{\boldsymbol{c}^2 \times \boldsymbol{c}^3}{V^c} \tag{2.17a}$$

$$\boldsymbol{c}_2 = \frac{\boldsymbol{c}^3 \times \boldsymbol{c}^1}{V^c} \tag{2.17b}$$

$$\boldsymbol{c}_3 = \frac{\boldsymbol{c}^1 \times \boldsymbol{c}^2}{V^c} \tag{2.17c}$$

The lattice points in Eqn. 2.10 can also be expressed by taking the three new vectors ($\boldsymbol{c}^i$) as a set of primitive vectors, thus forming another lattice known as the reciprocal lattice, i.e.,

$$\boldsymbol{a} = n^i \boldsymbol{c}_i = n_j \boldsymbol{c}^j \tag{2.18}$$

where $\boldsymbol{c}^j$ are the reciprocal primitive vectors. Combining the above Equation with Eqn. 2.14, the following can be shown

$$n_i = \boldsymbol{a} \cdot \boldsymbol{c}_i = n^j \boldsymbol{c}_j \cdot \boldsymbol{c}_i = n^j G_{ji} \tag{2.19a}$$

$$n^i = \boldsymbol{a} \cdot \boldsymbol{c}^i = n_j \boldsymbol{c}^j \cdot \boldsymbol{c}^i = n_j G^{ji} \tag{2.19b}$$

where

$$G_{ji} = \boldsymbol{c}_j \cdot \boldsymbol{c}_i \tag{2.20a}$$

$$G^{ji} = \boldsymbol{c}^j \cdot \boldsymbol{c}^i \tag{2.20b}$$

are called the metric and reciprocal metric tensor, respectively. With the above definition of metric and reciprocal metric tensor, the modulus of the vector $\boldsymbol{a}$ is

$$|\boldsymbol{a}| = \sqrt{\boldsymbol{a} \cdot \boldsymbol{a}} = \sqrt{(n^i \boldsymbol{c}_i) \cdot (n^j \boldsymbol{c}_j)} = \sqrt{n^i n^j \boldsymbol{c}_i \cdot \boldsymbol{c}_j} = \sqrt{n^i n^j G_{ij}} \tag{2.21}$$

or

$$|\boldsymbol{a}| = \sqrt{\boldsymbol{a} \cdot \boldsymbol{a}} = \sqrt{(n_i \boldsymbol{c}^i) \cdot (n_j \boldsymbol{c}^j)} = \sqrt{n_i n_j \boldsymbol{c}^i \cdot \boldsymbol{c}^j} = \sqrt{n_i n_j G^{ij}} \tag{2.22}$$

In the case of an orthonormal basis $\boldsymbol{e}_i$ where

$$\boldsymbol{e}_i \cdot \boldsymbol{e}_j = \delta_{ij} \tag{2.23}$$

its reciprocal basis is itself, i.e.,

$$\boldsymbol{e}_i = \boldsymbol{e}^i \tag{2.24}$$

Hence vectors and tensors expanded in an orthonormal basis can be written in lower subscripts only, i.e.,

$$\boldsymbol{x} = f^i \boldsymbol{e}_i = f_j \boldsymbol{e}^j, f^i = f_i \tag{2.25}$$

and

$$G_{ij} = G^{ij} = \delta^{ij} = \delta_{ij} \tag{2.26}$$

The modulus of the vector $\boldsymbol{a} = f_i \boldsymbol{e}_i$ when expressed in the orthonormal basis is thus simplified to

$$|\boldsymbol{a}| = \sqrt{\boldsymbol{a} \cdot \boldsymbol{a}} = \sqrt{(f^i \boldsymbol{e}_i) \cdot (f^j \boldsymbol{e}_j)} = \sqrt{f^i f^j \boldsymbol{e}_i \cdot \boldsymbol{e}_j} = \sqrt{f^i f^j G_{ij}} = \sqrt{f^i f^i} \tag{2.27}$$

A plane can be specified by its intercepts $(1/h_1, 1/h_2, 1/h_3)$ with the axes formed by those primitive vectors. The normal of that plane can be found as

$$\begin{aligned} \boldsymbol{m} &= \left(\frac{\boldsymbol{c}_1}{h_1} - \frac{\boldsymbol{c}_2}{h_2}\right) \times \left(\frac{\boldsymbol{c}_2}{h_2} - \frac{\boldsymbol{c}_3}{h_3}\right) = \frac{\boldsymbol{c}^1 \times \boldsymbol{c}^2}{h_1 h_2} - \frac{\boldsymbol{c}^1 \times \boldsymbol{c}^3}{h_1 h_3} + \frac{\boldsymbol{c}^2 \times \boldsymbol{c}^3}{h_2 h_3} \\ &= \frac{V_c}{h_1 h_2} \boldsymbol{c}^3 + \frac{V_c}{h_1 h_3} \boldsymbol{c}^2 + \frac{V_c}{h_2 h_3} \boldsymbol{c}^1 \\ &= \frac{V_c}{h_1 h_2 h_3} \left(h_1 \boldsymbol{c}^1 + h_2 \boldsymbol{c}^2 + h_3 \boldsymbol{c}^3\right) \end{aligned} \tag{2.28}$$

Hence the normal to the above plane can be written as

$$\boldsymbol{m} = \boldsymbol{h} = h_1 \boldsymbol{c}^1 + h_2 \boldsymbol{c}^2 + h_3 \boldsymbol{c}^3 \tag{2.29}$$

The triad of numbers $(h_1 h_2 h_3)$ is used to represent a plane orthogonal to the direction $(h_1 h_2 h_3)$ in the reciprocal basis. These numbers are known as the Miller indices for a plane. Indices written between curly brackets $\{h_1 h_2 h_3\}$ denote a family of equivalent planes (by lattice symmetry) to that by $(h_1 h_2 h_3)$. While plane normals are always expressed in the reciprocal basis in the Miller indices, directions are always expressed in the direct basis as $[v_1 v_2 v_3]$, or $\langle v_1 v_2 v_3 \rangle$. The angular brackets denote directions equivalent to $[v_1 v_2 v_3]$ by lattice symmetry. We adopt the above Miller indices when describing the crystallographic planes and directions throughout this Thesis.

The equation for all planes with the normal $\boldsymbol{h}$ defined in Eqn. 2.29 is

$$\boldsymbol{x} \cdot \boldsymbol{h} - C = 0 \tag{2.30}$$

When $\boldsymbol{x}$ are lattice points, the above equation is written as

$$\boldsymbol{a} \cdot \boldsymbol{h} - C = 0 \tag{2.31}$$

where C takes integer values. $C = 0$ and $C = 1$ represent two such closely spaced planes and their interplanar distance is

$$d = \frac{\boldsymbol{h} \cdot \dfrac{\boldsymbol{c_1}}{h_1}}{|\boldsymbol{h}|} = \frac{1}{|\boldsymbol{h}|} = \frac{1}{\sqrt{h_i h_j G^{ij}}} \tag{2.32}$$

There may be one or more atoms in a basis for each lattice point. The positions of those atoms with respect to that lattice point can be specified by basis vectors

$$\boldsymbol{\xi}_n = \xi_n^i \boldsymbol{c}_i \tag{2.33}$$

where ξ_n^i are usually chosen such that $|\xi_n^i| \leq \frac{1}{2}$. For crystals with only one atom at a basis, the lattice point can always be conveniently chosen such that $|\xi_1^i| = 0$. Many metals and alloys have only one atom per lattice point. These crystals are completely defined by lattice points alone. Since we focus on studying FCC metals, only the FCC lattice will be presented in the following section (Refer to Ref. [50–53] for a complete description of crystallography).

2.2.2 Face Centered Cubic Lattice

Figure 2.1 (a) shows a unit cell of FCC lattice where the edges of the cube form the cartesian coordinate axes. The FCC lattice has its lattice points at the corners and face centers of the cubic unit cell. The length of the cube is denoted as the lattice parameter a and is often taken as the unit length in the cartesian coordinate. If we denote the unit vectors along the three axes of the cartesian coordinates as $\boldsymbol{e}_i$, we have

$$\boldsymbol{e}_i \cdot \boldsymbol{e}_j = \delta_{ij} \tag{2.34a}$$

$$\boldsymbol{e}_i \times \boldsymbol{e}_j = \epsilon_{ijk} \boldsymbol{e}_k \tag{2.34b}$$

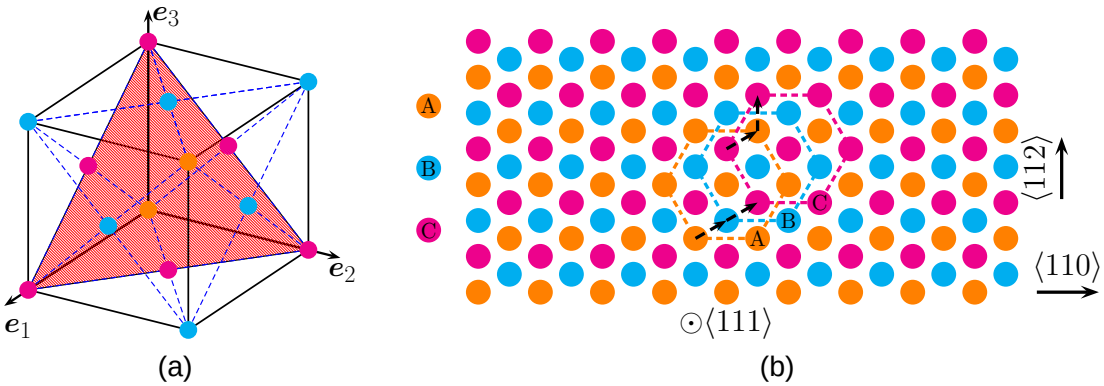

Figure 2.1: (a) The unit cell of a face-centered cubic (FCC) Bravais lattice; (b) FCC lattice viewed along the $\langle 111 \rangle$ direction. The arrows denote vectors of $1/6\langle 112 \rangle$ and represent the relative translational positions of each $\{111\}$ atom layers. In both figures, atoms are colored based on their translational positions in the $\{111\}$ planes, i.e., A, B, C layers are in orange, cyan and magenta.

The primitive vectors for the FCC lattice can be written in the orthonormal basis $\boldsymbol{e}_i$ as

$$\boldsymbol{c}_1 = \frac{1}{2}\boldsymbol{e}_2 + \frac{1}{2}\boldsymbol{e}_3 \tag{2.35a}$$

$$\boldsymbol{c}_2 = \frac{1}{2}\boldsymbol{e}_1 + \frac{1}{2}\boldsymbol{e}_3 \tag{2.35b}$$

$$\boldsymbol{c}_3 = \frac{1}{2}\boldsymbol{e}_1 + \frac{1}{2}\boldsymbol{e}_2 \tag{2.35c}$$

The volume of the primitive cell is

$$V_c = \boldsymbol{c}_1 \cdot (\boldsymbol{c}_2 \times \boldsymbol{c}_3) = \frac{1}{4}a^2 \tag{2.36}$$

and the reciprocal primitive vectors of the FCC lattice are

$$\boldsymbol{c}^1 = \frac{\boldsymbol{c}_2 \times \boldsymbol{c}_3}{V_c} = -\boldsymbol{e}_1 + \boldsymbol{e}_2 + \boldsymbol{e}_3 \tag{2.37a}$$

$$\boldsymbol{c}^2 = \frac{\boldsymbol{c}_3 \times \boldsymbol{c}_1}{V_c} = \boldsymbol{e}_1 - \boldsymbol{e}_2 + \boldsymbol{e}_3 \tag{2.37b}$$

$$\boldsymbol{c}^3 = \frac{\boldsymbol{c}_1 \times \boldsymbol{c}_2}{V_c} = \boldsymbol{e}_1 + \boldsymbol{e}_2 - \boldsymbol{e}_3 \tag{2.37c}$$

It is easy to recognize that the above reciprocal primitive vectors of FCC lattice form a body-centered cubic (BCC) lattice. The volume of the reciprocal primitive cell is

$$V^c = \boldsymbol{c}^1 \cdot \left(\boldsymbol{c}^2 \times \boldsymbol{c}^3\right) = 4/a^2 \tag{2.38}$$

The FCC lattice points expressed as a linear combination of the primitive vectors

$$\boldsymbol{a} = n^i \boldsymbol{c}_i \tag{2.39}$$

can now be written as

$$\begin{aligned} \boldsymbol{a} &= n^1 \left(\frac{1}{2}\boldsymbol{e}_2 + \frac{1}{2}\boldsymbol{e}_3\right) + n^2 \left(\frac{1}{2}\boldsymbol{e}_1 + \frac{1}{2}\boldsymbol{e}_3\right) + n^3 \left(\frac{1}{2}\boldsymbol{e}_1 + \frac{1}{2}\boldsymbol{e}_2\right) \\ &= \frac{1}{2}\left(n^2 + n^3\right)\boldsymbol{e}_1 + \frac{1}{2}\left(n^1 + n^3\right)\boldsymbol{e}_2 + \frac{1}{2}\left(n^1 + n^2\right)\boldsymbol{e}_3 \\ &= f^i \boldsymbol{e}_i \end{aligned} \tag{2.40}$$

where $\boldsymbol{f}^i$ are multiples of $1/2$. Given the great convenience by the orthonormal basis in calculating vector quantities, vectors in FCC lattices are often expressed directly in the unit cell basis $\boldsymbol{e}_i$ rather than in the primitive vectors $\boldsymbol{c}_i$. In the remaining of this Thesis, FCC lattice vectors are expressed in the orthonormal $\boldsymbol{e}_i$ basis unless otherwise noted. As an example, a direction written as $1/2[110]$ refers to the unit cell basis as $\boldsymbol{a} = 1/2\left(\boldsymbol{e}_1 + \boldsymbol{e}_2 + 0\boldsymbol{e}_3\right)$.

The unique features in the FCC lattice are best visualized when the lattice is viewed along its $\langle 111 \rangle$ direction as shown in Fig 2.1 (b), where a single atom is placed at each lattice point. The close-packed $\{111\}$ atom layers are stacked in a sequence of $ABCABCABC$, where A, B, and C layers are named based on their translational position in those $\{111\}$ planes. This is one of the methods to pack spheres in a regular lattice such that the resulting density is highest. In the figure, atoms on the A, B, and C layers are colored orange, cyan and magenta, respectively. Each of the atoms has 12 nearest neighbouring atoms located at $\sqrt{2}/2a$ apart as shown in Fig. 2.2. This number is defined as the lattice's coordination number N.

FCC lattice has 9 symmetry planes: 3 planes with the cubic unit cell unit vectors as normals (i.e., $\{100\}$ planes) and 6 planes whose normals make $\pm\pi/4$ with the unit cell unit vectors (i.e., $\{110\}$ planes). FCC lattice also has an inversion symmetry. This symmetry property can be used in differentiating the FCC lattice from other lattices, such as the hexagonal close-packed (HCP) lattice. It is worth to discuss a bit further the HCP lattice as some FCC materials (Ag,

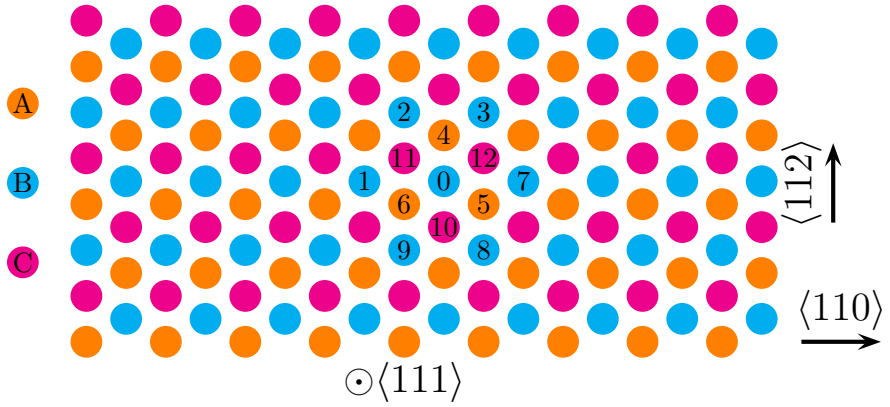

Figure 2.2: FCC lattice nearest neighbouring atoms. Atom denoted by numbers (1-12) is the nearest neighbouring atoms to the atom denoted by '0'. The FCC lattice is viewed along the $\langle 111 \rangle$ direction.

Au, Cu, etc.) frequently adopt HCP structure locally. In the HCP lattice, the close-packed atom layers are stacked in the sequence of $ABABAB$. This is another way of packing spheres to achieve highest density packing. The coordination number N for materials adopting HCP lattice is 12, the same as that of FCC lattice. However, HCP lattice does not have an inversion symmetry. In FCC and HCP materials, the nearest neighbouring atoms are stacked in the same way whereas the next nearest neighbouring atoms are stacked differently. Hence FCC materials adopting an HCP lattice will incur an energy cost, called the stacking fault energy. Materials with a low stacking fault energy, such as Cu, Au, Ag, etc., often contain a high density of stacking faults. Those growth nanotwins in Cu, the main focus of this study, are also a form of stacking fault. In the following, a detailed illustration on the stacking fault in FCC materials is given for its relevance and importance in the current study.

2.2.2.1 Stacking Faults in Face Centered Cubic Lattice

The stacking sequence of $ABCABCABC$ corresponds to the lowest energy state for materials having a FCC lattice. When this ideal stacking sequence is altered, a stacking fault is formed with an additional energy rise known as the stacking fault energy. There are various ways to alter the stacking sequence and thus create different types of stacking faults. Intrinsic stacking faults are formed when a layer of atoms are missing such that the stacking sequence becomes $ABCA|CABC$. This low energy stacking fault is usually generated by slipping on $\{111\}$ planes. Figure 2.3 illustrates one possible way to produce such an intrinsic stacking fault. The

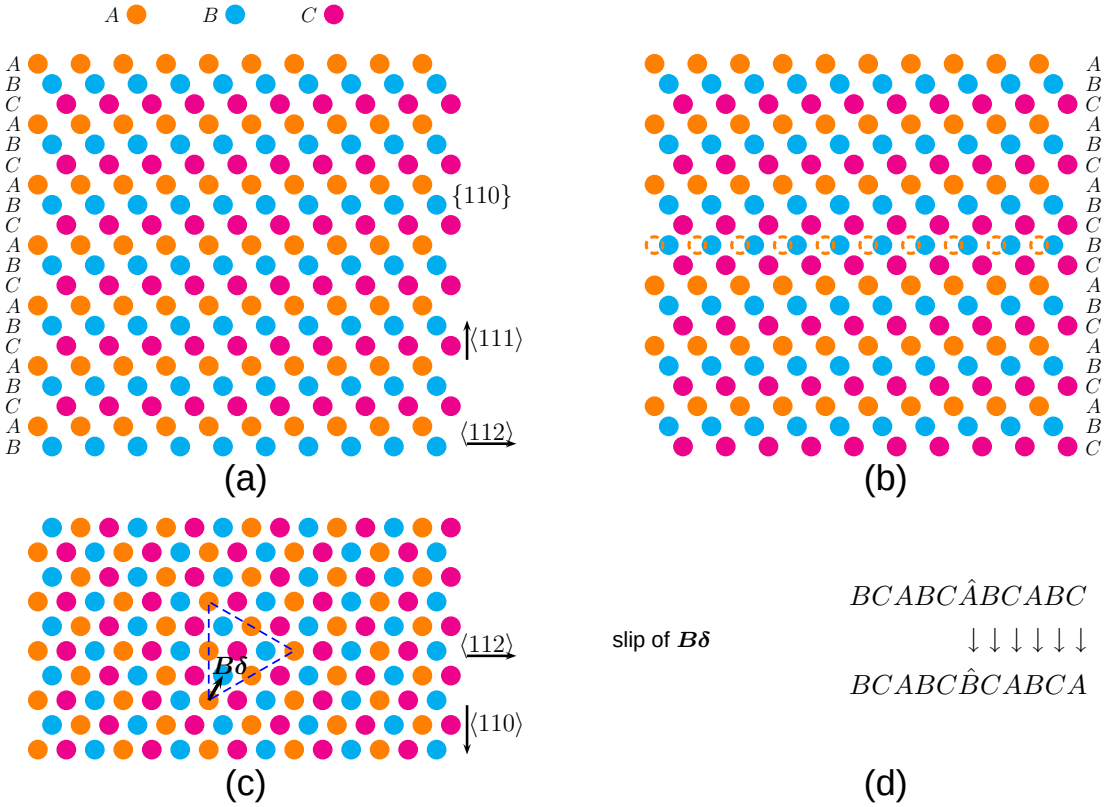

Figure 2.3: Formation of an FCC intrinsic stacking fault by slipping on a $\{111\}$ plane. Atoms are colored according to their ABC stacking sequence with A layer in orange, B layer in blue and C layer in magenta. (a) Perfect FCC lattice viewed along the $\langle 110\rangle$ direction. (b) FCC lattice with an intrinsic stacking fault by slipping of atoms on a $\{111\}$ plane. (c) The slipping vector viewed alone the $\langle 111\rangle$ direction. (d) Change of $\{111\}$ stacking sequence by the slipping process.

slipping process is completed by displacing all atoms on A layer and below with a vector of $1/6\langle 112\rangle$. See Fig. 2.3 (d) for the change of stacking sequence as a result of the above slip. The above intrinsic stacking fault can be annihilated by another slip of $1/6\langle 112\rangle$ on the previous $\{111\}$ plane as shown in Fig. 2.4.

As the layers of atoms are displaced by $1/6\langle 112\rangle$, the relative positions of the atoms near the slip plane vary and so does the energy rise associated with the above displacement. The maximum value of the energy rise in this process is called the unstable stacking fault energy γ_{usf} while the energy value corresponding to the displacment of $1/6\langle 112\rangle$ is known as the stable stacking fault energy, or simply stacking fault energy γ_{ssf}. The plot of the above energy

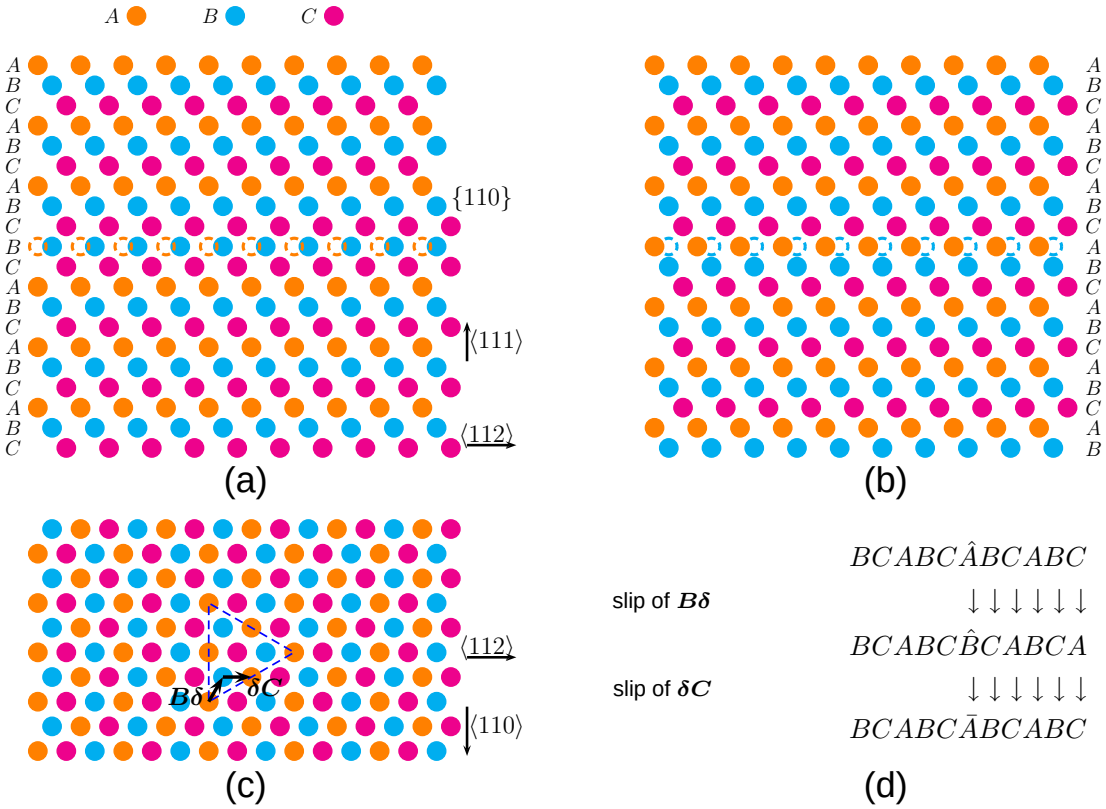

Figure 2.4: Annihilation of an intrinsic stacking fault by slip on $\{111\}$ plane in FCC lattice. Atoms are colored according to their ABC stacking sequence with A layer in orange, B layer in blue and C layer in magenta. (a) FCC lattice with an intrinsic stacking fault by slipping of atoms on a $\{111\}$ plane. (b) Clearing an intrinsic stacking fault by a second slipping of atoms on a $\{111\}$ plane. (c) The slipping vector viewed alone the $\langle 111 \rangle$ direction. (d) Change of $\{111\}$ stacking sequence by the slipping process.

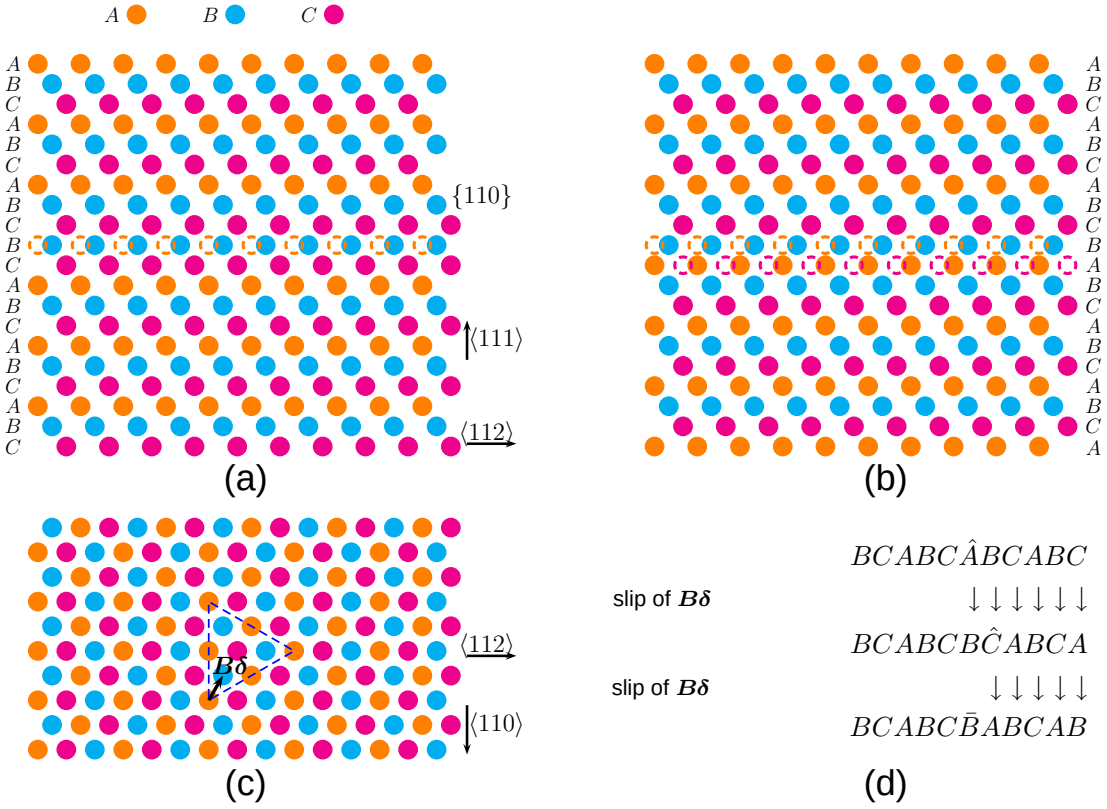

Figure 2.5: Formation of an FCC extrinsic stacking fault by slipping on a $\{111\}$ plane. Atoms are colored according to their ABC stacking sequence with A layer in orange, B layer in blue and C layer in magenta. (a) FCC lattice with an intrinsic stacking fault by slipping of atoms on a $\{111\}$ plane. (b) FCC lattice with an extrinsic stacking fault by second slipping of atoms on a $\{111\}$ plane. (c) The slipping vector viewed alone the $\langle 111 \rangle$ direction. (d) Change of $\{111\}$ stacking sequence by the slipping process.

rise with respect to the displacement along the $1/6\langle 112 \rangle$ direction is known as the generalized planar fault (GPF) energy curve [54, 55], which can be used as a measure to the ease of slipping.

Extrinsic stacking faults are formed when a layer of atoms are added such that the stacking sequence becomes, for example, $ABCABC\{B\}ABC$. Similar to the generation of intrinsic stacking faults, extrinsic stacking faults are usually generated by a slipping process on $\{111\}$ planes. Fig. 2.5 illustrates one possible process which generates an extrinsic stacking fault.

The above intrinsic and extrinsic stacking faults are the most commonly observed stacking faults in FCC materials. In addition, stacking faults can also be formed by arranging the stacking sequence in mirror symmetry about one of the $\{111\}$ planes, i.e., in $ABCAB\{C\}BACBA$,

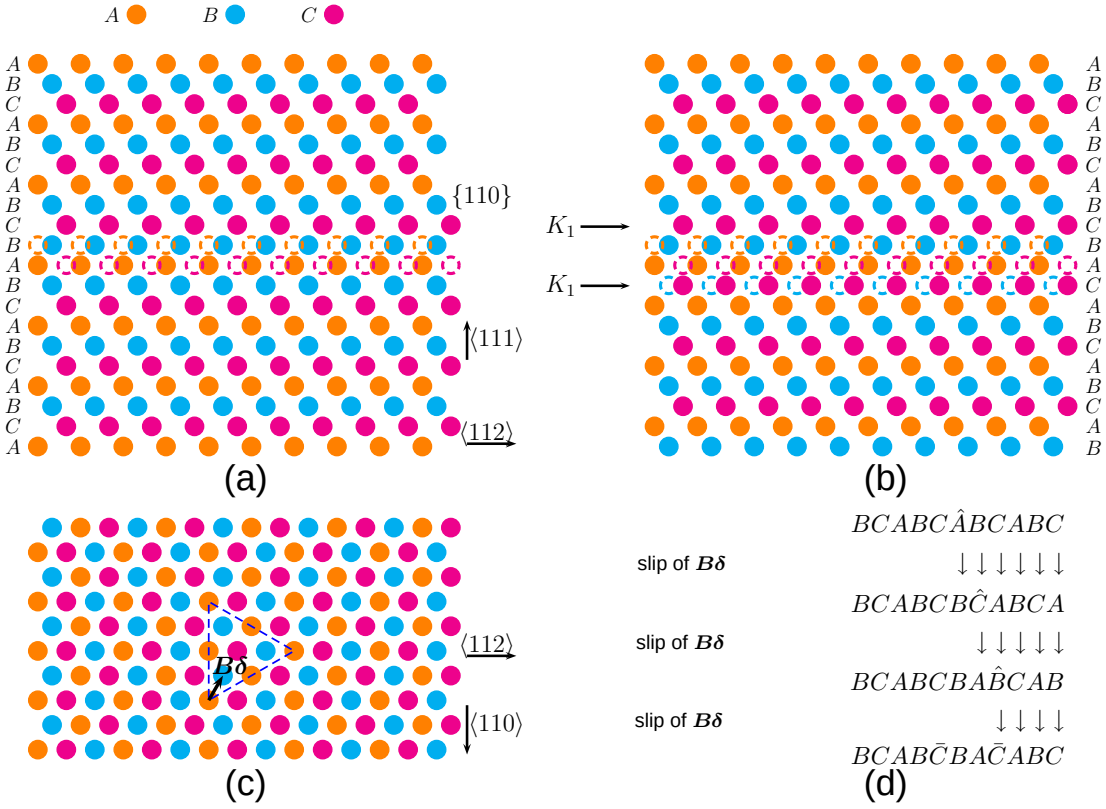

Figure 2.6: Formation of an FCC twin by slipping on nearest neighbouring $\{111\}$ planes. Atoms are colored according to their ABC stacking sequence with A layer in orange, B layer in blue and C layer in magenta. (a) FCC lattice with an extrinsic stacking fault by slipping of atoms on a $\{111\}$ plane. (b) FCC lattice with a twin by continuous slipping of atoms on nearest neighbouring $\{111\}$ planes. (c) The slipping vector viewed alone the $\langle 111 \rangle$ direction. (d) Change of $\{111\}$ stacking sequence by the slipping process.

thus forming a twin relation. The energy associated with this type of stacking fault is about half of that of intrinsic or extrinsic stacking faults. As illustrated in Fig. 2.6, slipping layer by layer with the same displacement vector can generate such a stacking sequence. This slip process also corresponds to the twin boundary migration. Similar to slip processes generating intrinsic stacking faults, the maximum value of the energy rise in the process of twin boundary migration is γ_{utm}

Stacking fault energy are typically low in metals when compared to that of other planar defect types. Typical values of stacking fault energy γ_{ssf} are 20 mJ/m^2 for Ag, 32 mJ/m^2 for Au, 45 mJ/m^2 for Cu, 125 mJ/m^2 for Ni and 140 mJ/m^2 for Al (see Ref. [56]). In general, the

lower the stacking fault energy, the higher the probability of forming such stacking faults. In practice, the above stacking fault formation processes as illustrated in Fig. 2.3-2.6 are usually accomplished through gliding of dislocations, which provide an easier path than the above uniform and homogeneous ones.

2.2.2.2 Dislocations in Face Centered Cubic Lattice

Frenkel [56] estimated the theoretical shearing strength of a single crystal on rational planes to be

$$\sigma_{theo} = \frac{\mu b}{2\pi d} \sim \frac{\mu}{15} \tag{2.41}$$

where μ is the shear modulus, b is the length of the smallest lattice translation vector (i.e., primitive vector) and d is the interplanar spacing between these rational shearing planes, as given by Eqn. 2.32. The model by Frenkel, although simple, is important in a few aspects. First, it gives the upper bound of the strength materials can achieve. It also suggests that crystals are likely to deform through slipping in the close-packed directions on the close-packed planes where the required shearing stress is minimal. In the FCC lattice, $1/2\langle 110\rangle$ is the shortest lattice translation vector and $\langle 100\rangle$ is the second shortest. The close-packed planes in FCC are those $\{111\}$ planes. Roundy et al. [57] calculated the ideal shear strengths of FCC Al and Cu at zero temperature using density functional theory within the local density approximation. Under structural relaxation of all five strain components other than the imposed shear strain, the shear strengths on $\{111\}$ planes are 1.85 and 2.65 GPa for Al and Cu (8% - 9% of the shear moduli), respectively, marching well to Eqn. 2.41.

It is energetically favorable for slipping on these $\{111\}$ planes in $\langle 110\rangle$ direction to take two steps in a "zig-zag" fashion as illustrated in Fig. 2.7. Instead of slipping by $1/2[110]$, atoms will first be displaced by $1/6[12\bar{1}]$ and followed by $1/6[211]$. The first slip in the above process creates an intrinsic stacking fault while the second one clears the stacking fault as following

$$\frac{1}{2}[110] \rightarrow \frac{1}{6}[12\bar{1}] + \text{intrinsic stacking fault} + \frac{1}{6}[211] \tag{2.42}$$

Slip by a lattice translation vector leaves behind a perfect crystal. Other types of slip will destroy the perfect lattice arrangement.

FCC crystal slip processes do not occur simultaneously and homogeneously on $\{111\}$ planes. It is rather completed section by section through the glides of dislocations that displace a small amount of atoms at a time. The lines separating slipped and unslipped regions

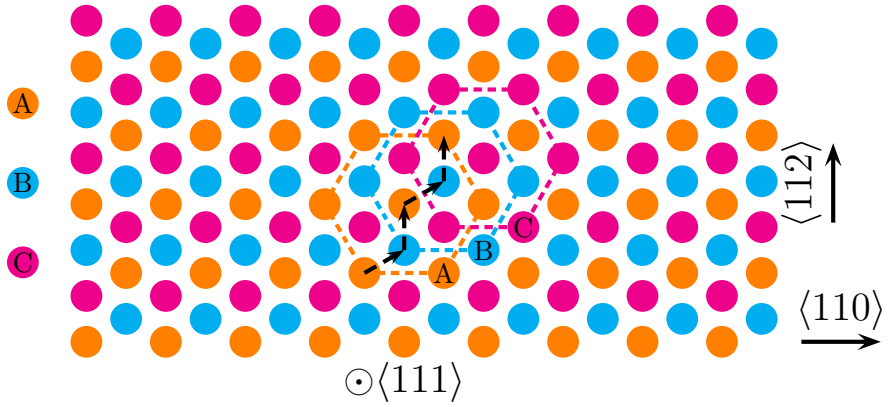

Figure 2.7: Slipping on $\{111\}$ planes in FCC lattice via a "zig-zag" fashion.

are called dislocation lines. In the above process, lines separating the first and second slip with slip vectors not being lattice translation vectors are both partial dislocation lines. These dislocations are called Shockley partial dislocations and are associated with slip vector of type $1/6\langle 112\rangle$. There is another type of partial dislocation which is common in FCC materials. It is the Frank partial dislocation which is formed by removing or inserting one close-packed $\{111\}$ layer of atoms, thus creating a stacking fault region. The line bounding the stacking fault plane contains a dislocation of Burgers vector $1/3\langle 111\rangle$. Shockley partials can move by gliding on $\{111\}$ planes while Frank partials can only climb. There are, of course, many other types of partial dislocations which are mainly formed through reactions of the above fundamental dislocations. We will describe them when we introduce the Thompson tetrahedron in Section. 2.2.2.3.

Dislocations are important as the plastic deformation of crystalline metals is usually accomplished through glide of dislocations. Metals can be softened by mobile dislocations and in some cases, the required shear stress to initiate plastic flow can drop by 2 orders of magnitude from the theoretical shear strength. Hence, the strengthening of crystalline metals is mainly focused on dislocations, either eliminating or proliferating them. The former creates dislocation starvation as in metallic nanowires and nanorods, while the latter creates dislocation forests, as in heavily deformed metals. A third method is by obstructing disloction glide with particles or interfaces such as nanoscale twin boundaries. We return to this point in Chapter. 3, where a detailed account on strengthening through interfaces is given.

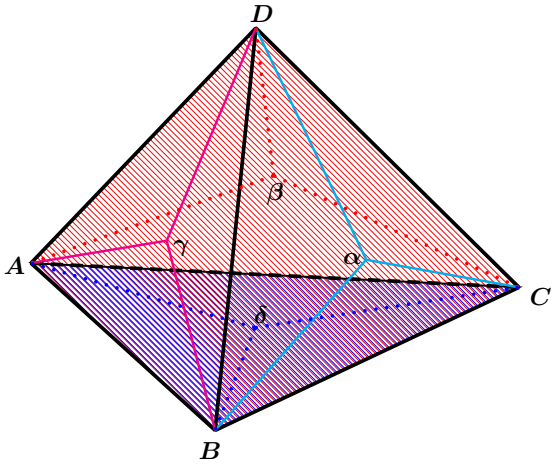

Figure 2.8: The FCC Thompson tetrahedron.

2.2.2.3 Slip Systems in Face Centered Cubic Lattice

The close-packed planes and close-packed directions in which dislocations glide form lattices' slip systems. In the FCC lattice, the close-packed planes and the close-packed directions are $\{111\}$ and $\langle 110\rangle$, forming a total of 12 slip systems in which dislocations tend to glide. Thompson [56] ingeniously represented these slip systems geometrically by using a tetrahedron, now known as the Thompson tetrahedron, as shown in Fig. 2.8. In the figure, the four vertices of the tetrahedron are labelled as $\boldsymbol{A}$, $\boldsymbol{B}$, $\boldsymbol{C}$ and $\boldsymbol{D}$. The middle points of the triangles opposite $\boldsymbol{A}$, $\boldsymbol{B}$, $\boldsymbol{C}$ and $\boldsymbol{D}$ are denoted by $\boldsymbol{\alpha}$, $\boldsymbol{\beta}$, $\boldsymbol{\gamma}$ and $\boldsymbol{\delta}$, respectively. The surfaces of the tetrahedron in the figure represent $\{111\}$ slip planes. Plane $\boldsymbol{a}$ is opposite corner $\boldsymbol{A}$; similarly for the other three slip planes in the tetrahedron. Dislocation Burgers vectors are indicated by ordered pairs of points, e.g., $\boldsymbol{A\gamma}$ or $\boldsymbol{AD}$. Figure 2.9 shows the unfolded Thompson tetrahedron with all the Burgers vectors written explicitly.

It is important to note that Burgers vectors represented by pairs of Roman letters, such as $\boldsymbol{AB}$, $\boldsymbol{CD}$, $\boldsymbol{AC}$, etc., are lattice translation vectors of $1/2\langle 110\rangle$. Dislocations having those as their Burgers vectors are perfect or full dislocations. On the other hand, Burgers vectors denoted by Roman-Greek, Greek-Greek pairs represent partial dislocations. Roman-Greek pairs formed by points on the same slip plane, such as $\boldsymbol{A\gamma}$, $\boldsymbol{B\delta}$, etc., are known as Shockley partials of $1/6\langle 112\rangle$ while those formed by points on different slip planes, such as $\boldsymbol{A\alpha}$, $\boldsymbol{B\beta}$, etc., are Frank partials of $1/3\langle 111\rangle$. Those Greek-Greek pairs represents stair-rod dislocations of $1/6\langle 110\rangle$

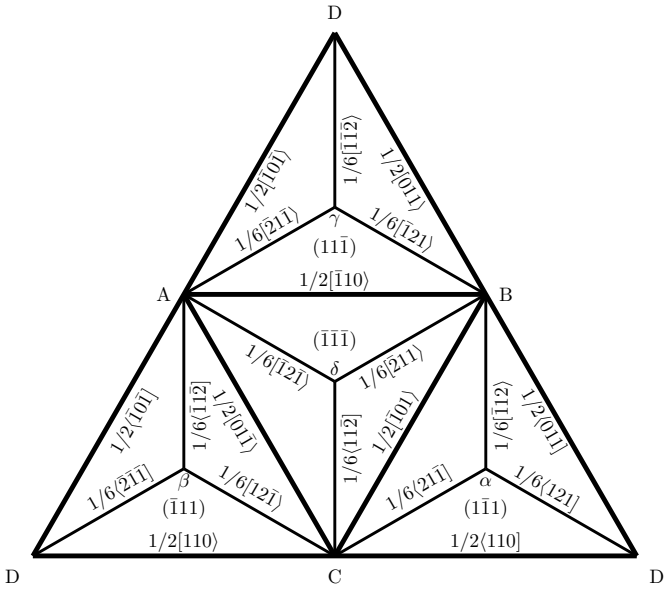

Figure 2.9: The unfolded FCC Thompson tetrahedron.

There are many other partial dislocations which can be formed by interactions of those fundamental ones. In addition, slip on non-$\{111\}$ planes, such as $\{001\}$, is also observed in some FCC materials [56].

2.2.3 Polycrystalline

Metallic solids are often composed of many arbitrarily oriented single crystal grains and grain boundaries which are regions where two or more grains join. The orientation between two grains can be described by a rotational operation (plus a translation if necessary) which brings one grain into coincidence with the other. Denoting the lattice of one grain as $\boldsymbol{a} = n^i \boldsymbol{c}_i$ and that of the other as $\boldsymbol{b} = f^j \boldsymbol{c}_j$, we have

$$\boldsymbol{b} = \boldsymbol{R} \cdot \boldsymbol{a} \tag{2.43}$$

where $\boldsymbol{R}$ is the rotational tensor. i.e.,

$$f^j = R^j_i n^i \tag{2.44}$$

f^j are usually not integer values. It is often convenient to express the new lattice with its own set of primitive vectors as $\boldsymbol{b} = m^j \boldsymbol{p}_j$ such that m^j are integers. The linear transformation between the two sets of primitive vectors can be written as a tensor such that

$$\boldsymbol{c}_j = L^i_j \boldsymbol{p}_i \tag{2.45}$$

Hence

$$m^k = L^k_j R^j_i n^i = C^k_i n^i \tag{2.46}$$

where C^k_i is called the correspondence tensor which combines the operation of both a rotation and a change of basis.

This rotational operation has 3 degrees of freedom (2 defining the rotational axis unit vector $\boldsymbol{\rho}$ and 1 defining the rotation angle θ). It is convenient to use the axis-angle rotational operation to describe the crystallographic relation between two arbitrarily oriented grains. However, this method often misses the crystallographic structures of the two grains and carries little physical information on the resulted lattice properties. Other alternative methods which make use of the particular lattice symmetry have been developed. When used appropriately in some special orientation relations, they provide better descriptions of the two lattices involved. Such methods include the coincidence site lattice (CSL) [58, 59], O-lattice [60, 61], and displacement shift complete (DSC) lattice [62]. The detailed descriptions of some special lattices are introduced when we use them in sebsequent Chapters.

2.2.3.1 Grain Boundary

A grain boundary has 5 macroscopic degrees of freedom (3 relating to the orientation of the crystallographic axes of one grain to those of the other and 2 to the inclination of the boundary plane) and 3 microscopic degrees of freedom (corresponding to rigid body translations of one grain relative to the other). The large number of degrees of freedom results in a large variation in the types of grain boundaries. There are a few different criteria, such as energy, structure and geometry, that are used to classify grain boundaries. However, the correlation between the current grain boundary classification and material properties seems to be weak as suggested by a recent survey by Olmsted et al. [63, 64]. Nonetheless, certain low energy grain boundaries play an important role in determining materials' properties. Such boundaries include low angle grain boundaries and twin boundaries. Since this Thesis is focused on twin boundaries, we devote our effort to the description of the crystallographics aspects of twinning below.

2.2.3.2 Crystallography of Twinning

Two crystals are twins of each other when their crystallographic orientation can be described either by a rotation of 180° about some axis or by a reflection across some plane. This is the classical definition of twin relation [1]. Figure 2.10 illustrates the crystallographic twinning

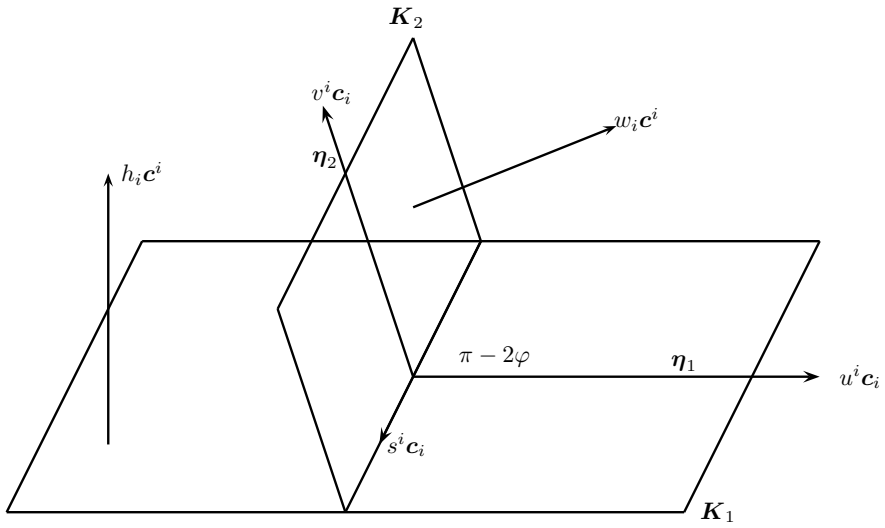

Figure 2.10: Crystallographic twinning elements: K_1 is the composition or twinning plane; K_2 is the invariant plane associated with K_1; η_1, η_2 lie in K_1, K_2 and are perpendicular to the line of intersection of K_1, K_2; η_1 is the shear or twinning direction; plane containing η_2 and perpendicular to K_2 is the plane of shear.

elements, where the two invariant planes are K_1 and K_2 and they are known as the twinning plane and the conjugate or reciprocal twinning plane. The plane defined by the intersection of K_1 and K_2 is the shearing plane. The two directions η_1 and η_2, lying in K_1 and K_2, are perpendicular to the line of intersection of K_1 and K_2. They are known as the twinning and conjugate or reciprocal twinning direction.

Conventionally, the two twin-related crystals are called matrix (M) and twin (T) crystals, respectively. The lattices defining the matrix and twin crystals can be written as

$$\boldsymbol{a} = n^i \boldsymbol{c}_i \tag{2.47}$$

and

$$\boldsymbol{a}^T = k^i \boldsymbol{p}_i \tag{2.48}$$

[1] See Ref. [65] for a generalized twinning theory.

where $\boldsymbol{c}_i$ and $\boldsymbol{p}_i$ denote the primitive lattice vector for the matrix and twin lattices, respectively. Since the two crystals have the same type of lattice, differing only in their orientations, the matrix and twin crystals have the same density and the twinning process does not change the volume of the crystal. This suggests twining is a pure shear operation (atomic shuffling is required for materials having more than one atoms at each lattice sites).

Bilby and Crocker [66] studied four classical cases of twinning operations:

1. reflection in K_1;
2. rotation of π about the normal to K_1;
3. reflection in the plane normal to η_1;
4. rotation of π about η_1;

The four fundamental twinning operations transform the matrix lattice into the twin lattice and vice versa. Employing Eqn. A.5 for rotational operation and Eqn. A.11 for reflection operation, the above four operations transforming the matrix lattice into the twin lattice can be written as

1.
$$\begin{aligned}\boldsymbol{p}_i &= \boldsymbol{c}_i - 2\frac{h_j\boldsymbol{c}^j}{|h_j\boldsymbol{c}^j|}\left(\frac{h_j\boldsymbol{c}^j}{|h_j\boldsymbol{c}^j|}\cdot\boldsymbol{c}_i\right)\\ &= \boldsymbol{c}_i - 2\left(dh_j\boldsymbol{c}^j\right)\left(dh_j\boldsymbol{c}^j\cdot\boldsymbol{c}_i\right)\\ &= \boldsymbol{c}_i - 2\left(dG^{ij}h_i\boldsymbol{c}_j\right)\left(dh_i\right)\\ &= \boldsymbol{c}_i - 2dh_im^j\boldsymbol{c}_j\end{aligned} \tag{2.49}$$

   where d is the interplanar spacing of the twinning plane K_1, $h_j\boldsymbol{c}^j$ is the normal of the twinning plane K_1, $dG^{ij}h_i\boldsymbol{c}_j = m^j\boldsymbol{c}_j$ is thus the unit normal of the K_1 plane, .

2.
$$\begin{aligned}\boldsymbol{p}_i &= -\boldsymbol{c}_i + 2\frac{h_j\boldsymbol{c}^j}{|h_j\boldsymbol{c}^j|}\left(\frac{h_j\boldsymbol{c}^j}{|h_j\boldsymbol{c}^j|}\cdot\boldsymbol{c}_i\right)\\ &= -\boldsymbol{c}_i + 2dh_im^j\boldsymbol{c}_j\end{aligned} \tag{2.50}$$

3.

$$\begin{aligned}\boldsymbol{p}_i &= \boldsymbol{c}_i - 2\frac{u^j\boldsymbol{c}_j}{|u^j\boldsymbol{c}_j|}\left(\frac{u^j\boldsymbol{c}_j}{|u^j\boldsymbol{c}_j|}\cdot\boldsymbol{c}_i\right)\\ &= \boldsymbol{c}_i - 2lu^j\boldsymbol{c}_j\left(lu^j\boldsymbol{c}_j\cdot\boldsymbol{c}_i\right)\\ &= \boldsymbol{c}_i - 2lb_iu^j\boldsymbol{c}_j\end{aligned} \tag{2.51}$$

where $u^j\boldsymbol{c}_j$ is the vector along η_1, $l^{-1} = |u^j\boldsymbol{c}_j|$ is the length of the vector $u^j\boldsymbol{c}_j$; $b_i = lu^j\boldsymbol{c}_j\cdot\boldsymbol{c}_i$ is the length of unit vector along η_1 projected onto the $\boldsymbol{c}_i$.

4.

$$\begin{aligned}\boldsymbol{p}_i &= -\boldsymbol{c}_1 + 2\frac{u^j\boldsymbol{c}_j}{|u^j\boldsymbol{c}_j|}\left(\frac{u^j\boldsymbol{c}_j}{|u^j\boldsymbol{c}_j|}\cdot\boldsymbol{c}_i\right)\\ &= -\boldsymbol{c}_i + 2lb_iu^j\boldsymbol{c}_j\end{aligned} \tag{2.52}$$

In lattices with an inversion symmetry, a reflection operation about a plane is equivalent to a rotational operation of π about the normal of that plane. Hence (1) and (2) are equivalent and are called Type I twinning. Case (3) and (4) are equivalent and are called Type II twinning. Type I twinning requires K_1 and η_2 to be rational while type II requires K_2 and η_1 to be rational. In most metallic crystals possessing high symmetry and the one studied in this Thesis, all the twinning elements are rational (known as compound twins) and it is indistinguishable between type I and type II twins in these materials [67]. This is true for twinning in FCC lattice when the shearing plane is a plane of symmetry. Hence in the following, we focus on the derivation of case (1) while the rest can be found in Ref. [65].

Denote a point on the matrix lattice as $q^i\boldsymbol{c}_i$, the twinning operation in case (1) will transform it into a point in the twin lattice as $r^i\boldsymbol{p}_i$ with

$$q^i\boldsymbol{c}_i - r^i\boldsymbol{p}_i = \left(2q^i\boldsymbol{c}_i\cdot m^j\boldsymbol{c}_j\right)m^j\boldsymbol{c}_j \tag{2.53}$$

or

$$q^i\boldsymbol{c}_i - r^i\left(\boldsymbol{c}_i - 2dh_im^j\boldsymbol{c}_j\right) = \left(2q^i\boldsymbol{c}_i\cdot m^j\boldsymbol{c}_j\right)m^j\boldsymbol{c}_j \tag{2.54}$$

i.e.,

$$\left(q^i - r^i\right)\boldsymbol{c}_i = \left(2q^i\boldsymbol{c}_i\cdot m^j\boldsymbol{c}_j\right)m^j\boldsymbol{c}_j - 2dr^ih_im^j\boldsymbol{c}_j \tag{2.55}$$

The reflection operation about the twinning plane K_1 also gives

$$q^i\boldsymbol{c}_i + r^i\boldsymbol{p}_i \tag{2.56}$$

lying on the twinning plane K_1. Using Eqn. 2.49 the above vector can be expressed as

$$\begin{aligned} q^i \boldsymbol{c}_i + r^i \boldsymbol{p}_i &= q^i \boldsymbol{c}_i + r^i \left(\boldsymbol{c}_i - 2d h_i m^j \boldsymbol{c}_j \right) \\ &= q^i \boldsymbol{c}_i + r^i \boldsymbol{c}_i - 2d r^i h_i m^j \boldsymbol{c}_j \end{aligned} \tag{2.57}$$

Hence

$$\left(q^i \boldsymbol{c}_i + r^i \boldsymbol{c}_i - 2d r^i h_i m^j \boldsymbol{c}_j \right) \cdot h_j \boldsymbol{c}^j = 0 \tag{2.58}$$

i.e.,

$$\begin{aligned} & \left(q^i \boldsymbol{c}_i + r^i \boldsymbol{c}_i \right) \cdot h_j \boldsymbol{c}^j - 2d r^i h_i m^j \boldsymbol{c}_j \cdot h_j \boldsymbol{c}^j \\ = & \left(q^i \boldsymbol{c}_i + r^i \boldsymbol{c}_i \right) \cdot h_j \boldsymbol{c}^j - 2d r^i h_i \left(d h_j \boldsymbol{c}^j \right) \cdot h_j \boldsymbol{c}^j \\ = & \left(q^i \boldsymbol{c}_i + r^i \boldsymbol{c}_i \right) \cdot h_j \boldsymbol{c}^j - 2d r^i h_i \left(d G^{ij} h_j \boldsymbol{c}_i \right) \cdot h_j \boldsymbol{c}^j \\ = & \left(q^i \boldsymbol{c}_i + r^i \boldsymbol{c}_i \right) \cdot h_j \boldsymbol{c}^j - 2 r^i \boldsymbol{c}_i \cdot h_j \boldsymbol{c}^j \\ = & \left(q^i \boldsymbol{c}_i - r^i \boldsymbol{c}_i \right) \cdot h_j \boldsymbol{c}^j \\ = & \, 0 \end{aligned} \tag{2.59}$$

Since $\left(q^i \boldsymbol{c}_i - r^i \boldsymbol{c}_i \right)$ is a lattice point lying on parallel planes to K_1 and there are an infinite number of such lattice points, K_1 must be a rational plane.

The reflection operation in case (1) on the matrix lattice $\boldsymbol{a}$ is also equivalent to a homogenous shear of that lattice. The reflection operation gives

$$\left(r^i \boldsymbol{p}_i + q^i \boldsymbol{c}_i \right) \cdot m^j \boldsymbol{c}_j = 0 \tag{2.60}$$

where q^i and r^i are integers. The above equation indicates the vector $\left(r^i \boldsymbol{p}_i + q^i \boldsymbol{c}_i \right)$ lies on a plane parallel to the twinning plane K_1.

$$\begin{aligned} r^i \boldsymbol{p}_i + q^i \boldsymbol{c}_i &= 2q^i \boldsymbol{c}_i - 2 \left(q^i \boldsymbol{c}_i \cdot m^j \boldsymbol{c}_j \right) m^j \boldsymbol{c}_j \\ &= H u^i \boldsymbol{c}_i \end{aligned} \tag{2.61}$$

where $u^i \boldsymbol{c}_i$ is the shearing direction and $H = (G_{ij} u^i u^j)^{1/2} \left(2q^i \boldsymbol{c}_i - 2 \left(q^i \boldsymbol{c}_i \cdot m^j \boldsymbol{c}_j \right) m^j \boldsymbol{c}_j \right)$ is the amount of shear. Hence in metals and their alloys, twinning are often conveniently expressed via a homogeneous shear deformation as depicted in Fig. 2.6. This homogeneous

shear operation can be written in the form of a shearing tensor as

$$\boldsymbol{a}^T = \boldsymbol{S}\boldsymbol{a} \tag{2.62}$$

or

$$f^j \boldsymbol{c}_j = \boldsymbol{S} n^i \boldsymbol{c}_i \tag{2.63}$$

where

$$\boldsymbol{S} = \boldsymbol{\delta}^i_j - s u^i \boldsymbol{c}_i h_j \boldsymbol{c}^j = \boldsymbol{\delta}^i_j - s u^i h_j \boldsymbol{c}_i \boldsymbol{c}^j \tag{2.64}$$

is the tensor defining the homogeneous shear.

2.2.3.3 Classification of Twins

Twins can be divided based on their genesis. In general it can be grouped into three categories: growth twins, transformation twins and deformation twins [68]. Transformation twins are formed during phase transformation and deformation twins are resulted from a homogeneous shear during plastic deformation [5–8]. Christian and Mahajan [69] provided a comprehensive review on deformation twinning in FCC, BCC and HCP metals and alloys. Niewczas [9] gave a recent review focusing on twin dislocation interactions in FCC crystals. Growth twins, which is believed to be caused by an accidential departure from equilibrium during growth, become an important subject in recent years when metals having low stacking fault energy can be grown to contain a high density of nanotwins [10–20]. In the following, we focus on growth twins in FCC lattice.

2.2.4 Growth Twins in Face Centered Cubic Lattice

Growth nanotwins [10–18] in FCC lattice are found to have the twinning plane K_1 as $\{111\}$ and the twinning direction η_1 as $\langle 112 \rangle$. The shearing plane $\{110\}$ is also a plane of symmetry. Hence the type I and II twinning are equivalent for those metallic FCC growth twins. It is important to note that in FCC lattices, the respective slip system in the matrix crystal are oriented differently from that in the twin crystal, resulting in a discontiniuty in slip systems across the twin boundary (see Section. B.1 in Appendix. B for an explicit listing of those equivalent crystallographic planes and directions).

2.2.4.1 Slip Systems in Twinned Face Centered Cubic Lattice

The slip systems of the twinned FCC crystals can be effectively described by a pair of Thompson tetrahedra placed in a mirror orientation [70, 71]. Figure 2.11 shows the pair of Thompson tetrahedra corresponding to the original FCC and twinned FCC crystals. The four vertices of the tetrahedron are labelled $\boldsymbol{A}$, $\boldsymbol{B}$, $\boldsymbol{C}$ and $\boldsymbol{D}$. The middle points of the triangles opposite $\boldsymbol{A}$, $\boldsymbol{B}$, $\boldsymbol{C}$ and $\boldsymbol{D}$ are denoted by $\boldsymbol{\alpha}$, $\boldsymbol{\beta}$, $\boldsymbol{\gamma}$ and $\boldsymbol{\delta}$, respectively. Symbols with superscript T represent objects in the twinned orientation. The mirror (twin) plane is the hatched $\boldsymbol{ACB}$ plane. The four $\{111\}$ slip planes in the upper tetrahedron are defined according to the right handed rule as $\boldsymbol{a} \Leftrightarrow \boldsymbol{BCD}$, $\boldsymbol{b} \Leftrightarrow \boldsymbol{CAD}$, $\boldsymbol{c} \Leftrightarrow \boldsymbol{ABD}$ $\boldsymbol{d} \Leftrightarrow \boldsymbol{ACB}$, and similarly in the lower tetrahedron, $\boldsymbol{a}^T \Leftrightarrow \boldsymbol{B}^T\boldsymbol{C}^T\boldsymbol{D}^T$, $\boldsymbol{b}^T \Leftrightarrow \boldsymbol{C}^T\boldsymbol{A}^T\boldsymbol{D}^T$, $\boldsymbol{c}^T \Leftrightarrow \boldsymbol{A}^T\boldsymbol{B}^T\boldsymbol{D}^T$ and $\boldsymbol{d}^T \Leftrightarrow \boldsymbol{A}^T\boldsymbol{C}^T\boldsymbol{B}^T$. The upper and lower Thompson tetrahedra, i.e., $\boldsymbol{ABCD}$ and $\boldsymbol{A}^T\boldsymbol{B}^T\boldsymbol{C}^T\boldsymbol{D}^T$, illustrate the slip systems of matrix and twin crystals.

Because of the mirror symmetry (exchange of left and right) between the two tetrahedra, the $\boldsymbol{c}^T$ plane is a mirror of the $\boldsymbol{c}$ plane, $\boldsymbol{b}^T$ mirrors $\boldsymbol{a}$, $\boldsymbol{a}^T$ mirrors $\boldsymbol{b}$, and the $\boldsymbol{d}^T$ and $\boldsymbol{d}$ planes are coincident. Vertices $\boldsymbol{A}$, $\boldsymbol{B}$ and $\boldsymbol{D}$ in the upper Thompson tetrahedron correspond to $\boldsymbol{B}^T$, $\boldsymbol{A}^T$ and $\boldsymbol{D}^T$ in the lower Thompson tetrahedron. Vertices $\boldsymbol{C}$ and $\boldsymbol{C}^T$ are coincident.

2.3 Continuum Description of Materials

2.3.1 Stiffness and Compliance Tensor for Cubic Materials

The cubic crystal system has cubic unit cell where $a = b = c$, $\alpha = \beta = \gamma = \pi/2$. Three Bravais lattices, simple cubic (SC), BCC and FCC, belong to the cubic crystal system. Cubic materials have 9 symmetry planes: 3 planes with the unit cell unit vectors as normals(i.e. $\{100\}$ planes) and 6 planes whose normals make $\pm\pi/4$ with the unit cell unit vectors(i.e. $\{110\}$ planes). When the unit vectors of the cartesian coordinate axis are taken as edges of the cubic

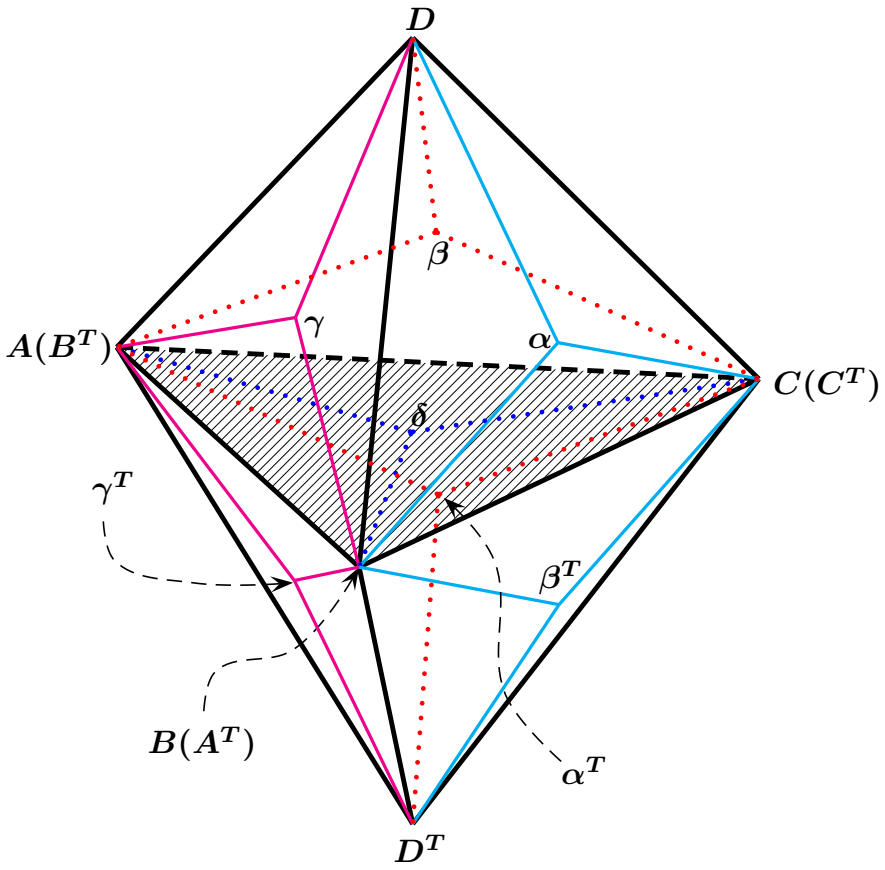

Figure 2.11: FCC twin hexahedron formed by two Thompson tetrahedra. In the upper Thompson tetrahedron $\boldsymbol{ABCD}$, the four $\{111\}$ slip planes $\boldsymbol{a}$, $\boldsymbol{b}$, $\boldsymbol{c}$ and $\boldsymbol{d}$ are defined by the right-handed rule as following: $\boldsymbol{a} \Leftrightarrow \boldsymbol{BCD}$, $\boldsymbol{b} \Leftrightarrow \boldsymbol{CAD}$, $\boldsymbol{c} \Leftrightarrow \boldsymbol{ABD}$, $\boldsymbol{d} \Leftrightarrow \boldsymbol{ACB}$. In the lower Thompson tetrahedron $\boldsymbol{A^TB^TC^TD^T}$, the four $\{111\}$ slip planes $\boldsymbol{a}^T$, $\boldsymbol{b}^T$, $\boldsymbol{c}^T$ and $\boldsymbol{d}^T$ are defined by the right-handed rule as following: $\boldsymbol{a}^T \Leftrightarrow \boldsymbol{B}^T\boldsymbol{C}^T\boldsymbol{D}^T$, $\boldsymbol{b}^T \Leftrightarrow \boldsymbol{C}^T\boldsymbol{A}^T\boldsymbol{D}^T$, $\boldsymbol{c}^T \Leftrightarrow \boldsymbol{A}^T\boldsymbol{B}^T\boldsymbol{D}^T$, $\boldsymbol{d}^T \Leftrightarrow \boldsymbol{A}^T\boldsymbol{C}^T\boldsymbol{B}^T$. Thompson tetrahedra $\boldsymbol{ABCD}$ and $\boldsymbol{A}^T\boldsymbol{B}^T\boldsymbol{C}^T\boldsymbol{D}^T$ have twin relationship with respect to each other. The hatched plane $\boldsymbol{ACB}$ highlights the mirror plane. Due to mirror symmetry (exchange of left and right), $\boldsymbol{c}$ is mirror to $\boldsymbol{c}^T$, $\boldsymbol{a}$ is mirror to $\boldsymbol{b}^T$, $\boldsymbol{b}$ is mirror to $\boldsymbol{a}^T$, the $\boldsymbol{d}$ and $\boldsymbol{d}^T$ planes are coincident. Vertices $\boldsymbol{C}$ and $\boldsymbol{C}^T$ are coincident. Vertices $\boldsymbol{A}$, $\boldsymbol{B}$ and $\boldsymbol{D}$ in the upper Thompson tetrahedron correspond to $\boldsymbol{B}^T$, $\boldsymbol{A}^T$ and $\boldsymbol{D}^T$ in the lower Thompson tetrahedron.

unit cell, the elastic stiffness tensor $\hat{C}_{ijkl}$ for cubic materials can be represented as

$$\hat{\boldsymbol{C}} = \begin{bmatrix} \hat{C}_{1111} & \hat{C}_{1122} & \hat{C}_{1122} & 0 & 0 & 0 \\ & \hat{C}_{1111} & \hat{C}_{1122} & 0 & 0 & 0 \\ & & \hat{C}_{1111} & 0 & 0 & 0 \\ & & & \hat{C}_{2323} & 0 & 0 \\ & & & & \hat{C}_{2323} & 0 \\ & & & & & \hat{C}_{2323} \end{bmatrix} = \begin{bmatrix} \alpha & \beta & \beta & 0 & 0 & 0 \\ & \alpha & \beta & 0 & 0 & 0 \\ & & \alpha & 0 & 0 & 0 \\ & & & \omega & 0 & 0 \\ & & & & \omega & 0 \\ & & & & & \omega \end{bmatrix} \tag{2.65}$$

It contains 3 independent elastic constant. If one makes orthorgonal coordinate transformation $\hat{\boldsymbol{x}} \rightarrow \boldsymbol{x}$, the elastic stiffness tensor would take the transformation of $\hat{\boldsymbol{C}} \rightarrow \boldsymbol{C}$ as following

$$C_{ijkl} = \hat{C}_{pqrs} \frac{\partial \hat{x}^p}{\partial x^i} \frac{\partial \hat{x}^q}{\partial x^j} \frac{\partial \hat{x}^r}{\partial x^k} \frac{\partial \hat{x}^s}{\partial x^l} \tag{2.66}$$

Thomas [72] showed that the above transformation when applied for for cubic materials can be simplified to the following

$$\begin{aligned} C_{ijkl} &= \hat{C}_{1122}\delta_{ij}\delta_{kl} + \hat{C}_{2323}(\delta_{ik}\delta_{jl} + \delta_{il}\delta_{jk}) + (\hat{C}_{1111} - \hat{C}_{1122} - 2\hat{C}_{2323})A_{iu}A_{ju}A_{ku}A_{lu} \\ &= \beta\delta_{ij}\delta_{kl} + \omega(\delta_{ik}\delta_{jl} + \delta_{il}\delta_{jk}) + (\alpha - \beta - 2\omega)A_{iu}A_{ju}A_{ku}A_{lu} \end{aligned} \tag{2.67}$$

where A_{ij} is the direction cosine matrix relating the two coordinate frames ($\hat{\boldsymbol{x}} \rightarrow \boldsymbol{x}$), i.e.,

$$\boldsymbol{x}_i = A_{ij}\hat{\boldsymbol{x}}_j \tag{2.68}$$

Using the FCC twin related grains in Fig. 2.12 as an example, the coordinate system in the matrix grain has its unit vectors along the $[11\bar{2}]$, $[111]$ and $[1\bar{1}0]$ directions, i.e.,

$$\begin{aligned} \boldsymbol{x}_1 &= \frac{1}{\sqrt{6}}(\hat{\boldsymbol{x}}_1 + \hat{\boldsymbol{x}}_2 - 2\hat{\boldsymbol{x}}_3) \\ \boldsymbol{x}_2 &= \frac{1}{\sqrt{3}}(\hat{\boldsymbol{x}}_1 + \hat{\boldsymbol{x}}_2 + \hat{\boldsymbol{x}}_3) \\ \boldsymbol{x}_3 &= \frac{1}{\sqrt{2}}(\hat{\boldsymbol{x}}_1 - \hat{\boldsymbol{x}}_2 + 0\hat{\boldsymbol{x}}_3) \end{aligned} \tag{2.69}$$

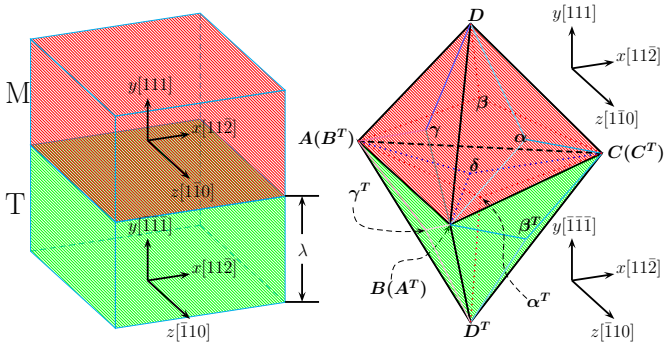

Figure 2.12: Two FCC twin related grain.

Hence, the direction cosine matrix A_{ij} is

$$A = \begin{bmatrix} \frac{1}{\sqrt{6}} & \frac{1}{\sqrt{6}} & \frac{-2}{\sqrt{6}} \\ \frac{1}{\sqrt{3}} & \frac{1}{\sqrt{3}} & \frac{1}{\sqrt{3}} \\ \frac{1}{\sqrt{2}} & \frac{-1}{\sqrt{2}} & 0 \end{bmatrix} \tag{2.70}$$

and the stiffness tensor is

$$
\boldsymbol{C} = \begin{bmatrix}
\frac{1}{2}(\alpha+\beta+2\omega) & \frac{1}{3}(\alpha+2\beta-2\omega) & \frac{1}{6}(\alpha+5\beta-2\omega) & 0 & 0 & -\frac{\sqrt{2}}{6}(\alpha-\beta-2\omega) \\
 & \frac{1}{3}(\alpha+2\beta+4\omega) & \frac{1}{3}(\alpha+2\beta-2\omega) & 0 & 0 & 0 \\
 & & \frac{1}{2}(\alpha+\beta+2\omega) & 0 & 0 & \frac{\sqrt{2}}{6}(\alpha-\beta-2\omega) \\
 & & & \frac{1}{3}(\alpha-\beta+\omega) & \frac{\sqrt{2}}{6}(\alpha-\beta-2\omega) & 0 \\
 & & & & \frac{1}{6}(\alpha-\beta+4\omega) & 0 \\
 & & & & & \frac{1}{3}(\alpha-\beta+\omega)
\end{bmatrix}
$$

$$
= \begin{bmatrix}
C_{1111} & C_{1122} & C_{1133} & 0 & 0 & C_{1112} \\
 & C_{2222} & C_{2233} & 0 & 0 & 0 \\
 & & C_{3333} & 0 & 0 & C_{3312} \\
 & & & C_{2323} & C_{2313} & 0 \\
 & & & & C_{1313} & 0 \\
 & & & & & C_{1212}
\end{bmatrix}
$$

$$
= \begin{bmatrix}
C_{11} & C_{12} & C_{13} & 0 & 0 & C_{16} \\
 & C_{22} & C_{23} & 0 & 0 & 0 \\
 & & C_{33} & 0 & 0 & C_{36} \\
 & & & C_{44} & C_{45} & 0 \\
 & & & & C_{55} & 0 \\
 & & & & & C_{66}
\end{bmatrix}
$$

(2.71)

Similarily, the coordinate system in the twin grain has its unit vectors along the $[11\bar{2}]$, $[\bar{1}\bar{1}\bar{1}]$ and $[\bar{1}10]$ directions, i.e.,

$$\begin{aligned} \boldsymbol{x}_1 &= \frac{1}{\sqrt{6}}\left(\hat{\boldsymbol{x}}_1 + \hat{\boldsymbol{x}}_2 - 2\hat{\boldsymbol{x}}_3\right) \\ \boldsymbol{x}_2 &= \frac{1}{\sqrt{3}}\left(-\hat{\boldsymbol{x}}_1 - \hat{\boldsymbol{x}}_2 - \hat{\boldsymbol{x}}_3\right) \\ \boldsymbol{x}_3 &= \frac{1}{\sqrt{2}}\left(-\hat{\boldsymbol{x}}_1 + \hat{\boldsymbol{x}}_2 + 0\hat{\boldsymbol{x}}_3\right) \end{aligned} \tag{2.72}$$

Hence, the direction cosine matrix A_{ij} is

$$\boldsymbol{A} = \begin{bmatrix} \frac{1}{\sqrt{6}} & \frac{1}{\sqrt{6}} & \frac{-2}{\sqrt{6}} \\ \frac{-1}{\sqrt{3}} & \frac{-1}{\sqrt{3}} & \frac{-1}{\sqrt{3}} \\ \frac{-1}{\sqrt{2}} & \frac{1}{\sqrt{2}} & 0 \end{bmatrix} \tag{2.73}$$

and the stiffness tensor is

$$
\boldsymbol{C} = \begin{bmatrix}
\frac{1}{2}(\alpha+\beta+2\omega) & \frac{1}{3}(\alpha+2\beta-2\omega) & \frac{1}{6}(\alpha+5\beta-2\omega) & 0 & 0 & \frac{\sqrt{2}}{6}(\alpha-\beta-2\omega) \\
 & \frac{1}{3}(\alpha+2\beta+4\omega) & \frac{1}{3}(\alpha+2\beta-2\omega) & 0 & 0 & 0 \\
 & & \frac{1}{2}(\alpha+\beta+2\omega) & 0 & 0 & -\frac{\sqrt{2}}{6}(\alpha-\beta-2\omega) \\
 & & & \frac{1}{3}(\alpha-\beta+\omega) & -\frac{\sqrt{2}}{6}(\alpha-\beta-2\omega) & 0 \\
 & & & & \frac{1}{6}(\alpha-\beta+4\omega) & 0 \\
 & & & & & \frac{1}{3}(\alpha-\beta+\omega)
\end{bmatrix}
$$

$$
= \begin{bmatrix}
C_{1111} & C_{1122} & C_{1133} & 0 & 0 & C_{1112} \\
 & C_{2222} & C_{2233} & 0 & 0 & 0 \\
 & & C_{3333} & 0 & 0 & C_{3312} \\
 & & & C_{2323} & C_{2313} & 0 \\
 & & & & C_{1313} & 0 \\
 & & & & & C_{1212}
\end{bmatrix}
$$

$$
= \begin{bmatrix}
C_{11} & C_{12} & C_{13} & 0 & 0 & C_{16} \\
 & C_{22} & C_{23} & 0 & 0 & 0 \\
 & & C_{33} & 0 & 0 & C_{36} \\
 & & & C_{44} & C_{45} & 0 \\
 & & & & C_{55} & 0 \\
 & & & & & C_{66}
\end{bmatrix}
$$

(2.74)

The stiffness tensors for the above two twin related grains share most of the terms with only a sign difference in the C_{16}, C_{36} and C_{45} term. In addition, the following

$$C_{14} = C_{15} = C_{24} = C_{25} = C_{34} = C_{35} = C_{46} = C_{56} = 0 \tag{2.75}$$

makes anti-plane deformation (u_3) uncoupled from the in plane deformation (u_1, u_2) for cubic materials when the coordinate axes are chosen to be one of the aboves [73]. This has important implications on dislocation image stresses to be discussed below.

2.3.2 Shearing Stress

Dislocations only move in response to shear stresses. The shear stress resolved on the slip plane in the slip direction drives slip. It is given by

$$\sigma = \frac{F}{A} \cos\phi \cos\lambda \tag{2.76}$$

where F is the applied force acting on an area A; ϕ is the angle between F and the normal of the slip plane and λ is the angle between F and the slip direction. $\cos\phi\cos\lambda$ is known as the Schmid factor. The shear stress σ required to initiate slip is called the critical resolved shear stress for slip.

2.3.3 Dislocation Burgers Vector

The dislocation Burgers vector in the continium model is given by the line integral of the elastic displacement $\boldsymbol{u}$ around the dislocation taken in a right-handed sense relative to the line direction $\boldsymbol{\xi}$

$$\boldsymbol{b} = \oint_C \frac{\partial \boldsymbol{u}}{\partial l} dl \tag{2.77}$$

In discrete lattices the Burgers vector can be expressed as

$$\boldsymbol{b} = \sum_{i=1}^{N} \Delta \boldsymbol{u}_i \tag{2.78}$$

where $\Delta \boldsymbol{u}_i$ is the difference between the actual and perfect reference lattice atom position and lattice site 1 to N form a closed loop in the perfect reference lattice. Eqn. 2.78 can be used to find Burgers vectors by forming Burgers loops on crystal lattices [74]. For MD simulations in subsequent Chapters, we used this method to determine those Burgers vectors.

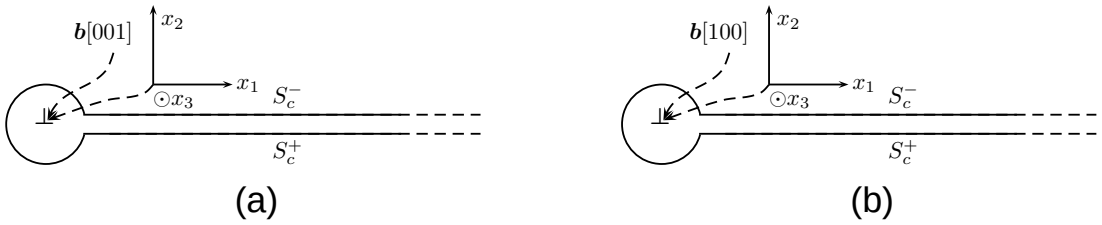

Figure 2.13: (a) A screw dislocation with its line direction along the x_3 axis; (b) An edge dislocation with its line direction along the x_3 axis and Burgers vector along the x_1 axis. The origin of the cartesian coordinates are conveniently selected at the dislocation locations in both figures.

2.3.4 Elastic Fields of Straight Dislocations

Dislocations can be classified based on the orientation between the Burgers vector $\boldsymbol{b}$ and line direction $\boldsymbol{\xi}$. The angle between $\boldsymbol{b}$ and $\boldsymbol{\xi}$ can be found as

$$\cos\theta = \frac{\boldsymbol{b}\cdot\boldsymbol{\xi}}{|\boldsymbol{b}||\boldsymbol{\xi}|} \tag{2.79}$$

Screw dislocations have their line direction $\boldsymbol{\xi}$ parallel to the Burgers vector $\boldsymbol{b}$, i.e., $\theta = 0$. Edge dislocation have $\boldsymbol{\xi}$ and $\boldsymbol{b}$ perpendicular to each other, i.e., $\theta = \pi/2$. Dislocations with $0 < \theta < \pi/2$ are mixed dislocations having both screw and edge character. Under isotropic linear elastic approximation, screw dislocations create an anti-plane strain deformation while edge dislocations create an in-plane strain deformation. We give the displacement fields of these two types of dislocations in infinite domain as these formulas are used as approximations in creating dislocations for MD simulations in latter Chapters.

Under the assumption of infinitesimal linear elastic approximation, the displacement vector $\boldsymbol{u}$ corresponding to an isotropic anti-plane deformation with the cartesian coordinate shown in Fig. 2.13 (a) simplifies to

$$u_1 = 0 \tag{2.80a}$$

$$u_2 = 0 \tag{2.80b}$$

$$u_3 = u_3(x_1, x_2) \tag{2.80c}$$

Hence, the strain tensor $\epsilon_{ij} = \frac{1}{2}\left(\frac{\partial u_i}{\partial x_j} + \frac{\partial u_j}{\partial x_i}\right)$takes the following form

$$\boldsymbol{\epsilon} = \frac{1}{2}\begin{bmatrix} 0 & 0 & u_{3,1} \\ & 0 & u_{3,2} \\ & & 0 \end{bmatrix} \tag{2.81}$$

and the stress tensor can be obtained by using Eqn. C.5

$$\boldsymbol{\sigma} = \mu\begin{bmatrix} 0 & 0 & u_{3,1} \\ & 0 & u_{3,2} \\ & & 0 \end{bmatrix} \tag{2.82}$$

The static equilibrium equation (Eqn. C.6) reduces to the following form

$$u_{3,11} + u_{3,22} = 0 \tag{2.83}$$

The boundary conditions for a screw dislocation can be written as

$$\oint_C \frac{\partial u_3}{\partial l} dl = b \tag{2.84}$$

The solution to the above Laplace equation (Eqn. 2.83) with boundary condition Eqn. 2.84 is

$$u_3 = \frac{b}{2\pi}\tan^{-1}\left(\frac{x_2}{x_1}\right) \tag{2.85}$$

The corresponding strain and stress tensors are thus found by direct differentiation as in Eqn. 2.81 and 2.82.

For the case of in-plane strain deformation corresponding to edge dislocations as shown in Fig. 2.13 (b), the displacement vector $\boldsymbol{u}$ takes the following form

$$u_1 = u_1(x_1, x_2) \tag{2.86a}$$

$$u_2 = u_2(x_1, x_2) \tag{2.86b}$$

$$u_3 = 0 \tag{2.86c}$$

Hence the strain tensor $\epsilon_{ij} = \frac{1}{2}\left(\frac{\partial u_i}{\partial x_j} + \frac{\partial u_j}{\partial x_i}\right)$takes the following form

$$\boldsymbol{\epsilon} = \frac{1}{2}\begin{bmatrix} 2u_{1,1} & u_{1,2}+u_{2,1} & 0 \\ & 2u_{2,2} & 0 \\ & & 0 \end{bmatrix} \tag{2.87}$$

and the stress tensor can be obtained by using Eqn. C.5 as following

$$\boldsymbol{\sigma} = \begin{bmatrix} 2\mu u_{1,1} + \lambda(u_{1,1}+u_{2,2}) & \mu\left(u_{1,2}+u_{2,1}\right) & 0 \\ & 2\mu u_{2,2} + \lambda(u_{1,1}+u_{2,2}) & 0 \\ & & \lambda(u_{1,1}+u_{2,2}) \end{bmatrix} \tag{2.88}$$

The static equilibrium equation (Eqn. C.6) reduces to the following form

$$\sigma_{i1,1} + \sigma_{i2,2} = 0 \tag{2.89}$$

or written in full

$$\sigma_{11,1} + \sigma_{12,2} = 0 \tag{2.90a}$$

$$\sigma_{21,1} + \sigma_{22,2} = 0 \tag{2.90b}$$

The boundary condition for the edge dislocation with its Burgers vector along the x_1 direction can be written as

$$\oint_C \frac{\partial u_1}{\partial l} dl = b \tag{2.91a}$$

$$\oint_C \frac{\partial u_2}{\partial l} dl = 0 \tag{2.91b}$$

The solution to Eqn. 2.90 can be found by introducing an Airy stress function [56] and can be

written as

$$\sigma_{11} = -\frac{\mu b}{2\pi(1-\nu)} \frac{x_2(3x_1^2 + x_2^2)}{(x_1^2 + x_2^2)^2} \tag{2.92a}$$

$$\sigma_{22} = \frac{\mu b}{2\pi(1-\nu)} \frac{x_2(x_1^2 - x_2^2)}{(x_1^2 + x_2^2)^2} \tag{2.92b}$$

$$\sigma_{12} = \frac{\mu b}{2\pi(1-\nu)} \frac{x_1(x_1^2 - x_2^2)}{(x_1^2 + x_2^2)^2} \tag{2.92c}$$

$$\sigma_{33} = -\frac{\mu b \nu}{\pi(1-\nu)} \frac{x_2}{x_1^2 + x_2^2} \tag{2.92d}$$

$$\sigma_{13} = \sigma_{23} = 0 \tag{2.92e}$$

The corresponding displacement field is given by

$$u_1 = \frac{b}{2\pi} \left[\tan^{-1} \frac{x_2}{x_1} + \frac{x_1 x_2}{2(1-\nu)(x_1^2 + x_2^2)} \right] \tag{2.93a}$$

$$u_2 = -\frac{b}{2\pi} \left[\frac{1-2\nu}{4(1-\nu)} \ln(x_1^2 + x_2^2) + \frac{x_1^2 - x_2^2}{4(1-\nu)(x_1^2 + x_2^2)} \right] \tag{2.93b}$$

$$u_3 = 0 \tag{2.93c}$$

2.3.5 The Force Exerted on Dislocations: Peach Koehler Force

Dislocations interact with stress caused by other sources excluding their self stress fields. The interaction energy can be written as

$$E_I = \int \boldsymbol{\epsilon} \boldsymbol{\sigma} dV \tag{2.94}$$

where $\boldsymbol{\epsilon}$ is the dislocation's strain field and $\boldsymbol{\sigma}$ is the stress field caused by external sources. Using the principle of virtual work, the interaction between a dislocation $\boldsymbol{b}$ and stress field $\boldsymbol{\sigma}$ can be computed by evaluating the work done by the stress field $\boldsymbol{\sigma}$ on the cutting surface during the displacement in creating the dislocation. A dislocation segment $d\boldsymbol{\xi}$ moves $d\boldsymbol{s}$ and sweeps an area of $d\boldsymbol{\xi} \times d\boldsymbol{s}$. The interaction energy difference before and after the movement is $\boldsymbol{b} \cdot \boldsymbol{\sigma} \cdot (d\boldsymbol{\xi} \times d\boldsymbol{s})$. The total work difference along the whole dislocation line is

$$-\Delta W_I = \int_l \boldsymbol{b} \cdot \boldsymbol{\sigma} \cdot (d\boldsymbol{\xi} \times d\boldsymbol{s}) \tag{2.95}$$

Hence the force acting on the dislocation in the direction of $d\boldsymbol{s}$ is

$$F_m = -\frac{\partial W_I}{\partial s} = \int_l \boldsymbol{b} \cdot \boldsymbol{\sigma} \cdot (d\boldsymbol{\xi} \times \boldsymbol{m}) \tag{2.96}$$

where $\boldsymbol{m}$ is the unit vector along $\boldsymbol{s}$, i.e., $d\boldsymbol{s} = \boldsymbol{m}ds$, F_m is the force component (along m) acting on the dislocation. The force component acting on the dislocation segment $d\boldsymbol{\xi}$ is

$$dF_m = \boldsymbol{b} \cdot \boldsymbol{\sigma} \cdot (d\boldsymbol{\xi} \times \boldsymbol{m}) = \boldsymbol{b} \cdot \boldsymbol{\sigma} \cdot (\boldsymbol{\xi} \times \boldsymbol{m})\, dl \tag{2.97}$$

Hence the force acting on a dislocation line segment $\boldsymbol{\xi}dl$ with Burgers vector $\boldsymbol{b}$ by an external stress field $\boldsymbol{\sigma}$ is

$$d\boldsymbol{F} = (\boldsymbol{\sigma} \cdot \boldsymbol{b}) \times \boldsymbol{\xi} dl \tag{2.98}$$

The above result was first generalized by Peach and Koehler [75] and the force is known as the Peach-Koehler force.

2.3.6 Dislocation Pile-ups

Dislocation pile-ups are frequently observed in crystalline metals. They govern many important phenomena, such as yielding and fracture, in the plastic deformation of these materials. Figure 2.14 (a) shows a single dislocation pile-up formed by straight dislocations of the same Burgers vector $\boldsymbol{b}$.

$$\boldsymbol{F} = n\left((\boldsymbol{\sigma} \cdot \boldsymbol{b}) \times \boldsymbol{\xi}\right) \tag{2.99}$$

where n is the number of similar dislocations in the pile-up, $\boldsymbol{\sigma}$ is the applied stress and $\boldsymbol{\xi}$ is the dislocation line direction. The above equation can be written in the usual scalar form as

$$F = n\sigma b = (n\sigma)\, b = \sigma_{lead} b \tag{2.100}$$

where σ is the shearing component of the applied stress $\boldsymbol{\sigma}$ projected onto the slip plane in the slip direction, σ_{lead} is thus the effective shearing stress on the leading dislocation in the pile-up. Eshelby et al. [76] solved the equilibrium position of each dislocation in the pile-up and showed that

$$n = cl\sigma \tag{2.101}$$

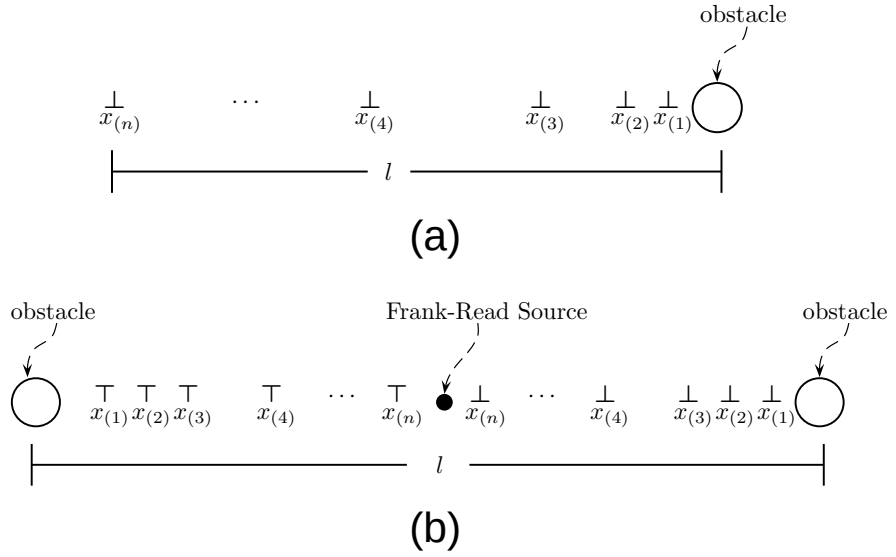

Figure 2.14: (a) Dislocation pile-up formed by straight dislocations of the same characters; (b) A double pile-up formed by dislocations of opposite line direction originated from a Frank-Read source.

where c is a constant and l is the pile-up distance. Combining Eqn. 2.100 and Eqn. 2.101 gives

$$\sigma \propto \sqrt{\frac{\sigma_{lead}}{l}} \tag{2.102}$$

Figure 2.14 (b) shows a double pile-up formed by dislocations with oppsite line direction originated from a Frank-Read [77] source . The scaling relation in Eqn. 2.102 still applies in the double pile-up case, which rationalizes the Hall-Petch relation [41, 42] governing the yielding stress of polycrystalline metals as a function of grain size

$$\sigma_y = \sigma_y^0 + \frac{A}{\sqrt{d}} \tag{2.103}$$

where σ_y^0 and A are constants.

2.3.7 Image Force of Dislocations in Anisotropic Bicrystals

Barnett and Lothe [78] derived an image force theorem for dislocations in infinite anisotropic bicrystals as illustrated in Fig. 2.15. Their theorem states that a straight dislocation situated at a distance h from the interface of an infinite anisotropic bicrystals experiences a virtual force

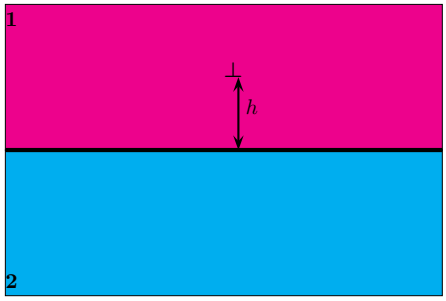

Figure 2.15: A straight dislocation located at a distance of h from the interface of a bicrystal consisting of two semi-infinite anisotropic crystals.

normal to the interface given by

$$f = \frac{E^{\infty} - E^{1-2}}{h} \tag{2.104}$$

where E^{∞} is the prelogarithmic energy factor of the dislocation located at an infinite homogeneous medium which has the same elastic properties as that of one of the halfspace. E^{1-2} is the prelogarithmic energy factor of the dislocation located at the interface of the bicrystals. The important point in the above theorem is that both E^{∞} and E^{1-2} depend only on the crystallographic orientation of the dislocation line direction $\boldsymbol{\xi}$ and Burgers vector $\boldsymbol{b}$ with respect to the two crystals. In Eqn. 2.104, the image force f on the dislocation diverges when $h \to 0$. Hence the condition $h > b$ is usually imposed as the limit for the above continuum theorem to be valid.

2.3.8 Image Force of Dislocations in Twin Bicrystals

Crystals with a twin relation such as that shown in Fig. 2.16 form a bicrystal structure. Dislocations located inside one of the two crystals usually experience image forces due to the different elastic stiffness tensors of the two twin related crystals (see Section. 2.3.1 for the stiffness tensor of twinned FCC crystals). In FCC materials, a pure screw dislocation creates an anti-plane shear deformation and its elastic field can be solved analytically (see Appendix D.1). It can be shown that there is no image force arising from the twin grain for pure screw dislocations in such materials (see Appendix D.2). However, an edge dislocation in FCC materials creates an in-plane deformation and in general its solution requires numerical calculation. An image force exists for edge dislocations in such twin related crystals. The above conclusion is also a direct, although subtle, result from the dislocation image theorem by Barnett and Lothe [78] (see

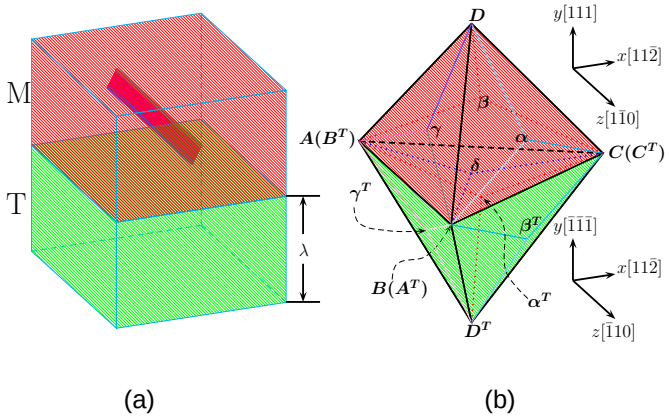

Figure 2.16: Dislocation in FCC twin related grains.

Section 2.3.7). Take a straight dislocation with its line direction $\boldsymbol{\xi}$ along the z axis as shown in Fig. 2.16 for example, if it is a pure screw dislocation with its Burgers vector $\boldsymbol{b} = \boldsymbol{AB}$, both $\boldsymbol{\xi}$ and $\boldsymbol{b}$ are crystallographically equivalent in both the matrix and twin crystals. Hence the prelogarithmic energy factor of the pure screw dislocation in either crystal will be the same and no image force exist. However, Burgers vector of a mixed dislocation with an edge component, such as $\boldsymbol{D\gamma}$ in Fig. 2.16, will be crystallographically different in the two crystals. The prelogarithmic energy factor due to the edge component will be different and an image force exists for such dislocations.

2.3.9 Dislocations Line Tension

Dislocation line tension was first conceptualized as

$$\tau = \frac{\delta U}{\delta l} \tag{2.105}$$

where δU is the increase of strain energy for an increase of δl in the length of the dislocation. There have been many attempts to calculate the dislocation line tension [79]. However, it is often adequate to approximate it as [80, 81]

$$\tau \approx \mu b^2 \tag{2.106}$$

where μ is the material's shearing modulus and b is the magnitude of the dislocation's Burgers vector.

2.4 Molecular Dynamics Simulations

Molecular dynamics (MD) simulations are computer simulations in which the atomic trajectory is determined by integrating the equations of motion according to Newton's second law for each atom in the system, i.e.,

$$\frac{d^2\boldsymbol{r}_{(i)}}{dt^2} = \frac{\boldsymbol{F}_{(i)}}{m_{(i)}} \tag{2.107}$$

where $\boldsymbol{r}_{(i)}$ and $m_{(i)}$ are the position and mass of atom i. $\boldsymbol{F}_{(i)}$ is the force acting on atom i due to interatomic interactions with other atoms in the system. Interatomic interactions in MD simulations are prescribed by potential functions of empirical or semi-empirical origin, i.e.,

$$\boldsymbol{F}_{(i)} = \frac{\partial E}{\partial \boldsymbol{r}_{(i)}} \tag{2.108}$$

where E is the total system energy. In MD simulations, position, velocity, forces acting on each individual atom are explicitly modelled. The time step used to integrate the Newton's second law is usually small (on the femtosecond scale for metals) so that atomic vibrations are sufficiently captured in simulations. Hence MD simulations provide atomic-level spatial and temporal resolution which are difficult to access from experiments. The above advantages are also accompanied by some fundamental limitations inherent in MD simulations. Time scale is one of the biggest bottlenecks in MD simulations. The availability and choice of appropriate interatomic potentials are also often questioned when complicated systems involving multiple elements and force sources are studied.

2.4.1 Embedded Atom Method (EAM)

There have been many types of interatomic potentials developed for atomistic simulations. For metals, two types of potentials, pair potentails (such as Lennard-Jones (LJ)) and embedded-atom method (EAM) potentials, are used frequently in the literature. EAM was first conceptualized by Stott and Zaremba [82] and developed by Murray and Baskes [46] to model metallic defects including impurities, dislocations, surfaces, etc. In the EAM formulation, the total system energy is given by

$$E = \sum_i G^{(i)} \left(\sum_{i \neq j} \rho^{(i)} \left(r^{(ij)} \right) \right) + \frac{1}{2} \sum_{ij} \phi_{(ij)} \left(r^{(ij)} \right) \tag{2.109}$$

where $r^{(ij)}$ is the distance between atomic site i and j; $\rho^{(i)}$ is the electron density function which gives electron density at atomic site i contributed by an atom at site j; $G^{(i)}$ is the embedding function which gives a cohensive energy when an atom is placed at site i under the electron environment of $\rho^{(i)}$; $\phi^{(ij)}$ is the pair potential function and the $1/2$ coefficient is to correct the double counting in the summation. (We write out the summation sign explicitly in Eqn. 2.109 so that it takes the same form as often found in literature). In principle the summation should be carried over all the atoms in the system. However, a cutoff radius is usually specified in the fitting of the respective potential. Thus, EAM potentials effectively describe short range forces. EAM potentials are many-body potentials and have some advantages over pair potentials such as the LJ potentials. For cubic metals, EAM potentials can be fitted to reproduce all the three elastic constants accurately and hence the elastic anisotropy of those materials. They also can be used to accurately model interfaces and surface properties, such as surface stress where EAM potentials exhibit surface contraction while pair potentials inaccurately show surface expansion. Although being many-body potentials, EAM potentials are computationally efficient. In the simulations of nanotwinned Cu and Al grain boundary in this Thesis, we use EAM potentials which are described below.

2.4.1.1 Cu Embedded Atom Method (EAM)

The $\{111\}$ stacking fault energy in FCC metals, γ_{ssf}, and the equilibrium separation between pairs of Shockley partial dislocations are known to be sensitive to the choice of interatomic potential employed in atomistic simulations. Therefore, the first step in performing simulations of nanotwinned Cu is the identification of an interatomic potential function that produces realistic values of the stacking fault energy. While many interatomic potentials are available for pure Cu, we chose the EAM potential [46, 82] by Mishin et al. [1] to study the plastic deformation of nanotwinned Cu. This Cu potential was fit to experimental and *ab initio* data, including the lattice parameter a_0, cohesive energy E_0, and the stacking fault energy γ_{ssf}. This Cu potential yields an intrinsic stacking fault energy of 44.42 mJ/m^2, an extrinsic stacking fault energy of 44.52 mJ/m^2 and a $\Sigma 3$ coherent twin boundary ($\{111\}\langle 112\rangle$) energy of 22.27 mJ/m^2, which are all in excellent agreement with available experimental data [56].

The above Cu potential also predicts the lattice properties accurately. Table 2.1 lists the lattice and elastic constants given by the potential. These constants are well within 1% of error when compared to experimental values.

	a_0 Å	E_0 eV/atom	B GPa	c_{11} GPa	c_{12} GPa	c_{44} GPa	γ_{ssf} mJ/m^2
experiment	3.615	-3.54	138.3	170.0	122.5	75.8	45
EAM Cu [1]	3.615	-3.54	138.3	169.9	122.6	76.2	44.4

Table 2.1: Lattice properties of Cu predicted by EAM Cu by Mishin et al. [1].

2.4.1.2 Al Embedded Atom Method (EAM)

In MD simulations at high temperature, the employed potential's ability to reproduce the material's melting properties is important. Al EAM potential by Mendelev et al. [2] was fitted to first-principle calculations and data measured from liquid diffraction. This Al potential predicts accurately on its melting point, liquid-phase diffusivities, etc. Hence we use it in the simulations of grain boundary faceting study where simulations at high temperature and those involving phase transitions are examined. Table 2.2 lists the lattice and elastic constants given by the potential.

	a_0 Å	E_0 eV/atom	B GPa	c_{11} GPa	c_{12} GPa	c_{44} GPa	γ_{ssf} mJ/m^2
experiment	4.032	-3.362	76	118	62	33	166, 120-144 [83]
EAM Al [2]	4.045	-3.411	58 (at T_m)	110	61	33	151.7

Table 2.2: Lattice properties of Al predicted by EAM Al by Mendelev et al. [2]. All properties except the bulk modulus B are obtained at T = 0 K.

2.4.2 Atomic Stress

One way to define the stress tensor at a single atomic site i is through the virial equation,

$$\beta_{pq}^{(i)} = \frac{1}{\Omega^{(i)}} \left[m^{(i)} v_p^{(i)} v_q^{(i)} + \sum_{j(\neq i)}^{M} f_p^{(ij)} r_q^{(ij)} \right] \tag{2.110}$$

where $\Omega^{(i)}$ is the atomic volume and M is the number of near neighbour atoms. In the square bracket, the first term is the kinetic energy contribution from atom i and the second term is the dipole force tensor arising from the pair-wise interaction energy. The atomic volume $\Omega^{(i)}$ can be taken as the atomic site's voronoi volume [84, 85]. The continuum stress tensor can be taken

as a volume average over a region under consideration

$$\sigma_{pq} = \frac{1}{K} \sum_{i=1}^{K} \beta_{pq}^{(i)} \tag{2.111}$$

where K is the number of atoms in the region. The above formulation is used throughout this work and applies to all subsequent Chapters when stresses are extracted from MD simulations (see Ref. [86] for a detailed formulation).

2.4.3 Ensemble

The micro-canonical or NVE ensemble simulates a system where the total number of atoms N, the volume V and the total energy E are conserved during the simulation. When the simulated atomic system interacts with an external environment or reservoir, special coupling can be used to model such interactions. A system exchanging heat with a thermostat can be modelled using a Nosé-Hoover temperature thermostat [87, 88] such that its temperature is maintained constant with the external thermostat. This results in an isothermal or canonical NVT ensemble where the total number of atoms N, the volume V and the temperature T are conserved during the simulation. The interaction with an external barostat can be modelled using a Nosé-Hoover pressure barostat [88, 89] such that its pressure is maintained constant with the external barostat. This can be achieved through adjusting the volume of the system which results in an isobaric ensemble. MD simulations presented in subsequent Chapters use the MD code LAMMPS' [90] isothermal isobaric or NPT ensemble, which combines the two coupling and results in a system where the total number of atoms N, the pressure P and the temperature T are constant during the simulation (see Ref. [88] for detailed formulation).

2.4.4 Computational Costs

The computational cost of each modelling methods varies significantly. The computing time required to perform MD simulations depends on the system being simulated. Systems with ionic bondings involve long range forces and are thus computationally expensive. The interatomic interactions in pure metals are often prescribed by EAM potentials which usually have only short range interactions. This makes the force analysis simpler, resulting in a much shorter computer time. Its ability to scale linearly on parallel machines or clusters with modern interconnects offers a great computational advantage over other methods. Using the widely adopted

parallel MD code LAMMPS [90] and Cu potential by Mishin et al. [1], a simulation of 100 million atoms (or a $\sim$ 106 $\times$ 106 $\times$ 106 nm cube) for one million time steps will take 10^5 cpu hours on a Xeon x5570 cluster, or approximately 5 days by summoning 1000 cpu cores. MD simulations have relatively low requirements on computer memory when compared to that of cpu time. The total memory required for the above run is less than 40 gigabytes (GB), an amount of memory even available on workstations nowadays.

MD simulations also generate a huge amount of raw data tracking atomic trajectories such as individual atom's position, velocity, etc. For a simulation of 100 million atoms, each time step produces 4.8×10^9 bytes (4.8 GB) of data. Such a simulation would require 4.8 petabytes of storage for one million time steps. Hence data analysis and filtering become an essential step in MD simulations.

2.4.5 Data Analysis and Visualization

It is imperative to perform simulations with sufficient length and time scale for realistic material behaviors. Hence MD simulations inevitably generate an enormous amount of data on atomic information. However, in simulations of crystalline metals, atoms on or near defect regions such as dislocation cores and grain boundaries are often the point of interest, while atoms on perfect lattices far away from those defects are less important. Furthermore, raw MD data carries little physical insight. Hence, identifying these defects and tracking their evolution become crucial in the analysis of simulation results. Various algorithms have been developed to identify and analyze crystalline defect structures. One straightforward method is the use of coordination number (n), which measures the number of nearest neighbouring atoms. While atoms on defect sites can have lower, equal or higher coordination numbers, those on surfaces often have a lower coordination number. In FCC lattices, $n = 12$ for perfect lattice environments. However, the coordination number for atoms on stacking fault in FCC lattice is equal to that of those on perfect lattice sites, making the stacking faults indistinguishable from perfect lattice environments. Certain atoms on grain boundaries can have higher, equal or lower coordination number compared to that for a perfect lattice. Hence, coordination number is often used as a preliminary analysis due to its ease of computation.

Another useful technique to identify FCC lattice defects is the use of the central symmetry

parameter [91]. For each lattice site, a unique number c_p can be defined as

$$c_p = \sum_{i=1}^{N_p} |\boldsymbol{r}_i + \boldsymbol{r}_{i+N_p}|^2 \tag{2.112}$$

where $\boldsymbol{r}_i$ and $\boldsymbol{r}_{i+N_p}$ are the relative (to the lattice site under consideration) position vectors of the ith pair of nearest neighbouring atoms and N_p is the total number such atom pairs. The FCC lattice has $N_p = 6$ (as shown in Fig. 2.2) and the BCC lattice has $N_p = 4$. c_p measures the local lattice inversion symmetry. For lattices having inversion symmetry (such as simple cubic, body centered cubic and face centered cubic), the central symmetry parameter is zero at perfect lattice sites and non-zero at defect sites (such as point defects, dislocation cores, stacking faults and interfaces). Hence it can be used effectively to identify sites in perfect and non-perfect lattice environments for materials possessing inversion symmetry. This is particularly useful in identifying stacking faults including twin boundaries in FCC lattices. However, c_p does not detect homogeneous deformation.

Chapter 3

Interface Strengthening in Crystalline Metals

In this Chapter we give a brief review on interface strengthening in metallic systems and point out the current development in this field. We then draw our attention to the topic of nanotwinned polycrystalline Cu, where both experimental and simulation studies are presented. We combine these studies and summarize the main discrepancies between previous experimental observations and simulation results related to materials having this unique microstructure. At the end of this Chapter we summarize the key open issues, which drive the simulations in Chapter 4 and Chapter 5.

3.1 The Need for Strengthening Metals

As a dislocation moves on its slip plane, its core energy varies periodically. The difference between the maximum and minimum of the dislocation core energy creates an energy barrier to dislocation motion. This barrier is known as the Peierls barrier [92] of dislocation. The Peierls barrier can be overcome by an applied stress (i.e., Peierls stress), thermal fluctuations or a combination of the two. Pure crystalline metals are usually soft as the stress required for dislocation glide can be orders of magnitude lower than the materials' theoretical shear strength. In FCC metals, the Peierls stress can be as low as a few tens of MPa [92–94]. Bujard et al. [95] estimated the Peierls stress for Cu and Al to be $1.2 \times 10^{-3}\mu$ ($\sim$ 58 MPa) and $8 \times 10^{-3}\mu$ ($\sim$ 208 MPa), respectively. The actual stress required for dislocations in these materials to glide can be much lower with the help of thermal fluctuations. Since dislocation

glide is the dominant carrier of plastic deformation in FCC metals and the stress required for that is low, the key to increasing the strength of FCC materials lies in: (1) creating barriers to dislocation glides; (2) reducing dislocation sources. Most conventional methods make use of first approach. These include strengthening through particles, interfaces, and strain hardening. On the other hand, materials with novel structures like nanowire or nanorod are usually strong because of the second. Nanocrystalline materials, depending on their grain size, can exhibit both features.

3.2 Interface Strengthening in Crystalline Metals

It has long been recognized that polycrystalline metals and their alloys can be strengthened through interfacial boundaries. The underlying principle for this strengthening mechanism relies on these boundaries serving as barriers to dislocation glide. Several factors, such as strain mismatch, image forces (also known as Koehler forces [96]), the necessity to create dislocations at interfaces (i.e., ledge creations at interfaces), and interaction with misfit dislocations, etc. can alter the effectiveness of these barriers [97]. Based on these factors, there has been relentless effort in developing strong and tough materials through interfacial boundaries. Table 3.1 shows some experimental work employing this approach in metallic systems. Based on this list, a few points are remarkable. The first is the characteristic length scale in these microstructures. It is evident that the microstructural length scales associated with interface (grain boundaries, twin boundaries or phase boundaries) separation play an important role in determining the mechanical properties of these metals. This also suggests that some length scale dependent mechanisms operate during yielding in these microstructures. For polycrystalline metals, a well-known length scale dependent deformation mechanism is the dislocation pile-ups. This results in the Hall-Petch relationship [41, 42] governing materials' yield strength as a function of their microstructure characteristic length scales (see Section. 2.3.6 for a brief explanation). The Hall-Petch law predicts the strength increases as the grain size decreases in the grain refinement process. This relation is known to be effective in a wide range of length scales. However, given the stringent requirements for the operation of dislocation pile-ups, it is still a surprise that the semi-phenomenological Hall-Petch relation works so well (especially when length scale $>$ 50 nm) in such a large class of materials and microstructures.

As the grain size decreases to below 100 nm, a controversy on the effect of grain boundary and Hall-Petch relation arises in nanocrystalline materials. While nanocrystalline samples

Materials	Structure	Strengthening	Softening
Cu [11]	tb & gb	Hall-Petch (8.4 μm - 0.056 μm)	no
Au/Co[37]	gb	Hall-Petch (>20 nm)	not shown
Ni [98]	tb & gb	Hall-Petch (>12 nm)	not shown
Cu [99]	gb	Hall-Petch (25 μm - 4 μm)	yes (<16 nm)
Pd [100]	gb	Hall-Petch (5-10 nm)	no
Cu [100]	gb	Hall-Petch (25-35 nm)	not shown
Pd [99]	gb	not shown	yes (<15 nm)
Ni/P [101]	gb	not shown	yes (<120 nm)
Cu/Cr [102]	pb	Hall-Petch (>50 nm)	saturating (<50 nm)
Cu/Nb [102]	pb	Hall-Petch (>50 nm)	no
Cu/Ni [102]	pb	Hall-Petch (>50 nm)	yes (< 5nm)
Cu [12]	tb	Hall-Petch (>20 nm)	yes (<15 nm)
Cu [14]	tb	Others	no
Cu [103]	tb	not shown	not shown
Cu/304 stainless steel [38]	pb & tb	Hall-Petch (>100 nm) and others (100 nm - 5 nm)	yes (<5nm)
Cu/330 stainless steel [104]	pb & tb	Hall-Petch (>50 nm)	saturating (<50 nm)

Table 3.1: Recent work on interfacial strengthening in metals. tb, gb and pb stand for twin boundary, grain boundary and phase boundary, respectively.

prepared from nano-particles through compression or rolling tend to show softening if their grain diameter is $\sim$10 nm [99, 101, 105–108], those prepared via a deposition process can show strengthening for grain size $<$ 10 nm [37, 98, 100, 109]. This discrepancy is partly resolved until recently by recognizing that sample preparation has a strong effect on the strength of nanocrystalline materials, especially when the grain size is below a few tens of nanometers. Another view point is that dislocation-mediated plasticity transforms into grain boundary mediated plasticity as the grain diameter reaches some critical size. Similarly, as in strengthening via grain boundaries, nanostructured materials strengthened via other types of interfacial boundaries also exhibit softening when their characteristic length scales are below a few tens of nanometers. Such examples include Cu/Ni [102], Cu [12], Cu/304 stainless steel [38], etc. However, the underlying mechanisms responsible for softening in these cases remain largely unknown.

While the microstructure characteristic length scales help to determine the resulting materials' properties, the interface types existing in the microstructure also have an important effect. During grain refinement and subsequent annealing, grain boundaries adjust two of their macroscopic degrees of freedom determining their boundary inclinations so that the overall grain boundary free energy is reduced. However, the other three macroscropic degrees of freedom remain fixed. Grain boundary refinement has limited control on the resulting grain boundary types and thus the effectiveness of those grain boundaries as barriers to dislocation glidings is compromised [81]. In addition, the uncontrolled grain boundaries can also act as dislocation sources. Hence, strengthening by conventional grain boundary refinement approach creates suboptimal materials. On the contrary, multi-layered nanocomposite systems prepared via a deposition process usually have selected interface types [11, 38, 102]. These interfaces serve as effective barriers to dislocation propagations from one layer to the other and hence enhance the strength of the resulting materials. However, microstructure refinement in multi-layered nanocomposites and nanocrystalline materials often leads to increased strength, but at the expense of decreased toughness. It is common for these materials to fail at a few percent tensile strain [109, 110].

Among the large number of interfaces available for manipulating material properties, coherent twin boundaries are especially effective at controlling strength because of their extraordinary stability (relative to other microstructural features) [10] and the discontinuity of slip systems across twin boundaries. Twin related grains have a mirror symmetry about the twin boundary, so do their slip systems. The discontinuity in the slip systems makes dislocation

nucleation or cross-slip necessary in the process of slip transfer across the twin boundary. This provides a strong barrier to dislocation glides and hence makes this unique microstructure an attractive candidate in creating ultrahigh strength materials. Growth nanotwins, which are believed to be caused by an accidential departure from equilibrium during growth, have been observed in many minerals [68] and metals [10–18, 20]. Modern growth techniques have made it possible to synthesize metals with growth nanotwins with highly tuned twin sizes, which can vary from a few hundred nanometers to a few nanometers. By controlling both the microstructural interface type and length scale, the resulting materials with growth nanotwins exhibit a combination of attractive properties, such as simultaneous ultrahigh strength, ductility, conductivity and strain hardening [12, 13]. This small microstructure inherent in nanomaterials opens the door to the development of ultrahigh strength metals [10–20]. In the following section, we present a detailed description on nanotwinned FCC metals.

3.3 Nanotwinned FCC Metals

There are mainly two popular methods to generate nanotwinned metals: (1) sputter deposition; (2) electrodeposition. Merz and Dahlgren [11] synthesized high-purity Cu specimens with grain size between 8.4 μm and 0.056 μm via high rate sputter deposition. Their samples contain a high density of twin boundaries parallel to the deposition plane and the 0.2% offset tensile strength follows the Hall-Petch relation with the yielding stress varying from 73.4 MPa to 481 MPa. Via magnetron-sputtering, Zhang et al. [38] synthesized Cu/304 stainless steel multilayers with maximum hardness of 5.5 GPa at a layer thickness of 5 nm, below which the material softens. Zhang et al. [104] also synthesized Cu/austenitic 330 stainless steel multilayered films with twin spacing of 3-4 nm in the stainless steel layer and a few tens of nanometers in the copper layer. The hardness of their samples follows the Hall-Petch law for layer thickness greater than 50 nm and saturates for thinner layers. Anderoglu et al. [14] synthesized epitaxial nanotwinned Cu films with a twin spacing varying from 7 to 16 nm. All the previously described materials share similar structures. They form films with columnar grains and the twinning planes are oriented normal to the growth direction, as they are all deposited via a layer-by-layer mechanism.

On the other hand, FCC metallic crystals grown by electrodeposition tend to contain growth twins. Poli and Bicelli [35] reported that numerous growth twins were found in electrodeposited Pd, Cu and Cd. Faust and John [36] observed growth twins in Ag dendrites grown by

electrodeposition. Lo et al. [37] found some twins in the electrodeposited Au samples. Zhong et al. [103] produced nanotwinned Cu nanowire by direct electrodeposition. Recently, Lu et al. [12] synthesized ultrafine pure polycrystalline Cu containing a high density of growth twins via a pulsed electrodeposition technique. The average twin spacing, varying between 4 and 96 nm in their samples, can be effectively controlled through the electrodeposition condition (on-off time and average deposition current density, see Ref. [43] for details). Unlike samples produced via a layer-by-layer deposition mechanism, their samples also demonstrated a true polycrystalline microstructure which simultaneously exhibited a high yield strength, high ductility, high strain-rate sensitivity and high electric conductivity [10, 39, 40].

3.3.1 Ultrafine Nanotwinned Copper

3.3.1.1 Yield Strength, Strain Hardening and Ductility

Those electrodeposited ultrafine pure Cu samples with growth nanotwins by Lu et al. [43] have many desirable properties. Their mechanical properties are unusual, as shown in Figure 3.1, which plots the variation of mechanical properties (in uniaxial tensile loading at a strain rate of 6×10^{-3} s^{-1}) as a function of twin spacing. The data in the figure is for samples with an average grain diameter between 400 nm and 600 nm. Figure 3.1 (a) shows the yielding stress σ as a function of twin spacing λ. The yield stress follows a Hall-Petch type relation for large twin spacings and reaches a maximum at $\lambda = 15$ nm. For samples with twin spacings smaller than 15 nm, the yield stress decreases with decreasing twin spacing. Figure 3.1 (b) and (c) show the strain hardening coefficient and strain at failure as a function of twin spacing. Unlike the yield stress which undergoes a strength transition at a critical twin spacing, both the strain hardening coefficient and strain at failure increase monotonically with decreasing twin spacing. In addition, samples with small twin spacing ($\lambda < 15$ nm) exhibit extraordinary strain hardening and ductility.

The trend of increasing yield strength with decreasing characteristic length scales is common in polycrystalline metals. The ultrahigh strength exhibited by these nanotwinned samples can be understood using Hall-Petch relation, based upon the twin boundary serving as barriers to dislocation glides, resulting (in some cases) in dislocation pile-ups at the interfaces. This is similar to grain boundary strengthening in nanocrystalline metals, where ultrahigh strength is often observed when the grain size is in the range of a few tens of nanometers. However, nanocrystalline metals often possess very low ductility and failure at only a few percent strain

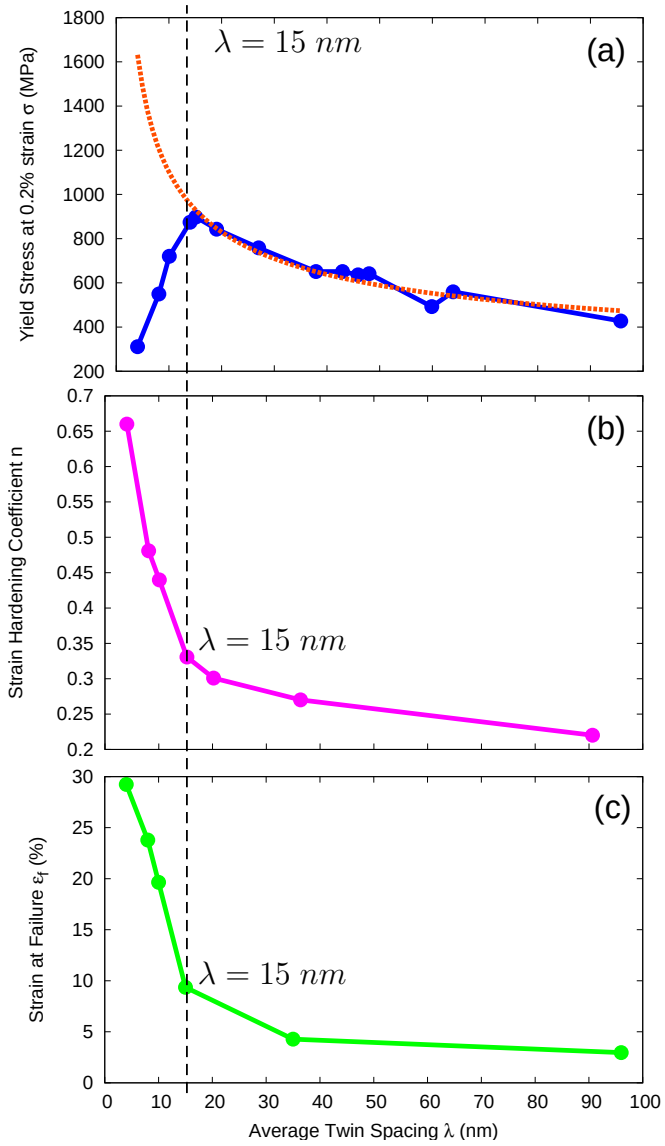

Figure 3.1: Experimental measurement of yielding stress, strain hardening coefficient, strain at failure for uniaxial tensile loading of ultrafine nanotwinned Cu samples at a strain rate of 6×10^{-3} s^{-1}. These figures are replotted by taking data from Lu et al. [43]. In all the figures, the dots represent the experimental data points and the solid lines simply connect these data points. (a) Yielding stress (at 0.2% strain) v.s. twin spacing λ. The dotted red curve is the best fit to the Hall-Petch function: $\sigma = \sigma_0 + k/\sqrt{\lambda}$ for $\lambda \geq 15$ nm. (b) Strain hardening coefficient n v.s. twin spacing λ. n is obtained by fitting the plastic deformation data to $\sigma = k_1 + k_2\epsilon^n$. (c) True strain at failure v.s. twin spacing λ.

are common [110]. Nanotwinned Cu is unusual in that it simultaneously exhibits ultrahigh strength and ductility. The exact reasons for this paradoxical and yet attractive property are not well understood and are currently under intensive research.

3.3.1.2 Key Observations from High Resolution TEM

The observations in the previous section suggest some unusual dislocation mechanisms associated with twin boundaries might operate during the plastic deformation of nanotwinned Cu samples. One way to verify this is to look at and compare the microstructure of as-grown and deformed samples. High-resolution transmission electron microscopy (TEM) is an effective technique for revealing microstructure at atomic levels. Observations of deformed samples can provide some understanding of the plastic deformation process in this unique microstructure. Below, we summarize previously reported TEM observations into three categories.

Dislocation Density The dislocation density increases tremendously with decreasing twin spacing. In samples with large twin spacings, the dislocation density is estimated to be on the order of 10^{14} to 10^{15} m^{-2} (for $\lambda = 96$ nm). For samples with small twin spacings, the density of dislocations is estimated to be 5×10^{16} m^{-2} [43].

Dislocation Network Pattern TEM observerations of the after-deformation samples show a difference in the dominant dislocation network pattern. While dislocation tangles and networks are formed in samples with large twin spacing, planar dislocations associated with twin boundaries are formed in samples with small twin spacing [43].

Twin Boundary Structure While the as-grown samples show a coherent twin boundary structure, the after-deformation samples show steps formed along twin boundaries. Twin boundaries lose coherency in the process of plastic deformations. In addition, a large number of debris are leftover in the vicinity of twin boundaries [10, 40].

The above facts suggest the plastic deformation process is related to dislocation-twin interactions and those interactions become dominant in samples with small twin spacing. However, the detailed atomistic mechanisms governing the dislocation-twin interaction, strain hardening, high ductility and strength transition still remain unclear based on these TEM observations. In view of this, there have been many computer simulation studies trying to reveal the nature of the process. We present a summary of existing work in the next section.

3.3.1.3 Nanotwinned Polycrystalline Metals and Thin Films

The nanotwinned microstructure and thin film structure share many common features. They both exhibit a layered structure with thicknesses in the range of a few micrometers and a few nanometers. The mechanical properties of materials adopting either structure are largely determined by the layer thickness. Nanotwinned materials and thin films exhibit high strength and their yield strength varies with their characteristic length scales (twin size and film thickness) according to the Hall-Petch relationship [41, 42] for twin size / film thickness larger than 50 nm. However, in thin films, the increase in strength with the decrease in film thickness is associated with the stress for driving the motion of individual threading dislocation within film layers and its deposition and interaction with misfit dislocations along film interfaces [111]. On the other hand, nanotwinned metals such as those nanotwinned Cu by Lu et al. [43] have a true polycrystalline structure and a distribution of twin sizes. The matrix and twin grains only differ by their lattice orientations. The twin interface is also a $\{111\}$ slip plane and contains a Shockley partial Burgers vector as its DSC lattice vector. Dislocations gliding along, crossing and interacting with twin interfaces are the main deformation mechanism. Hence the details of these atomistic dislocation-twin interactions are important and likely responsible for the unusual strength and ductility in nanotwinned metals.

3.3.2 Recent Simulation Works on Nanotwinned Metals

There have been many studies on how those growth nanotwins contribute to the materials' plastic deformation mechanisms and hence their observed properties. These studies can be broadly divided into two categories. The first studies the role of twin boundary migration (note that the coherent twin plane is also a slip plane in the FCC lattice) in the plastic deformation of nanotwinned metals while the second focuses on the dislocation-twin interactions. Froseth et al. [112, 113] studied the effect of growth twins on the deformation mechanisms in nanocrystalline Al, Ni, Cu. They found that twin migration is the preferred deformation mode in Al, but not in Ni or Cu. Their results were rationalized using the generalized planar fault (GPF) energy curve for the formation of intrinsic stacking fault, twin fault and twin migration. The energy barrier associated with the rigid shear for creating an intrinsic stacking fault (γ_{usf}) is nearly 3 times that of twin migration (γ_{utm}) for Al, which suggests twin migration is highly preferred over partial dislocation nucleation in this material. The ratio of $\gamma_{usf}/\gamma_{utm}$ is about 1 and 1.3 for Cu and Ni, respectively. Therefore in these two materials, slip with high Schmid factors

will be activated preferably. The above generalization using the shape of the GPF energy curve is consistent with experimental observations [12]. Dislocations are observed either piling-up along or across twin boundaries in Cu, while in nanocrystalline Al, twin migration is observed.

The coherent twin plane in the FCC lattice is one of the four slip planes on which dislocations tend to glide. Dislocations on the other three slip planes will interact with twin boundaries when they encounter them. Jin et al. [18, 20] performed MD simulations to study the interaction mechanisms of dislocation with twin boundaries for Cu, Ni and Al. They found that the detailed twin boundary mediated slip transfer mechanisms are material and loading condition dependent. Their results showed that pure screw dislocations cross-slip onto twin boundaries in Al, while those dislocations cross-slip into the twin crystal in Cu and Ni, - consistent with the observation of Froseth et al. [112, 113] discussed in the previous paragraph. In addition, dislocation locks are formed when non-screw dislocations interact with twin boundaries in their simulation. Using nudged elastic band (NEB) method, Zhu et al. [19] showed that twin boundaries are deep traps for screw dislocations and suggested that twin boundary mediated slip transfer is the rate-controlling mechanism for the observed increased strain rate sensitivity with increasing twin density. Chen et al. [114] performed MD simulations in combination with an atomistic path technique and showed that the screw dislocation twin boundary interaction is characterized by repulsive forces attributed to both the elasticity mismatch and distortion (shift and rotation) of deformation fields across the twin boundary. Afanasyev and Sansoz [44] studied a set of Au nanopillars with different twin spacings under uniaxial compression by MD simulations. They suggest the yield stress of Au nanopillars increases with reduction of twin spacing. Shabib and Miller [45] studied nanocrystalline Cu using MD simulations and found strength increases with decreasing twin spacing. Deng and Sansoz [115] studied the tensile loading of Au nanowire with twin boundaries and demonstrated twin boundaries contribute to ultrahigh plastic flow and work hardening.

The above simulation results are consistent in the sense that twin boundaries provide strong barriers to dislocation glides and hence their extraordinary strengthening effect in materials with this microstructure. Furthermore, all the above simulations demonstrated that the strength of nanotwinned metals increases as twin spacing decreases all the way to a few nanometers, inconsistent with experimental measurements which shows strength decreases with twin spacing for twin spacing below 15 nm.

Recently, an MD simulation study by Li et al. [116] demonstrated a softening mechanism arising from nucleation of dislocations at triple junctions of twin and grain boundaries and their

subsequent glides parallel to twin boundaries at small twin spacing ($\lambda \sim 0.63$ to 1.25 nm). They suggested that plastic deformation in this unique microstructure switched from strengthening based on Hall-Petch dislocation pile-ups to softening through twin migration. However, high resolution TEM observations [43] of those after-deformation nanotwinned Cu samples showed a high density of dislocations blocked at twin boundaries even for samples having a small twin spacing ($\lambda \sim 4$ nm), suggesting dislocation interacting and crossing twin boundaries are important in samples with small twin spacing. The presence of these dislocations is not consist with the MD simulation results and model [116]. In addition, experimental tensile loading data as shown in Fig. 3.1 shows the ductility of nanotwinned Cu increases rapidly when the twin spacing decreases below 15 nm. It is unlikely to achieve a high ductility through plastic deformation via twin migration only as five independent slip systems are required to meet the condition of a general strain. Other deformation mechanisms, such as activation of other slip systems other than those on twin planes and grain boundary activities, must operate during the extensive plastic deformation of the nanotwinned Cu, especially in those samples having small twin spacings.

3.3.3 Important Open Issues

Combining the experimental observations and MD simulation results in Section 3.3.1 and 3.3.2 suggests that a few important issues remain unsolved. First, the origin of the high density dislocations in Cu samples with small twin spacing is unclear. Two scenarios are likely. First, these dislocations are nucleated from twin steps during twin migration. Second, dislocations nucleated from grain boundaries cut through twin boundaries during the subsequent plastic deformation. Other important questions relating to the current observations are: what are the actual mechanisms corresponding to yield and what governs the strength transition in this unique microstructure? In current MD simulations, the yield stress is often dictated by dislocation nucleation events due to the small sample and grain size simulated. This may not be true for samples in experiments where other mechanisms, such as dislocations crossing interface boundaries, may define the yield stress. Finally, the mechanisms responsible for the unusual high ductility and strain hardening are also not well understood. We address these questions in Chapter 4 and 5 together with new sets of simulation results and discussions.

Chapter 4

Plastic Deformation of Nanotwinned FCC Metals

In this Chapter, we present MD simulations employing a Cu EAM interatomic potential to examine a microstructure containing an ultrafine array of growth twins under uniaxial, fixed true strain-rate conditions. We examine the deformation mechanisms by monitoring the evolution of the dislocation-twin microstructure during the initiation and propagation of plastic deformation with atomic resolution. New mechanisms of twin mediated slip transfer across twin boundaries are described. One of these is the generation of a $\{001\}\langle 110\rangle$ Lomer dislocation from the interaction of a 60° full dislocation and a twin boundary. The subsequent dissociation of the Lomer dislocation into Shockley, stair-rod and Frank partial dislocations are studied in detail. In addition, we also observe a new mechanism in which a 30° partial dislocation interacts with the twin boundary to generate three new Shockley partial dislocations during the twin-mediated slip transfer. We discuss the contribution of these mechanisms towards the observed mechanical properties followed by a summary of all the known dislocation twin interaction mechanisms at the end of this Chapter.

4.1 Simulation Setup

For the simulation described in this Chapter, we constructed the simulation cell, shown in Fig. 4.1, as following. First, a pair of parallel, vertical grain boundaries are introduced into the original perfect FCC crystal via a 9° rotation about the z axis (i.e., z $\parallel$ $[\bar{1}10]$). The original and tilted matrix grains are labeled M and M_t, respectively. The second step is to introduce a

parallel set of twins in both the original and tilted matrix grains by performing 180° rotations of the "twinned" crystal about the $[11\bar{2}]$ direction (this is the x-axis in the original matrix grains). This process is repeated to produce the desired number of twins in the untilted and tilted grains, T and T_t. Grains labelled M and T have crystallographic orientations x$[11\bar{2}]$, y$[111]$, z$[1\bar{1}0]$ and x$[11\bar{2}]$, y$[\bar{1}\bar{1}\bar{1}]$, z$[\bar{1}10]$, respectively, and thus have a twin relationship with respect to each other. The grains in the central region of the simulation cell are labelled M_t and T_t and are rotated by 9° about the $[\bar{1}10]$ axis, relative to the M and T grains, respectively, and thus M_t and T_t are twin related with respect to each other as well. The "$\diamond$" symbols denote the positions of the twin boundaries in the figure. There are several types of grain boundaries in the unit cell, corresponding to the junctions of the following grain pairs $M - M_t$, $T - T_t$, $M - T_t$ and $T - M_t$. However, we note that the $M - M_t$ and the $T - T_t$ boundaries are equivalent, as are the $M - T_t$ and $T - M_t$ boundaries. In the images of the simulation cell illustrated throughout this Chapter, only the atoms for which the central symmetry parameter c_p [91] (as described in Section 2.4.5) differs from that of the perfect FCC crystal ($c_p = 0$) are shown. Atoms in non-FCC environments, such as in twin boundaries, grain boundaries, stacking faults, and dislocation cores, are shown with a color that depends on the value of the parameter c_p (e.g., blue corresponds to $c_p \sim 0.04$, cyan to $c_p \sim 0.171$, yellow to $c_p \sim 0.285$, and red to $c_p \sim 0.36$. The simulation cell dimensions are $\sim 475 \times 950 \times 153$ $\mathring{A}$ in the x, y and z directions, respectively, such that the total number of atoms in the system is 5,834,519. The average spacing between twin boundaries is ~ 160 $\mathring{A}$ in the simulation cell.

Molecular dynamics simulations presented in this and subsequent Chapters were performed using LAMMPS [90]. The simulation cell in Fig. 4.1 was first equilibrated for 50 ps, then heated to 600 K at 1000 K/ns using molecular dynamics in an ensemble where the number of particles N, the stress tensor $\boldsymbol{\sigma}$, and the temperature were fixed (i.e., the $N\boldsymbol{\sigma}T$ ensemble). Periodic boundary conditions were imposed in all directions in the simulation. Tensile loading simulations were performed in an ensemble in which N and T were fixed, a constant true strain rate of 10^8/s was imposed in the x-direction, and all stresses were fixed (at zero), except for σ_{xx}.

4.2 Dislocation Nucleation and Evolution

The initial simulation cell contains a regular array of coherent twin boundaries, a pair of "low angle tilt" grain boundaries and no dislocations, as shown in Fig. 4.1. This microstructure is

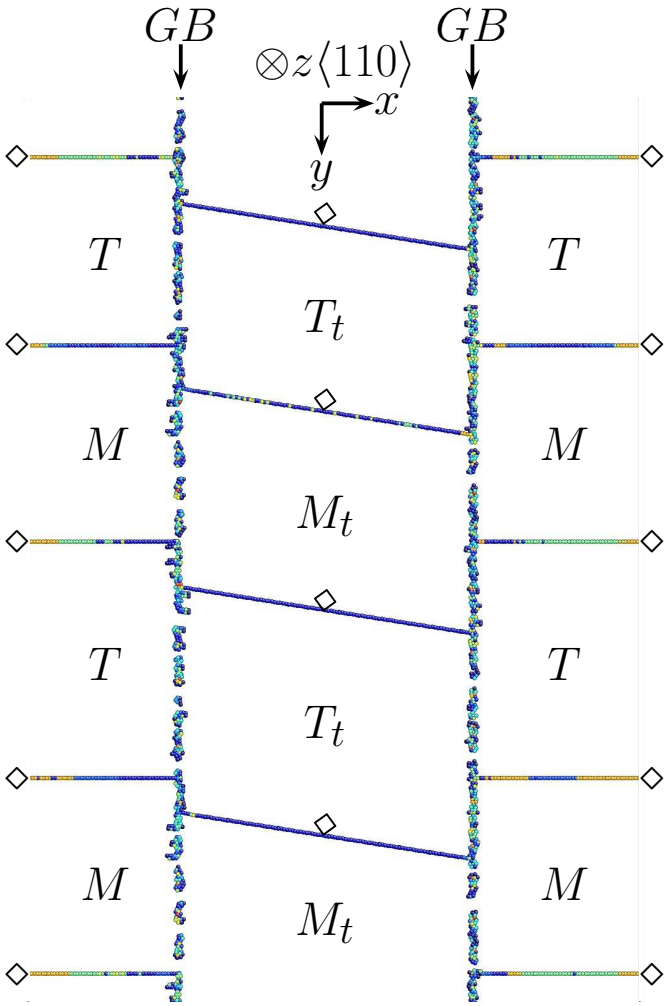

Figure 4.1: A section of the simulation unit cell containing two vertical grain boundaries (GB) and an array of parallel twin boundaries. The matrix M and twin T domains are oriented with respect to the external coordinate frame as x$[11\bar{2}]$, y$[111]$, z$[1\bar{1}0]$ and x$[11\bar{2}]$, y$[\bar{1}\bar{1}\bar{1}]$, z$[\bar{1}10]$, respectively. The grain in the center of the unit cell is rotated or tilted with respect to the grains on the left and right by a 9° rotation with respect to the z-axis. The matrix and twin domains in the central grain are labeled, M_t and T_t, respectively. The "$\diamond$" indicate the positions of the twin boundaries. Atoms are only shown if the central symmetry parameter differs from that of the perfect FCC crystal. Atom coloring is also determined based on the central symmetry parameter, as described in the text. The x, y, and z dimensions of the simulation cell are $\sim 475\mathring{A}$, $\sim 950\mathring{A}$, and $\sim 153\ \mathring{A}$, respectively, and the simulation cell contains 5,834,519 atoms. Periodic boundary conditions are imposed in the x, y, and z-directions. Atomic configurations presented in this and subsequent Chapters are pre-processed in MD simulations and visualized in Atomeye [117].

similar to the as-sputtered microstructures reported in [118]; in particular, both the simulations and experiments contain low angle ($\sim 9^\circ$) boundaries and a set of parallel coherent twin boundaries ($\sim$ 15 nm apart). In the present study, we examine dislocation nucleation mechanisms and the subsequent evolution of the dislocation structure and compare these results to the experimental observations. While earlier atomistic simulation studies examined similar deformation behavior [19, 20], those studies were idealized in the sense that they examined straight dislocations parallel to the twin boundary under loading conditions that generated pure glide Peach-Koehler forces. In the present study, we examine the more realistic situation where the applied load is such that slip can be activated simultaneously on several different slip systems and, in addition, there are stresses that do not contribute to glide on any of the slip systems. In the present simulations, the initial dislocation structure is formed as a result of dislocation nucleation and migration (i.e., not straight dislocations parallel to the twin boundary). This allows us to examine the generality of the previous results and their applicability to the actual experiments. Our goal is to understand the mechanisms that produce the experimental reports of simultaneous ultrahigh strengthening and ductility in nanotwinned metallic systems.

Figure 4.2 shows the evolution of the system during plastic deformation. Figure 4.2 (a) shows the onset of plastic deformation when dislocations are first nucleated from the grain boundaries. We note that the grain boundaries formed where crystals M and T_t or M_t and T meet are general gain boundaries (i.e., not low angle tilt nor low Σ boundaries) and boundaries joining crystals M and M_t or T and T_t are 9° low angle tilt boundaries. The low angle tilt boundaries consist of regularly spaced lattice dislocations lying on $\{111\}$ planes, as predicted for low angle grain boundaries. The dislocations that make up the low angle boundaries split into pairs of partial dislocations separated by intrinsic stacking faults. The two types of grain boundaries serve as dislocation nucleation sites for two different types of dislocations which dominate the initial stage of plastic deformation. Type I is an extended 60° full dislocation in crystal M with Burgers vector $\boldsymbol{DB}$ slipping on the $\boldsymbol{c}$ plane, or equivalently, an extended 60° full dislocation in crystal T with Burgers vector $\boldsymbol{D}^T\boldsymbol{A}^T$ slipping on the $\boldsymbol{c}^T$ plane (our notation for Burgers vectors and slip planes are as described in Fig. 2.11 in Section 2.2.4.1 of Chapter 2). This dislocation splits into a 30° leading partial $\boldsymbol{\gamma B}$, an intrinsic stacking fault and a 90° trailing partial $\boldsymbol{D\gamma}$ ($\boldsymbol{\gamma}^T\boldsymbol{A}^T$ and $\boldsymbol{D}^T\boldsymbol{\gamma}^T$ for dislocation in crystal T). This type of dislocation is nucleated near the triple junction where a general grain boundary (formed by crystal of type M and T_t), a low angle tilt grain boundary (formed by crystal of type M and M_t) and a twin boundary meet. The detailed nucleation process is shown in Fig. 4.3 (a). Type

II is a Shockley partial dislocation loop with a circular intrinsic stacking fault and on slip planes of type $\boldsymbol{a}$ (recall that $\boldsymbol{a}$, $\boldsymbol{b}$, $\boldsymbol{a}^T$ and $\boldsymbol{b}^T$ are equivalent with respect to the current loading direction). Type II dislocations are nucleated at steps on the stacking fault planes associated with the dislocations that make up the low angle tilt grain boundaries (Fig. 4.3 (b)). The upper case letters in Fig. 4.2 (a) denote newly nucleated dislocations (circled). Labels A-D denote the nucleation of Type I dislocations. Dislocation A is an extended 60° dislocation ($\boldsymbol{DB}$ on $\boldsymbol{c}$ plane, Type I dislocation). Dislocation B is a 30° leading partial dislocation $\boldsymbol{\gamma B}$ slipping on the $\boldsymbol{c}$ plane and trailing an intrinsic stacking fault. The trailing partial has not yet nucleated in Fig. 4.2 (a). Dislocations C and D are 30° leading partials $\boldsymbol{\gamma B}$ and $\boldsymbol{\gamma}^T\boldsymbol{B}^T$ on slip plane $\boldsymbol{c}$ and $\boldsymbol{c}^T$, respectively. Dislocations E-H indicate recently nucleated Type II partial dislocations on $\boldsymbol{a}$-type slip planes.

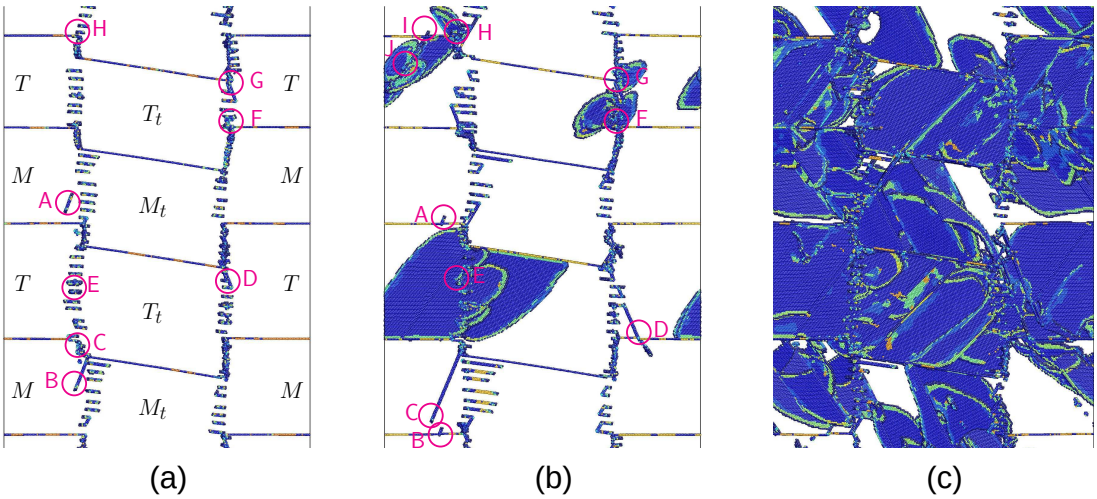

Figure 4.2: Evolution of the nanotwinned Cu system during tensile loading. Figure (a) shows the onset of plastic deformation shortly after dislocations are first nucleated from the grain boundary. Figure (b) shows dislocations interacting with twin boundaries. Figure (c) shows the dislocation/twin/grain boundary microstructure after significant plastic deformation. The upper case Roman letters highlight recently nucleated dislocations in (a) and the same notation is used in the subsequent panels.

Figure 4.2 (b) shows the system at the point in time where dislocations start to impinge upon the twin boundaries. Dislocations A and B are extended 60° dislocations (Type I) blocked by the twin boundaries. Dislocation C is a 30° leading partial $\boldsymbol{\gamma B}$ slipping on plane $\boldsymbol{c}$ and leaving a $\sim$ 12 nm wide stacking fault behind. This stacking fault is $\sim$ 3 times wider than dislocation A

in Fig. 4.2 (a) because the 90° trailing partial dislocation $\boldsymbol{D\gamma}$ has not yet nucleated (nucleation is a stochastic process). Dislocation D ($\boldsymbol{D}^T\boldsymbol{B}^T$, Type I) in Fig. 4.2 (b) glides on the $\boldsymbol{c}^T$ plane, passes through a twin boundary, and transforms into a Lomer or Lomer-Cottrell dislocation $\boldsymbol{CD}$ on a $\{001\}$ plane of crystal M. Shockley partial dislocation (E-H) loops are nucleated and grow along their respective slip planes until blocked by twin boundaries (see Fig. 4.2 (b)). The expansion of these leading partial loops creates a high density of stacking faults on $\boldsymbol{a}$-type slip planes. Dislocation I in this figure is an extended 60° dislocation (Type I) that is partially transmitted through a twin boundary. A Lomer dislocation ($\boldsymbol{C}^T\boldsymbol{D}^T$ on $\{001\}^T$ plane in crystal T) is generated from this dislocation-twin interaction. The Lomer dislocation on the $\{001\}^T$ plane further dissociates into two Shockley partial dislocations and one stair-rod dislocation which forms a Lomer-Cottrell barrier (dislocation J in Fig. 4.2 (b)). This mechanism is discussed in detail in the following Section 4.3. We note that dislocations A, B and I are all Type I dislocations with the same Schmid factor. However, only dislocation I passes through the twin boundary, while dislocations A and B are blocked by the twin boundary (even though they were nucleated earlier than dislocation I). This suggests that slip transfer across the twin boundary requires thermal activation (there is an energy barrier associated with nucleating a new dislocation on the other side of the twin boundary).

A high density of Shockley partial dislocations and stacking fault planes are generated upon further tensile loading of the system, as shown in Fig. 4.2 (c). These Shockley partial dislocations are either nucleated from the grain boundaries or resulted from the dislocation-twin interaction during twin-mediated slip transfer. In addition to the dislocation-twin interaction mechanisms discussed by Jin et al. [18, 20], we observed two additional dislocation-twin interaction mechanisms. These provide a mechanism for strain hardening and are one of the main foci of this Chapter. The first of the two new mechanisms is the generation and dissociation of a $\{001\}\langle 110\rangle$ Lomer dislocation from the interaction of a 60° full dislocation and a twin boundary. The second is the generation of three Shockley partial dislocations from the interaction of a 30° Shockley partial with a twin boundary. We present detailed analysis of these two mechanisms below.

4.3 Dislocation-Twin Interaction Mechanisms

Dislocations can be blocked where they first make contact with twin boundaries. As more of the dislocation encounters the twin boundary, a long, straight dislocation segment forms at the

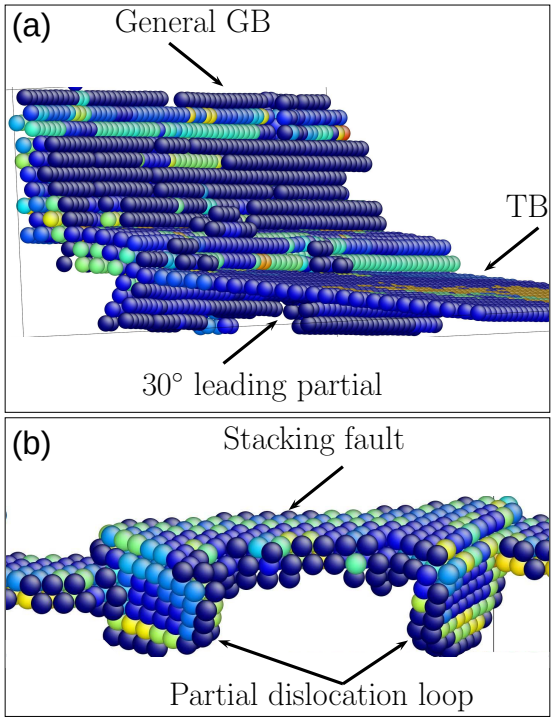

Figure 4.3: Dislocation nucleation from grain boundaries. Figure (a) shows partial dislocation nucleation from the triple junction of a general, a low angle and a twin boundary. Figure (b) shows partial dislocation loop nucleation from steps on an intrinsic stacking fault.

intersection of the slip plane and the twin boundary. Because the dislocations intersecting the twin boundary are straight in the FCC system, we need only focus on three types of lattice dislocation: (i) a screw dislocation ($\boldsymbol{AB}$ on $\boldsymbol{c}$ plane for example), (ii) a 60° dislocation with a 30° leading partial and a 90° trailing partial ($\boldsymbol{\gamma B}$ and $\boldsymbol{D\gamma}$ on plane $\boldsymbol{c}$) and (iii) a 60° dislocation with a 90° leading partial and a 30° trailing partial ($\boldsymbol{D\gamma}$ and $\boldsymbol{\gamma B}$ on plane $\boldsymbol{c}$). Only the screw dislocations, which consist of a pair of Shockley partials in the matrix grain, can be transmitted across the twin boundary while leaving the twin boundary intact. On the other hand, the screw dislocation can be absorbed into the twin boundary thereby creating steps on the twin boundary. The interaction of non-screw dislocations with the twin boundary is more complicated; the detailed mechanisms of which depend on material properties and loading conditions [20]. This makes it impossible to determine the dislocation-twin interaction mechanisms during the twin-mediated slip transfer based solely on conservation of Burgers vector considerations. Below we describe, in detail, the two new mechanisms for dislocation-twin interaction observed under general stress conditions (i.e., applied stress that involving both do and do not contribute to the Schmid factor) and their contributions toward strain hardening of the nanotwinned structure.

4.3.1 Generation and Dissociation of Lomer Dislocations

The simulation results presented above show the generation of $\{001\}\langle 110\rangle$ Lomer dislocations as a result of dislocation-twin interactions. In describing the mechanism by which this occurs, we focus attention on the structure shown in Fig. 4.4 and the corresponding schematic illustration in Fig. 4.5. A leading 30° partial dislocation ($\boldsymbol{\gamma B}$ on $\boldsymbol{c}$) is nucleated from a grain boundary (refer to Fig. 4.3 (a)). The glide of the leading partial leaves a widening intrinsic stacking fault behind. As the leading partial propagates further, a trailing 90° partial dislocation ($\boldsymbol{D\gamma}$ on the same $\boldsymbol{c}$ plane) is nucleated from the grain boundary. The glide of the trailing partial annihilates the stacking fault left behind by the leading partial dislocation, as shown in Fig. 4.4 (a1-c1) and illustrated in Fig. 4.5 (a). This can be summarized as follows:

$$\begin{array}{ccccc} \boldsymbol{DB} & \rightarrow & \boldsymbol{\gamma B} & + & \boldsymbol{D\gamma} \\ 1/2[011] & \rightarrow & 1/6[\bar{1}21] & + & 1/6[112] \\ \text{lattice dislocation} & \rightarrow & 30^\circ \text{ leading partial} & + & 90^\circ \text{ trailing partial} \end{array} \tag{4.1}$$

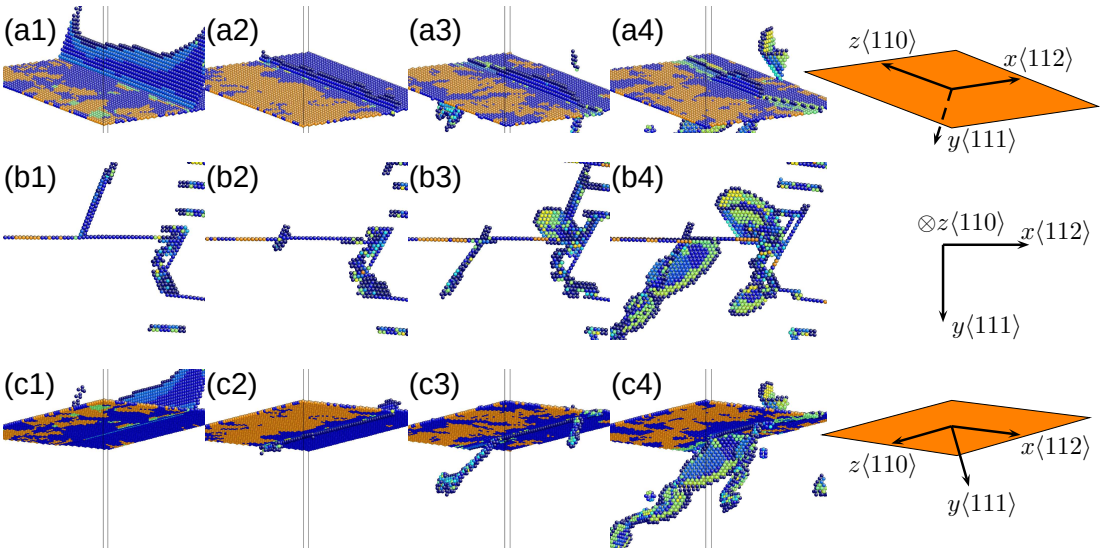

Figure 4.4: Three views (a-c) of a 60° extended dislocation passing a twin boundary and the generation and dissociation of a $\{001\}^T\langle 110\rangle^T$ Lomer dislocation. Time evolves from left to right (1-4). The last column shows the coordinate axis triads of the three views. The nearly horizontal planes of atoms represent a twin plane and the canted planes of atoms represent stacking faults.

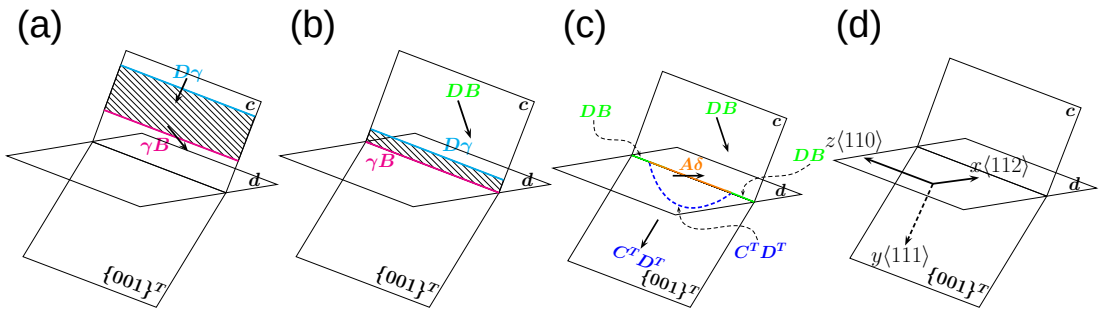

Figure 4.5: Schematic illustration of a 60° dislocation passing through a twin interface and the generation of a $\{001\}^T\langle 110\rangle^T$ Lomer dislocation. Figure (a) shows a 30° leading partial $\boldsymbol{\gamma B}$ and a 90° trailing partial $\boldsymbol{D\gamma}$ slipping on the $\boldsymbol{c}$ plane. The hatched area highlights the intrinsic stack fault enclosed by the two Shockley partial dislocations. Figure (b) shows the $\boldsymbol{\gamma B}$ partial dislocation blocked by the twin boundary and the $\boldsymbol{D\gamma}$ trailing partial "catching up" with the leading partial and narrowing the stacking fault. Figure (c) shows the $\boldsymbol{\gamma B}$ and $\boldsymbol{D\gamma}$ partials recombining into a $\boldsymbol{DB}$ dislocation and a Lomer dislocation $\boldsymbol{C^TD^T}$ on $\{001\}^T$ being nucleated in the twinned crystal. A Shockley partial dislocation $\boldsymbol{A\delta}$ is left on the twin boundary where the Lomer dislocation was nucleated. Figure (d) shows the coordinate axis triad for the schematic view.

The leading partial ($\boldsymbol{\gamma B}$) is blocked by the twin boundary ($\boldsymbol{d}$) while the trailing partial dislocation ($\boldsymbol{D\gamma}$) continues to slip towards it, narrowing the intervening stacking fault (see Fig. 4.4 (a2-c2) and Fig. 4.5 (b)). This process continues until a segment of the trailing partial ($\boldsymbol{D\gamma}$) merges with a segment of the leading partial ($\boldsymbol{\gamma B}$) to form a full lattice dislocation $\boldsymbol{DB}$ at the twin interface (removing the intervening stacking fault). A Lomer dislocation ($\boldsymbol{C^T D^T}$) segment is then nucleated on the $\{001\}^T$ plane at the full dislocation $\boldsymbol{DB}$. As the Lomer dislocation glides into the twinned crystal, it leaves behind a partial dislocation $\boldsymbol{A\delta}$ on the twin interface $\boldsymbol{d}$ as shown in Fig. 4.4 (a3-c3) and Fig. 4.5 (c). This reaction can be expressed as

$$\begin{array}{ccccccccccc}
\boldsymbol{\gamma B} & + & \boldsymbol{D\gamma} & \rightarrow & \boldsymbol{DB} & \rightarrow & \boldsymbol{C^T D^T} & + & \boldsymbol{A\delta} \\
1/6[\bar{1}21] & + & 1/6[112] & \rightarrow & 1/2[011] & \rightarrow & 1/2[\bar{1}\bar{1}0]^T & + & 1/6[\bar{1}2\bar{1}] \\
30^\circ \text{ leading partial on } \boldsymbol{c} & + & 90^\circ \text{ trailing partial on } \boldsymbol{c} & \rightarrow & \text{lattice dislocation} & \rightarrow & \text{Lomer on } \{001\}^T & + & \text{partial on TB}
\end{array} \tag{4.2}$$

While the mechanism of Lomer dislocation generation from the twin boundary has been previously reported for the uniaxial deformation of a Cu nanowire [119] and a Au nanopillar [44], the importance of the Lomer dislocation, its subsequent dissociation, and the generality of this mechanism has not been thoroughly analyzed. We provide such an analysis here. Both the Lomer $\boldsymbol{C^T D^T}$ and partial $\boldsymbol{A\delta}$ dislocations are glissile. The $\boldsymbol{A\delta}$ dislocation on the twin plane may also be described as a step, the motion of which shifts the twin plane by one atomic plane normal to itself. The Lomer dislocation ($\boldsymbol{C^T D^T}$ on $\{001\}^T$) in the twinned crystal is mobile: its Burgers vector lies in the slip plane. However, the Peierls stress for the motion of the Lomer dislocation is expected to be higher than that of lattice dislocations on $\{111\}$ planes. The Lomer dislocation expands as a semi-circular loop on the $\{001\}^T$ plane with its two ends in the twin boundary, as illustrated in Fig. 4.5 (c). As the Lomer dislocation loop expands, a section of the loop becomes parallel to its Burgers vector and, hence, is a screw. The screw segment dissociates into a pair of Shockley partial dislocations that subsequently move on the two $\{111\}^T$ slip planes ($\boldsymbol{a}^T$ and $\boldsymbol{b}^T$) that intersect the initial Lomer screw segment, as shown in Fig. 4.6 (a). These two Shockley partial dislocations ($\boldsymbol{\alpha^T D^T}$ on $\boldsymbol{a}^T$ and $\boldsymbol{C^T \beta^T}$ on $\boldsymbol{b}^T$) expand quickly into circular partial dislocation loops the inside of which are intrinsic stacking faults. A stair-rod dislocation ($\boldsymbol{\beta^T \alpha^T}$) is left at the position of the original Lomer screw segment and

thus forms a Lomer-Cottrell lock. The above dissociation, was first noted by Cottrell [56] and can be expressed as

$$\begin{array}{lcllcllcl} \boldsymbol{C}^T\boldsymbol{D}^T & \rightarrow & \boldsymbol{C}^T\boldsymbol{\beta}^T & + & \boldsymbol{\beta}^T\boldsymbol{\alpha}^T & + & \boldsymbol{\alpha}^T\boldsymbol{D}^T \\ 1/2[\bar{1}\bar{1}0]^T & \rightarrow & 1/6[\bar{1}\bar{2}1]^T & + & 1/6[\bar{1}10] & + & 1/6[\bar{1}\bar{2}\bar{1}] \\ \text{Lomer on } \{001\}^T & \rightarrow & \text{Shockley partial on } \boldsymbol{b}^T & + & \text{stair-rod dislocation} & + & \text{Shockley partial on } \boldsymbol{a}^T \end{array} \tag{4.3}$$

We performed an MD simulation in which we constructed a $\{001\}\langle 110\rangle$ Lomer screw dislocation and found that under zero stress, it evolved into the extended configuration described by Eqn. 4.3. Application of Frank's dislocation reaction criterion [56] also shows that dissociation, as per Eqn. 4.3, is energetically favorable. Because the Lomer screw dislocation spontaneously dissociates, the Peierls barrier could not be readily deduced through MD simulations.

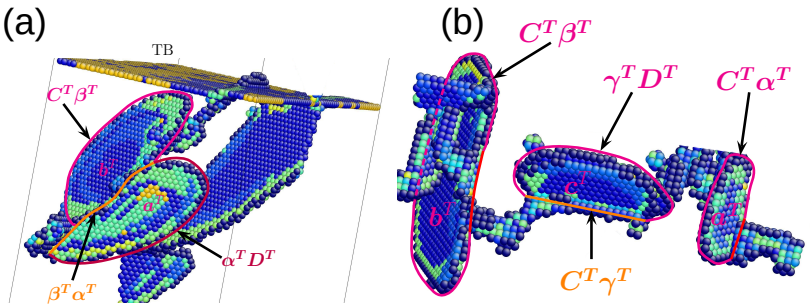

Figure 4.6: Dissociation of $\{001\}^T\langle 110\rangle^T$ Lomer dislocation. Figure (a) shows a Lomer dislocation $\boldsymbol{C}^T\boldsymbol{D}^T$ dissociates into two Shockley partial dislocations $\boldsymbol{C}^T\boldsymbol{\beta}^T$ and $\boldsymbol{\alpha}^T\boldsymbol{D}^T$ on $\boldsymbol{b}^T$ and $\boldsymbol{a}^T$ plane respectively. A stair-rod dislocation $\boldsymbol{\beta}^T\boldsymbol{\alpha}^T$ is resulted from the dissociation. Figure (b) shows dissociation of the $\{001\}^T\langle 110\rangle^T$ Lomer dislocation into a Shockley partial dislocation $\boldsymbol{\gamma}^T\boldsymbol{D}^T$ and a Frank dislocation $\boldsymbol{C}^T\boldsymbol{\gamma}^T$. The Lomer dislocation also serves as nucleation sites for Shockley partial dislocation $\boldsymbol{C}^T\boldsymbol{\beta}^T$ and $\boldsymbol{C}^T\boldsymbol{\alpha}^T$ on $\boldsymbol{b}^T$ and $\boldsymbol{a}^T$ plane, respectively.

There is a geometric requirement for the Lomer dislocation dissociation to occur. The Lomer dislocation segment can only dissociate once it becomes aligned with the intersection of the two $\{111\}^T$ slip planes (i.e., this corresponds to a pure screw orientation). Only a small segment of the expanding Lomer loop satisfies this geometric requirement; the rest of the loop is either of edge or mixed character. The Lomer edge segment undergoes another type of

dissociation, as shown in Fig. 4.6 (b). The Lomer edge dislocation ($\boldsymbol{C}^T\boldsymbol{D}^T$) dissociates into a Frank dislocation with a Burgers vector $\boldsymbol{C}^T\boldsymbol{\gamma}^T$ perpendicular to the $\boldsymbol{c}^T$ plane and a Shockley dislocation with Burgers vector $\boldsymbol{\gamma}^T\boldsymbol{D}^T$ on the $\boldsymbol{c}^T$ plane. The Frank dislocation ($\boldsymbol{C}^T\boldsymbol{\gamma}^T$) is sessile since its Burgers vector is perpendicular to the $\{111\}^T$ slip plane and the Shockley dislocation forms as a pure screw that ($\boldsymbol{\gamma}^T\boldsymbol{D}^T$) expands into a circular partial dislocation loop enclosing an intrinsic stack fault. We express the dissociation as

$$\begin{array}{lcllcl} \boldsymbol{C}^T\boldsymbol{D}^T & \rightarrow & \boldsymbol{C}^T\boldsymbol{\gamma}^T & + & \boldsymbol{\gamma}^T\boldsymbol{D}^T \\ 1/2[\bar{1}\bar{1}0]^T & \rightarrow & 1/3[\bar{1}\bar{1}1]^T & + & 1/6[\bar{1}\bar{1}\bar{2}]^T \\ \text{Lomer on } \{001\}^T & \rightarrow & \text{Frank partial on } \boldsymbol{c}^T & + & \text{Shockley partial on } \boldsymbol{c}^T \end{array} \tag{4.4}$$

Just like the Lomer dislocation can dissociate when in a screw orientation, so the Lomer dislocation can dissociate when in an edge orientation; the mixed Lomer dislocation cannot dissociate. Applying Frank's dislocation reaction criterion [56] shows the dissociation of the Lomer edge segment in Eq. 4.4 is energetically favorable. Figure 4.6 (b) also shows the Shockley partial dislocation ($\boldsymbol{C}^T\boldsymbol{\beta}^T$ on $\boldsymbol{b}^T$ and $\boldsymbol{C}^T\boldsymbol{\alpha}^T$ on $\boldsymbol{a}^T$) nucleation from screw Lomer dislocation line segments. This suggests the slip of a Lomer dislocation on the $\{001\}^T$ plane is unstable relative to dissociation and the subsequent slip of the Shockley partials on $\{111\}^T$ planes.

The remaining undissociated Lomer dislocation segments which do not satisfy geometric requirement for dissociation (pure screw or pure edge) continue to slip on the $\{001\}^T$ plane in the twinned crystal until they meet the next twin boundary. Twin mediated slip transfer occurs again and the Lomer dislocation line segment transforms into two Shockley partial dislocations which glide into the matrix and a Shockley partial dislocation is left on the twin boundary. The above slip transfer can be expressed as following:

$$\begin{array}{lcllcllcl} \boldsymbol{C}^T\boldsymbol{D}^T & \rightarrow & \boldsymbol{\gamma B} & + & \boldsymbol{D\gamma} & + & \boldsymbol{\delta A} \\ 1/2[\bar{1}\bar{1}0]^T & \rightarrow & 1/6[\bar{1}21] & + & 1/6[112] & + & 1/6[1\bar{2}1] \\ \text{Lomer on } \{001\}^T & \rightarrow & 30^\circ \text{ partial on } \boldsymbol{c} & + & 90^\circ \text{ partial on } \boldsymbol{c} & + & \text{partial on TB} \end{array} \tag{4.5}$$

However, the two Shockley partial dislocations, $\boldsymbol{\gamma B}$ and $\boldsymbol{D\gamma}$, slip on next nearest neighbouring

$\boldsymbol{c}$ planes, thus forming an extrinsic stacking fault. The slip process on the respective $\boldsymbol{c}$ planes is

$$\begin{array}{ll} & BCABC\hat{A}BCABC \\ \text{slip of } \boldsymbol{D\gamma} & \downarrow\downarrow\downarrow\downarrow\downarrow \\ & ABCAB\hat{A}BCABC \\ \text{slip of } \boldsymbol{\gamma B} & \qquad\qquad\qquad\downarrow\downarrow\downarrow\downarrow\downarrow \\ & ABCAB\hat{A}CABCA \end{array}$$

where we have used the classical $\{111\}$ plane stacking notation and $\hat{A}$ indicates the $\{111\}$ atomic plane above and below which the two partials slip. The slip of a $\boldsymbol{D\gamma}$ partial displaces atoms on and above the C layer by $1/6[112]$. This results a change in the stacking sequence from the original $BCABC\hat{A}BCAB$ to $ABCAB\hat{A}BCABC$. The slip of partial $\boldsymbol{\gamma B}$ displaces atoms on and below the B layer by $1/6[\bar{1}21]$, thereby changing the stacking sequence from the previous $ABCAB\hat{A}BCABC$ to $ABCAB\hat{A}CABCA$ and forming an extrinsic stacking fault.

We summarize the above process of generation and dissociation of Lomer dislocations at the twin boundary in the dislocation path diagram illustrated in Fig. 4.7.

4.3.2 30° Shockley Partial Dislocation - Twin Boundary Interaction

The simulations show that a large number of Shockley partial dislocation loops (Type II) are generated at the grain boundaries during plastic deformation. Some of these partial dislocations meet twin boundaries before the trailing partials are formed at the grain boundary. The interaction of these partial dislocations with twin boundaries generates an additional set of dislocations which augment the ductility of the material. We describe the process here. Figure 4.8 shows leading partial dislocations, without trailing partials, passing through a twin boundary. Figure 4.9 (a-d) is a schematic illustration of the interaction mechanism. In Fig. 4.9 (a), a leading partial dislocation ($\boldsymbol{C\beta}$ on $\boldsymbol{b}$) is nucleated from a grain boundary (as seen in Fig. 4.3 (b)) and forms a circular dislocation loop enclosing an intrinsic stacking fault. The expanding $\boldsymbol{C\beta}$ dislocation loop is blocked where it meets the twin boundary ($\boldsymbol{d}$), as shown in Fig. 4.9 (b). As the loop continues to expand it forms a larger and larger straight dislocation segment at the intersection of the slip plane and the twin boundary. This dislocation segment at the twin boundary is a 30° partial. A semi-circular partial dislocation ($\boldsymbol{C}^T\boldsymbol{\alpha}^T$ on $\boldsymbol{a}^T$) is then nucleated from this straight 30° partial in the twin boundary. This new loop propagates into the twinned

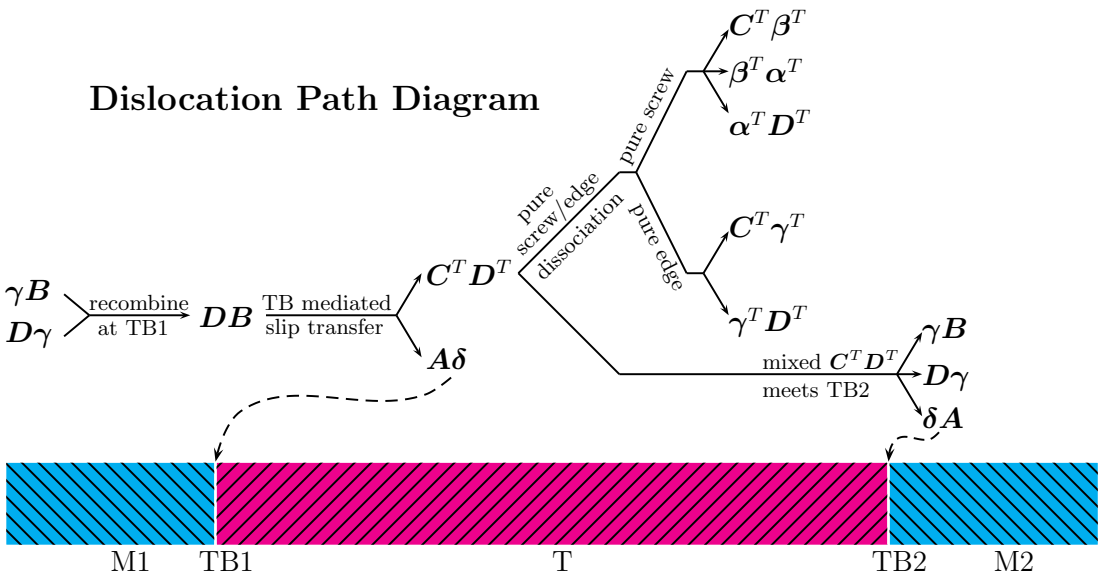

Figure 4.7: Schematic illustration of the dislocation path for a 60° full dislocation interacting with twin boundaries. A pair of Shockley partials, $\boldsymbol{\gamma B}$ and $\boldsymbol{D\gamma}$ from Crystal M1, transforms as indicated from left to right in the diagram. The two partials in M1 recombine at the first twin boundary (TB1) to form the lattice dislocation $\boldsymbol{DB}$ which dissociates into a Lomer dislocation $\boldsymbol{C^T D^T}$ in the twinned crystal T and leaves a Shockley partial dislocation $\boldsymbol{A\delta}$ on TB1. The Lomer dislocation $\boldsymbol{C^T D^T}$ expands as a loop and the screw segments dissociate into Shockley partials $\boldsymbol{C^T\beta^T}$, $\boldsymbol{\alpha^T D^T}$ and a stair-rod $\boldsymbol{\beta^T\alpha^T}$ dislocation. The edge segments of the Lomer dislocation dissociate into a Frank partial $\boldsymbol{C^T\gamma^T}$ and a Shockley partial $\boldsymbol{\gamma^T D^T}$. The mixed Lomer segments interacts with the next twin boundary (TB2) and react to form two Shockley partial dislocations, $\boldsymbol{\gamma B}$ and $\boldsymbol{D\gamma}$, on next nearest neighbouring slip planes in crystal M2 (same crystallographic orientation as M1) and a Shockley partial dislocation, $\boldsymbol{\delta A}$ that remains in TB2.

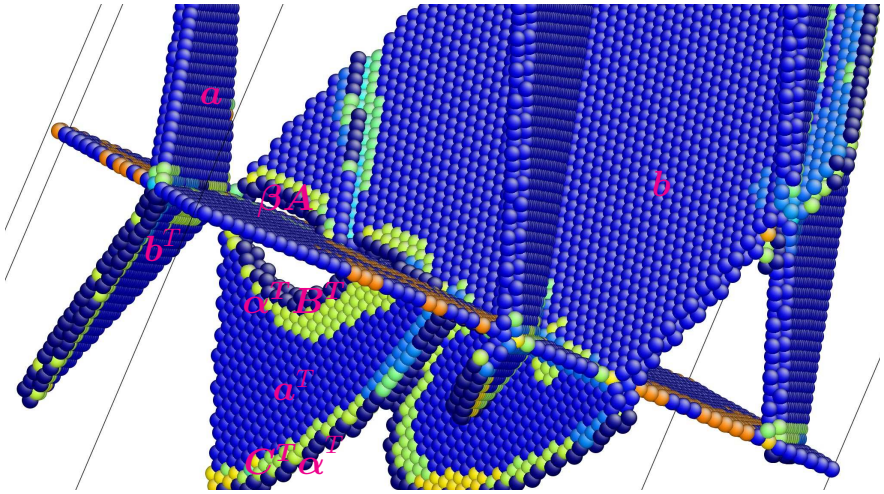

Figure 4.8: 30° partial dislocations impinging on the twin boundary from above and emerging into the twin crystal (below) as they pass through the twin boundary.

crystal, leaving behind a semi-circular intrinsic stacking fault on the $\boldsymbol{a}^T$ plane, as illustrated in Fig. 4.9 (c). The above slip transfer across the twin boundary can be expressed as

$$\begin{array}{ccccc} \boldsymbol{C\beta} & \rightarrow & \boldsymbol{C}^T\boldsymbol{\alpha}^T & + & \boldsymbol{\alpha}^T\boldsymbol{\beta} \\ 1/6[\bar{1}\bar{2}1] & \rightarrow & 1/6[\bar{2}\bar{1}1]^T & + & 2/9[\bar{1}\bar{1}\bar{1}] \\ \text{Shockley partial on } \boldsymbol{b} & \rightarrow & \text{Shockley partial on } \boldsymbol{a}^T & + & \text{Frank partial on TB} \end{array} \tag{4.6}$$

Following the expansion of the leading partial dislocation loop $\boldsymbol{C}^T\boldsymbol{\alpha}^T$ in the twin grain (and the corresponding extension of the stacking fault), an additional pair of partial dislocation loops are formed. One of these is the trailing partial dislocation in the twin grain $\boldsymbol{\alpha}^T\boldsymbol{B}^T$ and the other is in the matrix grain $\boldsymbol{\beta A}$. The slip of the $\boldsymbol{\alpha}^T\boldsymbol{B}^T$ partial in the twin grains annihilates the stacking fault left behind by the leading partial $\boldsymbol{C}^T\boldsymbol{\alpha}^T$, while the slip of the $\boldsymbol{\beta A}$ partial in the matrix grain removes the stacking fault left behind by the initial $\boldsymbol{C\beta}$ partial, as shown in

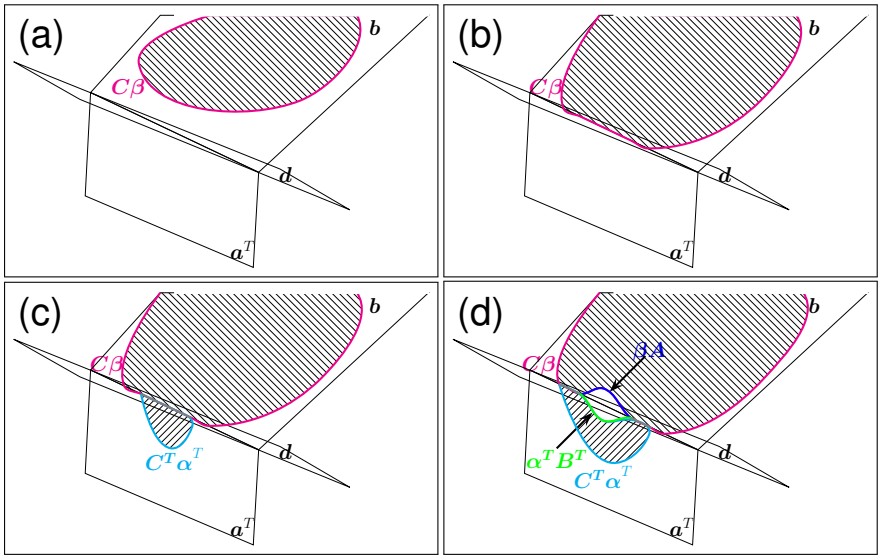

Figure 4.9: Schematic illustration of a 30° partial dislocation passing through a twin boundary. Figure (a) shows a Shockley partial dislocation loop $\boldsymbol{C\beta}$ gliding on the $\boldsymbol{b}$ plane. Figure (b) shows the $\boldsymbol{C\beta}$ partial dislocation blocked by the twin boundary $\boldsymbol{d}$ producing a straight, 30° partial dislocation line segment. Figure (c) shows a Shockley partial dislocation $\boldsymbol{C^T\alpha^T}$ loop nucleated from the intersection of the slip plane $\boldsymbol{b}$ and the twin boundary $\boldsymbol{d}$ that glides into the twinned crystal on plane $\boldsymbol{a}^T$, leaving a Frank-type dislocation behind on the twin boundary. Figure (d) shows the nucleation of $\boldsymbol{\alpha^T B^T}$ and $\boldsymbol{\beta}A$ dislocations on the $\boldsymbol{a}^T$ and $\boldsymbol{b}$ planes in the twinned crystal and matrix, respectively. The slip of the $\boldsymbol{\alpha^T B^T}$ and $\boldsymbol{\beta}A$ partial dislocations clear the stacking faults created by the $\boldsymbol{C^T\alpha^T}$ and $\boldsymbol{C\beta}$ partial dislocations, respectively. The hatched areas denote intrinsic stacking faults.

Fig. 4.9 (d). This dislocation process can be expressed as

$$\begin{array}{ccccc} \boldsymbol{\alpha}^T\boldsymbol{\beta} & \rightarrow & \boldsymbol{\beta A} & + & \boldsymbol{\alpha}^T\boldsymbol{B}^T \\ 2/9[\bar{1}\bar{1}\bar{1}] & \rightarrow & 1/6[1\bar{1}2] & + & 1/6[\bar{1}12]^T \\ \text{Frank partial on TB} & \rightarrow & \text{Shockley partial on } \boldsymbol{b} & + & \text{Shockley partial on } \boldsymbol{a}^T \end{array} \tag{4.7}$$

The unique feature of this mechanism is that it represents a dislocation multiplication effect. One 30° dislocation reacts to form three Shockley partial dislocations at the twin boundary, while leaving the original twin boundary intact and containing no dislocation debris.

4.4 Discussion

Many different dislocation generation mechanisms operate in coarse-grained materials. For example, a classic Frank-Read source can generate dislocation after dislocation, thereby providing a continuous supply of dislocations to sustain plastic deformation. However, when the grain size is on the nanometer scale, most of the dislocation generation mechanisms that operate in coarse-grained materials shut down, leaving a dearth of operative dislocation sources and what has become known as dislocation starvation. This scarcity of dislocations in pure nanocrystalline metals often leads to ultrahigh strength and hardness, yet very low ductility (failure strains in tension of only a few percent are common [110]). As discussed in the Introduction, metals with a high density of nanotwins exhibit simultaneous ultrahigh yield strength and ductility. To achieve these two , often conflicting, mechanical properties in a material that deforms via dislocation plasticity, the material must contain both (a) a high dislocation density and (b) significant barriers to their motion.

The two dislocation-twin interaction mechanisms described in Section. 4.3 imply that twin boundaries can act not only as dislocation barriers but also as sources for dislocation multiplication. The first mechanism is based upon the generation of $\{001\}\langle 110\rangle$ Lomer dislocations from the interaction of 60° dislocations with a twin boundary. Although this mechanism has been previously reported to be one of the strengthening mechanisms in effect in metallic nanowires [119] and nanopillars [44], its role as a dislocation source through its dissociation is first reported here. The dissociation of the Lomer dislocation creates new Shockley partial dislocations on three $\{111\}$ slip planes and hence activates three additional slip systems in the

dislocation-starved grain on the opposite side of the twin boundary. When this decomposition occurs, the original Lomer dislocation survives. This is because this dissociation occurs only on the pure edge and pure screw segments of the Lomer dislocation. The surviving segments of the Lomer dislocation continue to slip on the $\{001\}$ plane. New Shockley partial dislocations can then form via the dissociation of the surviving Lomer dislocation as they curve during subsequent migration and via interaction with the next twin boundary in these nanotwinned structures. The twin mediated slip transformation of a 60° dislocation into a $\{001\}\langle 110\rangle$ Lomer dislocation leaves behind a Shockley partial dislocation on the twin boundary which activates yet another slip system.

In the second mechanism reported in Section. 4.3.2, when a 30° Shockley partial dislocation impinges upon a twin boundary, three new Shockley partial dislocations are formed at the intersection of the 30° Shockley partial dislocation slip plane and the twin boundary. One of the nucleated partial dislocation slips back into the grain from which the initial Shockley partial came (removing the stacking fault that it trailed behind), while the other two partial dislocations slip in the grain on the opposite side of the twin boundary - thereby activating additional slip systems.

These two mechanisms provide dislocation nucleation through dislocation-twin interaction and the activation of several additional slip systems. The high twin boundary density in these materials provides copious opportunities for lattice dislocation-twin boundary interactions. This is how these nano-structured materials simultaneously achieve their remarkably high ductility.

In order to achieve the ultrahigh strength and hardness reported in these nanotwinned materials, barriers to dislocation migration must be present. It has long been recognized that twin boundaries, like general grain boundaries, strengthen metals [11, 120]. However, the atomistic mechanisms by which dislocation-twin interaction strengthen metals remained unclear until recently, when the MD simulation results of Jin et al. [18, 20] and Zhu et al. [19] were reported. In short, they demonstrated that dislocations are blocked by the twin boundary because of the discontinuity in the slip systems of the two crystals (associated with the mirror symmetry there). In order for slip from one grain to its twin to occur, dislocation nucleation or cross-slip must occur at the twin boundary. Even at high stress, thermal activation is usually required to overcome the energy barrier associated with dislocation nucleation. In our simulation, the generation of the Lomer dislocation on the $\{001\}$ plane shown in Section. 4.3.1 contributes to strain hardening through its dissociation. From the dissociation of the Lomer dislocation,

stair-rod and Frank-type dislocations are formed and tend to restrict the motion of the Lomer dislocation. These sessile dislocations also serve as barriers to other dislocations in the system. Our simulations also show the frequent formation of Lomer-Cottrell locks via reactions between Shockley partial dislocations slipping on different $\{111\}$ planes. These sessile dislocations, together with the glissile dislocations and closely spaced stacking faults and twin boundaries, form complex dislocation barriers and networks, as well as point defects, intrinsic and extrinsic stacking faults and stacking fault tetrahedra during plastic deformation (e.g., see Fig. 4.2 (c)). This is consistent with TEM observations in which a relatively defect-free, as-deposited nanotwinned metallic sample contains a high density of dislocations and other debris following tensile loading [10].

4.5 Slip Transfer across Twin Boundary in FCC Lattice

There have been many studies on the interactions of lattice dislocations with coherent twin boundaries. At this point of writing, it is appropriate and beneficial to make a collection of all the known interaction mechanisms. Below we make such a summary as shown in Fig. 4.10. Since gliding dislocations will be blocked and form straight dislocation lines when they encounter interfacial barriers, there are only three categories of lattice dislocation need to be considered [121] :

(i) a screw dislocation ($\boldsymbol{AB}$ on $\boldsymbol{c}$ plane for example);

(ii) a 60° dislocation with a 90° leading partial and a 30° trailing partial ($\boldsymbol{D\gamma}$ and $\boldsymbol{\gamma B}$ on plane $\boldsymbol{c}$).

(iii) a 60° dislocation with a 30° leading partial and a 90° trailing partial ($\boldsymbol{\gamma B}$ and $\boldsymbol{D\gamma}$ on plane $\boldsymbol{c}$) and

In the case where the interface is a coherent twin boundary, the interaction mechanisms seem to be quite limited. However, the problem is also complex as the mechanisms of dislocation-twin interaction are known to be material properties and loading conditions dependent [20]. This makes it impossible to determine the dislocation-twin interaction mechanisms during the twin-mediated slip transfer based solely on conservation of Burgers vector considerations.

We start with the simpler case of screw dislocation first. Screw dislocations can cross slip onto twin boundaries which are also $\{111\}$ slip planes. Figure 4.10 (a) depicts such a

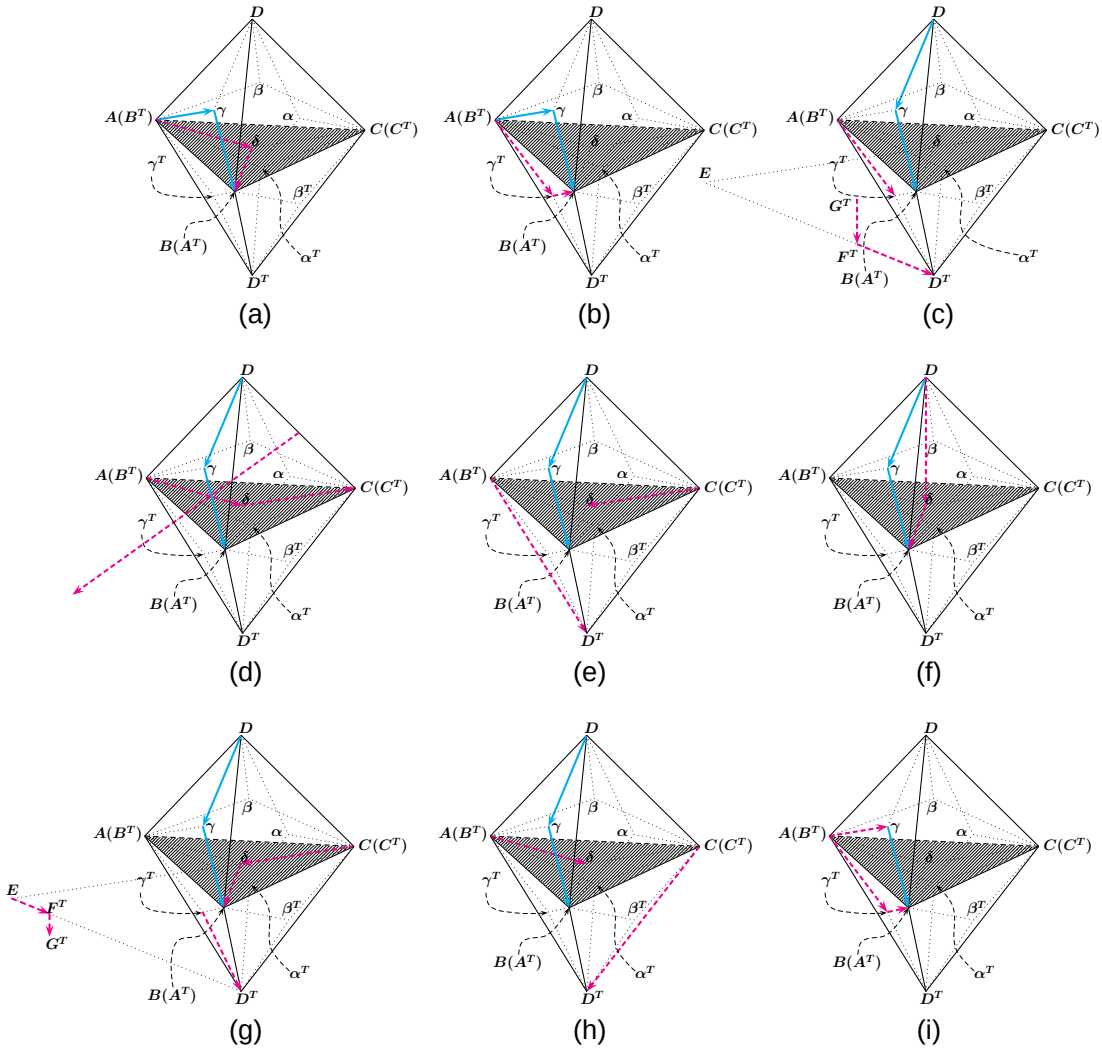

Figure 4.10: Slip transfer of dislocations across an FCC $\{111\}$ twin boundary. (a-b) show screw dislocation cross slip onto the twin boundary $\boldsymbol{d}$ and $\boldsymbol{c}^T$ in the twin crystal respectively. (c-d) show interaction mechanisms of a 60° dislocation (consisting of a 90° leading partial and a 30° trailing partial) with the twin boundary . (e-h) show interaction mechanism of a 60° dislocation (consisting of a 30° leading partial and a 90° trailing partial) with the twin boundary. (i) shows the interaction mechanism of a 30° partial dislocation with the twin boundary.

mechanism. In this twin boundary mediated slip transfer, a pair of partial dislocations $\boldsymbol{A\gamma}$ and $\boldsymbol{\gamma B}$ with an intrinsic stacking fault in between slip on plane $\boldsymbol{c}$ and they constrict into a full dislocation $\boldsymbol{AB}$ with pure a screw character as they encounter the twin boundary $\boldsymbol{d}$:

$$\begin{array}{ccccccc} \boldsymbol{A\gamma}+ & \text{Intrinsic SF} & + & \boldsymbol{\gamma B} & \rightarrow & \boldsymbol{AB} & \\ 1/6[\bar{2}1\bar{1}] & & + & 1/6[\bar{1}21] & \rightarrow & 1/2[\bar{1}10] & (4.8) \\ 30^\circ \text{ partial on } \boldsymbol{c} & & + & 30^\circ \text{ partial on } \boldsymbol{c} & \rightarrow & \text{full lattice dislocation} & \end{array}$$

The discontiniuty of the slip system at the twin boundary makes the above dislocation being blocked. The full dislocation $\boldsymbol{AB}$ is now lying at the intersection of three $\{111\}$ slip planes, namely $\boldsymbol{c}$, $\boldsymbol{d}$ and $\boldsymbol{c}^T$. Both the Schmid factors on the respective slip system and the energy barriers to nucleate new dislocations can influence which slip systems will be activated in the subsequent slip transfer. The first factor is loading condition dependent while the second depends on material properties. The general observation from MD simulations [18, 112, 113] is that dislocations tend to cross slip onto twin boundaries in materials with a high unstable stacking fault energy barrier γ_{usf} compared to that of a unstable twin migration energy barrier γ_{utm}. Al is such a material with $\gamma_{usf}/\gamma_{utm} \sim 3$ and the slip transfer for the above dislocation in Al tends to be

$$\begin{array}{ccccccc} \boldsymbol{AB} & \rightarrow & \boldsymbol{A\delta} & + & \boldsymbol{\delta B} & & \\ 1/2[\bar{1}10] & \rightarrow & 1/6[\bar{1}2\bar{1}] & + & 1/6[\bar{2}11] & & (4.9) \\ \text{full lattice dislocation} & \rightarrow & \text{Shockley partial on } \boldsymbol{d} & + & \text{Shockley partial on } \boldsymbol{d} & & \end{array}$$

Materials such as Cu and Ni have low ratios of $\gamma_{usf}/\gamma_{utm}$. In these materials, the constricted dislocation $\boldsymbol{AB}$ can not only cross onto the twin boundary as described by Eqn. 4.9, but also cross slip onto plane $\boldsymbol{c}^T$ in the twin crystal as illustrated in Fig. 4.10 (b). The latter slip transfer process is

$$\begin{array}{ccccccc} \boldsymbol{AB} & \rightarrow & \boldsymbol{\gamma}^T\boldsymbol{A}^T & + & \boldsymbol{B}^T\boldsymbol{\gamma}^T & & \\ 1/2[\bar{1}10] & \rightarrow & 1/6[\bar{1}2\bar{1}] & + & 1/6[\bar{2}11] & & (4.10) \\ \text{full lattice dislocation} & \rightarrow & \text{Shockley partial on } \boldsymbol{d} & + & \text{Shockley partial on } \boldsymbol{d} & & \end{array}$$

Figure 4.10 (c) shows the dislocation twin interaction mechanism for a 60° dislocation ($\boldsymbol{DB}$ on plane $\boldsymbol{c}$) consisting of a 90° leading partial ($\boldsymbol{D\gamma}$) and a 30° trailing partial ($\boldsymbol{\gamma B}$) observed in Cu MD simulations by Jin et al. [20]. The partial pair constrict at the twin boundary as following

$$\begin{array}{lcccc} \boldsymbol{D\gamma} + & \text{Intrinsic SF} & + & \boldsymbol{\gamma B} & \rightarrow & \boldsymbol{DB} \\ 1/6[\bar{2}1\bar{1}] & & + & 1/6[\bar{1}21] & \rightarrow & 1/2[011] \\ 90^\circ \text{ leading partial on } \boldsymbol{c} & & + & 30^\circ \text{ trailing partial on } \boldsymbol{c} & \rightarrow & \text{full lattice dislocation} \end{array} \tag{4.11}$$

After the constriction of the partial pair at the twin boundary, a Shockley partial $\boldsymbol{B}^T\boldsymbol{\gamma}^T$ is nucleated on plane $\boldsymbol{c}^T$ in the twin crystal, leaving a pair of partial dislocations ($1/3\boldsymbol{\delta}^T\boldsymbol{D}^T$ and $1/3\boldsymbol{A}^T\boldsymbol{B}^T/\boldsymbol{C}^T\boldsymbol{D}^T$) pinned at the twin boundary. The slip transfer process can be written as

$$\begin{array}{lcccccc} \boldsymbol{DB} & \rightarrow & \boldsymbol{B}^T\boldsymbol{\gamma}^T & + & 1/3\boldsymbol{\delta}^T\boldsymbol{D}^T & + & 1/3\boldsymbol{A}^T\boldsymbol{B}^T/\boldsymbol{C}^T\boldsymbol{D}^T \\ 1/2[011] & \rightarrow & 1/6[1\bar{2}\bar{1}]^T & + & 1/9[\bar{1}\bar{1}\bar{1}]^T & + & 1/3[100]^T \\ \text{full lattice dislocation} & \rightarrow & \text{Shockley partial on } \boldsymbol{c}^T & + & \text{Mismatch} & + & \text{Hirth lock} \end{array} \tag{4.12}$$

The above 60° dislocation $\boldsymbol{DB}$ on plane $\boldsymbol{c}$ (consisting of a 90° leading partial $\boldsymbol{D\gamma}$ and 30° trailing partial $\boldsymbol{\gamma B}$) has a different slip transfer mechanism in Al, as shown in Fig. 4.10 (d). The pair of partial dislocations constricts at the twin boundary into a full dislocation as described in Eqn. 4.11. However, the resultant slip transfer in Al is different from that in Cu. In Al, a pair of Shockley partials are nucleated on the twin boundary, leaving behind a stair-rod dislocation ($\boldsymbol{CD/AB}$) at the intersection of the plane $\boldsymbol{c}$ and the twin boundary $\boldsymbol{d}$. This again demonstrates the ease of nucleating dislocations on twin boundaries in Al, which can be attributed to its high value of $\gamma_{usf}/\gamma_{utm}$. The above slip transfer process can be written as

$$\begin{array}{lcccccc} \boldsymbol{DB} & \rightarrow & \boldsymbol{A\delta} & + & \boldsymbol{\delta C} & + & \boldsymbol{CD/AB} \\ 1/2[011] & \rightarrow & 1/6[\bar{1}2\bar{1}] & + & 1/6[11\bar{2}] & + & [001] \\ \text{full lattice dislocation} & \rightarrow & \text{Shockley partial on } \boldsymbol{d} & + & \text{Shockley partial on } \boldsymbol{d} & + & \text{Hirth lock} \end{array} \tag{4.13}$$

Figure 4.10 (e) shows the dislocation twin interaction mechanism for a 60° dislocation ($\boldsymbol{DB}$ on plane $\boldsymbol{c}$) consisting of a 30° leading partial ($\boldsymbol{\gamma B}$) and 90° trailing partial ($\boldsymbol{D\gamma}$) observed in Cu MD simulations [20]. The pair of partial dislocations constricts at the twin boundary into a full dislocation as described in Eqn. 4.11 above. A pair of Shockley partials are nucleated on plane $\boldsymbol{c}^T$ in the twin crystal, leaving behind a Shockley partial dislocation ($\boldsymbol{C\delta}$) on the twin boundary $\boldsymbol{d}$. The slip transfer process can be written as

$$\begin{array}{lcllcll} \boldsymbol{DB} & \rightarrow & \boldsymbol{B}^T\boldsymbol{\gamma}^T & + & \boldsymbol{\gamma}^T\boldsymbol{D}^T & + & \boldsymbol{C\delta} \\ 1/2[011] & \rightarrow & 1/6[1\bar{2}\bar{1}]^T & + & 1/6[\bar{1}\bar{1}\bar{2}]^T & + & 1/6[\bar{1}\bar{1}2] \\ \text{full lattice dislocation} & \rightarrow & \text{Shockley partial on } \boldsymbol{c}^T & + & \text{Shockley partial on } \boldsymbol{c}^T & + & \text{Shockley partial on } \boldsymbol{d} \end{array} \tag{4.14}$$

Figure 4.10 (f) shows the dislocation twin interaction mechanism for a 60° dislocation ($\boldsymbol{DB}$ on plane $\boldsymbol{c}$) consisting of a 30° leading partial ($\boldsymbol{\gamma B}$) and 90° trailing partial ($\boldsymbol{D\gamma}$) observed in Ni MD simulations [20]. The pair of partial dislocations constricts at the twin boundary into a full dislocation as described in Eqn. 4.11 above. Shockley partials are nucleated on twin plane $\boldsymbol{d}$, leaving behind a Frank type partial dislocation ($\boldsymbol{D\delta}$) on the twin boundary $\boldsymbol{d}$. The slip transfer process can be written as

$$\begin{array}{lcllcl} \boldsymbol{DB} & \rightarrow & \boldsymbol{\delta B} & + & \boldsymbol{D\delta} \\ 1/2[011] & \rightarrow & 1/6[\bar{2}11] & + & 1/3[111] \\ \text{full lattice dislocation} & \rightarrow & \text{Shockley partial on } \boldsymbol{d} & + & \text{Frank partial on } \boldsymbol{d} \end{array} \tag{4.15}$$

At larger strains, the above 60° dislocation $\boldsymbol{DB}$ on plane $\boldsymbol{c}$ (consisting of a 30° leading partial $\boldsymbol{\gamma B}$ and 90° trailing partial $\boldsymbol{D\gamma}$) gives a different slip transfer mechanisms as shown in Fig. 4.10 (g). Shockley partial dislocations are nucleated on the twinning plane $\boldsymbol{d}$ ($\boldsymbol{C\delta}$ and $\boldsymbol{\delta B}$) and plane $\boldsymbol{c}^T$ ($\boldsymbol{\gamma}^T\boldsymbol{D}^T$) in the twin crystal, leaving behind a sessile dislocation ($1/6\boldsymbol{A}^T\boldsymbol{B}^T/\boldsymbol{C}^T\boldsymbol{D}^T+$

$1/18\boldsymbol{D\delta}$) on the twin boundary. The slip transfer process can be written as

$$\begin{array}{lllllll}
\boldsymbol{DB} & \rightarrow \boldsymbol{C\delta} & + \boldsymbol{\delta B} & + \boldsymbol{\gamma}^T\boldsymbol{D}^T & + 1/6\boldsymbol{A}^T\boldsymbol{B}^T/\boldsymbol{C}^T\boldsymbol{D}^T & + 1/18\boldsymbol{D\delta} \\
1/6[\bar{1}\bar{1}2] & \rightarrow 1/6[\bar{1}\bar{1}2] & + 1/6[\bar{2}11] & + 1/6[\bar{1}\bar{1}\bar{1}]^T & + 1/6[100]^T & + 1/18[111] \\
\text{full lattice dislocation} & \rightarrow \begin{array}{c}\text{Shockley}\\ \text{partial}\\ \text{on } \boldsymbol{d}\end{array} & + \begin{array}{c}\text{Shockley}\\ \text{partial}\\ \text{on } \boldsymbol{d}\end{array} & + \begin{array}{c}\text{Shockley}\\ \text{partial}\\ \text{on } \boldsymbol{c}^T\end{array} & + \begin{array}{c}\text{sessile}\\ \text{partial}\\ \text{on } \boldsymbol{d}\end{array} & + \begin{array}{c}\text{sessile}\\ \text{partial on } \boldsymbol{d}\end{array}
\end{array} \tag{4.16}$$

Figure 4.10 (h) and (i) are the mechanisms described in the previous section and are not repeated here.

4.6 Summary

In this Chapter, we presented molecular dynamics simulation results for the uniaxial tensile loading of Cu with a microstructure similar to that produced by a pulsed electrodeposition or a magnetron-sputtering technique (i.e., an ultrafine grained microstructure containing a high density of growth nanotwins). The plastic deformation of the initially dislocation free sample is initiated by dislocation nucleation from the grain boundaries. The applied load couples to multiple slip systems producing both Schmid and non-Schmid stresses. We observe two new dislocation-twin interaction mechanisms that lead to copious dislocation generation and the production of sessile dislocation debris. The interaction of a 60° dislocation with a twin boundary generates a $\{001\}\langle 110\rangle$ Lomer dislocation in the twin-related grain and a Shockley partial dislocation on the twin boundary during twin-mediated slip transfer. The Lomer dislocation line segment subsequently dissociates into Shockley, stair-rod and Frank partial dislocations. The interaction of a 30° partial dislocation with a twin boundary generates three additional Shockley partial dislocations during twin-mediated slip transfer. Two of the Shockley partial dislocation glide into the twinned crystal, while the third slips back into the matrix from whence the original partial dislocation came. Through the generation of the Shockley partial dislocations, these new mechanisms activate additional slip systems and hence contribute to the ductility of the material during plastic deformation. The sessile stair-rod and Frank partial dislocations, together with the high-density twin boundaries, provide barriers to dislocation motion and hence strengthen the material. Our simulation results here suggest that twin boundaries can act both as dislocation barriers and multipliers during plastic deformation.

These, in turn, are likely responsible for the experimentally observed simultaneous ultrahigh strength and ductility in this unique microstructure.

We also summarized the known dislocation twin interaction mechanisms in FCC materials and emphasize that the actual mechanisms are material properties and loading condition dependent. The simulations in this Chapter employ a very special, "bi-crystal" structure. It is not clear if the results from this simulation cell are valid in polycrystalline simulations. In addition, the strength transition as a function of twin spacing has not been studied so far. In the next Chapter, we address these points.

Chapter 5

Dislocation Mechanisms Transition in Nanotwinned FCC Metals

The simulation results in the previous Chapter suggest that twin boundaries are effective barriers to dislocation motion and these barriers are not impenetrable. The interactions of dislocation with twin boundaries play an important role in the plastic deformation of nanotwinned metals. In this Chapter, we extend the previous observation based on a "bi-crystal" simulation cell to a polycrystalline cell and examine how deformation mechanisms change by simulating samples over a wide range of twin spacing.

We first present large-scale MD simulations of polycrystalline Cu with nanotwins. We observe the nanotwinned Cu deforms not only through twin migrations, but also through dislocations cutting across twin boundaries as well. Our polycrystalline simulation also demonstrates frequent occurrences of the Lomer dislocation formation and dissociation mechanism as described in our earlier "bi-crystal" simulation in the previous Chapter. Since Lomer dislocations are formed frequently in our simulation and their dissociation mechanism depends on the radius of curvature (i.e., a length scale relating to the twin spacing), we further perform an extensive study on the deformation mechanism of nanotwinned Cu as a function of twin spacing. We identify a change in deformation mechanism at small twin spacing and show that this change in mechanism is consistent with the experimentally observed critical twin spacing for softening. We use these results to develop a model for the twin spacing at which the classical increase in strength with decreasing microstructural length scale breaks down and provide a simple approach to predict the optimal microstructural length scale. Our simulation results suggest that the deformation mechanism changes when the twin spacing is below a critical

value, which can be a source of the experimentally observed softening effect in nanotwinned Cu.

In the simulations in this Chapter, uniaxial tensile loading was simulated at a constant true strain rate of 0.1 ns^{-1} by stretching the simulation box in one direction while the other two dimensions were adjusted through the Nosé-Hoover pressure barostat to maintain zero normal stress. In the following, we describe the polycrystalline simulation first, followed by simulations focusing on the twin spacing variation.

5.1 Polycrystalline Molecular Dynamics Simulations

5.1.1 Simulation Model

In the current study, we constructed a polycrystalline simulation cell through a Voronoi tessellation as illustrated in Fig. 5.1. We first created a group of Voronoi sites arranged in a body-centered cubic (BCC) lattice. The Voronoi polyhedron associated with each Voronoi site (or the bcc super lattice site) is a truncated octahedron as shown in Fig. 5.1 (a). The cubic simulation unit cell encloses 16 such Voronoi sites and its dimensions were scaled to be $\sim 90 \times 90 \times 90$ nm as drawn in Fig. 5.1 (b). The 16 truncated octahedra were then filled with nanotwinned FCC crystals ($\lambda \sim 11.27$ nm) with random orientations such that the total number of atoms in the simulation unit cell is 61,386,312. The atomic configuration was relaxed at 0 K via a conjugate gradient algorithm. The system was then heated to a temperature of 900 K and a hydrostatic pressure of 1 GPa for 100 ps followed by cooling to room temperature (300 K) and zero hydrostatic pressure in another 50 ps. Uniaxial tensile loading was then carried out along the z direction in Fig. 5.1 (a). Figure 5.1 (c) and (d) show two views of the atomistic configuration of the simulation cell in which only atoms in non-perfect fcc lattice environment are shown. (see Fig 5.1 caption for coloring scheme and viewing orientation)

5.1.2 Simulation Results

Figure 5.2 shows the evolution of the defect structure in the nanotwinned polycrystalline Cu sample during tensile loading. Figure 5.2 (a) shows the onset of plastic deformation when leading partial dislocations were first nucleated at grain boundary triple junctions. These newly nucleated partial dislocations glided and created wide stacking faults (~ 10 nm) until they were blocked by twin boundaries. Figure 5.2 (b) is the sample at a later stage of the deformation where dislocations (both pure screw and 60°) started to cross twin boundaries. Those screw

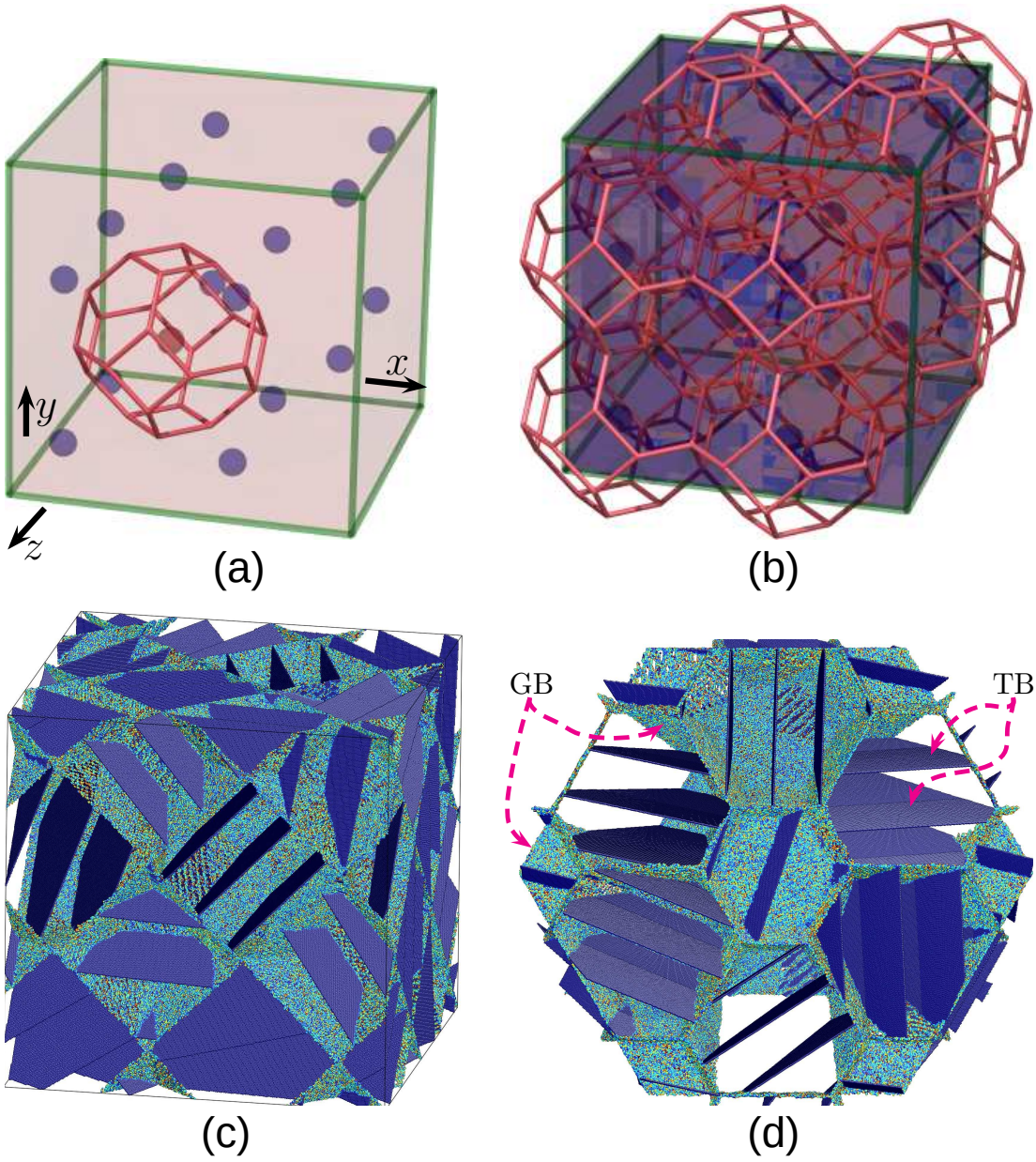

Figure 5.1: Schematic and atomistic view of the polycrystalline molecular dynamics simulation cell. (a) 16 Voronoi sites (dark blue spheres) arranged in a BCC lattice inside the cubic unit cell. The red truncated octahedron is the Voronoi polyhedron associated with one of the Voronoi site; (b) the simulation cell with all the Voronoi polyhedra drawn; (c) atomistic view of the polycrystalline simulation cell (constructed from (b)) when plastic deformation first initiated through partial dislocation nucleations at grain boundary triple junctions. (d) simulation cell in (c) viewed along the $\langle 111 \rangle$ direction in the simulation box coordinates. In both figure (c) and (d), atoms are shown only if their central symmetry parameters [91] differ from that of the perfect FCC crystal; the colors indicate the local symmetry: twin boundaries (TB), dislocations, intrinsic and extrinsic stacking faults are shown in dark blue, magenta or yellow, etc. (depending on dislocation type), sky blue and dark blue, respectively.

dislocations (e.g., $\boldsymbol{AB}$ in Fig. 2.11) crossed twin boundaries by slipping on $\{111\}$ and $\{111\}^T$ planes in the matrix and twin grains alternatively [18, 19]. This process keeps the twin boundary intact. In the simulation, it is also observed that pure screw dislocations cross-slipped onto twin boundaries (forming $\boldsymbol{A\delta}$ and $\boldsymbol{\delta B}$) and created pairs of twin steps. The interactions of 60° dislocations (e.g., $\boldsymbol{DA}$, $\boldsymbol{DB}$) with twin boundaries are different from those pure screw ones. Lomer dislocations were frequently formed on the $\{001\}^T$ plane in the next twin crystal when 60° dislocations passed through a twin boundary. Locations where such dislocation mechanism occurred are highlighted as blue ellipses in the figure. Glide on the unusual $\{001\}^T$ plane in the twinned material occurred because of the very high Schmid factor on this slip system.

In addition to the dislocation twin boundary interactions, twin migration via twin step through Shockley partial dislocation nucleation at twin/grain junctions was also observed in some grains (see Fig. 5.2 (b)). Li et al. [116] attributed this as the softening mechanism in their recent study. Close examination of Fig. 5.2b only reveals two twin steps despite the fact that the total twin area in the sample is quite large (the initial total twin boundary area is 7 μm^2). On the other hand, Fig. 5.2 shows many dislocations crossing between twins. Analysis of the deformation at 3% strain suggests that the ratio of the plastic strain associated with twin boundary migration to that from dislocation migration between twin boundaries is approximately 0.15. The simulation here and those of Li et al. [116] show that dislocation nucleation at the twin/grain boundary junctions and subsequent twin boundary migration is not the dominant deformation mechanism for twin spacings above 3 nm. (Note, dislocations that cross the twin boundaries can also leave steps on the twin boundaries and these steps can also contribute to twin boundary migration. This is a consequence of the dislocations cutting twin boundaries and is a different mechanism than suggested by Li et al. [116].)

Figure 5.2 (c) and (d) show the system at a true strain of 7.5% and 8.5%, respectively. In these figures, many leading partial dislocations were blocked by twin boundaries while the trailing partial dislocations had not yet been nucleated. In some cases, the trailing partial does form, combines with the leading partial at a twin boundary (under the action of the applied stress), cuts through the twin boundaries and forms a Lomer dislocation (on a $\{001\}^T$ plane). The number of dislocations that cut through twin boundaries is small relative to the total number of dislocations formed.

The fact that the yield stresses in the experimental nanotwinned polycrystalline Cu samples [43] ($\lambda \geq 15nm$) follow a Hall-Petch relation with respect to twin spacing (i.e., the yield

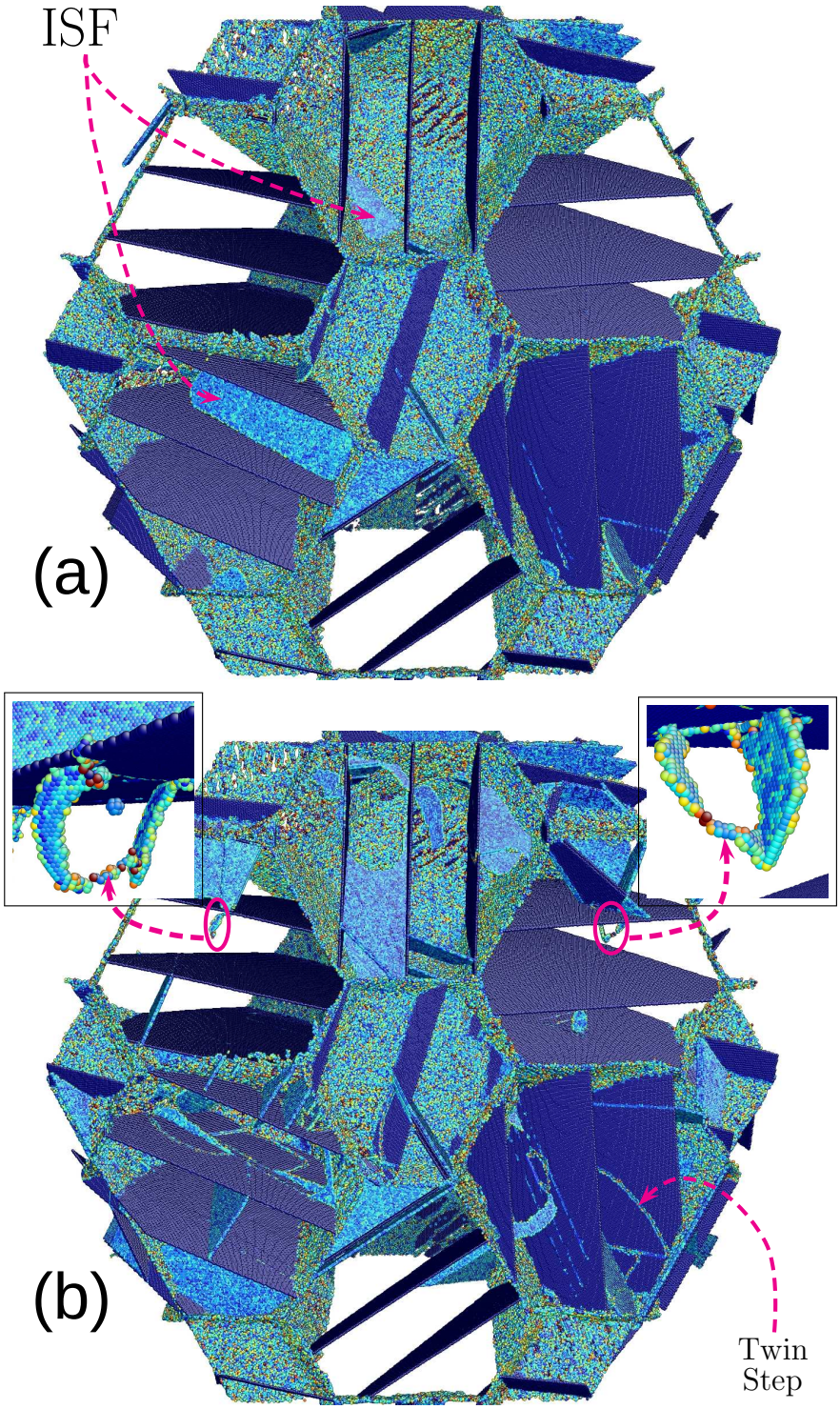

Figure 5.2: Dislocation evolution in the nanotwinned polycrystalline Cu during tensile loading. (a) Partial dislocation nucleations at grain boundary triple junctions and creating intrinsic stacking faults (ISF). (b) Dislocations passing through some twin boundaries and forming Lomer dislocations on the $\{001\}$ plane. Twin migration through a twinning dislocation is also observed in some of the grains.

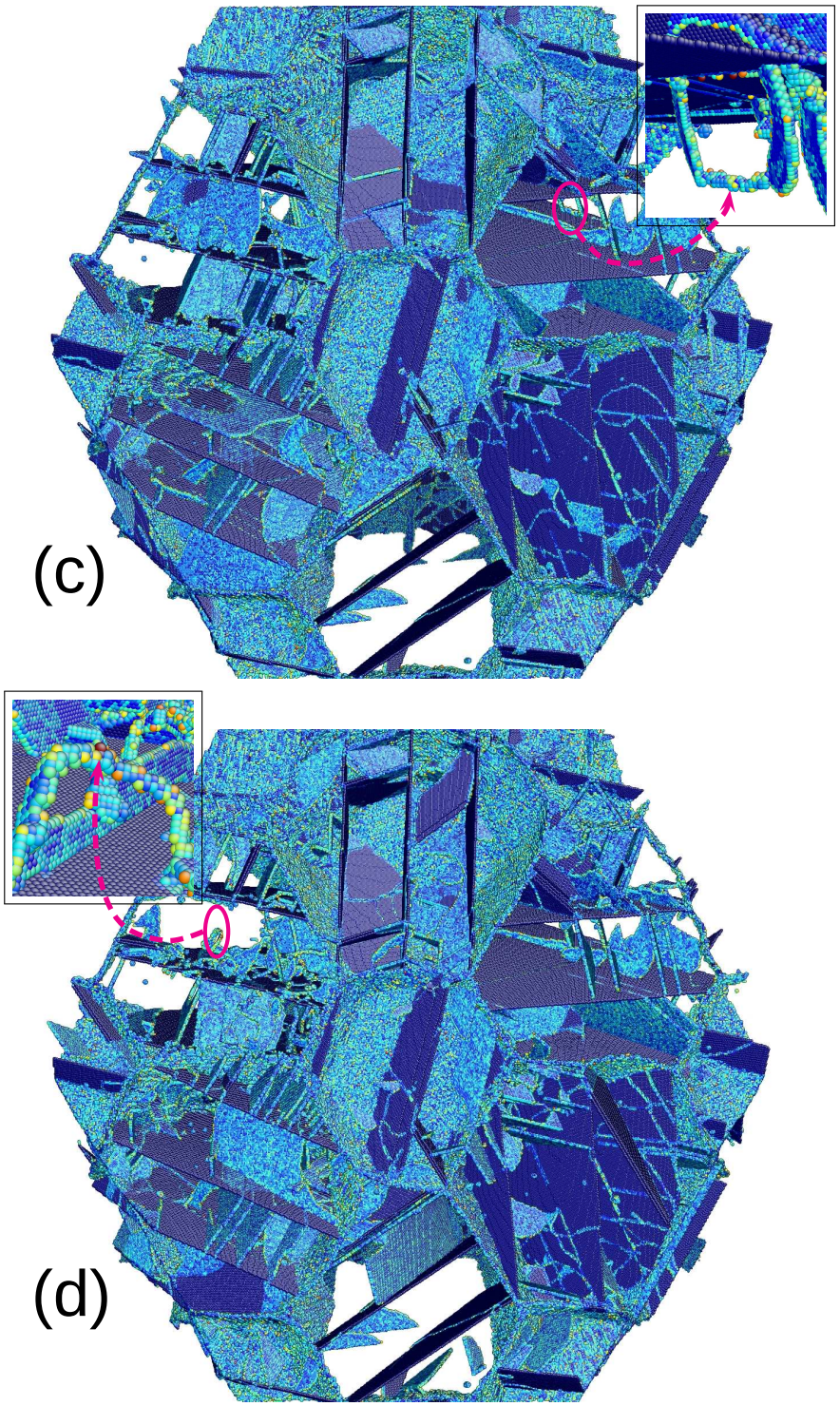

Figure 5.2: (continued) dislocation evolution in the nanotwinned polycrystalline Cu during tensile loading. (c) and (d) shows the dislocation/twin/grain boundary microstructure at true strain of 7.5% and 8.5%, respectively. In figures (b), (c) and (d), the magenta ellipses highlight sites where Lomer dislocations form and dissociate.

strength increases as the inverse square root of the twin spacing) suggests that the twin boundaries are finite barriers to dislocations and it is the cutting of twin boundaries that is critical in the yielding process. Since the formation and dissociation of Lomer dislocations through 60° full dislocations passing through twin boundaries occurs readily in our simulation (and its dissociation mechanism depends on its radius of curvature and the twin spacing) and is the event that determines the flow stress, we designed a series of simulations to explicitly examine the effect of twin spacing on this mechanism. We do this by tracing the positions and type of dislocations (and their reactions) through the plasticity evolution process in each of the simulations. Interestingly, a dislocation mechanism transition occurs when the twin spacing reaches a lower critical value in our simulation. We describe these simulations in detail in the following section.

5.2 Dislocation Deformation Mechanism as a Function of Twin Spacing

5.2.1 Simulation Model

We designed a set of simulations with simulation cells constructed as shown schematically in Fig. 5.3. The simulation cells consist of two types of twin-related grains M (matrix) and T (twin). A pair of dislocations with Burgers vectors $\boldsymbol{DB}$ and $\boldsymbol{BD}$ were introduced in the upper and lower grains in Fig. 5.3, respectively. This is achieved by displacing atoms from their original perfect FCC lattice positions to new positions according to the isotropic, linear elastic displacement fields [56] (see Section. 2.3.4). If two atoms were too close together, one was removed and if voids were detected, additional atoms were inserted in the structure to fill the voids (as dictated by crystal symmetry) prior to the beginning of the simulations. The unstrained simulation cell has dimensions $\sim 70.8 \times 170 \times 20.4$ nm in the x, y and z directions, respectively, corresponding to 20,850,080 Cu atoms, and the twin boundary spacing λ is varied between ~ 1.88 and ~ 31.3 nm (i.e., the number of twins varies with the choice of λ). These atomic configurations were relaxed at 0 K via a conjugate gradient algorithm. These systems were then heated to room temperature (300 K) within 100 ps and held at room temperature for another 50 ps. Uniaxial tensile loading was then carried out along the y direction in Fig. 5.3. The Burgers vector of the dislocations in the grains were determined using the classical Burgers circuit construction (see Section. 2.3.3) while those on the twin boundaries were deduced by applying the conservation of Burgers vector between slip transfers.

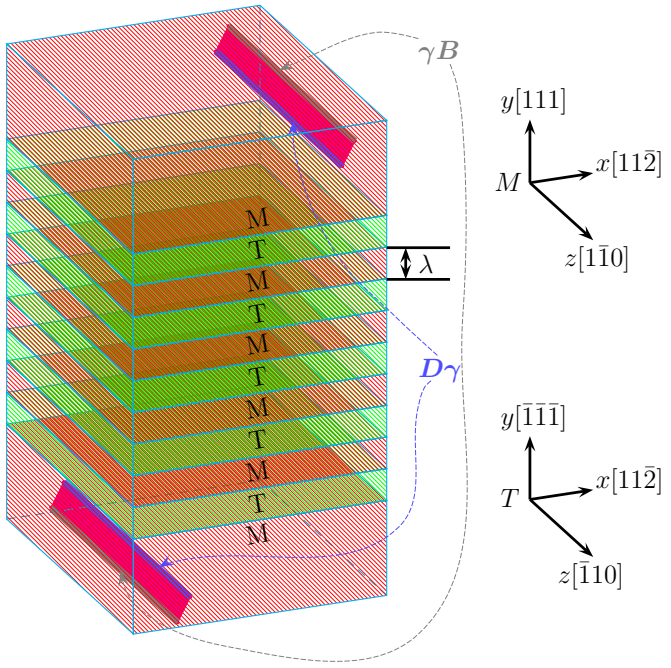

Figure 5.3: Schematic illustrations of the molecular dynamics unit cell. The simulation cell consists of alternating matrix (M) and twin (T) grains, each of thickness λ. The crystallographic orientations of the matrix and twin grains are also shown. $\langle 110 \rangle$ dislocations $\boldsymbol{DB}$ and $\boldsymbol{BD}$ are introduced in the top and bottom grains at the beginning of the simulations, which then dissociate into Shockley partial dislocations ($\boldsymbol{D\gamma} + \boldsymbol{\gamma B}$). (refer to Fig. 2.11 for Burgers vectors and notations)

5.2.2 Simulation Results

The set of specially constructed simulation cells as shown in Fig. 5.3 share a few common features. In these simulation cells, the total number of atoms, the simulation cell dimensions and the simulation conditions are the same. The only difference is the twin spacing among them. These special settings allow us to estimate how the stress required for dislocation crossing the twin boundaries σ_c changes as a function of twin spacing λ. The possible source for such a dependence between σ_c and λ is the image forces arising from the orientation difference between the matrix and twin crystals. Figure 5.4 shows the σ_c v.s. λ obtained from the MD simulations. It is clear that σ_c decreases with λ. However, the simulations show that for twin spacing from 15 nm to 1.8 nm, there is only a $\sim 5\%$ difference between the maximum and minimum value of σ_c. This suggests the variation of image forces as a function of twin spacing is minor and insufficient to give a difference of nearly 3-fold in the experimentally measured yield stress (see Fig. 3.1). Nevertheless, the set of simulations show a dislocation mechanisms transition in large and small twin spacing. Figure 5.5 shows an atomic view (only atoms in non-fcc local environments are shown) of the evolution of the dislocations as they pass through twin boundaries for (a) large ($\lambda = 18.8$ nm) and (b) small ($\lambda = 1.88$ nm) twin boundary spacing simulations. Figure 5.6 is an idealized illustration of the dislocation processes exhibited in Fig. 5.5. In both figures, time and strain evolve from left to right. We describe these two deformation mechanisms in detail below.

5.2.2.1 Deformation at Large Twin Spacings

We first summarize the evolution of the dislocation microstructure at large twin spacing ($\lambda = 18.8$ nm) in atomistic detail and in schematic form in Figures 5.5 (a) and 5.6 (a). A partial dislocation from the dissociated 60° dislocation ($\boldsymbol{D\gamma} + \boldsymbol{\gamma B}$ on slip plane $\boldsymbol{c}$ - see Fig. 5.6 (a1)) constricts into a full dislocation ($\boldsymbol{DB}$) at the intersection of slip plane $\boldsymbol{c}$ and twin boundary $\mathbf{TB}_1$ (Fig. 5.6 (a2)) and cross-slips onto a $\{001\}^{\boldsymbol{T}}$ plane in the twin grain, thus forming a $\{001\}^T\langle 110\rangle^T$ Lomer dislocation ($\boldsymbol{C}^T\boldsymbol{D}^T$ in Fig. 5.6 (a3)). While the remaining $\boldsymbol{DB}$ segments on the twin boundary continue to cross-slip, the cross-slipped Lomer dislocation glides further and adopts a semi-circular shape under the resolved shear stress (see Fig. 5.6 (a4)). As the Lomer dislocation line evolves, part of the dislocation line (near the twin boundary) rotates such that its line direction becomes parallel to its Burgers vector; thus forming a pure Lomer screw dislocation. Since $\{001\}^T$, $\boldsymbol{a}^T$ and $\boldsymbol{b}^T$ planes intersect at a single line, this screw segment

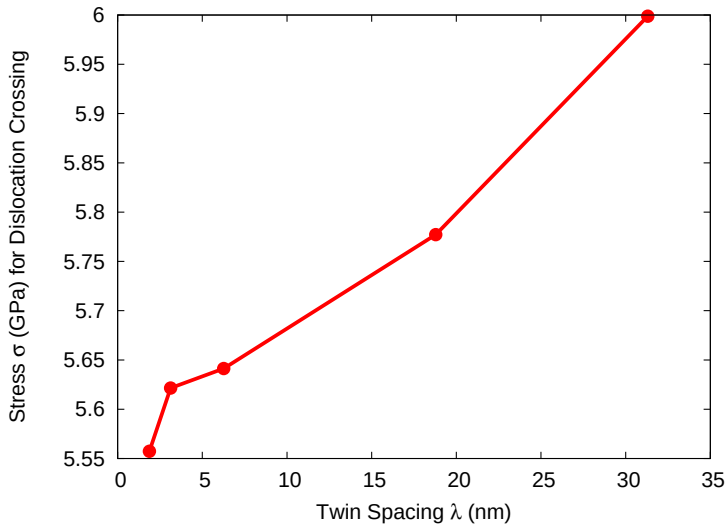

Figure 5.4: Tensile stress required for a 60° dislocation to cross twin boundary at various twin spacings in MD simulations.

cross-slips onto one of the $\{111\}^T$ slip planes in the twin grain ($\boldsymbol{b}^T$ in Fig. 5.6 (a5)) and dissociates into the usual Shockley partial pair ($\boldsymbol{C}^T\boldsymbol{\beta}^T$ and $\boldsymbol{\beta}^T\boldsymbol{D}^T$). These cross-slip and dissociation events are energetically favorable (based on Frank's dislocation reaction criterion [56]). The newly formed Shockley partial pair glide on their usual $\{111\}^T$ slip plane and form a 60° dislocation (equivalent to the initial $\boldsymbol{DB}$) when they impinge on the next twin boundary, allowing the Lomer dislocation generation-dissociation process to repeat. Pure screw segments cross-slip onto the $\boldsymbol{a}^T$ plane with Shockley partials $\boldsymbol{C}^T\boldsymbol{\alpha}^T$ and $\boldsymbol{\alpha}^T\boldsymbol{D}^T$ equally possible under the loading condition in our simulation. In addition, we observe the pure screw Lomer dislocations cross-slip onto both $\boldsymbol{a}^T$ and $\boldsymbol{b}^T$ to form a stair-rod segment at the intersection of the above two slip planes. This is illustrated in Fig. 5.6 (a7-a10), where a different view with all the Burgers vector labeled is shown as well (see the inset of Fig. 5.5 (a5) and Fig. 5.6 (a7)). The Shockley dislocations, cross-slipped from the Lomer, glide on their respective $\{111\}^T$ slip planes while dragging the sessile stair-rod dislocation $\boldsymbol{\alpha}^T\boldsymbol{\beta}^T$ through a junction zipping-unzipping process [122]. Those Shockley partial dislocations and remaining Lomer dislocation segments glide on different slip planes, restricted by the sessile junctions that are formed where they meet. The restriction on the motion of the Lomer dislocation further curves the dislocation line, making cross-slip and dissociation favorable. Through the cross-slip and dissociation of Lomer dislocations, the system develops a complicated 3D dislocation structure contain-

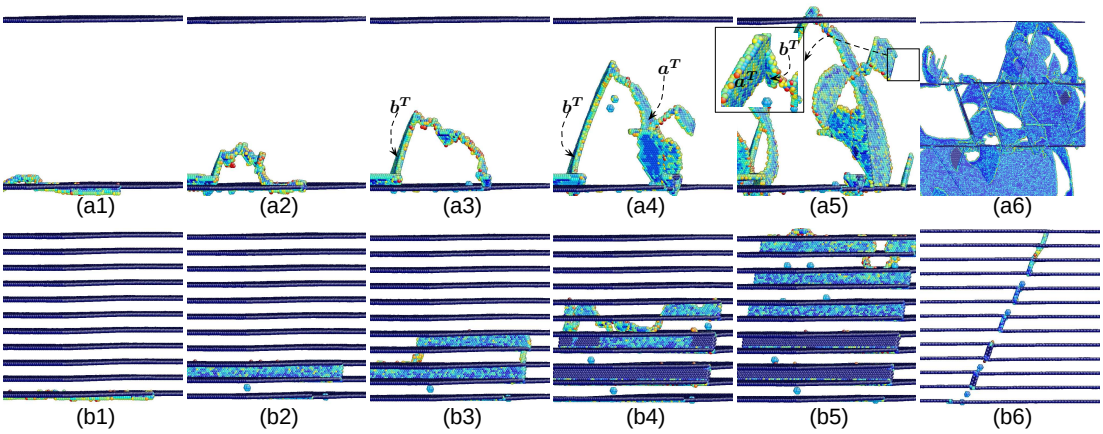

Figure 5.5: Atomistic view of dislocations passing twin boundaries for case (a) large ($\lambda = 18.8$ nm) and (b) small ($\lambda = 1.88$ nm) twin boundary spacing (the image shows the same size section of the simulation cell in each case). In both figures, time evolves from left to right (1-6). For $\lambda = 18.8$ nm, (a1) a segment of the dissociated 60° dislocation constricts to pass through a twin boundary. (a2) The dislocation segment cross-slipped onto a $\{001\}^T$ plane forming a semi-circular $\{001\}^T\langle 110\rangle^T$ Lomer dislocation. (a3) A pure screw segment of the Lomer dislocation starts to cross-slip onto $\boldsymbol{b}^T$ plane. (a4) Additional pure screw segments of the Lomer dislocation cross-slips onto $\boldsymbol{a}^T$ and $\boldsymbol{b}^T$. (a5) Pure screw segments of the Lomer dislocation cross-slipped onto $\boldsymbol{a}^T$ and $\boldsymbol{b}^T$ and form a stair-rod dislocation at the junction (see inset of Fig. 5.6 (a7) for their dislocation Burgers vectors). (a6) A late stage of the deformation. For $\lambda = 1.88$ nm, (b1) shows the dissociated 60° dislocation constricts to pass through a twin boundary, as in (a1). (b2) and (b3) show a dislocation passing subsequent twin boundaries, leaving behind intrinsic stacking faults in the matrix grains, but not the twin grains. (b4) shows a segment of the Lomer dislocation gliding in the twin grain without cross-slip or dissociation (see Fig. 5.6 (b) for details). (b4) and (b5) shows that the intrinsic stacking faults in the matrix grain are converted to extrinsic stacking faults by the passage of an additional Shockley partial. (b6) A late stage of the deformation showing a structure with extrinsic stacking faults bridging matrix grains and Shockley partial dislocations on each twin boundary.

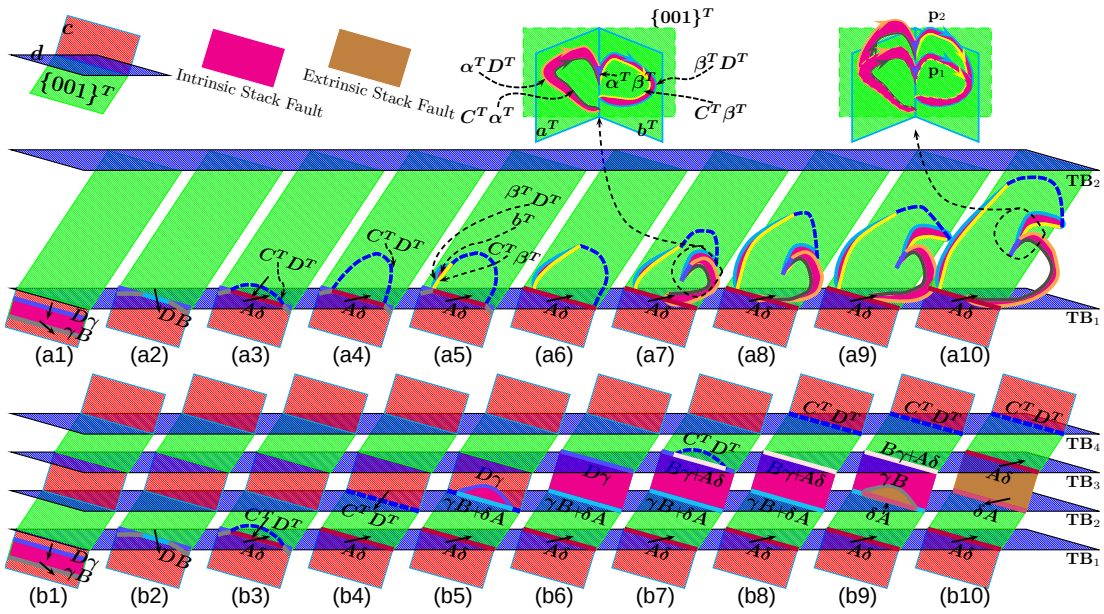

Figure 5.6: Schematic illustration of dislocations passing twin boundaries with different twin spacing, corresponding to the atomistic images in Fig. 5.5. The key identifying the slip planes and stacking faults are shown above the dislocation schematics. The inset of Fig. a7 shows a Lomer dislocation segment cross-slipped onto the $\boldsymbol{a}^T$ and $\boldsymbol{b}^T$ planes, forming a stair-rod dislocation segment at the intersection. The inset of Fig. (a10) illustrates the above dislocation structure migrating from "$\mathbf{p}_1$" to "$\mathbf{p}_2$" through a junction zipping-unzipping process.

ing both glissile and sessile dislocations on various slip planes. Figure 5.5 (a6) shows such a dislocation structure at a late stage of the deformation.

5.2.2.2 Deformation at Small Twin Spacings

Figure 5.5 (b) shows the case where the twin spacing $\lambda = 1.88$ nm. We use Fig. 5.6 (b) as a schematic illustration to describe the dislocation activity. A Lomer dislocation $\boldsymbol{C}^T\boldsymbol{D}^T$ is formed through the same mechanism (Fig. 5.6 (b1 - b3)) as described earlier. However, instead of dissociation or cross-slip, $\boldsymbol{C}^T\boldsymbol{D}^T$ glides on the $\{001\}^T$ plane in the twin grain until it impinges on the next twin boundary $\mathbf{TB}_2$ (see Fig. 5.6 (b4)). The Lomer dislocation cross-slips to the usual $\{111\}$ slip plane with a Shockley partial dislocation $\boldsymbol{D\gamma}$ in the matrix grain after passing through $\mathbf{TB}_2$. This leaves a dislocation with combined Burgers vector $\boldsymbol{\gamma B} + \boldsymbol{\delta A}$ on that twin boundary. An intrinsic stacking fault is generated as $\boldsymbol{D\gamma}$ glides in the matrix grain (Fig. 5.6 (b5)). $\boldsymbol{D\gamma}$ is blocked as it meets the next twin boundary, i.e., $\mathbf{TB}_3$. At a later stage, the blocked leading Shockley partial dislocation $\boldsymbol{D\gamma}$ cross-slips onto a $\{001\}^T$ plane in the next twin grain, forming a new $\{001\}^T\langle 110\rangle^T$ Lomer dislocation $\boldsymbol{C}^T\boldsymbol{D}^T$ as shown in Fig. 5.6 (b7). This leaves a dislocation with combined Burgers vector $\boldsymbol{B\gamma} + \boldsymbol{A\delta}$ on $\mathbf{TB}_3$. The newly formed Lomer dislocation $\boldsymbol{C}^T\boldsymbol{D}^T$ glides in the twin grain until it meets the next twin boundary $\mathbf{TB}_4$ (see Fig. 5.6 (b8)). As the Lomer glides, a Shockley partial dislocation $\boldsymbol{\gamma B}$ glides from $\mathbf{TB}_2$ in the matrix grain and annihilates with dislocation $\boldsymbol{B\gamma}$ on $\mathbf{TB}_3$. However, $\boldsymbol{\gamma B}$ glides on the $\{111\}$ plane adjacent to the one on which $\boldsymbol{D\gamma}$ previously glided, thus forming an extrinsic stacking fault. This process is illustrated in Fig. 5.6 (b9). The resulting configuration is shown in Fig. 5.6 (b10). The Lomer dislocation $\boldsymbol{C}^T\boldsymbol{D}^T$ on $\mathbf{TB}_4$ now has the same configuration as the previous one on $\mathbf{TB}_2$ in Fig. 5.6 (b4). This means that the whole process repeats at every second twin boundary as observed in the MD simulations and shown in Fig. 5.5 (b1 - b5). In summary, the dislocation glides on $\{111\}$ and $\{001\}^T$ planes, alternatively in the matrix and twin grains, leaving behind a Shockley partial dislocation on each twin boundary and an extrinsic stacking fault in each of the matrix grains.

Examining the deformation process in simulations performed over a wide range of twin spacing λ, suggests that this process of cross-slip and dissociation does not occur at small twin spacing. We suggest that this change in dislocation mechanism is a source of the experimentally observed maximum in the strength of nanotwinned Cu as a function of twin spacing, as discussed below. A comparison of Fig. 5.5 (a6) and (b6) suggests a different dislocation structure results depending on the operative dislocation mechanism. The former mechanism

involves the cross-slip and dissociation of a Lomer dislocation that forms a complex 3D dislocation network, while in the latter case, slip is constrained to the original slip system such that a 2D dislocation microstructure is maintained. The feature that is common between these two cases is that both processes can repeat.

5.3 Analytical Model and Discussion

The simulations in Section. 5.2.2 show a transition in deformation mechanism resulted from the cross-slip and dissociation of the Lomer dislocation. But what governs this change? As the applied stress increases and eventually reaches a critical level τ_c, the constricted 60° dislocation segment passes through the twin boundary and cross-slips to form a Lomer dislocation segment. The newly formed Lomer segment adopts an arc shape under the action of this stress τ_c, the two ends of which are on the twin boundary (see Fig. 5.7 (a)). The equilibrium radius of curvature r_c of the arc can be approximated through the balance between the applied shear stress τ_c and its line tension T:

$$r_c = \frac{T}{b\tau_c}, \tag{5.1}$$

where b is the Burgers vector of the dislocation. As time evolves, more of the original 60° dislocation passes through the twin boundary and cross-slips onto the $\{001\}^T$ plane, the Lomer dislocation arc grows larger and adopts a new configuration (this is the evolution from the dashed arc "$\mathbf{s}_1$" to "$\mathbf{s}_2$" in Fig. 5.7 (a)). However, Eqn. 5.1, governing the radius of curvature of those arcs, remains valid and the evolving dislocation arc in Fig. 5.7 (a) retains the same radius of curvature.

As this process proceeds, the Lomer dislocation eventually reaches a semi-circular shape (denoted as the solid half circle in Fig. 5.7 (a)) and the sections of the dislocation arcs that are near the twin boundary become parallel to the Burgers vector and hence become pure screw dislocation segments. It is these pure screw segments that can cross-slip and dissociate easily, as observed in the MD simulations. The Lomer dislocation is able to form this semi-circular configuration (and form pure screw segments) if the expanding loop can continue to grow into the semi-circular geometry *before* it hits the next twin boundary. In other words, the cross-slip process can only occur if the twin spacing is larger than the semi-circular arc radius of curvature r_c. In cases where the twin spacing λ is smaller than r_c, such as those shown in Fig. 5.7 (b) and (c), the leading Lomer dislocation arc is blocked by the next twin boundary. In this case, the

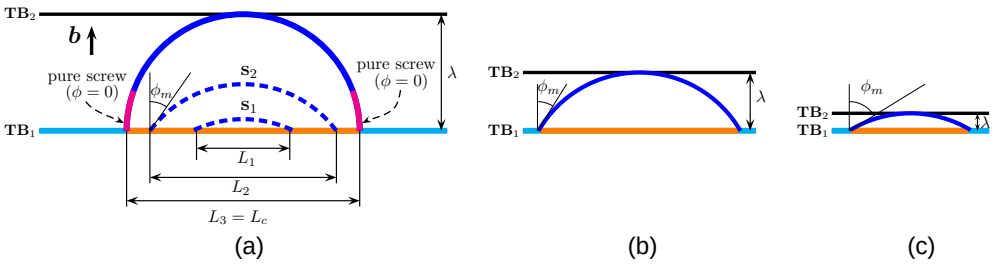

Figure 5.7: Schematic illustrations of the Lomer dislocation gliding in the twin grain at different twin spacings. ϕ_m is the minimum angle between the dislocation Burgers vector $\boldsymbol{b}$ and its line direction. (a) The Lomer dislocation evolves from the dashed arc "$\mathbf{s}_1$" of size L_1 to "$\mathbf{s}_2$" of size L_2. The expanding Lomer dislocation arch becomes a semi-circular half-loop (shown as a solid arc) at size L_3. The line segments of the half-loop in contact with twin make an angle $\phi_m = 0$ with respect to the Burgers vector and hence become locally pure screws (denoted as segments with magenta color). The radius of the semi-circular loop r_c is equal to the twin spacing λ (measured in the slip plane) in this case. (b) The Lomer dislocation gliding in a twin grain with a twin spacing that is too small for the arc to become semi-circular and no pure screw segments are formed. In this case, the leading Lomer dislocation arc is block by twin boundary $\mathbf{TB}_2$. (c) The Lomer dislocation gliding in a grain with even smaller twin spacing. As in (b), no screw segments are formed.

minimum angle between the dislocation Burgers vector and its line direction ϕ_m does not go to zero (i.e., a pure screw does not form). Hence, the Lomer dislocation will not form a semi-circular shape, no screw segments are formed, and no cross-slip and dissociation are possible. Therefore, it is the relative size of the critical radius of curvature r_c and the spacing between twin boundaries λ that determines which deformation mechanism will be operative.

We now validate this conjecture through quantitative comparisons between this prediction and our MD simulations. The simulations show that for all $\lambda \geq 3.13$ nm, Lomer dislocation cross-slip and dissociation occur. For the smallest twin boundary spacing for which MD simulations were performed $\lambda = 1.88$ nm, no cross-slip or dissociation occurs. This implies that the critical twin spacing for the Lomer dislocation to form pure screw segments (a necessary condition for cross-slip) lies between 1.88 nm and 3.13 nm. In order to calculate the critical twin boundary spacing/critical radius of curvature, we must calculate the dislocation line tension T. In the isotropic elastic limit (and neglecting the dependence of line tension on line direction), we can write $T = \alpha\mu b^2$ [56], where $\alpha \approx 0.5$ [80, 81]. For Cu, we use this definition of the line tension and the experimental values of the parameters: $\mu = 48$ GPa and $b = 0.256$ nm. For τ_c in Eqn. 5.1, we take $\tau_c = 2.6$ GPa, which is the minimum applied stress resolved onto the slip

system needed to form the Lomer dislocation into the twin grain. This stress, corresponding to a 5.5 GPa uniaxial tensile stress, is the minimum stress required to pass dislocations through the entire twinned structure and hence can be thought of as the yield strength of the materials for the present simulation conditions (The yielding stress for the polycrystalline simulation described in Section 5.1 is $\sim$ 2.2 GPa). Using this approach, the predicted transition in deformation mechanism should occur at $\lambda = r_c \approx 2.4$ nm. This theoretical value is consistent with our MD simulation observation for where the dislocation mechanism changes; i.e., 1.88 nm $< \lambda < 3.13$ nm.

It is not reasonable to expect that the simulation prediction will carry directly over to experiments, given the fact that MD simulations are performed on a much shorter time scale, necessitating much higher loading rates than that in experiment. Since flow stress typically increases with strain rate, this necessitates re-examining how τ_c is determined for the sake of comparison with experiment. If we replace our estimate of τ_c with the experimentally measured tensile yielding stress $\sim$1 GPa of nanotwinned Cu [12] in Eqn. 5.1 and use the line tension above, we will find a critical twin spacing λ_c approximately 5 times that we obtained using the τ_c estimate from the MD simulations. This suggests the critical twin spacing for the deformation mechanism transition to occur should be $\sim$ 13 nm. This is in excellent agreement with the experimentally observed maximum in the strength at $\lambda = 15$ nm.

The fact that the three slip planes, $\{001\}^T$, $\boldsymbol{a}^T$ and $\boldsymbol{b}^T$, intersect at a single line and the dislocation energy is reduced by dissociation leads to the spontaneous cross-slip and dissociation of the pure screw Lomer dislocation. The cross-slip and dissociation of the Lomer dislocation simultaneously activates several slip systems and leads to the evolution of a complex 3D dislocation structure. This structure favors the formation of many Lomer-Cottrell dislocation locks [56] and hardening. Sessile dislocations resulting from the Lomer dislocation cross-slip and dissociation can restrict the motion of the Lomer dislocation itself and also serve as barriers for other dislocations in the system. In the small λ case, where the Lomer dislocation does not form a pure screw segment and no cross-slip and dissociation occurs, a Shockley partial dislocation with alternating Burgers vector is produced on each twin boundary during Lomer dislocation glide. The number (and density) of these Shockley partials at twin boundaries increases with decreasing twin spacing. These Shockley partial dislocations correspond to steps on the twin (their Burgers vectors lie in the twinning plane). While these twin steps may lead to softening the material (see [43]), perhaps their most important role is as dislocation emission sites, as found in MD simulations [45]. Our simulations thus indicate the operation

of both a strengthening mechanism (Lomer cross-slip and dissociation) and a mechanism for increased ductility (through twin step formation), both of which operate above and below a critical twin spacing. The above analysis on the critical radius for reaching a pure screw configuration is demonstrated and verified for this special case of Lomer dislocation half-loop. However, we would expect the above theory to be generally applicable to other types of dislocation half-loops. The proposed critical radius of curvature controls the formation of pure screw dislocation segments, which in turn determines the cross-slip/non-cross-slip behavior of dislocations in the nanotwinned microstructure.

Earlier studies [19, 43] suggest the plastic deformation process in this unique microstructure is related to dislocation-twin interactions and that these interactions become dominant in samples with small twin spacing. Lu et al. [43] showed that while dislocation tangles and networks are formed in samples with large twin spacings, planar dislocations associated with twin boundaries (and twin steps) are formed in samples with small twin spacing. The two different dislocation mechanisms operating at large and small twin spacing presented in the previous section result in dislocation patterns which are consistent with the above experimental facts. Hence, the mechanism suggested here matches closely not only in the transition length scale but also in the resultant dislocation pattern.

The experimental data on the deformation of pure, nanotwinned Cu [43] suggest that it is possible to simultaneously obtain ultrahigh strength and ductility. The peak in the yield stress occurs at a twin spacing $\lambda \approx 15$ nm. While no such peak is observed in either the hardening coefficient nor the strain to failure, both of these quantities show a monotonic increase with decreasing λ. Nonetheless, close examination of the stress-strain curves for nanotwinned Cu experimental data reported in [43] indicates a rapid rise in the ductility (strain to failure) when λ is decreased below ~ 20 nm (there is only one experimental data point reported for 10 nm $< \lambda < 35$ nm). This observation is consistent with a change in deformation mechanism at a critical twin spacing that is very close to the measured (and predicted) λ_c. The pronounced increase in the ductility at $\lambda < \lambda_c$ may be attributed to the formation of steps on the twin boundary in this twin spacing regime, as discussed above.

5.4 Limitations of MD Simulations

The analysis presented above is largely based on mechanistic understanding. For the polycrystalline MD simulations, it would be highly desirable to have some quantitative measurements

of yield and flow stresses as a function of twin spacing. However, these stresses in MD simulations are mainly dictated by dislocation nucleation events, which in turn are determined by the underlying microstructure details (such as dislocation sources and grain boundary types and distribution) within simulation samples. The microstructure details are often randomized in current polycrystalline MD simulations. Hence the effect of dislocation mechanism on the macroscopic mechanical property would only be revealed through very large samples simulated at relatively low strain rate. This will require simulations of polycrystalline samples with large number of grains, large grain sizes and a variety of twin sizes. Another important point worth noting is the fact that experimental samples have a distribution of twin spacings while current MD simulations focus on a single twin spacing. The distribution of twin sizes within grains might have important effects on dislocation nucleation events.

It has long been recognized that FCC metals such as Cu [123, 124] and Ni [125] have high strain rate sensitivities. The strain rate of 0.1 ns^{-1} used in current MD simulations is extremely high when compared to the typical experimental strain rate of 10^{-3} s^{-1}. The realistic strain rate is simply not accessible to current MD simulations consisting of tens of millions of atoms. Hence it is very common that yield stresses in MD simulations are a few times higher than those in experiments. The typical, high strain rate of 0.1 ns^{-1} used in MD simulations necessarily creates a high stress condition in the simulations. A lower stress would make the critical twin spacing for dislocation mechanism transition larger, which is discussed in Section 5.3. It would be highly desirable to perform MD simulations at lower strain rates and to find the rate controlling mechanisms in nanostructured materials. In addition, time dependent processes such as dislocation nucleations, cross slips are likely to be affected by the strain rate.

Since dislocation crossing twin boundaries is the critical event in plastic deformation of nanotwinned structures and this event is likely to be rate-dependent [126, 127], the applied strain rate may also play an important role in dislocation cross-slip processes during the twin mediated slip transfer. Dislocation twin interactions other than those described in Fig. 4.10 are possible at different loading rates. For example, cross slip of the 60° full dislocation onto the $\{001\}^T$ plane might be a stress and time-dependent process. Under lower strain rates and lower stresses, gliding on the unusual $\{001\}^T$ plane may not be favored. However, the proposed mechanism based on the critical dislocation half-loop radius after dislocation crossing twin boundaries should still be operative for other types of dislocations and the formation of pure screw dislocation segments within the matrix/twin grains is important as it determines the cross-slip/non-cross-slip behavior of dislocations in space-constrained microstructures such as

nanotwins and thin films. On the other hand, the cross slip and dissociation of the pure screw Lomer dislocation segments are driven by a reduction of dislocation line energy, which is a spontaneous process. This process is not likely to be sensitive to the applied strain rate.

It is well known that FCC twin boundaries are preferential crack initiation sites[128–133]. Previous studies focused on twin boundaries' effect on fatigue properties where the twin size was of micrometer scale. Both dislocation[134] and elastic theory [128, 132, 135] were proposed to explain the unexpected role twin boundaries play during cyclic loading. On the other hand, there are very few studies on fatigue properties of materials with nanometer twin sizes [136, 137]. Present TEM observations [43] suggest a high density of dislocation near twin boundaries. However, it is unclear whether these dislocations are resulted from grain boundaries or from local stress concentration sites at twin boundaries due to strain incompatibility[128, 135]. The MD simulations here suggest that dislocations are nucleated from grain boundaries and accumulate near twin boundaries, thus forming complicated dislocation structures. In future, it would be interesting to investigate the effect of the above dislocation mechanisms on fatigue properties of such nanotwinned microstructure.

5.5 Summary

We presented large scale MD simulations of plastic deformation of polycrystalline nanotwinned Cu. It is found that dislocation nucleation from grain boundary triple junctions initiates plastic deformation in the simulations. Twin boundary migration via twin steps formed either by Shockley partial dislocation nucleation at twin/grain boundary junctions or by absorption of pure screw dislocations are observed. Pure screw and 60° dislocations crossing twin boundaries are more dominant in our simulations and the latter generates Lomer dislocations which further dissociate into Shockley and stair-rod partial dislocations. Simulations of Cu samples over a wide range of twin spacing is also carried out and these simulations reveal a transition in the deformation mechanism at a small, critical twin spacing. Based upon these observations, we proposed an analytical model for the magnitude of the critical twin spacing. Comparisons of the predicted critical twin spacing with both our MD results and experimental data show that the model leads to excellent quantitative agreement. This, in turn, confirms our assertion that the transition of dislocation mechanism is a source for the experimentally observed [43] transition of the strength of nanotwinned Cu with twin spacing.

Chapter 6

Grain Boundary Finite Length Faceting in FCC Metallic System

In systems where the boundary free energy is strongly anisotropic with respect to boundary inclination, the boundary may lower its free energy by faceting. Faceting is the decomposition of the boundary into sections with low energy inclinations, connected by sections of possibly higher energy boundary inclinations such that the average boundary inclination is consistent with the two macroscopic inclinations degrees of freedom. The coherent twin boundaries studied in the previous Chapters are special faceted boundarie in the sense that the boundary plane is equally shared by both crystals in twin relationship. They have a relatively simple boundary structure, extremely low boundary energy and possess excellent stability. In this Chapter, we study more general, commonly observed, faceted boundaries which also have a relatively simple structure and low boundary energy. While in previous Chapters we focused on the dislocation twin boundary interactions in the plastic deformation process of those nanotwinned metals, here we focus on the thermodynamic and equilibrium structures of these more general faceted boundaries. Our main objective is to study the factors governing the facet length scale in these boundaries.

6.1 Continuum Description of Faceted Grain Boundaries

The decomposition of a high energy grain boundary into a hill and valley shape results in that boundary adopting a faceted structure. The equilibrium of those faceted grain boundaries can be described using a model that accounts for facets and the linear junctions where they meet, as

shown in Fig. 6.1. Arrows along the facets meeting at junction 1 (j_1) represent the force on the junction associated with grain boundary tension. The Burgers vector symbols ($\perp$) show that the dislocations associated with adjacent junctions have alternating signs and are of the type $\pm\mathbf{b} = \pm(\mathbf{t}_1 - \mathbf{t}_2)$, where $\mathbf{t}_1$ and $\mathbf{t}_2$ are the characteristic translation vectors of the two facets [34]. We refer to the distance between one junction and the next of the same type along the average grain boundary inclination as the facet length Λ. The facet orientations and the angles between facets meeting at a junction are invariant with respect to change in the facet length Λ. Hence, the facet structure is completely determined by the fixed orientations of the facets and the facet length Λ in a continuum approximation.

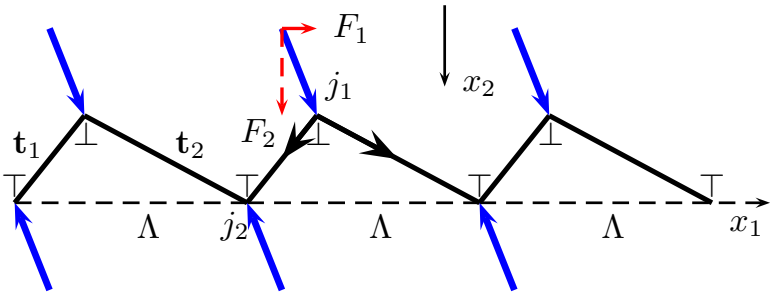

Figure 6.1: Schematic of a faceted grain boundary. Arrows along the facets represent grain boundary tension. These tensions create a force on the junction that is the vector sum of the two grain boundary tensions and can be decomposed into effective forces acting on the junctions perpendicular to the junction line and either parallel, F_1, or perpendicular, F_2, to the boundary plane. Λ is the faceting period, measured parallel to the boundary and perpendicular to the junction lines. x_1, x_2 directions are as indicated and x_3 points inside the paper. Same coordinate directions are used throughout this Chapter.

The total energy of the grain boundary shown in Fig. 6.1 is the sum of the energies of the short and long facets, junction energies, and long-range junction-junction interaction energies (i.e., described as the interactions between dislocations, between surface tension line forces, and between dislocations and line forces). The interaction energies of the junctions will change with the facet length Λ. Hence, the energy density of the faceted grain boundary can be expressed as

$$\gamma_{gb} = \gamma_{f1} + \gamma_{f2} + \frac{2\gamma_j + \gamma_d^I(\Lambda) + \gamma_f^I(\Lambda) + \gamma_{df}^I(\Lambda)}{\Lambda}, \tag{6.1}$$

where γ_{f1} and γ_{f2} are the energies (per unit area) of the two facets meeting at a junction line, γ_j is the energy (per unit length) of the junction and $\gamma_d^I(\Lambda)$ is the dislocation-dislocation

interaction energy, $\gamma_f^I(\Lambda)$ is the junction-junction line force interaction energy, and $\gamma_{df}^I(\Lambda)$ is the dislocation-junction line force interaction energy. Omitting the junction interactions, the above equation has a form of $A + B/\Lambda$, which indicates a monotonic decrease of the energy density with increasing facet size. Hamilton showed the energy density has a form of $(A_1/\Lambda)\ln\Lambda + B_1/\Lambda + C_1$ when the various interaction energy are included. Equations for A_1 and B_1 can be obtained from Ref. [49].

6.2 Molecular Dynamics Simulations

6.2.1 Molecular Dynamics Simulations Setup

To analyze grain boundary faceting, we performed a set of molecular dynamics simulations in an ensemble where the number of particles N, the stress tensor σ, and the temperature were fixed; i.e., the $N\sigma T$ ensemble (the stresses were always fixed at $\sigma = 0$). The grain boundaries were constructed by choosing the orientation of the two crystals, truncating the two crystals at the x_1x_3 plane (see Fig. 6.1), and joining the two crystals at the grain boundary. The extent of the crystals parallel to x_1 and x_2 was chosen to make the system periodic. However, this can result in large elastic energies (maximum strain of $\sim 0.5\%$ in quasi-periodic boundaries; however, in the $\Sigma 3$ case, the system is perfectly matched without strain). A plane of point defects were introduced at the left/right borders of the simulation cell (Fig. 6.2 c) to accommodate these strains (resulting in a lower energy configuration than the uniformly strained system). Throughout the simulations, no point defect diffusion towards grain boundaries was observed. All energy measurements were made far from this plane. Because the system is periodic in all three directions, each simulation cell contains two grain boundaries. Since the grain boundary structure is sensitive to the translation state, several initial translation (parallel to x_1 and x_3) states were examined. We always focus on the grain boundaries with the lowest energy translation state (following T = 0 K energy minimization). The grain boundary energy is also sensitive to the atomic arrangements at the boundary. Therefore, we also investigated the effects of removing atoms from the boundary that were under the greatest stress and retained those configurations that yielded minimum energy boundaries at T = 0 K.

In the present study, we focus on FCC aluminium, both because grain boundaries in Al have been widely studied via experiment and simulation and because grain boundary faceting has been observed in this system. An embedded-atom method (EAM) type interatomic potential [46] was used in earlier studies of faceting in Al [49]. Unfortunately, this Al potential

shows a zero-pressure melting point below 700 K, which is much smaller than the experimental value of 933 K. Therefore, we have employed both the original EAM potential [138] (EAM Potential 1) and a newer Al potential of the same type [2] that yields a melting point and liquid diffusivity in excellent agreement with experiment (EAM Potential 2). The correct diffusivity at T_m predicted by the employed potential is important here as the current study involves simulations performed over a wide range of temperatures (200 K - T_m) and phase transformations which could be diffusion-controlled processes. Facet coarsening at temperatures near materials' melting points may also be a diffusion-controlled process.

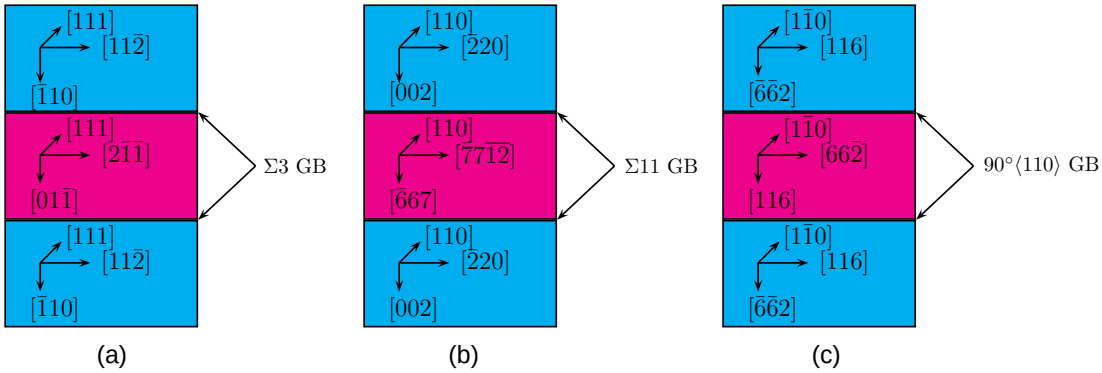

Figure 6.2: The geometries of the simulation cell used to simulate (a) Case I (i.e., a pair of $\Sigma 3\{110\}$ grain boundaries; (b) Case II (i.e., a pair of $\Sigma 11$ grain boundaries formed through the rotation of the center grain by $50.4788°$ about the $[110]$ direction) and (c) Case III (i.e., a pair of quasi-periodic boundaries formed by the rotation of the center grain by $90°$ about the $[1\bar{1}0]$ direction). The simulations cell sizes in Case I, Case II and III are $\sim 97 \times 169 \times 48\mathring{A}$(containing 50120 atoms), $499 \times 397 \times 34.2\mathring{A}$ (containing 414,252 atoms) and $646.2 \times 246 \times 40\mathring{A}$ (containing 387,236 atoms), respectively.

We focus on three different grain boundaries in this study. Case I is the symmetric $\Sigma 3\{110\}$ boundary that facets into a set of $\Sigma 3\{112\}$ twins. These twins are among the most commonly observed grain boundaries in FCC metals. The faceting behavior of this boundary has been studied both experimentally [22, 23] and via computer simulations [49, 139]. The geometry of Case II is shown in Fig. 6.2 (a). To form the two $\Sigma 11$ asymmetric tilt boundaries shown, the middle grain was rotated along the $\langle 110 \rangle$ axis by $50.4788°$. The boundary planes of this grain boundary are (002) relative to one grain (represented in green in Fig. 6.2 (a)) and $(\bar{6}67)$ with respect to the other. Case III (see Fig. 6.2 (b)) corresponds to the rotation of the middle grain about the $\langle 110 \rangle$ axis by $90°$ to form a pair of non-CSL asymmetric tilt boundaries. The

boundary planes of this grain boundary are (116) relative to one grain (represented in red in Fig. 6.2 (b)) and $(\bar{6}\bar{6}2)$ with respect to the other. This quasi-periodic boundary has been examined experimentally [30] and was shown to exhibit very small facets. These three cases were chosen to represent a wide variety of boundary types, all of which are known to facet (see Section. B.2 in Appendix. B for the calculation of Σ values for these three cases).

6.2.2 Molecular Dynamics Simulations Results

6.2.2.1 Case I: $\Sigma 3\{110\}$

Hsieh and Balluffi [23] observed twin boundaries in aluminium with an average $\{110\}$ orientation that form facets of the $\{112\}$ type with facets length on the $\sim$100 nm scale at low temperature ($\sim$0.3 T_m) which defacet upon heating to temperatures greater than 0.54 T_m. Daruka and Hamilton [139] proposed a lattice model for the faceting-defaceting phase transition of this twin boundary and demonstrated the presence of this grain boundary phase transition via Monte Carlo (MC) and MD simulations using EAM Potential 1.

In our first set of simulations, we equilibrated the system at high temperature (500 K for EAM Potential 1 and 400 K for EAM Potential 2) for 0.1 ns, cooled it at a rate of 100 K/ns for 2 ns and then heated to its original temperature at the same rate (the simulation cell dimensions are $\sim$ 97 $\times$ 169 $\times$ 48$\mathring{A}$, same as that in Ref. [139]). A faceting-defaceting phase transition was observed to occur between $\sim$425 K and $\sim$475 K using EAM Potential 1 (in agreement with Daruka and Hamilton [139]) and between $\sim$250 K and $\sim$330 K using EAM Potential 2. We quote finite temperature ranges here due to the hysteresis in the phase transition and the finite rates of cooling and heating. To ensure that the results were not overly sensitive to initial conditions, the simulations were repeated for several different initial atomic velocity distributions. In all cases, after the onset of the phase transition, the facets grow very quickly such that only two facets (one on each boundary) are observed over the entire width of the simulation cell.

Next, we repeated the simulations with a simulation cell width which was 4 times larger in the x_1 direction and 2 times larger in the x_2 direction. Figure 6.3 shows the faceting of the twin boundary in an EAM Potential 1 simulation. Figure 6.3 (a) shows the boundary at 425 K; the temperature where faceting is first observed upon cooling. Figure 6.3 (b) shows the boundary configuration upon cooling to 375 K, where faceting is nearly complete. Finally, Fig. 6.3 (c) shows the result of reheating the system to 435 K and holding for 1 ns; note that

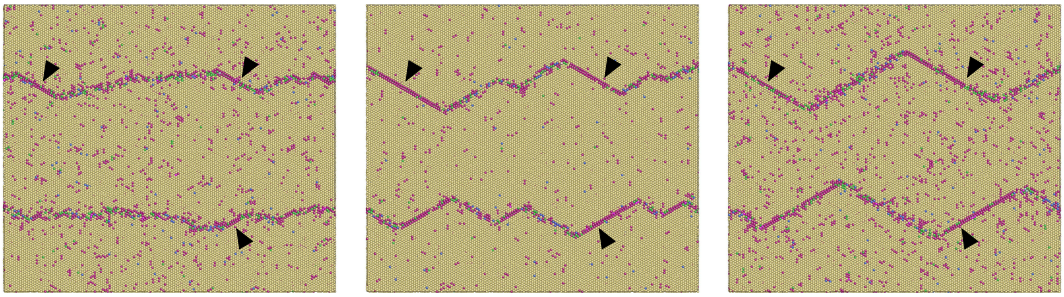

Figure 6.3: The atomic configuration of the $\Sigma 3$ $\{110\}$ grain boundary for the simulation using EAM Potential 1. The sample is equilibrated at 500 K and then cooled to 300 K at 100 K/ns. Figure (a) is the configuration of the system at 425 K and (b) at 375 K during the cooling. Figure (c) shows the configuration following reheating the sample from 300 K to 435K and holding at 435 K for 1 ns. The simulation cell size is 39.54 nm $\times 34.2$ nm $\times 4.9$ nm with $\sim$ $401,000$ atoms. The viewing plane is $\{111\}$. The facet planes are $\{112\}$ twins. The atoms are colored according to their coordination number n (the same color scheme is adopted throughout this Chapter). $n = 12$ (e.g., atoms in the perfect crystal) is shown in yellow, lower coordination numbers $n = 9, 10$, and 11 in magenta, green and red, respectively, and higher coordination numbers $n = 13$ and 14 in blue and pink. The arrows in (a) point to newly formed $\{112\}$ twin facets separated by unfaceted $\{110\}$ boundary segments. These twin facets develop from the nominally flat $\{110\}$ boundary. The arrows in (b) and (c) are in the same positions as in (a) and show how the $\{112\}$ twin facets nucleated at the lower temperature (and earlier time) have grown out to encompass the entire, originally unfaceted boundary. We note that in addition to fast growth, additional facet nucleation has occurred (between (a) and (b)).

this coarsens the facets that were shown in Fig. 6.3 (b). The atoms are colored according to their coordination number n (the same color scheme is adopted throughout this Chapter). The perfect crystal $n = 12$ is shown in yellow, lower coordination numbers $n = 9, 10$, and 11 in magenta, green and red, respectively, and higher coordination numbers $n = 13$ and 14 in blue and pink.

Figure 6.4 shows the faceting of the same boundary in a simulation performed using the EAM Potential 2. Upon cooling from 400 K, the facets were seen to first form at 250 K (see Fig. 6.4 (a)). By the time the system has cooled to 227 K (Fig. 6.4 (b)) the faceting is nearly complete. Figure 6.4 (c) shows the system upon reheating to 303 K and holding for 1 ns. Comparison of Figs. 6.4 (b) and 6.4 (c) shows that some coarsening of the facet size has occurred (see especially the boundary on the top in Fig. 6.4).

As evident in Figs. 6.3 (a) and 6.4 (a) (see the location of the arrows in these figures), the

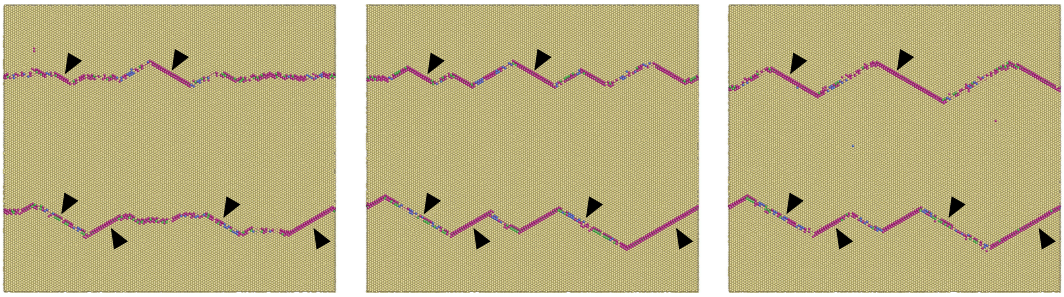

Figure 6.4: The atomic configuration of the $\Sigma 3$ $\{110\}$ grain boundary for the simulation using EAM Potential 2. The sample is equilibrated at 400 K and then cooled to 200 K at 100 K/ns. Figure (a) is the configuration of the system at 250 K and (b) at 227 K during the cooling. Figure (c) shows the configuration following reheating the sample from 200 K to 303 K and holding at 303 K for 1 ns. The arrows in (a) point to newly formed $\{112\}$ twin facets separated by unfaceted $\{110\}$ boundary segments. These twin facets develop from the nominally flat $\{110\}$ boundary. The arrows in (b) and (c) are in the same positions as in (a) and show how the $\{112\}$ twin facets nucleated at the lower temperature (and earlier time) have grown out to encompass the entire, originally unfaceted boundary. We note that in addition to fast growth, additional facet nucleation has occurred (between (a) and (b)).

$\{112\}$ facets begin to form at several, separated locations rather than forming simultaneously along the entire $\{110\}$ boundary. Examinations of the dynamics of the facet formation process show that many facets form and then disappear unless they are sufficiently large. The driving force for facet nucleation is the lower free energy of the $\{112\}$ boundaries as compared with the original $\{110\}$ boundary (we note that in the recent survey by Olmsted et al. [63, 64] employing a different EAM potential, the 0 K grain boundary energy of the $\{112\}$ boundary is higher than that of the $\{110\}$ boundary). However, formation of a pair of $\{112\}$ boundaries requires formation of a line junction where the two $\{112\}$ boundaries meet plus two line junctions where the $\{112\}$ boundaries join the remaining $\{110\}$ boundary segments. Forming these junctions costs energy and hence provides a barrier for facet nucleation. We note that during the initial stage of the phase transformation process, the nucleated $\{112\}$ twin facets are connected by unfaceted $\{110\}$ boundary segments. These facets grow and spread from those $\{112\}$ twin facets nucleated earlier. This is consistent with the faceting being a first order/nucleation and growth phase transition as described by Oswald et al. [140]. It is difficult in the simulations to make an accurate determination of the critical facet nucleus size.

When we lower the temperature from that in Figs. 6.3 (a) and 6.4 (a) to those in Figs. 6.3 (b) and 6.4 (b), we observe the completion of the faceting process and facet coarsening. However, we note that the facet coarsening does not go to completion, but rather we end up with finite size facets. Upon heating the systems to the temperatures of Figs. 6.3 (c) and 6.4 (c), we observe more facet coarsening; yet again the facets do not coarsen to the size of the simulation cell. The fact that there is some coarsening of facet length during annealing is consistent with the observations of Medlin [24] on the same boundary in Au. By the end of our simulations, the facets have become quite regular, yet are smaller than those observed in the Al experiments of Hsieh and Balluffi [23] by a factor of approximately 5 (i.e., 20 nm vs. 100 nm). This is not surprising given the fact that Hsieh and Balluffi's experiments on Al were performed on time scales which are more than a factor of 10^{12} longer than in the simulations performed here.

The simulations performed in this section show that $\Sigma 3\{112\}$ facets form below the facet-defaceting transition temperature and completely replace the original $\Sigma 3\{110\}$ boundary. The facets coarsen over time and coarsen faster at higher temperatures. If the simulation cell size is very small, such as in the simulations reported by Daruka and Hamilton [139], the facets can readily grow to the simulation cell size. However, if the simulation cell is large, such as shown in Figs. 6.3 and 6.4, there is insufficient time for the facets to grow to the simulation cell size. Nonetheless, our results demonstrate that the facet lengths grow with increasing time and grow faster at high temperature - consistent with the idea that facet coarsening is thermally activated. As the facet size increases, the driving force for facet coarsening decreases and hence the rate of facet coarsening slows over time.

6.2.2.2 Case II: $\Sigma 11\ \{002\}_1/\{667\}_2$

The well studied $\Sigma 3$ grain boundary case is special in many respects. The overall bicrystal symmetry is high. The faceting of such boundaries into symmetric $\{112\}$ twins is also special in the sense that these symmetric twins have remarkably low energy. Therefore, to understand faceting more generally, we must turn to grain boundaries which are much less special. The first such boundary we study is the $\Sigma 11$ boundary corresponding to a 58.4788° rotation about the $\langle 110\rangle$ axis and the asymmetric boundary plane orientation where the (002) plane of crystal 1 meets the $(\bar{6}67)$ of crystal 2 (i.e., $(002)_1/(\bar{6}67)_2$), as shown in Fig. 6.2 (a). For this asymmetrical boundary, we perform simulations using both potentials at low temperature, but only

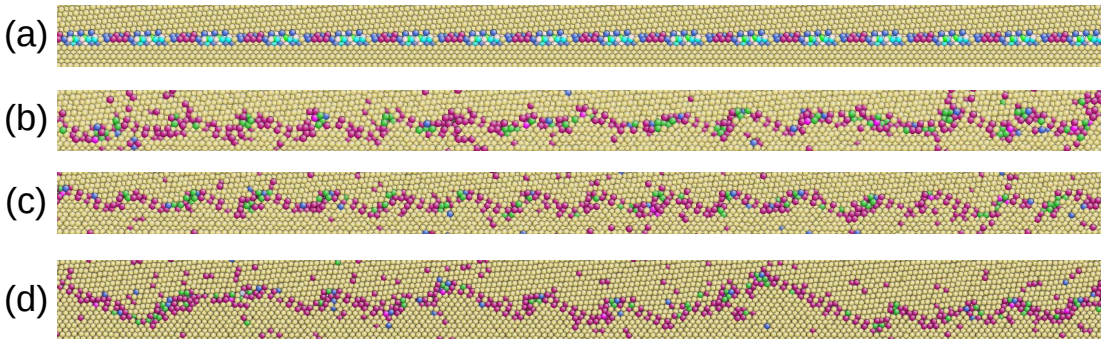

Figure 6.5: Faceting of the $\Sigma 11$ $(002)_1/(\bar{6}67)_2$ grain boundary. The as-constructed system with the grain boundary is shown in (a). The structures produced by annealing for 1 ns at T = 400 K using EAM Potential 1 and 600 K using EAM Potential 2 are shown in (b) and (c), respectively. The period of the boundary in all (a)-(c) is 3.2 nm. (d) shows the result of annealing the structure in (c) at 850 K for 1 ns and cooling back to 600 K (like in (c)). In all cases, the viewing plane is $\{110\}$ and the long and short facets are of the $\{225\}_1/\{441\}_2$ and $\{667\}_1/\{001\}_2$ types, respectively.

EAM Potential 2 at high temperatures (recall that EAM Potential 1 has an unphysically small melting point).

Figure 6.5 (a) shows the as-constructed $\Sigma 11$ $\langle 110 \rangle$ boundary with the average boundary plane $\{002\}_1/\{667\}_2$. Heating this boundary to room temperature and holding for 1 ns leave the flat boundary profile intact in simulations using EAM potential 1 and 2. However, heating this boundary to 400 K using EAM Potential 1 (see Fig. 6.5 (b)) or heating to 600 K using EAM Potential 2 (see Fig. 6.5 (c)) leads to the formation of $\{667\}_1/\{001\}_2$ and $\{225\}_1/\{441\}_2$ facets. Comparison of these annealed boundaries with the as-constructed boundary shows that the annealed structures have the same periodicity as the as-constructed boundaries. Cooling these boundaries to room temperature leaves the facet period unchanged. These results suggest that the flat boundary structure is metastable with respect to the faceted boundary.

Heating the faceted boundary from Fig. 6.5 (c) to within 10% of the melting point ($T/T_m = 850/933$) and annealing it there for 1 ns (and then cooling back to 600 K, the same temperature as Fig. 6.5 (c)) produces the faceted structure seen in Fig. 6.5 (d). The first thing to note is that unlike the $\Sigma 3$ boundary of Case I, this boundary does not undergo a facet-defaceting transition. Second, we see that annealing at this high temperature leads to a slight coarsening of the scale of the faceting.

6.2.2.3 Case III: $90^\circ\langle 110\rangle\ \{662\}_1/\{116\}_2$

Although the grain boundary in Case II is of much lower symmetry than that in Case I, both boundaries are still special in the sense that they are low Σ boundaries. The boundary examined in this section is both asymmetric and not exactly a CSL boundary. Figure 6.6 (a) shows the as-constructed asymmetric tilt boundary, which can be described as a 90° rotation about the $\langle 110\rangle$ axis and a boundary plane, relative to the two crystals, of $\{662\}_1/\{116\}_2$. Upon heating this system to 50 K, the entire boundary begins to facet within 1 ps. The structure change appears to begin simultaneously along the entire planar boundary. The fact that the boundary transforms so quickly and so uniformly at such a low temperature suggests that the as-constructed flat boundary is unstable with respect to faceting. Heating to 293 K leads to complete faceting into a series of $\{111\}_1/\{112\}_2$ and $\{001\}_1/\{110\}_2$ facets within 0.1 ns. Figures 6.6 (b) and 6.6 (c) show this boundary after holding at 293 K for 5 ns for EAM Potentials 1 and 2, respectively. Annealing the boundary from Fig. 6.6 (c) for 1 ns at 900 K and cooling back to 293 K within 1 ns produces the structure shown in Fig. 6.6 (d). First, we note that even by T = 900 K ($\sim$0.965 T_m), the boundary has not undergone a defaceting transition (as did the $\Sigma 3$ boundary of Case I). Second, we note that the period of the faceting developed near 50 K remains unchanged on heating to 900 K. This suggests that the initial facet period is remarkably stable. However, we note that since the total duration of the simulations is only several nanoseconds, it is unclear whether the structure will show some evolution on experimentally accessible time scales. Nonetheless, the length scale of this faceting is much more stable than either those observed in Cases I and II.

6.3 Grain Boundary Energetics

The results presented above show that in the high symmetry, $\Sigma 3$ system of Case I, the faceting period increases with time and temperature. Similarly, the asymmetric $\Sigma 11$ system of Case II, also shows that the facet period increases with further annealing at an elevated temperature. Therefore, we expect that faceting in both Cases are controlled by the same phenomena and that the coarsening process is thermally activated. Because of the similarity of the two cases and the fact that coarsening occurs much more readily in Case I than Case II we focus on the former. The fact that the $90^\circ\ \langle 110\rangle$ system of Case III shows facets that are remarkably resistant to facet coarsening suggests that there is an additional feature in this general grain boundary case that is missing in Cases I and II. In this section, we perform an analysis of the

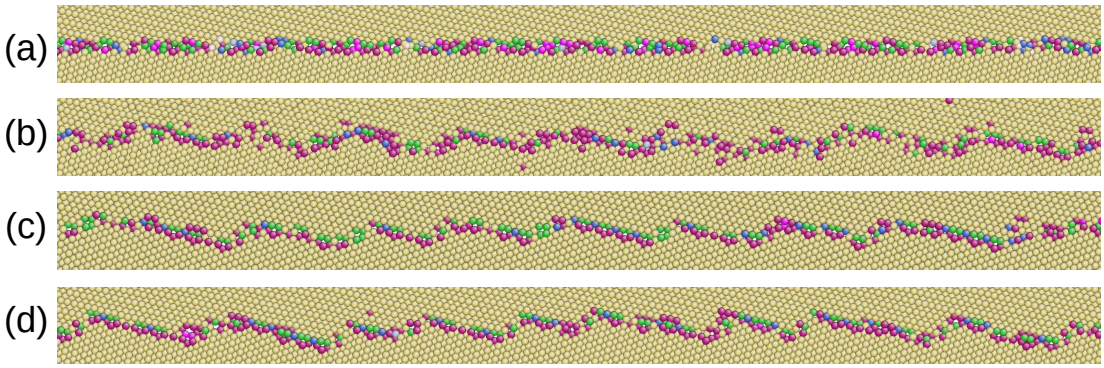

Figure 6.6: Faceting of the 90° $\langle 110 \rangle$ $(116)_1/(\bar{6}\bar{6}2)_2$ grain boundary. The as-constructed system with the grain boundary is shown in (a). The structures produced by annealing for 5 ns at T = 293 K using EAM Potential 1 and EAM Potential 2 are shown in (b) and (c), respectively. (d) shows the result of annealing the structure in (c) at 900 K for 1 ns and cooling back to 293 K (like in (c)). The period of the boundary in all (a)-(d) is 4.5 nm. In all cases, the viewing plane is $\{110\}$ and the long and short facets are of the $\{001\}_1/\{110\}_2$ and $\{111\}_1/\{112\}_2$ types, respectively.

grain boundary energy versus facet period to see if this additional feature is of thermodynamic or kinetic origin.

To examine the effect of facet period on grain boundary energy, we construct a series of faceted grain boundaries with different facet lengths. For Case I, we fixed the total length of the cell as $1190 \times 530 \times 7\mathring{A}$ in the x_1, x_2, and x_3 directions, respectively, such that the total number of atoms in the system is 265,440. The boundaries were constructed by truncating the two crystals along the facet planes observed in the MD simulations; i.e., the $\{112\}$ planes. The length of each facet is identical and chosen according to the desired period Λ (measured as the distance between two neighboring peaks in the facet landscape in the direction parallel to the mean boundary plane). These structures were relaxed by minimizing the total energy at T = 0 K using a conjugate gradient algorithm.

Figure 6.7 shows the energy versus facet period (in the unit of a_0, where a_0 is the T = 0 K FCC Al lattice parameter) for these Case I boundaries using the EAM Potential 2. The grain boundary energy density γ decreases monotonically with increasing facet period Λ. These data are fitted to the analytical expression for the faceted boundary energy suggested by Hamilton et al. [49] (i.e., $\gamma = (A_1/\Lambda)\ln\Lambda + B_1/\Lambda + C_1$). Clearly, the analytical expression provides an excellent fit to the data. This is consistent with the simulation results of Hamilton et al.

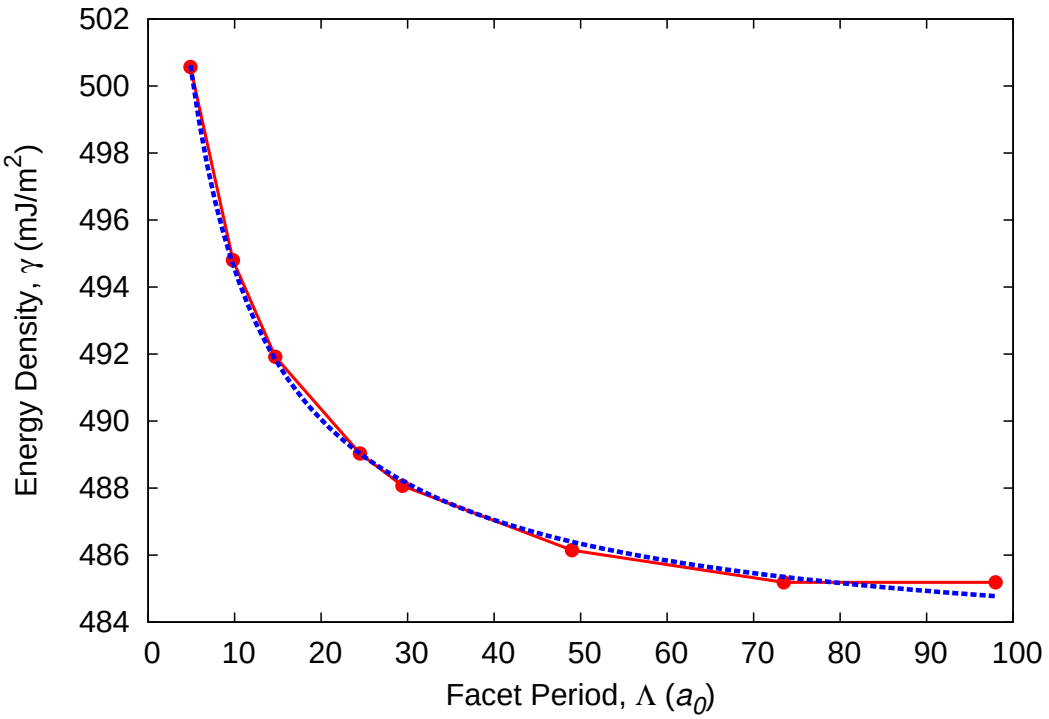

Figure 6.7: The T = 0 K $\Sigma 3\{110\}$ (Case I) grain boundary energy γ versus facet period Λ obtained by energy minimization using EAM Potential 2. The red circles represent the simulation data, the red line simply connects these data points, and the dotted blue line is the best fit to the functional form suggested by Hamilton et al. [49]: $\gamma = (A_1/\Lambda)\ln\Lambda + B_1/\Lambda + C_1$.

[49] using the EAM Potential 1. This result implies that there are no energetic barriers to grain boundary facet coarsening that are significantly longer than a few interatomic spacings in extent.

We also determine the grain boundary energy versus facet period for the grain boundaries of Case III. In this case, the simulation cell is $\sim 258 \times 83 \times 4$ nm in the x_1, x_2, and x_3 directions, respectively, such that the total number of atoms in the system is $\sim 5 \times 10^6$. Such a large simulation cell was chosen to minimize the incompatibility in the size of the two crystals (this boundary is only quasi-periodic, as discussed in Section 6.2.1). As in Case I, the faceted boundary structure was constructed by truncating the two crystals along the facet planes observed in the MD simulations; i.e., the $\{111\}_1/\{112\}_2$ and $\{001\}_1/\{110\}_2$ planes. Figure 6.8 shows the energy of the Case III faceted grain boundaries with facet periods in the $3 - 90a_0$ range. This

figure shows that while there is a trend of decreasing grain boundary energy with increasing facet period, similar to that seen for Case I, the fluctuations in γ versus Λ is extremely large in Case III. The same analytical expression for the faceted grain boundary energy versus facet period suggested by Hamilton et al. [49] and validated above for Case I (EAM Potential 2) was applied to the data in Fig. 6.8. This functional form shows a good fit to the average data. The very large fluctuations in γ versus Λ are not captured by the analytical model. The form of this curve suggests that while it is energetically favorable to increase facet period, the barriers for doing so are very large. This further suggests that the boundary may be "trapped" at the facet period that developed at the beginning of the faceting process. We return to this suggestion in Section 6.4.

6.4 Discussion

All three grain boundaries examined in this study show facet formation. However, there are pronounced differences in the facet formation, size and coarsening process amongst them. A reversible facet-defaceting phase transition is evident only in Case I, while no such reversible phase transition is observed in either Cases II or III at temperatures as high as 0.9 T_m. In Case I, the $\Sigma3\{110\}$ boundary transforms into a series of $\Sigma3\{112\}$ twin upon cooling (the exact transition temperature was not determined because of hysteresis on heating and cooling) and vice versa upon heating. On cooling at 100 K/ns, the $\Sigma3\{112\}$ twin facets form with a period of $5 \sim 10$ nm and grow to $\sim$20 nm upon annealing for 1 ns at 303 K (EAM Potential II). The faceting transformation in this case is consistent with a first order/nucleation and growth phase transition. In Case II, facets form at low temperature (from the originally constructed grain boundary) with a period of ~ 3.2 nm. Interestingly, this is the periodicity of the original, flat $\{002\}_1/\{667\}_2$ grain boundary. While some facet coarsening does occur upon annealing for 1 ns at 850 K ($\sim$ 0.9 T_m), this coarsening is very slow compared with that for Case I at a much lower temperature. In Case III, the as-constructed boundary is unstable with respect to faceting. Even with annealing for 1 ns at 900 K (~ 0.965 T_m), the ~ 4.5 nm facet period formed initially at low temperature do not show perceptible coarsening. The fact that no reversible facet-defaceting phase transition is observed in either Case II or III suggests that it is inappropriate to classify these observations of facet formation as a phase transition at all, let alone a first order/nucleation and growth or a spinodal decomposition phase transforma-

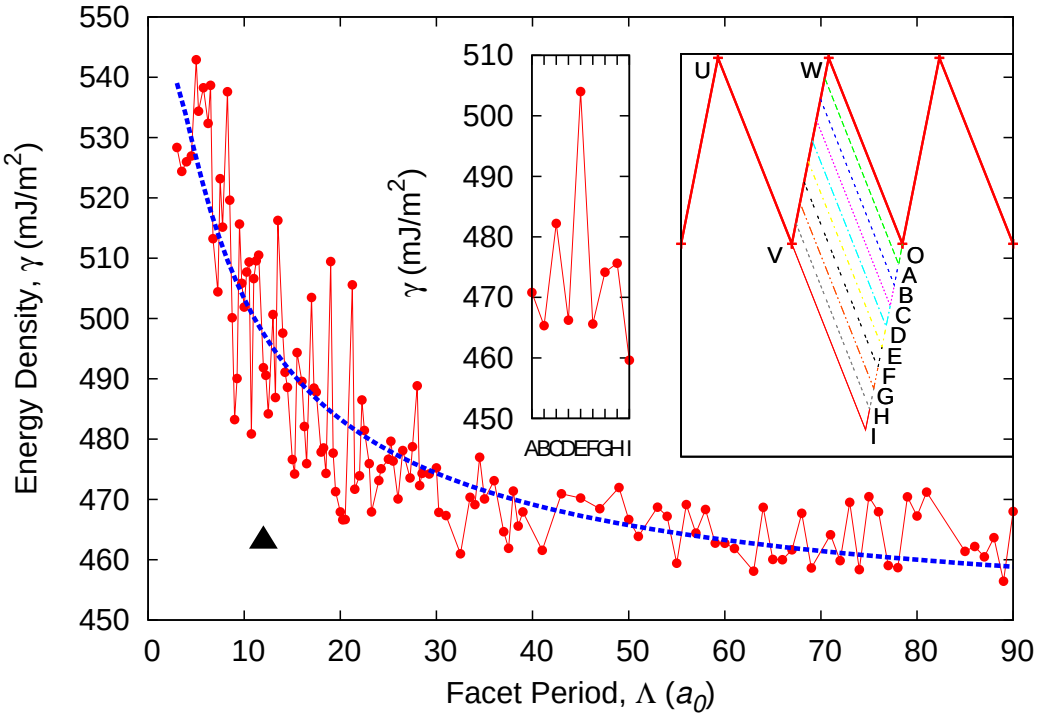

Figure 6.8: The T = 0 K $\langle 110 \rangle$ 90° (Case III) grain boundary energy γ versus facet period Λ obtained by energy minimization using EAM Potential 2. The red circles represent the simulation data, the red line simply connects these data points, and the dotted blue line is the best fit to the functional form suggested by Hamilton et al. [49]: $\gamma = (A_1/\Lambda)\ln\Lambda + B_1/\Lambda + C_1$. The large black triangle shows the energy and average period of the faceted grain boundary shown in Fig. 6.6 (c) which was then quenched to T = 0 K. The inset on the right shows the translation of a single facet and that on the left shows the grain boundary energy for each translation state of the facet shown on the right.

tion [140]. The constructed flat boundaries in these two cases are either metastable (Case II) or unstable (Case III) with respect to faceting.

To understand the differences between facet coarsening in Case I and Case III, we performed simulations to determine the grain boundary energy as a function of facet period, Λ. We saw that in both cases, the boundary energy is well described by the analytical form $\gamma = A_1/\Lambda \ln \Lambda + B_1/\Lambda + C_1$, where A_1, B_1, and C_1 were determined by fitting to the data. The nature of these agreement between this form and the data indicate that the boundary energy is well-described on the basis of facet energies, junction energies, and junction-junction interactions. In Case I, the γ vs. Λ plot (Fig. 6.7) shows a smooth, monotonic decay with increasing facet period. On the other hand, the γ vs. Λ plot for Case III (Fig. 6.8) shows a similar decaying trend with increasing facet period, but this plot also exhibits a superimposed large amplitude oscillation with facet period. The amplitude of these oscillations in grain boundary energy with facet length is as large as 40 mJ/m^2 (as compared with the boundary energy of ~ 500 mJ/m^2).

While the grain boundary energy versus facet period results suggest that it is thermodynamically favorable for the facet period to continue to increase, this is only observed for Case I, where the γ vs. Λ plot is smooth. We can understand the resistance to facet coarsening in Case III by consideration of its very rough γ vs. Λ plot. The large roughness of this plot suggests that if a boundary facet period corresponds to a local minimum in γ, a large positive energy excursion is necessary to coarsen the facet period. This barrier to facet length coarsening is much too large to overcome even upon heating to near the melting point in simulations of the duration of those performed here. (We assume that slight coarsening may be possible if these boundaries are held at the temperature for very long anneals and anneals 10^{12} longer are common in experiments but inaccessible in MD simulations).

Although facet coarsening is thermodynamically favorable, this does not mean that is kinetically accessible. To consider kinetic effects, we must first examine how coarsening occurs. Figures 6.3 (b) and 6.3 (c) show facet coarsening for EAM Potential 1 in Case I, Figs. 6.4 (b) and 6.4 (c), show facet coarsening for EAM Potential 2 in Case I, and Figs. 6.5 (b) and 6.5 (c) show coarsening for EAM Potential 2 in Case II. In all cases, we see that coarsening occurs via the migration of a facet (perpendicular to itself) until its plane meets another facet of the same type. This process is illustrated schematically in the inset on the right in Fig. 6.8, where facet WO translates through a series of planes from A to I until it reaches facet UV and forms facet UI by annihilation of facet WV and junctions V and W. The inset on the left in Fig. 6.8 shows how the energy varies as facet WO migrates toward UV. (keeping all other facet lengths fixed.

In each case, we minimize the energy with respect to atomic coordinates.) This plot shows that the energy of the system undergoes ~ 45 mJ/m^2 energy fluctuations as it migrates. This implies that the barrier to such facet migration is approximately as large as that implied by the γ versus Λ plot and is too large to overcome during our simulations. We have repeated these facet translation simulations for the $\Sigma 3$ boundary of Case I and find that the energy variation with facet translation is no larger than 1 mJ/m^2. Therefore, while it is thermodynamically favorable to coarsen the facet period in both Cases I and III, it is only possible, kinetically, for Case I.

The results presented above show that there is a tremendous variation in the barriers to facet migration between the Case I $\Sigma 3$ twin and the asymmetric, non-CSL boundary of Case III. This difference is consistent with the observation of much larger facets in Case I than that in Case III in our own simulations. While these large differences in barriers explain the simulation results on facet coarsening, they do not address the question as to why these large differences in barrier heights exist from boundary-to-boundary. We can get a hint of the structural origin of the variation of the boundary energy with facet period by considering the atomic structure of the boundary in Case III. Figure 6.9 shows the atomic structure of the boundary in Case III, (a) as-constructed with facets, (b) the same boundary after energy minimization and (c) the boundary structure observed when the boundary naturally facets starting from the flat boundary. Examination of Fig. 6.9 (a) shows that some of the long facets ($\{001\}_1/\{110\}_2$) have readily observable excess volume (i.e., low density), while others have the atoms on the two sides of the facet plane very close together. This facet-to-facet variation is a natural result of the fact that the top and bottom crystals are incommensurate (i.e., it is not possible to construct a periodic boundary, with equal facet sizes, where all of the facets are identical). The relaxation of the facet structure (Fig. 6.9 (b)) involves the straining of the two crystals to close the open space between the lattice planes on both sides of the facet. This necessarily induces significant elastic strain in the grains near the facets. As the facet translates from location A to I in the inset to Fig. 6.8, the atomic matching between the two planes vary and thus the elastic strain energy varies accordingly. This suggests that the barriers to facet coarsening are associated with mismatch of the atomic structure across the boundary (i.e., the excess volume of the grain boundary) and the variation of the elastic energy with facet displacement. Such terms are not included in the energetic analysis of Ref. [49]. (We note that the atomic structures of the facets seen in Fig. 6.9 (b) are very similar to those observed in the case in which faceting naturally occurs, Fig. 6.9 (c).)

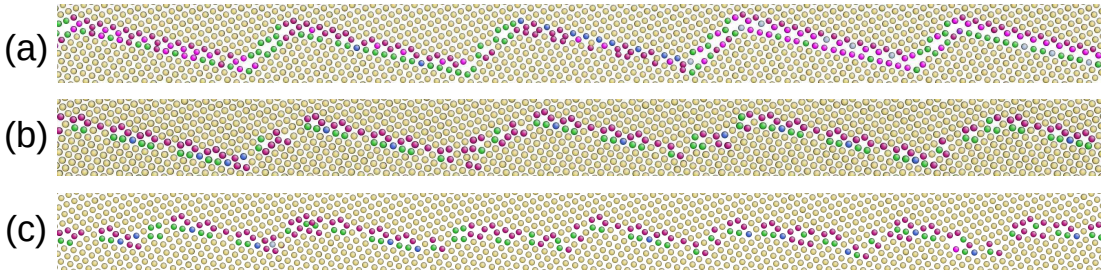

Figure 6.9: The $\langle 110 \rangle$ 90° faceted grain boundary structure (a) as-constructed, (b) following energy minimization with respect to the atomic structure of the boundary in (a), and (c) in the grain boundary where faceting naturally occurs starting from the flat boundary, as shown in Fig. 6.6 (c).

In Case I, where the facets are symmetric twins, the atomic planes on both sides of the facet are equivalent and facets migrate by transforming one plane of atoms from one side to the other side of the boundary with no change in boundary density. Our MD simulations show that such migration occurs by forming a step on the twin near a junction, followed by step migration. In Case III, where the facets are $\{001\}_1/\{110\}_2$ and $\{111\}_1/\{112\}_2$, the facet energy varies substantially from one location to the next as it translates. When faceting initially occurs in our MD simulations starting from a flat boundary, the system naturally selects a distribution of facet locations where the atomic matching is very good. Translation of the facets away from this "natural" facet structure requires significant energy and hence is unlikely. This is the structural and energetic origins of the resistance to facet coarsening.

A good indicator of the degree of mismatch between the two sides of a facet is the ratio of the atomic plane spacings parallel to the facet in the two crystals of the facet, G; i.e., the $\{001\}$ and $\{110\}$ interplanar spacing for Case III. If the facets are formed by $\{hkl\}_1/\{opq\}_2$ planes, the ratio of the atomic plane spacing is

$$G = \left(\frac{h^2 + k^2 + l^2}{o^2 + p^2 + q^2} \right)^{1/2}. \tag{6.2}$$

Commensurate boundaries have rational values of G. When G is rational, there are a finite number of facet plane translation steps necessary for the boundary structure and energy to repeat. If G is unity, then every facet translation state has the same energy and there are no (or small) barriers to facet translation. When G is irrational, the energy versus translation plot can vary widely, without repeating. For the three cases examined here,

Case I. $\Sigma 3\{112\}$ - the boundary facets are commensurate (twins) - both facets have G = 1 - coarsening readily occurs,

Case II. $\{225\}_1/\{441\}_2$ and $\{667\}_1/\{001\}_2$ - the boundary facets are commensurate - the first facet has G=1 and the second G = 11 - coarsening occurs but much more slowly than in Case I,

Case III. $\{001\}_1/\{110\}_2$ and $\{111\}_1/\{112\}_2$ - the boundary is incommensurate - the facets have $G = 1/\sqrt{2}$ - no coarsening is observed.

These results are consistent with the analysis above. The present coarsening, energetic and structural arguments are internally consistent, however, this does not mean that they are observed in experiment. Fortunately, each of the boundaries examined by MD here, were also observed experimentally. $\Sigma 3\{112\}$ facets in Case I were observed to have facet length of $\sim$ 100 nm in experiments in Al [23]. Facets formed by $\{225\}_1/\{441\}_2$ and $\{667\}_1/\{001\}_2$ boundaries in Case II were observed to have facet lengths of $\sim$ 50 nm in Al after high temperature ($\sim$ 0.96 T_m) annealing [23]. The facet length of $\sim$ 4.5 nm found here in Case III corresponds well with the experimentally observed facet length scale of the same boundary in Al [30]. In addition, experimental data from recrystallized stainless steel and copper collected in [141, 142] showed that all of the large facets (0.28 μm $\sim$ 2.34 μm) observed in the sample correspond to commensurate grain boundaries (this data set consists of 186 facets with $\Sigma = 9, 27, 81, 243$). We plot the mean facet length Λ' vs. G for $G = 1, 3, 9$ in Fig. 6.10. The plot indicates that facet planes with smaller values of G have larger mean length. Combining the above facts and the three cases studies in the current work, we suggest that coarsening of facets with smaller values of G is easier compared with that of facets with large and/or irrational values of G. The ease with which facets coarsen often dictates the observed facet size, since the observed facet lengths are controlled by their coarsening kinetics.

It is important to recognize that the above discussion of facet length scales Λ and boundary interplanar spacing ratio G is different from the general observation of grain boundary population distribution. In general, faceted boundaries have low energies and hence low mobilities. These boundaries can potentially cause grain growth stagnation [143]. High angle grain boundaries meeting the criterion by Herring [47] tend to decompose into low energy, stable facets, suggesting these low energy facets will have a higher populations than those boundaries with higher energies, high mobilities/less stabilities. This is consistent with the broad observation that grain boundary populations are inversely correlated with boundary energies [144, 145].

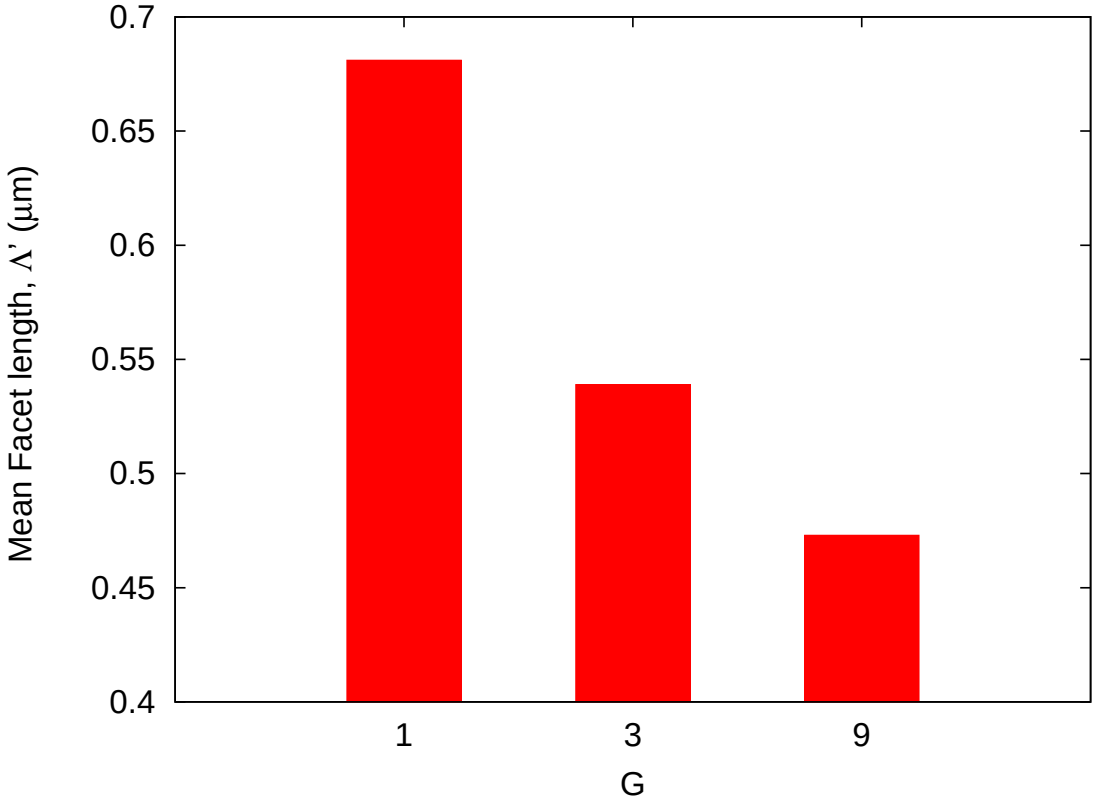

Figure 6.10: Mean facet length Λ' vs. the ratio of the atomic plane spacings parallel to the facet G. The data consists of 186 facets of recrystallized stainless steel and copper with $G = 1, 3, 9$ from [141, 142].

However, the quantitative relation between these low enegy, nanometer scale facets and grain boundary population has yet to be established.

6.5 Summary

In this Chapter, we examined three aluminium grain boundaries that exhibit finite size faceting using molecular dynamics simulations employing two different EAM potentials. All three boundaries showed faceting in the simulations using both potentials. In Case I, the $\Sigma3\{110\}$ boundary showed a reversible facet-defaceting phase transition, while no such reversible phase transition was observed in either Case II $\Sigma11\{002\}_1/\{667\}_2$ or Case III non-CSL $90°\langle110\rangle$ $\{116\}_1/\{662\}_2$. We observed that the initial sizes of $\Sigma3\{112\}$ twin facets in Case I were determined by the relative positions of the facet nucleation sites and the facet coarsening processes in Cases I and II require thermal activation. In Case II, the facets formed by $\{225\}_1/\{441\}_2$ and $\{667\}_1/\{001\}_2$ boundaries showed some, but at a slower rate when compared to that of $\Sigma3\{112\}$ twin facets in Case I. Facets formed by the $\{111\}_1/\{112\}_2$ and $\{001\}_1/\{110\}_2$ boundaries in Case III were found to be stable under thermal annealing and no coarsening was observed during the simulation. We also examined the dependence of the grain boundary energy density change on facet period for Cases I and III. In both cases, the boundary energy density was well described by the same analytical form $\gamma = A_1/\Lambda \ln \Lambda + B_1/\Lambda + C_1$. In Case I, the $\Sigma3\{112\}$ faceted boundary energy density showed a smooth monotonic decay with increasing facet period. However, in Case III, facets formed by $\{111\}_1/\{112\}_2$ and $\{001\}_1/\{110\}_2$ boundary exhibited a similar trend with increasing facet length, albeit with very large amplitude oscillations. The non-smoothness in the faceted boundary energy density in Case III may be attributed to the atomic mismatch between the two planes forming the facets, which necessarily induces additional elastic strain energy near the facets. These elastic strain energy increments, associated with mismatch of the atomic structure across the boundary, create barriers to facet coarsening. Unlike in the energy analysis that successfully described Case I, we find facet coarsening is also controlled by the boundary plane matching instead of facet junctions alone. The results of the current study suggest that grain boundary tension is too small to stabilize the finite length faceting in both $\Sigma3\{112\}$ twin and asymmetrical $\{111\}_1/\{112\}_2$ and $\{001\}_1/\{110\}_2$ facets. The observed finite facet sizes are dictated by facet coarsening kinetics which can be strongly retarded by deep local energy minima associated with atomic matching across the boundary.

Chapter 7

Conclusions and Future Work

7.1 Conclusions

In this Thesis we studied two categories of problems relating to faceted grain boundaries which are frequently observed in metals and their alloys. Growth nanotwins are very special, faceted grain boundaries and materials with a high density of growth nanotwins exhibit a combination of attractive properties including simultaneous ultrahigh strength, ductility, conductivity and strain hardening. Understanding on the underlying atomistic mechanisms contributing to these extraordinary properties is important not only as scientific curiosities, but in engineering applications as well. Through very large scale "bi-crystal" and polycrystal molecular dynamics simulations involving more than 60 million atoms, a few improtant dislocation twin interaction mechanisms that lead to copious dislocation generation and the production of sessile dislocation debris during plastic deformation were revealed. The interaction of a 60° dislocation with a twin boundary generates a $\{001\}\langle 110\rangle$ Lomer dislocation in the twin-related grain and a Shockley partial dislocation on the twin boundary during twin-mediated slip transfer. The Lomer dislocation line segment subsequently dissociates into Shockley, stair-rod and Frank partial dislocations. The interaction of a 30° partial dislocation with a twin boundary generates three additional Shockley partial dislocations during twin-mediated slip transfer. While the generation of Shockley partial dislocations activates additional slip systems and hence contributes to the ductility of the material during plastic deformation, the sessile stair-rod and Frank partial dislocations, together with the high-density twin boundaries, provide barriers to dislocation motion and hence strengthen the material. These findings highlight the importance of interplay between the carriers of and barriers to plastic deformation in achieving simultaneous

ultrahigh strength and ductility.

We also studied the deformation of nanotwinned Cu for a wide range of twin spacings and found a dislocation mechanism transition at a small twin spacing. While at large twin spacing, cross-slip and dissociation of the Lomer dislocations create dislocation locks which restrict and block dislocation motion and thus enhance strength. At twin spacing below a critical size, cross-slip does not occur, steps on the twin boundaries form and deformation is much more planar. These twin steps can further migrate and serve as dislocation nucleation sites, thus softening the material. Based on these mechanistic observations, a simple, analytical model for the critical twin spacing was proposed and the predicted critical twin spacing was shown to be in excellent agreement both with respect to the atomistic simulations and experimental observation. We thus suggested the above dislocation mechanism transition is a cause of the observed transition in nanotwinned Cu strength.

For the problem on grain boundary finite length faceting, we studied a set of generally faceted boundaries and revealed the factors determining the facet length scales. We demonstrated facet formation, coarsening, reversible phase transition of $\Sigma 3\{110\}$ boundary into $\Sigma 3\{112\}$ boundary and vice versa in molecular dynamics simulations. These results are consistent with earlier experimental studies and theoretical models. The $\Sigma 11\{002\}_1/\{667\}_2$ boundary shows faceting into $\{225\}_1/\{441\}_2$ and $\{667\}_1/\{001\}_2$ boundaries and coarsens with a slower rate when compared to $\Sigma 3\{112\}$ facets. However, facets formed by $\{111\}_1/\{112\}_2$ and $\{001\}_1/\{110\}_2$ boundaries from a $\{116\}_1/\{662\}_2$ boundary are stable against finite temperature annealing. In the above faceted boundary, elastic strain energy induced by atomic mismatch across the boundary creates barriers to facet coarsening. Grain boundary tension is too small to stabilize the finite length faceting in both $\Sigma 3\{112\}$ twin and asymmetrical $\{111\}_1/\{112\}_2$ and $\{001\}_1/\{110\}_2$ facets. The observed finite facet sizes are dictated by facet coarsening kinetics which can be strongly retarded by the deep local energy minima associated with atomic matching across the boundary.

7.2 Future Work

There has been considerable research effort in engineering nanotwinned metallic materials. Apart from Cu, other metals like Ag, Au, Ni and their alloys are good candidates in the sense that these materials have relatively low stacking fault energy. The potential of the nanotwinned microstructure in FCC materials may also be realized in materials with other lattice structures

such as BCC and HCP. There are also several questions that remain unsolved for these nanotwinned materials. Currently two mechanisms are proposed to rationalize the experimentally observed strength transition at a critical twin spacing of 15 nm in nanotwinned polycrystalline Cu. Twin migration induced softening provides a possible mechanism. However, this has only been demonstrated via MD simulations in cases where the twin spacing is below a few nanometers. In addition, it does not provide clear sources for those dislocations blocked at twin boundaries as seen in TEM observations. The mechanism by dislocations passing through twin boundaries, generating unusual dislocations, activating several slip systems and creating twin steps is another likely source to induce strength transition. This mechanism is based on the mechanistic observation of full dislocations passing through twin boundaries and cross-slipping onto $\{001\}$ planes in twin crystals. These two mechanisms may also coexist and cooperate during the plastic deformation of nanotwinned materials. Furthermore, nanotwinned materials' high strain hardening behavior is missing in current MD simulations. The difficulty to reveal those experimental observations might be attributed to the small grain sizes and high strain rates used in current simulations including those presented here. Hence it is worthwhile to focus on addressing these issues in future work.

Lastly, we wish to emphasize that computer simulations provide valuable insights into the understanding of physical problems and allow us to peek into processes nature does. Nevertheless, simulations have their own limitations such as the time scale in MD simulations. In simulations where the central problem is plastic deformation, the time scale difference with experiments can be as large as 10^{12}, which necessarily creates artefacts from the high stress/high rate/short time conditions in nearly all such simulations. We end with the cautionary note that results obtained from these simulations have to be interpreted with care and verified by experiments.

Appendix A

Geometric Operations

A.1 Rotation About an Axis

The rotational operation can be described by several different ways mathematically. The choice of representation is merely a result of convienence and efficiency in applications. For example, a rotation can be represented in an axis-angle pair $(\boldsymbol{n} - \theta)$

$$f(\boldsymbol{x}) = \boldsymbol{x}\cos\theta + \boldsymbol{n}(\boldsymbol{n}\cdot\boldsymbol{x})(1-\cos\theta) + \sin\theta(\boldsymbol{n}\times\boldsymbol{x}) \tag{A.1}$$

where $\boldsymbol{n}$ is the axis about which the rotation takes place and θ is the angle of rotation. Rotation can also be expressed in the form of an orthogonal tensor

$$f(\boldsymbol{x}) = \boldsymbol{R}\cdot\boldsymbol{x} \tag{A.2}$$

where

$$R_{ij} = \cos\theta\delta_{ij} + n_i n_j(1-\cos\theta) - \epsilon_{ijk}n_k\sin\theta \tag{A.3}$$

or

$$\boldsymbol{R} = \begin{bmatrix} \cos\theta + n_1^2(1-\cos\theta) & n_1 n_2(1-\cos\theta) - n_3\sin\theta & n_1 n_3(1-\cos\theta) + n_2\sin\theta \\ n_1 n_2(1-\cos\theta) + n_3\sin\theta & \cos\theta + n_2^2(1-\cos\theta) & n_2 n_3(1-\cos\theta) - n_1\sin\theta \\ n_1 n_3(1-\cos\theta) - n_2\sin\theta & n_2 n_3(1-\cos\theta) + n_1\sin\theta & \cos\theta + n_3^2(1-\cos\theta) \end{bmatrix} \tag{A.4}$$

When $\theta = \pi$, Eqn. A.1 simplifies to

$$f(\boldsymbol{x}) = -\boldsymbol{x} + 2\boldsymbol{n}(\boldsymbol{n}\cdot\boldsymbol{x}) \tag{A.5}$$

and

$$\boldsymbol{R} = \begin{bmatrix} -1+2n_1^2 & 2n_1 n_2 & 2n_1 n_3 \\ 2n_1 n_2 & -1+2n_2^2 & 2n_2 n_3 \\ 2n_1 n_3 & 2n_2 n_3 & -1+2n_3^2 \end{bmatrix} \tag{A.6}$$

A.2 Rotational Tensor between Two Arbitrarily Oriented Bases

Two arbitrarily oriented bases can be brought into coincidence through a combination of rotational and translational operation. The rotational operation can be expressed as a tensor in various forms as discussed in the previous section. In studies of polycrystalline materials, it is often desirable to find the corresponding rotational tensor given the orientations of two crystals or two bases. In the following, we derive the rotational tensor using Fig. A.1, where two arbitrarily oriented bases, $\{\boldsymbol{s}_i\}$ and $\{\boldsymbol{o}_i\}$, are shown. The following conditions are given

$$\boldsymbol{e}_i = A_i^j \boldsymbol{s}_j = B_i^l \boldsymbol{o}_l \tag{A.7}$$

and there exists a rotational tensor $\boldsymbol{R}$ (plus a translational) which brings $\{\boldsymbol{s}_i\}$ and $\{\boldsymbol{o}_i\}$ into coincidence, i.e.,

$$\boldsymbol{s}_i = R_i^k \boldsymbol{o}_k \tag{A.8}$$

Substituting the above equation into Eqn. A.7 gives

$$A_i^j R_j^k \boldsymbol{o}_k = B_i^l \boldsymbol{o}_l \tag{A.9}$$

Hence

$$R_j^k = (\boldsymbol{A}^{-1})_l^k B_j^l \tag{A.10}$$

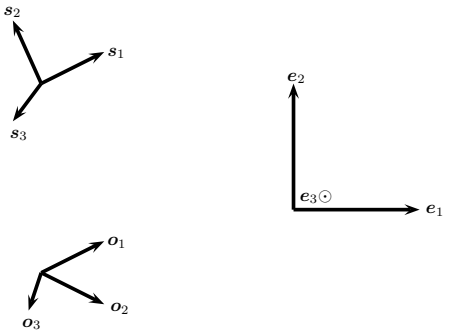

Figure A.1: Rotational tensor between two arbitrarily oriented bases.

A.3 Reflection about a Plane

A reflection is a mirror operation that transforms any vector $\boldsymbol{x}$ into its mirror image across some plane defined by a unit normal $\boldsymbol{n}$.

$$f(\boldsymbol{x}) = \boldsymbol{x} - 2\boldsymbol{n}\,(\boldsymbol{n} \cdot \boldsymbol{x}) \tag{A.11}$$

Comparison of the above equation with that of a rotation of π about some axis (Eqn. A.5) shows reflection about a plane is equivalent to a rotation of π about the normal of that plane plus an inversion operation.

Appendix B

Crystallography

B.1 Crystallographical Equivalence of FCC Twinned Crystals

The crystallographic equivalence of the matrix and twin lattice as shown in Fig. 2.11 can be worked out by a rotational tensor corresponding to a rotation of π about axis $\boldsymbol{\delta C} = [n_1 n_2 n_3] = 1/\sqrt{6}[11\bar{2}]$. Employing Eqn. A.6 the following is obtained

$$\boldsymbol{R} = \begin{bmatrix} -1+2n_1^2 & 2n_1n_2 & 2n_1n_3 \\ 2n_1n_2 & -1+2n_2^2 & 2n_2n_3 \\ 2n_1n_3 & 2n_2n_3 & -1+2n_3^2 \end{bmatrix} = 1/3 \begin{bmatrix} -2 & 1 & -2 \\ 1 & -2 & -2 \\ -2 & -2 & 1 \end{bmatrix} \tag{B.1}$$

Hence the equivalence between the matrix and twin lattice can be found as shown in Table. B.1.

B.2 Coincidence Site Lattice (CSL)

Two lattices interpenetrating in space and sharing a common origin contain a sublattice which is common to both lattices. The sublattice is called the Coincidence Site Lattices (CSL). The fraction of lattice points which are also the coincidence sites is a rational fraction $1/\Sigma$. Σ is always an odd integer and is often used to indicate the local atomic fit of an interface when that interface is a rational plane or close to a rational plane in the CSL. Σ can be found by the transformation tensor relating the two forming lattice. If $\boldsymbol{R}$ is such a tensor and an integer h

In Matrix			In Twin			Equivalent In Matrix
plane $\boldsymbol{a}$	$\boldsymbol{A\alpha}$	$1/3[\bar{1}1\bar{1}]$	$\boldsymbol{a}^T$	$\boldsymbol{A}^T\boldsymbol{\alpha}^T$	$1/3[\bar{1}1\bar{1}]^T$	$1/9[5\bar{1}\bar{1}]$
	$\boldsymbol{BC}$	$1/2[10\bar{1}]$		$\boldsymbol{B}^T\boldsymbol{C}^T$	$1/2[10\bar{1}]^T$	$1/2[01\bar{1}]$
	$\boldsymbol{BD}$	$1/2[0\bar{1}\bar{1}]$		$\boldsymbol{B}^T\boldsymbol{D}^T$	$1/2[0\bar{1}\bar{1}]^T$	$1/6[141]$
	$\boldsymbol{CD}$	$1/2[\bar{1}\bar{1}0]$		$\boldsymbol{C}^T\boldsymbol{D}^T$	$1/2[\bar{1}\bar{1}0]^T$	$1/6[114]$
plane $\boldsymbol{b}$	$\boldsymbol{B\beta}$	$1/3[1\bar{1}\bar{1}]$	$\boldsymbol{b}^T$	$\boldsymbol{B}^T\boldsymbol{\beta}^T$	$1/3[1\bar{1}\bar{1}]^T$	$1/9[\bar{1}5\bar{1}]$
	$\boldsymbol{AC}$	$1/2[01\bar{1}]$		$\boldsymbol{A}^T\boldsymbol{C}^T$	$1/2[01\bar{1}]^T$	$1/2[10\bar{1}]$
	$\boldsymbol{AD}$	$1/2[\bar{1}0\bar{1}]$		$\boldsymbol{A}^T\boldsymbol{D}^T$	$1/2[\bar{1}0\bar{1}]^T$	$1/6[411]$
	$\boldsymbol{CD}$	$1/2[\bar{1}\bar{1}0]$		$\boldsymbol{C}^T\boldsymbol{D}^T$	$1/2[\bar{1}\bar{1}0]^T$	$1/6[114]$
plane $\boldsymbol{c}$	$\boldsymbol{C\gamma}$	$1/3[\bar{1}\bar{1}1]$	$\boldsymbol{c}^T$	$\boldsymbol{C}^T\boldsymbol{\gamma}^T$	$1/3[\bar{1}\bar{1}1]^T$	$1/9[\bar{1}\bar{1}5]$
	$\boldsymbol{AB}$	$1/2[\bar{1}10]$		$\boldsymbol{A}^T\boldsymbol{B}^T$	$1/2[\bar{1}10]^T$	$1/2[1\bar{1}0]$
	$\boldsymbol{AD}$	$1/2[\bar{1}0\bar{1}]$		$\boldsymbol{A}^T\boldsymbol{D}^T$	$1/2[\bar{1}0\bar{1}]^T$	$1/6[411]$
	$\boldsymbol{BD}$	$1/2[0\bar{1}\bar{1}]$		$\boldsymbol{B}^T\boldsymbol{D}^T$	$1/2[0\bar{1}\bar{1}]^T$	$1/6[141]$
plane $\boldsymbol{d}$	$\boldsymbol{D\delta}$	$1/3[111]$	$\boldsymbol{d}^T$	$\boldsymbol{D}^T\boldsymbol{\delta}^T$	$1/3[111]^T$	$1/3[\bar{1}\bar{1}\bar{1}]$
	$\boldsymbol{AB}$	$1/2[\bar{1}10]$		$\boldsymbol{A}^T\boldsymbol{B}^T$	$1/2[\bar{1}10]^T$	$1/2[1\bar{1}0]$
	$\boldsymbol{AC}$	$1/2[01\bar{1}]$		$\boldsymbol{A}^T\boldsymbol{C}^T$	$1/2[01\bar{1}]^T$	$1/2[10\bar{1}]$
	$\boldsymbol{BC}$	$1/2[10\bar{1}]$		$\boldsymbol{B}^T\boldsymbol{C}^T$	$1/2[10\bar{1}]^T$	$1/2[01\bar{1}]$

Table B.1: Equivalence between the matrix and twin in FCC lattice.

can be found such that all the elements of $\boldsymbol{R}$ are integers without a common factor, h is the Σ value relating the two lattice [146]. Hence the tensor in the above Eqn. B.1 results in a $\Sigma = 3$ CSL.

For the grain boundary faceting cases shown in Fig. 6.2 in Chapter. 6, the respective Σ value can be calculated by forming the rotational tensor through Eqn. A.10.

Case I

$$\boldsymbol{A} = \begin{bmatrix} 1/\sqrt{6} & 1/\sqrt{6} & -2/\sqrt{6} \\ -1/\sqrt{2} & 1/\sqrt{2} & 0 \\ 1/\sqrt{3} & 1/\sqrt{3} & 1/\sqrt{3} \end{bmatrix} \tag{B.2}$$

$$\boldsymbol{A}^{-1} = \begin{bmatrix} 1/\sqrt{6} & -1/\sqrt{2} & 1/\sqrt{3} \\ 1/\sqrt{6} & 1/\sqrt{2} & 1/\sqrt{3} \\ -2/\sqrt{6} & 0 & 1/\sqrt{3} \end{bmatrix} \tag{B.3}$$

$$\boldsymbol{B} = \begin{bmatrix} 2/\sqrt{6} & -1/\sqrt{6} & -1/\sqrt{6} \\ 0 & 1/\sqrt{2} & -1/\sqrt{2} \\ 1/\sqrt{3} & 1/\sqrt{3} & 1/\sqrt{3} \end{bmatrix} \tag{B.4}$$

hence

$$\boldsymbol{R} = \boldsymbol{A}^{-1} \cdot \boldsymbol{B} = 1/3 \begin{bmatrix} 2 & -1 & 2 \\ 2 & 2 & -1 \\ -1 & 2 & 2 \end{bmatrix} \tag{B.5}$$

Hence $\Sigma = 3$.

Case II

$$\boldsymbol{A} = \begin{bmatrix} -1/\sqrt{2} & 1/\sqrt{2} & 0 \\ 0 & 0 & 1 \\ 1/\sqrt{2} & 1/\sqrt{2} & 0 \end{bmatrix} \tag{B.6}$$

$$\boldsymbol{A}^{-1} = \begin{bmatrix} -1/\sqrt{2} & 0 & 1/\sqrt{2} \\ 1/\sqrt{2} & 0 & 1/\sqrt{2} \\ 0 & 1 & 0 \end{bmatrix} \tag{B.7}$$

$$\boldsymbol{B} = \begin{bmatrix} -7/\sqrt{242} & 7/\sqrt{242} & -12/\sqrt{242} \\ -6/11 & 6/11 & 7/11 \\ 1/\sqrt{2} & 1/\sqrt{2} & 0 \end{bmatrix} \tag{B.8}$$

hence

$$\boldsymbol{R} = \boldsymbol{A}^{-1} \cdot \boldsymbol{B} = 1/11 \begin{bmatrix} 9 & 2 & 6 \\ 2 & 9 & -6 \\ -6 & 6 & 7 \end{bmatrix} \tag{B.9}$$

Hence $\Sigma = 11$.

Case III

$$\boldsymbol{A} = \begin{bmatrix} 1/\sqrt{38} & 1/\sqrt{38} & 6/\sqrt{38} \\ -6/\sqrt{76} & -6/\sqrt{76} & 2/\sqrt{76} \\ 1/\sqrt{2} & -1/\sqrt{2} & 0 \end{bmatrix} \tag{B.10}$$

$$\boldsymbol{A}^{-1} = \begin{bmatrix} 1/\sqrt{38} & -6/\sqrt{76} & 1/\sqrt{2} \\ 1/\sqrt{38} & -6/\sqrt{76} & -1/\sqrt{2} \\ 6/\sqrt{38} & 2/\sqrt{76} & 0 \end{bmatrix} \tag{B.11}$$

$$\boldsymbol{B} = \begin{bmatrix} 6/\sqrt{76} & 6/\sqrt{76} & -2/\sqrt{76} \\ 1/\sqrt{38} & 1/\sqrt{38} & 6/\sqrt{38} \\ 1/\sqrt{2} & -1/\sqrt{2} & 0 \end{bmatrix} \tag{B.12}$$

hence

$$\boldsymbol{R} = \boldsymbol{A}^{-1} \cdot \boldsymbol{B} = \begin{bmatrix} 3\sqrt{2}/38 & -9/19 & -1/\sqrt{38} \\ 1/38 & -3\sqrt{2}/38 & -3/\sqrt{38} \\ 3\sqrt{2}/\sqrt{38} & -1/\sqrt{38} & 0 \end{bmatrix} \tag{B.13}$$

Hence the two crystals do not form a CSL.

Appendix C

Linear Elasticity

C.1 Generalized Hooke's Law

The generalized Hooke's law for continuum medium can be expressed as following

$$\boldsymbol{\sigma} = \mathbf{C} : \boldsymbol{\epsilon} \tag{C.1}$$

where $\boldsymbol{\sigma}$ and $\boldsymbol{\epsilon}$ are the stress and strain tensor, respectively (we assume infinitesimal linear elasticity throughout the Thesis). $\mathbf{C}$ in the above equation is a tensor characterizing materials' stiffness, i.e., materials' linear deformation in response to applied load. It is a fourth order tensor and has 81 components in three dimensional spaces (among the 81, only 21 are independent for general anisotropic materials). The stiffness tensor obeys the general rules of basis transformation as following

$$\mathbf{C} = \mathbf{Q} :: \hat{\mathbf{C}} \tag{C.2}$$

where

$$Q_{ijkl}^{pqrs} = \frac{\partial \hat{x}^p}{\partial x_i} \frac{\partial \hat{x}^q}{\partial x_j} \frac{\partial \hat{x}^r}{\partial x_k} \frac{\partial \hat{x}^s}{\partial x_l} \tag{C.3}$$

Eqn. C.1 written in indicial notation is as following

$$\sigma_{ij} = C_{ijkl} \epsilon_{kl} \tag{C.4}$$

For isotropic medium, the above equation reduces to

$$\sigma_{ij} = 2\mu\epsilon_{ij} + \lambda\delta_{ij}\epsilon_{kk} \tag{C.5}$$

where μ is the shear modulus and λ is the Lame constant and $\lambda = \dfrac{2\mu\nu}{1-2\nu}$, ν is the poisson's ratio. The static equilibrium equation can be expressed as a function of the strain and stiffness tensor as following

$$\sigma_{ij,j} = C_{ijkl}\epsilon_{kl,j} = F_i \tag{C.6}$$

Under the assumption of infinitesimal strain, the above equation can be written in terms of the displacement vector

$$\sigma_{ij,j} = C_{ijkl}\epsilon_{kl,j} = C_{ijkl}\frac{1}{2}\left(u_{k,lj} + u_{l,kj}\right) = C_{ijkl}u_{k,lj} = F_i \tag{C.7}$$

The generalized Hooke's law can also be expressed in terms of the compliance tensor

$$\boldsymbol{\epsilon} = \mathbf{S} : \boldsymbol{\sigma} \tag{C.8}$$

or in indicial notation

$$\epsilon_{ij} = S_{ijkl}\sigma_{kl} \tag{C.9}$$

C.2 Contracted Notation

The contracted notation allows us to write the strain and stress tensor in vector forms and the stiffness and compliance tensor in matrix forms with the following transformation:

$$\sigma_\alpha = \sigma_{ij} \tag{C.10}$$

$$\epsilon_\alpha = \begin{cases} \epsilon_{ij} & \text{if } i = j \\ \epsilon_{ij} + \epsilon_{ji} & \text{if } i \neq j \end{cases} \tag{C.11}$$

$$C_{\alpha\beta} = C_{ijkl} \tag{C.12}$$

where

$$\alpha(\text{ or } \beta) = \begin{cases} i & \text{if } i = j \text{ (or if } k = l) \\ 9 - i - j & \text{if } i \neq j \text{ (or if } k \neq l) \end{cases} \tag{C.13}$$

The generalized Hooke's law written in the contracted notation is

$$\sigma_\alpha = C_{\alpha\beta}\epsilon_\beta \tag{C.14}$$

or in explicit form as following

$$\begin{bmatrix} \sigma_1 \\ \sigma_2 \\ \sigma_3 \\ \sigma_4 \\ \sigma_5 \\ \sigma_6 \end{bmatrix} = \begin{bmatrix} \sigma_{11} \\ \sigma_{22} \\ \sigma_{33} \\ \sigma_{23} \\ \sigma_{31} \\ \sigma_{12} \end{bmatrix} \tag{C.15}$$

$$\begin{bmatrix} \epsilon_1 \\ \epsilon_2 \\ \epsilon_3 \\ \epsilon_4 \\ \epsilon_5 \\ \epsilon_6 \end{bmatrix} = \begin{bmatrix} \epsilon_{11} \\ \epsilon_{22} \\ \epsilon_{33} \\ \epsilon_{23} + \epsilon_{32} \\ \epsilon_{31} + \epsilon_{13} \\ \epsilon_{12} + \epsilon_{21} \end{bmatrix} = \begin{bmatrix} \epsilon_{11} \\ \epsilon_{22} \\ \epsilon_{33} \\ 2\epsilon_{23} \\ 2\epsilon_{31} \\ 2\epsilon_{12} \end{bmatrix} \tag{C.16}$$

$$\boldsymbol{C} = \begin{bmatrix} C_{11} & C_{12} & C_{13} & C_{14} & C_{15} & C_{16} \\ & C_{22} & C_{23} & C_{24} & C_{25} & C_{26} \\ & & C_{33} & C_{34} & C_{35} & C_{36} \\ & & & C_{44} & C_{45} & C_{46} \\ & & & & C_{55} & C_{56} \\ & & & & & C_{66} \end{bmatrix} = \begin{bmatrix} C_{1111} & C_{1122} & C_{1133} & C_{1123} & C_{1113} & C_{1112} \\ & C_{2222} & C_{2233} & C_{2223} & C_{2213} & C_{2212} \\ & & C_{3333} & C_{3323} & C_{3313} & C_{3312} \\ & & & C_{2323} & C_{2313} & C_{2312} \\ & & & & C_{1313} & C_{1312} \\ & & & & & C_{1212} \end{bmatrix} \tag{C.17}$$

The generalized Hooke's law expressed in the compliance matrix is as following

$$\epsilon_\alpha = S_{\alpha\beta}\sigma_\beta \tag{C.18}$$

where

$$S_{\alpha\beta} = \begin{cases} S_{ijkl} & \text{if both } \alpha, \beta \leq 3 \\ 2S_{ijkl} & \text{if either } \alpha, \beta \leq 3 \\ 4S_{ijkl} & \text{if both } \alpha, \beta > 3 \end{cases} \tag{C.19}$$

or write in explicit form

$$\boldsymbol{S} = \begin{bmatrix} S_{11} & S_{12} & S_{13} & S_{14} & S_{15} & S_{16} \\ & S_{22} & S_{23} & S_{24} & S_{25} & S_{26} \\ & & S_{33} & S_{34} & S_{35} & S_{36} \\ & & & S_{44} & S_{45} & S_{46} \\ & & & & S_{55} & S_{56} \\ & & & & & S_{66} \end{bmatrix} = \begin{bmatrix} S_{1111} & S_{1122} & S_{1133} & 2S_{1123} & 2S_{1113} & 2S_{1112} \\ & S_{2222} & S_{2233} & 2S_{2223} & 2S_{2213} & 2S_{2212} \\ & & S_{3333} & 2S_{3323} & 2S_{3313} & 2S_{3312} \\ & & & 4S_{2323} & 4S_{2313} & 4S_{2312} \\ & & & & 4S_{1313} & 4S_{1312} \\ & & & & & 4S_{1212} \end{bmatrix} \tag{C.20}$$

Appendix D

Anti-plane Deformation

D.1 Anti-plane Strain in Cubic Materials

The anti-plane and in-plane deformation can be decoupled if the materials' stiffness tensor satisfies Eqn. 2.75. One such example is a screw dislocation in FCC lattice with the coordinate system chosen as that of one of the grains in Fig. 2.12. The stiffness tensor has the following form

$$\boldsymbol{C} = \begin{bmatrix} C_{11} & C_{12} & C_{13} & 0 & 0 & C_{16} \\ & C_{22} & C_{23} & 0 & 0 & 0 \\ & & C_{33} & 0 & 0 & C_{36} \\ & & & C_{44} & C_{45} & 0 \\ & & & & C_{55} & 0 \\ & & & & & C_{66} \end{bmatrix} \tag{D.1}$$

The displacement field $\boldsymbol{u}$ corresponds to such an anti-plane shear deformation can be expressed as

$$u_1 = 0,\ u_2 = 0,\ u_3 = u(x_1, x_2) \tag{D.2}$$

Hence the strain tensor has the following form

$$\epsilon_{ij} = \begin{bmatrix} \epsilon_{11} \\ \epsilon_{22} \\ \epsilon_{33} \\ 2\epsilon_{23} \\ 2\epsilon_{13} \\ 2\epsilon_{12} \end{bmatrix} = \begin{bmatrix} 0 \\ 0 \\ 0 \\ \dfrac{\partial u(x_1, x_2)}{\partial x_2} \\ \dfrac{\partial u(x_1, x_2)}{\partial x_1} \\ 0 \end{bmatrix} \tag{D.3}$$

and the stress tensor is

$$\sigma_{ij} = \begin{bmatrix} \sigma_{11} \\ \sigma_{22} \\ \sigma_{33} \\ \sigma_{23} \\ \sigma_{13} \\ \sigma_{12} \end{bmatrix} = \begin{bmatrix} 0 \\ 0 \\ 0 \\ 2C_{44}\epsilon_{23} + 2C_{45}\epsilon_{13} \\ 2C_{45}\epsilon_{23} + 2C_{55}\epsilon_{13} \\ 0 \end{bmatrix} = \begin{bmatrix} 0 \\ 0 \\ 0 \\ C_{44}\dfrac{\partial u(x_1, x_2)}{\partial x_2} + C_{45}\dfrac{\partial u(x_1, x_2)}{\partial x_1} \\ C_{45}\dfrac{\partial u(x_1, x_2)}{\partial x_2} + C_{55}\dfrac{\partial u(x_1, x_2)}{\partial x_1} \\ 0 \end{bmatrix} \tag{D.4}$$

In the absence of body force, the equilibrium equation written in Eqn. C.6 has the expanded form as

$$\begin{aligned} \sigma_{11,1} + \sigma_{12,2} + \sigma_{13,3} = 0 \\ \sigma_{21,1} + \sigma_{22,2} + \sigma_{23,3} = 0 \\ \sigma_{31,1} + \sigma_{32,2} + \sigma_{33,3} = 0 \end{aligned} \tag{D.5}$$

Substitute the stress into the above equation we have

$$C_{55}\frac{\partial^2 u(x_1, x_2)}{\partial x_1^2} + 2C_{45}\frac{\partial^2 u(x_1, x_2)}{\partial x_1 \partial x_2} + C_{44}\frac{\partial^2 u(x_1, x_2)}{\partial x_2^2} = 0 \tag{D.6}$$

In the following we seek the displacement of a screw dislocation in infinite domain as illustrated in Fig. D.1. The boundary condition due to a screw dislocation with Burgers vector

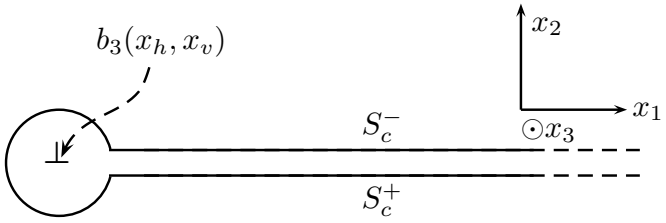

Figure D.1: Anti-plane shear deformation in cubic materials.

b_3 at (x_h, x_v) is prescribed as following

$$u(x_1, x_v^-) - u(x_1, x_v^+) = b_3 H(x_1 - x_h) \tag{D.7}$$

We apply a coordinate transformation technique [147, 148] to convert Eqn. D.6 into a Laplace's equation in a transformed domain. The transformation has the following form

$$\begin{bmatrix} X_1 \\ X_2 \end{bmatrix} = \begin{bmatrix} 1 & \kappa \\ 0 & \chi \end{bmatrix} \begin{bmatrix} x_1 \\ x_2 \end{bmatrix} \tag{D.8}$$

where

$$\begin{bmatrix} \kappa \\ \chi \end{bmatrix} = \frac{1}{C_{44}} \begin{bmatrix} -C_{45} \\ \sqrt{C_{44}C_{55} - C_{45}^2} \end{bmatrix} \tag{D.9}$$

Hence in the transformed domain Eqn. D.6 has the form

$$\frac{\partial^2 u(X_1, X_2)}{\partial X_1^2} + \frac{\partial^2 u(X_1, X_2)}{\partial X_2^2} = 0 \tag{D.10}$$

and the boundary condition D.7 due to the screw dislocation is written as

$$u(X_1, X_V^-) - u(X_1, X_V^+) = b_3 H(X_1 - X_H) \tag{D.11}$$

where

$$\begin{aligned} X_H &= x_h + \kappa x_v \\ X_V &= \chi x_v \end{aligned} \tag{D.12}$$

The solution to the Laplace equation in Eqn. D.10 becomes trivial in the transformed domain. It has the same form as that of the isotropic case as following

$$u(X_1, X_2) = \frac{b_3}{2\pi} \tan^{-1} \frac{X_2 - X_V}{X_1 - X_H} \tag{D.13}$$

and in the original anisotropic domain

$$\begin{aligned} u(x_1, x_2) &= \frac{b_3}{2\pi} \tan^{-1} \left(\frac{\frac{\sqrt{C_{44}C_{55} - C_{45}^2}}{C_{44}} (x_2 - x_v)}{x_1 - x_h - \frac{C_{45}}{C_{44}}(x_2 - x_v)} \right) \\ &= \frac{b_3}{2\pi} \tan^{-1} \left(\frac{\sqrt{C_{44}C_{55} - C_{45}^2}(x_2 - x_v)}{C_{44}(x_1 - x_h) - C_{45}(x_2 - x_v)} \right) \\ &= \frac{b_3}{2\pi} \tan^{-1} \left(\frac{\chi(x_2 - x_v)}{x_1 - x_h + \kappa(x_2 - x_v)} \right) \end{aligned} \tag{D.14}$$

The strain field can be obtained by direct differentiation of the displacement field as following

$$\begin{aligned} \epsilon_{23} &= \frac{\partial u}{\partial x_2} \\ &= \frac{b_3}{2\pi} \frac{1}{1 + \left(\frac{\chi(x_2 - x_v)}{x_1 - x_h + \kappa(x_2 - x_v)} \right)^2} \frac{\partial}{\partial x_2} \left(\frac{\chi(x_2 - x_v)}{x_1 - x_h + \kappa(x_2 - x_v)} \right) \\ &= \frac{b_3}{2\pi} \frac{1}{1 + \left(\frac{\chi(x_2 - x_v)}{x_1 - x_h + \kappa(x_2 - x_v)} \right)^2} \frac{\chi\left(x_1 - x_h + \kappa(x_2 - x_v)\right) - \kappa\chi(x_2 - x_v)}{\left(x_1 - x_h + \kappa(x_2 - x_v)\right)^2} \\ &= \frac{b_3}{2\pi} \frac{\chi(x_1 - x_h)}{\left(x_1 - x_h + \kappa(x_2 - x_v)\right)^2 + \chi^2 \left(x_2 - x_v\right)^2} \end{aligned} \tag{D.15}$$

$$\begin{aligned}
\epsilon_{13} &= \frac{\partial u}{\partial x_1} \\
&= \frac{b_3}{2\pi} \frac{1}{1+\left(\dfrac{\chi(x_2-x_v)}{x_1-x_h+\kappa(x_2-x_v)}\right)^2} \frac{\partial}{\partial x_1}\left(\frac{\chi(x_2-x_v)}{x_1-x_h+\kappa(x_2-x_v)}\right) \\
&= \frac{b_3}{2\pi} \frac{1}{1+\left(\dfrac{\chi(x_2-x_v)}{x_1-x_h+\kappa(x_2-x_v)}\right)^2} \frac{-\chi(x_2-x_v)}{\left(x_1-x_h+\kappa(x_2-x_v)\right)^2} \\
&= \frac{b_3}{2\pi} \frac{-\chi(x_2-x_v)}{\left(x_1-x_h+\kappa(x_2-x_v)\right)^2+\chi^2\left(x_2-x_v\right)^2}
\end{aligned} \tag{D.16}$$

and the stress field by Hook's law

$$\begin{aligned}
\sigma_{23} &= C_{44}\frac{\partial u}{\partial x_2} + C_{45}\frac{\partial u}{\partial x_1} \\
&= \frac{b_3}{2\pi} \frac{C_{44}\chi(x_1-x_h) - C_{45}\chi(x_2-x_v)}{\left(x_1-x_h+\kappa(x_2-x_v)\right)^2+\chi^2\left(x_2-x_v\right)^2}
\end{aligned} \tag{D.17}$$

$$\begin{aligned}
\sigma_{13} &= C_{45}\frac{\partial u}{\partial x_2} + C_{55}\frac{\partial u}{\partial x_1} \\
&= \frac{b_3}{2\pi} \frac{C_{45}\chi(x_1-x_h) - C_{55}\chi(x_2-x_v)}{\left(x_1-x_h+\kappa(x_2-x_v)\right)^2+\chi^2\left(x_2-x_v\right)^2}
\end{aligned} \tag{D.18}$$

The elastic strain energy can be found as following

$$\begin{aligned}
E^{\infty} &= \frac{1}{2}\int_V \sigma_{ij}u_{i,j}dV \\
&= \frac{1}{2}\int_V \left(\sigma_{31}u_{3,1} + \sigma_{32}u_{3,2}\right)dV
\end{aligned} \tag{D.19}$$

Without loss of generality we set the origin at (x_h, x_v) and the total elastic strain energy can be found as

$$E^{\infty} = \frac{b_3^2}{8\pi^2}\int_V \left(\frac{\chi^2\left(C_{44}x_1^2 - 2C_{45}x_1x_2 + C_{55}x_2^2\right)}{\left(\left(x_1+\kappa x_2\right)^2+\chi^2x_2^2\right)^2}\right)dV \tag{D.20}$$

D.2 Anti-plane Strain in Bi-layer Semi-infinite Cubic Materials

In the following we solve the anti-plane shear deformation in semi-infinite bi-layer twin structure for cubic materials as illustrated in Fig. D.2. The coordinate origin is set at the twin interface.

Ma et al. [149, 150] solved the above elastic problem in multilayered medium through a coordinate transform method. Their solution can be applied directly in the case of nanotwinned materials. We follow their derivation closely in the following. In addition, the nanotwinned structure has the following feature

$$\begin{aligned} C_{44}^{j} &= C_{44} \\ C_{55}^{j} &= C_{55} \\ C_{45}^{j} &= (-1)^{j} C_{45} \end{aligned} \tag{D.21}$$

where

$$\begin{aligned} j = 1 \text{ for the upper semi-infinite domain} \\ j = 2 \text{ for the lower semi-infinite domain} \end{aligned} \tag{D.22}$$

Hence Eqn. D.6 can be written as below

$$C_{55}\frac{\partial^2 u^{(j)}(x_1,x_2)}{\partial x_1^2} + (-1)^j 2C_{45}\frac{\partial^2 u^{(j)}(x_1,x_2)}{\partial x_1 \partial x_2} + C_{44}\frac{\partial^2 u^{(j)}(x_1,x_2)}{\partial x_2^2} = 0 \tag{D.23}$$

We apply a coordinate transformation technique [147, 148] to convert Eqn. D.23 into a Laplace's equation in a transformed domain. The transformation has the following form

$$\begin{bmatrix} X_1 \\ X_2 \end{bmatrix} = \begin{bmatrix} 1 & (-1)^j\kappa \\ 0 & \chi \end{bmatrix} \begin{bmatrix} x_1 \\ x_2 \end{bmatrix} \tag{D.24}$$

where

$$\begin{bmatrix} \kappa \\ \chi \end{bmatrix} = \frac{1}{C_{44}} \begin{bmatrix} C_{45} \\ \sqrt{C_{44}C_{55} - C_{45}^2} \end{bmatrix} \tag{D.25}$$

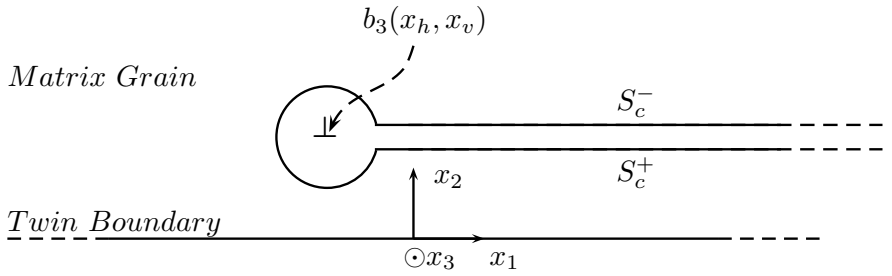

Figure D.2: Schematics of the bi-layer semi-infinite twin structure.

The equilibrium equations Eqn. C.6 in the transformed coordinate are

$$\mu\left(\frac{\partial^2 u^{(j)}(X_1,X_2)}{\partial X_1^2}+\frac{\partial^2 u^{(j)}(X_1,X_2)}{\partial X_2^2}\right)=0 \tag{D.26}$$

where

$$\mu=\sqrt{C_{44}C_{55}-C_{45}^2} \tag{D.27}$$

The linear transformation in Eqn. D.24 changes the original bi-layer twinned anisotropic problem to an isotropic homogenous problem. The solution of the latter becomes trivial. The continuity requirements of the displacement and traction at the nanotwin interfaces in the transformed domain, although satisfied implicitly, have the following form

$$\begin{aligned} u^{(1)}(X_1,X_2)&=u^{(2)}(X_1,X_2)\\ \sigma_{23}^{(1)}(X_1,X_2)&=\sigma_{23}^{(2)}(X_1,X_2)\end{aligned} \tag{D.28}$$

The boundary condition due to the screw dislocation in the transformed domain can be prescribed as below

$$u^{(m)}(X_1,X_V^-)-u^{(m)}(X_1,X_V^+)=b_3H(X_1-X_H) \tag{D.29}$$

where

$$\begin{aligned} X_H &= x_h + (-1)^m \kappa x_v \\ X_V &= \chi x_v \end{aligned} \tag{D.30}$$

$$\begin{aligned} &m = 1 \text{ if the dislocation is in the upper semi-infinite domain} \\ &m = 2 \text{ if the dislocation is in the lower semi-infinite domain} \end{aligned} \tag{D.31}$$

The Laplace equation in Eqn. D.26 with boundary condition prescribed above has the following solution

$$u(X_1, X_2) = \frac{b_3}{2\pi} \tan^{-1} \frac{X_2 - X_V}{X_1 - X_H} \tag{D.32}$$

and in the original nanotwinned anisotropic domain

$$u^{(j)}(x_1, x_2) = \frac{b_3}{2\pi} \tan^{-1} \frac{\chi(x_2 - x_v)}{x_1 - x_h + \kappa((-1)^j x_2 - (-1)^m x_v)} \tag{D.33}$$

It is straight forward to find the corresponding strain and stress field once the displacement field has been obtained by employing the definition of strain and Hooke's law. The shearing strain are found by direct differentiation of the displacement field as below.

$$\begin{aligned} \epsilon_{23}^j &= \frac{\partial u^{(j)}}{\partial x_2} \\ &= \frac{b_3}{2\pi} \frac{1}{1 + \left(\dfrac{\chi x_2 - \chi x_v}{x_1 - x_h + \kappa\left((-1)^j x_2 - (-1)^m x_v\right)} \right)^2} \frac{\partial}{\partial x_2} \frac{\chi x_2 - \chi x_v}{x_1 - x_h + \kappa\left((-1)^j x_2 - (-1)^m x_v\right)} \\ &= \frac{b_3}{2\pi} \frac{1}{1 + \left(\dfrac{\chi x_2 - \chi x_v}{x_1 - x_h + \kappa\left((-1)^j x_2 - (-1)^m x_v\right)} \right)^2} \\ &\quad \times \left(\frac{\chi\left(x_1 - x_h + \kappa\left((-1)^j x_2 - (-1)^m x_v\right)\right) - (-1)^j \kappa\left(\chi x_2 - \chi x_v\right)}{\left(x_1 - x_h + \kappa\left((-1)^j x_2 - (-1)^m x_v\right)\right)^2} \right) \\ &= \frac{b_3}{2\pi} \frac{\chi\left(x_1 - x_h + x_v \kappa\left((-1)^j - (-1)^m\right)\right)}{\left(x_1 - x_h + \kappa\left((-1)^j x_2 - (-1)^m x_v\right)\right)^2 + \left(\chi x_2 - \chi x_v\right)^2} \end{aligned} \tag{D.34}$$

$$\begin{aligned}
\epsilon_{13}^{j} &= \frac{\partial u^{(j)}}{\partial x_1} \\
&= \frac{b_3}{2\pi} \frac{1}{1+\left(\dfrac{\chi x_2 - \chi x_v}{x_1 - x_h + \kappa\left((-1)^j x_2 - (-1)^m x_v\right)}\right)^2} \frac{\partial}{\partial x_1} \frac{\chi x_2 - \chi x_v}{x_1 - x_h + \kappa\left((-1)^j x_2 - (-1)^m x_v\right)} \\
&= \frac{b_3}{2\pi} \frac{1}{1+\left(\dfrac{\chi x_2 - \chi x_v}{x_1 - x_h + \kappa\left((-1)^j x_2 - (-1)^m x_v\right)}\right)^2} \left(\frac{-\left(\chi x_2 - \chi x_v\right)}{\left(x_1 - x_h + \kappa\left((-1)^j x_2 - (-1)^m x_v\right)\right)^2}\right) \\
&= \frac{b_3}{2\pi} \frac{-\chi\left(x_2 - x_v\right)}{\left(x_1 - x_h + \kappa\left((-1)^j x_2 - (-1)^m x_v\right)\right)^2 + \left(\chi x_2 - \chi x_v\right)^2}
\end{aligned} \tag{D.35}$$

and the stress as following

$$\begin{aligned}
\sigma_{23}^{j} &= C_{44}\frac{\partial u^{(j)}}{\partial x_2} + (-1)^j C_{45}\frac{\partial u^{(j)}}{\partial x_1} \\
&= \frac{b_3}{2\pi} \frac{\chi\left(C_{44}\left(x_1 - x_h + x_v\kappa\left((-1)^j - (-1)^m\right)\right) - (-1)^j C_{45}\left(x_2 - x_v\right)\right)}{\left(x_1 - x_h + \kappa\left((-1)^j x_2 - (-1)^m x_v\right)\right)^2 + \left(\chi x_2 - \chi x_v\right)^2}
\end{aligned} \tag{D.36}$$

$$\begin{aligned}
\sigma_{13}^{j} &= (-1)^j C_{45}\frac{\partial u^{(j)}}{\partial x_2} + C_{55}\frac{\partial u^{(j)}}{\partial x_1} \\
&= \frac{b_3}{2\pi} \frac{\chi\left((-1)^j C_{45}\left(x_1 - x_h + x_v\kappa\left((-1)^j - (-1)^m\right)\right) - C_{55}\left(x_2 - x_v\right)\right)}{\left(x_1 - x_h + \kappa\left((-1)^j x_2 - (-1)^m x_v\right)\right)^2 + \left(\chi x_2 - \chi x_v\right)^2}
\end{aligned} \tag{D.37}$$

When the screw dislocation is at the interface, the above field strain and stress field simplifies to

$$\epsilon_{23}^{j} = \frac{b_3}{2\pi} \frac{\chi x_1}{\left(x_1 + \kappa\left((-1)^j x_2\right)\right)^2 + \left(\chi x_2\right)^2} \tag{D.38}$$

$$\epsilon_{13}^{j} = \frac{b_3}{2\pi} \frac{-\chi x_2}{\left(x_1 + \kappa\left((-1)^j x_2\right)\right)^2 + \left(\chi x_2\right)^2} \tag{D.39}$$

and the stress as following

$$\sigma_{23}^{j} = \frac{b_3}{2\pi} \frac{\chi\left(C_{44}x_1 - (-1)^j C_{45}x_2\right)}{\left(x_1 + \kappa\left((-1)^j x_2\right)\right)^2 + \left(\chi x_2\right)^2} \tag{D.40}$$

$$\sigma_{13}^{j} = \frac{b_3}{2\pi} \frac{\chi \left((-1)^j C_{45} \left(x_1 \right) - C_{55} \left(x_2 \right) \right)}{\left(x_1 + \kappa \left((-1)^j x_2 \right) \right)^2 + \left(\chi x_2 \right)^2} \tag{D.41}$$

The elastic strain energy can be found as following

$$\begin{aligned} E^{\infty} &= \frac{1}{2} \int_V \sigma_{ij} u_{i,j} dV \\ &= \frac{1}{2} \int_{V_1} \left(\sigma_{31} u_{3,1} + \sigma_{32} u_{3,2} \right) dV + \frac{1}{2} \int_{V_2} \left(\sigma_{31} u_{3,1} + \sigma_{32} u_{3,2} \right) dV \end{aligned} \tag{D.42}$$

where V_1 and V_2 are the volumes in the upper and lower parts, respectively. The total elastic strain energy can be found as

$$E^{\infty} = \frac{b_3^2}{8\pi^2} \int_V \left(\frac{\chi^2 \left(C_{44} x_1^2 - 2 C_{45} x_1 x_2 + C_{55} x_2^2 \right)}{\left(\left(x_1 + \kappa x_2 \right)^2 + \chi^2 x_2^2 \right)^2} \right) dV \tag{D.43}$$

which is the same as that of a screw dislocation in an infinite domain.

Bibliography

[1] Y. Mishin, M. J. Mehl, D. A. Papaconstantopoulos, A. F. Voter, and J. D. Kress. Structural stability and lattice defects in copper: Ab initio, tight-binding, and embedded-atom calculations. *Physical Review B*, 63(22):224106, 2001. xii, 49, 50, 52

[2] M. I. Mendelev, M. J. Kramer, C. A. Becker, and M. Asta. Analysis of semi-empirical interatomic potentials appropriate for simulation of crystalline and liquid Al and Cu. *Philosophical Magazine*, 88(12):1723–1750, 2008. xii, 50, 112

[3] G. E. Moore. Cramming more components onto integrated circuits. *Electronics*, 38(8), April 1965. 1

[4] W.T. Read. *Dislocations in Crystals*. McGraw-Hill, New York, January 1953. 1

[5] X. Z. Liao, F. Zhou, E. J. Lavernia, S. G. Srinivasan, M. I. Baskes, D. W. He, and Y. T. Zhu. Deformation mechanism in nanocrystalline Al: Partial dislocation slip. *Applied Physics Letters*, 83(4):632–634, 2003. 2, 31

[6] X. Z. Liao, F. Zhou, E. J. Lavernia, D. W. He, and Y. T. Zhu. Deformation twins in nanocrystalline Al. *Applied Physics Letters*, 83(24):5062–5064, 2003.

[7] M. Chen, E. Ma, K. J. Hemker, H. Sheng, Y. Wang, and X. Cheng. Deformation twinning in nanocrystalline aluminum. *Science*, 300(5623):1275–1277, 2003.

[8] X. Wu, E. Ma, and Y. T. Zhu. Deformation defects in nanocrystalline nickel. *Journal of Materials Science*, 42(5):1427–1432, March 2007. 31

[9] M. Niewczas. Chapter 75. Dislocations and twinning in face centred cubic crystals. volume 13, pages 263–364. Elsevier, 2007. 31

[10] M. Dao, L. Lu, Y. F. Shen, and S. Suresh. Strength, strain-rate sensitivity and ductility of copper with nanoscale twins. *Acta Materialia*, 54(20):5421–5432, 2006. 4, 31, 57, 58, 59, 61, 83

[11] M. D. Merz and S. D. Dahlgren. Tensile strength and work hardening of ultrafine-grained high-purity copper. *Journal of Applied Physics*, 46(8):3235–3237, August 1975. 3, 4, 56, 57, 58, 82

[12] L. Lu, Y. F. Shen, X. H. Chen, L. H. Qian, and K. Lu. Ultrahigh strength and high electrical conductivity in copper. *Science*, 304(5669):422–426, April 2004. 2, 3, 4, 56, 57, 58, 59, 63, 105

[13] E. Ma, Y. M. Wang, Q. H. Lu, M. L. Sui, L. Lu, and K. Lu. Strain hardening and large tensile elongation in ultrahigh-strength nano-twinned copper. *Applied Physics Letters*, 85(21):4932–4934, 2004. 2, 58

[14] O. Anderoglu, A. Misra, H. Wang, F. Ronning, M. F. Hundley, and X. Zhang. Epitaxial nanotwinned Cu films with high strength and high conductivity. *Applied Physics Letters*, 93(8):083108, 2008. 4, 56, 58

[15] A. A. Karimpoor, U. Erb, K. T. Aust, and G. Palumbo. High strength nanocrystalline cobalt with high tensile ductility. *Scripta Materialia*, 49(7):651–656, October 2003. 4

[16] X. Zhang, A. Misra, H. Wang, M. Nastasi, J. D. Embury, T. E. Mitchell, R. G. Hoagland, and J. P. Hirth. Nanoscale-twinning-induced strengthening in austenitic stainless steel thin films. *Applied Physics Letters*, 84(7):1096–1098, February 2004.

[17] L. L. Shaw, J. Villegas, J. Y. Huang, and S. Chen. Strengthening via deformation twinning in a nickel alloy. *Materials Science and Engineering: A-Structural Materials, Properties, Microstructure and Processing*, 480(1-2):75–83, May 2008.

[18] Z. H. Jin, P. Gumbsch, E. Ma, K. Albe, K. Lu, H. Hahn, and H. Gleiter. The interaction mechanism of screw dislocations with coherent twin boundaries in different face-centred cubic metals. *Scripta Materialia*, 54(6):1163–1168, March 2006. 4, 31, 58, 63, 70, 82, 85, 93

[19] T. Zhu, J. Li, A. Samanta, H. G. Kim, and S. Suresh. Interfacial plasticity governs strain rate sensitivity and ductility in nanostructured metals. *Proceedings of the National Academy of Sciences*, 104(9):3031–3036, February 2007. 5, 63, 68, 82, 93, 106

[20] Z. H. Jin, P. Gumbsch, K. Albe, E. Ma, K. Lu, H. Gleiter, and H. Hahn. Interactions between non-screw lattice dislocations and coherent twin boundaries in face-centered cubic metals. *Acta Materialia*, 56(5):1126–1135, March 2008. 2, 4, 31, 58, 63, 68, 70, 72, 82, 83, 86, 87

[21] G. H. Bishop, W.H. Hartt, and G. A. Bruggeman. Grain boundary faceting of $\langle 1010 \rangle$ tilt boundaries in zinc. *Acta Metallurgica*, 19(1):37–47, January 1971. 3

[22] P. J. Goodhew, T.Y. Tan, and R. W. Balluffi. Low energy planes for tilt grain boundaries in gold. *Acta Metallurgica*, 26(4):557–567, April 1978. 3, 112

[23] T. E. Hsieh and R. W. Balluffi. Observations of roughening/de-faceting phase transitions in grain boundaries. *Acta Metallurgica*, 37(8):2133–2139, August 1989. 3, 112, 113, 116, 126

[24] D. L. Medlin. Morphological evolution and junction dynamics at faceted grain boundaries. *Microscopy and Microanalysis*, 8:1400–1401, August 2002. 3, 116

[25] T. Muschik, W. Laub, M. W. Finnis, and W. Gust. Energetic and kinetic aspects of the faceting transformation of a $\Sigma 3$ grain boundary in Cu. *Acta Metallurgica et Materialia*, 41(7):2163–2171, July 1993. 3

[26] A. I. Barg, E. Rabkin, and W. Gust. Faceting transformation and energy of a $\Sigma 3$ grain boundary in silver. *Acta Metallurgica et Materialia*, 43(11):4067–4074, November 1995. 3

[27] S. B. Lee, N. M. Hwang, D. Y. Yoon, and M. F. Henry. Grain boundary faceting and abnormal grain growth in nickel. *Metallurgical and Materials Transactions A-Physical Metallurgy and Materials Science*, 31(3A):985–994, March 2000. 3

[28] A. M. Donald and L. M. Brown. Grain boundary faceting in Cu-Bi alloys. *Acta Metallurgica*, 27(1):59–66, January 1979. 3

[29] W. Krakow and D. A. Smith. The observation of various grain boundary atomic structures in Au by high-resolution electron microscopy. *Journal of Materials Research*, 1: 47–59, January 1986. 3

[30] K. H. Westmacott and D. Dahmen. Studies of faceting by high voltage/high resolution microscopy. In S. Ranganathan, C.S. Pande, and B.B. Rath, editors, *Interfaces: Structure and Properties*, chapter 3, pages 133–146. Trans Tech Pubn, 1993. ISBN 0878496130. 3, 7, 113, 126

[31] T. Gemming, S. Nufer, W. Kurtz, and M. Rühle. Structure and chemistry of symmetrical tilt grain boundaries in α-Al_2O_3: I, Bicrystals with "clean" interface. *Journal of the American Ceramic Society*, 86(4):581–589, April 2003. 3

[32] S. B. Lee, W. Sigle, and M. Rühle. Faceting behavior of an asymmetric $SrTiO_3$ $\Sigma 5$ $[001]$ tilt grain boundary close to its defaceting transition. *Acta Metarialia*, 51(15):4583–4588, September 2003. 3

[33] Y. K. Cho and D. Y. Yoon. Faceting of high-angle grain boundaries in titanium-excess $BaTiO_3$. *Journal of the American Ceramic Society*, 87(3):438–442, 2004. 3

[34] R. C. Pond and V. Vitek. Periodic grain boundary structures in aluminium. I. A combined experimental and theoretical investigation of coincidence grain boundary structure in aluminium. *Proceedings of the Royal Society of London. Series A, Mathematical and Physical Sciences*, 357(1691):453–470, November 1977. 3, 110

[35] G. Poli and L. P. Bicelli. Discussion of "growth twins in the FCC metals" [j. w. faust, and h. f. john (pp. 463–464, vol. 110, no. 5)]. *Journal of Electrochemical Society*, 110 (12):1291–1292, December 1963. 3, 58

[36] J. W. Faust and H. F. John. Growth twins in the FCC metals. *Journal of Electrochemical Society*, 110(5):463–464, May 1963. 3, 58

[37] C. C. Lo, J. A. Augis, and M. R. Pinnel. Hardening mechanisms of hard gold. *Journal of Applied Physics*, 50(11):6887–6891, 1979. 3, 56, 57, 59

[38] X. Zhang, A. Misra, H. Wang, T. D. Shen, J. G. Swadener, J. D. Embury, H. Kung, R. G. Hoagland, and M. Nastasi. Strengthening mechanisms in nanostructured copper/304

stainless steel multilayers. *Journal of Materials Research*, 18(7):1600–1606, July 2003. 3, 56, 57, 58

[39] L. Lu, D. Ming, T. Zhu, and J. Li. Size dependence of rate-controlling deformation mechanisms in nanotwinned copper. *Scripta Materialia*, 60(12):1062–1066, June 2009. 4, 59

[40] L. Lu, R. Schwaiger, Z. W. Shan, M. Dao, K. Lu, and S. Suresh. Nano-sized twins induce high rate sensitivity of flow stress in pure copper. *Acta Materialia*, 53(7):2169–2179, 2005. 4, 59, 61

[41] E. O. Hall. The deformation and ageing of mild steel: III Discussion of results. *Proceedings of the Physical Society. Section B*, 64(9):747, 1951. 5, 45, 55, 62

[42] N. J. Petch. The cleavage strength of polycrystals. *The Journal of the Iron and Steel Institute*, 174:25, 1953. 5, 45, 55, 62

[43] L. Lu, X. Chen, X. Huang, and K. Lu. Revealing the maximum strength in nanotwinned copper. *Science*, 323(5914):607–610, January 2009. 5, 59, 60, 61, 62, 64, 93, 105, 106, 108

[44] K. A. Afanasyev and F. Sansoz. Strengthening in gold nanopillars with nanoscale twins. *Nano Letters*, 7(7):2056–2062, July 2007. 5, 63, 74, 81

[45] I. Shabib and R. E. Miller. Deformation characteristics and stress-strain response of nanotwinned copper via molecular dynamics simulation. *Acta Materialia*, 57(15):4364–4373, September 2009. 5, 63, 105

[46] S. D. Murray and M. I. Baskes. Embedded-atom method: Derivation and application to impurities, surfaces, and other defects in metals. *Physical Review B*, 29(12):6443, 1984. 5, 48, 49, 111

[47] C. Herring. Some theorems on the free energies of crystal surfaces. *Physical Review*, 82 (1):87–93, April 1951. 7, 126

[48] A. P. Sutton and R. W. Balluffi. *Interfaces in Crystalline Materials (Monographs on the Physics and Chemistry of Materials)*. Oxford University Press, USA, 1995. ISBN 019921106X. 7

[49] J. C. Hamilton, D. J. Siegel, I. Daruka, and F. Leonard. Why do grain boundaries exhibit finite facet lengths? *Physical Review Letters*, 90(24):246102, June 2003. 7, 8, 111, 112, 119, 120, 121, 122, 124

[50] C. J. Bradley and A. P. Cracknell. *The mathematical theory of symmetry in solids*. Clarendon Press, 1972. 10, 14

[51] C. Kittel. *Introduction to Solid State Physics*. Wiley, 1995.

[52] P. Kidd A. Kelly, G. W. Groves. *Crystallography and Crystal Defects*. Wiley, 2000.

[53] M. I. Aroyo, U. Mller, and H. Wondratschek. *International Tables for Crystallography*, volume A1, chapter 1.1, pages 2–5. International Union of Crystallography, 2006. 10, 14

[54] V. Vitek. Intrinsic stacking faults in body-centred cubic crystals. *Philosophical Magazine*, 18(154):773–786, 1968. 20

[55] S. Kibey, J. B. Liu, D. D. Johnson, and H. Sehitoglu. Generalized planar fault energies and twinning in cu–al alloys. *Applied Physics Letters*, 89(19):191911, 2006. 20

[56] J. P. Hirth and J. Lothe. *Theory of Dislocations*. John Wiley & Sons, 2 edition, 1982. 21, 22, 24, 25, 42, 49, 75, 76, 96, 99, 104, 105

[57] D. Roundy, C. R. Krenn, M. L. Cohen, and J. W. Morris. Ideal shear strengths of fcc aluminum and copper. *Physical Review Letters*, 82(13):2713, 1999. 22

[58] M. L. Kronberg and F. H. Wilson. Secondary re-crystallization in copper. *Transactions of the American Institute of Mining and Metallurgical Engineers*, 185:501, 1949. 26

[59] K. T. Aust and J. W. Rutter. Temperature dependence of grain migration in high purity lead containing small additions of tin. *Transactions of the American Institute of Mining and Metallurgical Engineers*, 215:820–831, 1959. 26

[60] W. Bollmann. On the geometry of grain and phase boundaries I. General theory. *Philosophical Magazine*, 16(140):363–381, August 1967. 26

[61] W. Bollmann. *Crystal Defects and Crystalline Interfaces*. Springer-Verlag New York, LLC, November 1970. 26

[62] D. G. Brandon. The structure of high-angle grain boundaries. *Acta Metallurgica*, 14: 1479–1484, 1966. 26

[63] D. L. Olmsted, S. M. Foiles, and E. A. Holm. Survey of computed grain boundary properties in face-centered cubic metals: I. Grain boundary energy. *Acta Materialia*, 57 (13):3694–3703, August 2009. 26, 115

[64] D. L. Olmsted, E. A. Holm, and S. M. Foiles. Survey of computed grain boundary properties in face-centered cubic metals: II. Grain boundary mobility. *Acta Materialia*, 57(13):3704–3713, August 2009. 26, 115

[65] M. Bevis and A. G. Crocker. Twinning shears in lattices. *Proceedings of the Royal Society of London. Series A, Mathematical and Physical Sciences*, 304(1476):123–134, 1968. 27, 29

[66] B. A. Bilby and A. G. Crocker. The theory of the crystallography of deformation twinning. *Proceedings of the Royal Society of London. Series A, Mathematical and Physical Sciences*, 288(1413):240–255, 1965. 28

[67] J. W. Christian. *The Theory of Transformations in Metals and Alloys*. Pergamon, 2002. 29

[68] M. J. Buerger. The genesis of twin crystals. *American Mineralogist*, 30:469–482, 1945. 31, 58

[69] J. W. Christian and S. Mahajan. Deformation twinning. *Progress in Materials Science*, 39(1-2):1–157, 1995. 31

[70] S. Mahajan and G.Y. Chin. Twin-slip, twin-twin and slip-twin interactions in co-8 wt.% fe alloy single crystals. *Acta Metallurgica*, 21(2):173–179, February 1973. 32

[71] L. Remy. Twin-slip interaction in FCC crystals. *Acta Metallurgica*, 25(6):711–714, June 1977. 32

[72] T. Y. Thomas. On the stress-strain relations for cubic crystals. *Proceedings of the National Academy of Sciences of the United States of America*, 55(2):235–239, February 1966. 34

[73] T.C. T. Ting. *Anisotropic Elasticity*. Oxford University Press, February 1996. 39

[74] V. Bulatov and W. Cai. *Computer Simulations of Dislocations*. Oxford University Press, USA, 2006. 39

[75] M. Peach and J. S. Koehler. The forces exerted on dislocations and the stress fields produced by them. *Physical Review*, 80(3):436–439, November 1950. 44

[76] J. D. Eshelby, F. C. Frank, and F. R. N. Nabarro. The equilibrium of linear arrays of dislocations. *Philosophical Magazine*, 42(327):351–364, April 1951. 44

[77] F. C. Frank and W. T. Read. Multiplication processes for slow moving dislocations. *Physical Review*, 79(4):722–723, August 1950. 45

[78] D. M. Barnett and J. Lothe. An image force theorem for dislocations in anisotropic bicrystals. *Journal of Physics F: Metal Physics*, 4(10):1618–1635, 1974. 45, 46

[79] J. W. Christian and V. Vitek. Dislocations and stacking faults. *Reports on Progress in Physics*, 33(1):307–, 1970. 47

[80] A. D. Brailsford. Effective line tension of a dislocation. *Physical Review*, 139(6A): A1813–, September 1965. 47, 104

[81] M. Koning, R. Miller, V. V. Bulatov, and F. F. Abraham. Modelling grain-boundary resistance in intergranular dislocation slip transmission. *Philosophical Magazine A*, 82 (13):2511–2527, 2002. 47, 57, 104

[82] M. J. Stott and E. Zaremba. Quasiatoms: An approach to atoms in nonuniform electronic systems. *Physical Review B*, 22(4):1564, 1980. 48, 49

[83] Y. Mishin, D. Farkas, M. J. Mehl, and D. A. Papaconstantopoulos. Interatomic potentials for monoatomic metals from experimental data and ab initio calculations. *Phys. Rev. B*, 59(5):3393–, February 1999. 50

[84] K. Sugihara S. N. Chiu A. Okabe, B. Boots and S. N. Chiu. *Spatial Tessellations: Concepts and Applications of Voronoi Diagrams*. Wiley, 2 edition, 2000. 50

[85] M. van Kreveld M. de Berg, O. Cheong and M. Overmars. *Computational Geometry: Algorithms and Applications*. Springer-Verlag, 3 edition, 2008. 50

[86] A. P. Thompson, S. J. Plimpton, and W. Mattson. General formulation of pressure and stress tensor for arbitrary many-body interaction potentials under periodic boundary conditions. *Journal of Chemical Physics*, 131(15):154107–6, October 2009. 51

[87] W. G. Hoover. Canonical dynamics: Equilibrium phase-space distributions. *Physical Review A*, 31(3):1695–, March 1985. 51

[88] S. Melchionna, G. Ciccotti, and B. L. Holian. Hoover NPT dynamics for systems varying in shape and size. *Molecular Physics: An International Journal at the Interface Between Chemistry and Physics*, 78(3):533–544, 1993. 51

[89] W. G. Hoover. Constant-pressure equations of motion. *Physical Review A*, 34(3):2499–2500, September 1986. 51

[90] S. Plimpton. Fast parallel algorithms for short-range molecular dynamics. *Journal of Computational Physics*, 117(1):1–19, March 1995. 51, 52, 66

[91] C. L. Kelchner, S. J. Plimpton, and J. C. Hamilton. Dislocation nucleation and defect structure during surface indentation. *Physical Review B*, 58(17):11085, 1998. 53, 66, 92

[92] F. R. N. Nabarro. Theoretical and experimental estimates of the peierls stress. *Philosophical Magazine A*, 75(3):703–711, 1997. 54

[93] V. V. Bulatov, O. Richmond, and M. V. Glazov. An atomistic dislocation mechanism of pressure-dependent plastic flow in aluminum. *Acta Materialia*, 47(12):3507–3514, September 1999.

[94] D. L. Olmsted, K. Y. Hardikar, and R. Phillips. Lattice resistance and peierls stress in finite size atomistic dislocation simulations. *Modelling and Simulation in Materials Science and Engineering*, 9(3):215, 2001. 54

[95] M. Bujard, G. Gremaud, and W. Benoit. Study of the dislocation mechanism responsible for the bordoni relaxation in aluminum by the two-wave acoustic coupling method. *Journal of Applied Physics*, 62(8):3173–3183, 1987. 54

[96] J. S. Koehler. Attempt to design a strong solid. *Physical Review B*, 2(2):547–551, July 1970. 55

[97] R. G. Hoagland, R. J. Kurtz, and C. H. Henager. Slip resistance of interfaces and the strength of metallic multilayer composites. *Scripta Materialia*, 50(6):775–779, March 2004. 55

[98] G. D. Hughes, S. D. Smith, C. S. Pande, H. R. Johnson, and R. W. Armstrong. Hall-petch strengthening for the microhardness of twelve nanometer grain diameter electrodeposited nickel. *Scripta Metallurgica*, 20(1):93–97, January 1986. 56, 57

[99] A. H. Chokshi, A. Rosen, J. Karch, and H. Gleiter. On the validity of the hall-petch relationship in nanocrystalline materials. *Scripta Metallurgica*, 23(10):1679–1683, October 1989. 56, 57

[100] G. W. Nieman, J. R. Weertman, and R. W. Siegel. Microhardness of nanocrystalline palladium and copper produced by inert-gas condensation. *Scripta Metallurgica*, 23 (12):2013–2018, December 1989. 56, 57

[101] K. Lu, W. D. Wei, and J. T. Wang. Microhardness and fracture properties of nanocrystalline Ni-P alloy. *Scripta Metallurgica et Materialia*, 24(12):2319–2323, December 1990. 56, 57

[102] A. Misra, M. Verdier, Y. C. Lu, H. Kung, T. E. Mitchell, M. Nastasi, and J. D. Embury. Structure and mechanical properties of Cu-X (X = Nb,Cr,Ni) nanolayered composites. *Scripta Materialia*, 39(4-5):555–560, August 1998. 56, 57

[103] S. Zhong, T. Koch, M. Wang, T. Scherer, S. Walheim, H. Hahn, and T. Schimmel. Nanoscale twinned copper nanowire formation by direct electrodeposition. *Small*, 5 (20):2265–2270, 2009. 56, 59

[104] X. Zhang, A. Misra, H. Wang, T. D. Shen, M. Nastasi, T. E. Mitchell, J. P. Hirth, R. G. Hoagland, and J. D. Embury. Enhanced hardening in Cu/330 stainless steel multilayers by nanoscale twinning. *Acta Materialia*, 52(4):995–1002, February 2004. 56, 58

[105] T. G. Nieh and J. Wadsworth. Hall-Petch relation in nanocrystalline solids. *Scripta Metallurgica et Materialia*, 25(4):955–958, April 1991. 57

[106] S. Yip. Nanocrystals: The strongest size. *Nature*, 391(6667):532–533, February 1998.

[107] J. Schiotz, F. D. Di. Tolla, and K. W. Jacobsen. Softening of nanocrystalline metals at very small grain sizes. *Nature*, 391(6667):561–563, February 1998.

[108] J. Schiotz and K. W. Jacobsen. A maximum in the strength of nanocrystalline copper. *Science*, 301(5638):1357–1359, September 2003. 57

[109] P. G. Sanders, J. A. Eastman, and J. R. Weertman. Elastic and tensile behavior of nanocrystalline copper and palladium. *Acta Materialia*, 45(10):4019–4025, October 1997. 57

[110] E. Ma. Instabilities and ductility of nanocrystalline and ultrafine-grained metals. *Scripta Materialia*, 49(7):663–668, October 2003. 57, 61, 81

[111] W. Nix. Mechanical properties of thin films. *Metallurgical and Materials Transactions A*, 20(11):2217–2245, 1989. 62

[112] A. G. Froseth, H. Van Swygenhoven, and P. M. Derlet. The influence of twins on the mechanical properties of nc-Al. *Acta Materialia*, 52(8):2259–2268, May 2004. 62, 63, 85

[113] A. G. Froseth, P. M. Derlet, and H. Van Swygenhoven. Grown-in twin boundaries affecting deformation mechanisms in nc-metals. *Applied Physics Letters*, 85(24):5863–5865, 2004. 62, 63, 85

[114] Z. M. Chen, Z. H. Jin, and H. J. Gao. Repulsive force between screw dislocation and coherent twin boundary in aluminum and copper. *Physical Reivew B*, 75(21):212104–4, June 2007. 63

[115] C. Deng and F. Sansoz. Enabling ultrahigh plastic flow and work hardening in twinned gold nanowires. *Nano Letters*, 9(4):1517–1522, April 2009. 63

[116] X. Y. Li, Y. J. Wei, L. Lu, K. Lu, and H. J. Gao. Dislocation nucleation governed softening and maximum strength in nano-twinned metals. *Nature*, 464(7290):877–880, April 2010. 63, 64, 93

[117] J. Li. Atomeye: an efficient atomistic configuration viewer. *Modelling and Simulation in Materials Science and Engineering*, 11(2):173–177, 2003. 67

[118] X. Zhang, H. Wang, X. H. Chen, L. Lu, K. Lu, R. G. Hoagland, and A. Misra. High-strength sputter-deposited Cu foils with preferred orientation of nanoscale growth twins. *Applied Physics Letters*, 88(17):173116–3, April 2006. 68

[119] J. Wang and H. C. Huang. Novel deformation mechanism of twinned nanowires. *Applied Physics Letters*, 88(20):203112–3, May 2006. 74, 81

[120] L. E. Murr, E. Moin, F. Greulich, and K. P. Staudhammer. The contribution of deformation twins to yield stress: The Hall-Petch law for inter-twin spacing. *Scripta Metallurgica*, 12(11):1031–1035, 1978. 82

[121] C. S. Hartley. The effect of uniaxial stress on dislocation reactions at coherent twin boundaries in FCC metals. *Materials Science and Engineering*, 81:543–551, August 1986. 83

[122] V. Bulatov, F. F. Abraham, L. Kubin, B. Devincre, and S. Yip. Connecting atomistic and mesoscale simulations of crystal plasticity. *Nature*, 391(6668):669–672, February 1998. 99

[123] P. S. Follansbee and U. F. Kocks. A constitutive description of the deformation of copper based on the use of the mechanical threshold stress as an internal state variable. *Acta Metallurgica*, 36(1):81–93, January 1988. 107

[124] L. Lu, R. Schwaiger, Z. W. Shan, M. Dao, K. Lu, and S. Suresh. Nano-sized twins induce high rate sensitivity of flow stress in pure copper. *Acta Materialia*, 53(7):2169–2179, April 2005. 107

[125] R. Schwaiger, B. Moser, M. Dao, N. Chollacoop, and S. Suresh. Some critical experiments on the strain-rate sensitivity of nanocrystalline nickel. *Acta Materialia*, 51(17): 5159–5172, October 2003. 107

[126] J. Bonneville and B. Escaig. Cross-slipping process and the stress-orientation dependence in pure copper. *Acta Metallurgica*, 27(9):1477–1486, September 1979. 107

[127] J. Bonneville, B. Escaig, and J. L. Martin. A study of cross-slip activation parameters in pure copper. *Acta Metallurgica*, 36(8):1989–2002, August 1988. 107

[128] P. Neumann. Analytical solution for the incompatibility stresses at twin boundaries in cubic crystals. In X.R. Wu and Z.G. Wang, editors, *Fatigue 99: Proceedings of the Seventh International Fatigue Congress in Beijing, China*, pages 107–114, Beijing, China, 1999. Higher Education Press. 108

[129] C. Blochwitz and W. Tirschler. Influence of texture on twin boundary cracks in fatigued austenitic stainless steel. *Materials Science and Engineering A*, 339(1-2):318–327, January 2003.

[130] P. Gopalan and H. Margolin. Elastic stresses, twin boundaries and fatigue cracking. *Materials Science and Engineering: A*, 142(1):11–23, August 1991.

[131] A. Heinz and P. Neumann. Crack initiation during high cycle fatigue of an austenitic steel. *Acta Metallurgica et Materialia*, 38(10):1933–1940, October 1990.

[132] P. Neumann and A. Tonnessen. Cyclic deformation and crack initiation. In R.O. Ritchie and E.A. Starke, editors, *Fatigue 87: Proceedings of the Third International Conference on Fatigue and Fatigue Thresholds*, pages 3–22, Charlottesville, 1987. 108

[133] S. Qu, P. Zhang, S.D. Wu, Q.S. Zang, and Z.F. Zhang. Twin boundaries: Strong or weak? *Scripta Materialia*, 59(10):1131–1134, November 2008. 108

[134] N. Thompson. Fracture. In B.L. Averbach, D.K. Felbeck, J.T. Hahn, and D.S. Thomas, editors, *Proceedings of the International Conference on Atomic Mechanisms of Fracture*, pages 354–375, London, 1959. Chapman and Hall. 108

[135] Z. R. Wang and H. Margolin. Mechanism for the formation of high cycle fatigue cracks at FCC annealing twin boundaries. *Metallurgical and Materials Transactions A*, 16(5): 873–880, May 1985. 108

[136] C. J. Shute, B. D. Myers, S. Xie, T. W. Barbee Jr., A. M. Hodge, and J. R. Weertman. Microstructural stability during cyclic loading of multilayer copper/copper samples with nanoscale twinning. *Scripta Materialia*, 60(12):1073–1077, June 2009. 108

[137] L. Lu. Current progress of mechanical properties of metals with nano-scale twins. *Journal of Materials Science and Technology*, 24(4):473–482, 2008. 108

[138] A. F. Voter and S. P. Chen. Accurate interatomic potentials for Ni, Al and Ni_3Al. In R. W. Siegel, J. R. Weertman, and R. Sinclair, editors, *Charaterization of Defects in Materials*, volume 82, pages 175–180. Materials Research Society, 1987. 112

[139] I. Daruka and J. C. Hamilton. Atomistic and lattice model of a grain boundary defaceting phase transition. *Physical Review Letters*, 92(24):246105, June 2004. 112, 113, 116

[140] A. Oswald, W. Laub, W. Gust, and R. A. Fournelle. Kinetic aspects of the faceting transformation of grain boundaries. In D. E. Laughlin W. A. Soffa W. C. Johnson, J. M. Howe, editor, *Solid-Solid Phase Transformations*. TMS International, 1994. 115, 123

[141] G. D. Sukhomlin and A. V. Andreeva. Particular properties of $\Sigma = 3^n$ boundaries in FCC polycrystals. I. Crystallographical parameters and grain boundary faceting during annealing. *Physica Status Solidi*, 78A(1):333–341, 1983. 126, 127

[142] V. Randle. The role of the grain boundary plane in cubic polycrystals. *Acta Materialia*, 46(5):1459–1480, March 1998. 126, 127

[143] E. A. Holm and S. M. Foiles. How grain growth stops: A mechanism for grain-growth stagnation in pure materials. *Science*, 328(5982):1138–1141, May 2010. 126

[144] D. M. Saylor, B. S. El Dasher, A. D. Rollett, and G. S. Rohrer. Distribution of grain boundaries in aluminum as a function of five macroscopic parameters. *Acta Materialia*, 52(12):3649–3655, July 2004. 126

[145] J. Li, S. J. Dillon, and G. S. Rohrer. Relative grain boundary area and energy distributions in nickel. *Acta Materialia*, 57(14):4304–4311, August 2009. 126

[146] H.K.D.H. Bhadeshia. *Worked examples in the Geometry of Crystals*. the Institute of Materials, 2 edition, 2001. 137

[147] S. G. Lekhnitskii. *Theory of elasticity of an anisotropic elastic body*. Holden-Day series in mathematical physics. San Francisco, Holden-Day, 1963. 146, 149

[148] I. S. Sokolnikoff. *Mathematical Theory of Elasticity*. Krieger Pub Co, Jun 1983. 146, 149

[149] R. L. Lin and C. C. Ma. Antiplane deformations for anisotropic multilayered media by using the coordinate transform method. *Journal of Applied Mechanics*, 67(3):597–605, September 2000. 149

[150] C. C. Ma and H. T. Lu. Theoretical analysis of screw dislocations and image forces in anisotropic multilayered media. *Physical Review B*, 73(14):144102–12, April 2006. 149